AN INVESTIGATION OF MIXED OXIDE COMBUSTION CATALYSTS

By

Mairead U. Feeley, B. Sc (Hons)

A Thesis presented to Dublin City University for the degree of Doctor of Philosophy.

This work was carried out under the supervision of Dr. Odilla Finlayson and Dr. Michael Tiernan, School of Chemical Sciences, at Dublin City University.

June, 2004

I hereby certify that this material, which I now submit for assessment on the programme of study leading to the award of PhD is entirely my own work and has not been taken from the work of others save and to the extent that such work has been cited and acknowledged within the text of my work.

Signed: Mairead Feely

ID No : 95306960

Date : 11-06-04

Chapter 2: Preparation and Characterisation Techniques Used.

Chapter 3: Preparation and Investigation of Ceria-Zirconia Combustion Catalysts.

Chapter 4: Preparation and Investigation of Manganese-Zirconia Mixed Oxide Combustion Catalysts.

Chapter 5: Preparation and Investigation of Cobalt-Zirconia and Copper-Zirconia Mixed Oxide Combustion Catalysts.

ABSTRACT

A variety of transition metal oxides, consisting of a transition metal (manganese, copper, cerium or cobalt) oxide and zirconia, were investigated for the combustion of methane and propane and attempts were made to associate surface, redox and structural properties with catalytic activity. In particular, the manganese-zirconia system was studied in detail. The effect of high temperature (800°C) aging on the surface areas, structure, reducibility and activity of the calcined catalysts was determined.

The preparation method used had a significant effect on the structures of all the oxides studied. Ceria-zirconia mixed oxides prepared by a modified sol-gel method had higher surface areas and higher activity than the corresponding samples prepared by the co-precipitation method. Manganese-zirconia, cobalt-zirconia and copper-zirconia mixed oxides were all prepared by the co-precipitation method and the final properties of the oxides were very sensitive to changes in preparation parameters within this method. Variations investigated included stirring time of precursor solution prior to addition of base, precursor concentrations, pH or volume of base added and addition of base to precursor solution or vica versa.

Of all the mixed oxides studied, the manganese-zirconia system, prepared by addition of ammonium hydroxide, show the best potential as possible alternatives to noble metal catalysts. Manganese oxide and manganese-zirconia mixed oxides were more active for methane combustion than a 0.5 wt% Pt/Al_2O_3. On aging, the mixed oxides gained activity in propane oxidation, while the temperatures at which 50% conversion of methane occurred remained the same, despite a significant decrease in surface. An increase in reducibility, as indicated by a decrease in the temperature corresponding to maximum reduction, occurred on aging for the mixed oxides. Under the same conditions, only a small decrease in activity of manganese oxide for both propane and methane oxidation occurred on aging, suggesting that the preparation method, as well as the presence of zirconium, may play an important role in the increased activity and reducibility on aging.

ACKNOWLEDGEMENTS

I wish to thank my supervisors, Dr. Odilla Finlayson and Dr. Michael Tiernan, for their support and guidance throughout my time at Dublin City University. I would also like to thank my fellow postgraduate students and all the technical staff in the School of Chemical Sciences, in particular Maurice and John.

I am very grateful to Phil Barnes and Elena Fesenko in the Center of Applied Catalysis in Huddersfield for allowing me to use their equipment on an ongoing basis and for all their hospitality, advice and patience during my visits. Also a word of thanks to Jim Rooney for all his help with the SDTA-TG work.

I must thank all present and past members of lab X149, in particular Orla and Mick, who have made the last few years very enjoyable and also the members of Brett Pauls group, with whom I have shared many a lunch over the years.

Finally, a very special thanks to my family and friends, especially my parents, my brother Enda, the girls and Derek, for all their support, advice and help.

Chapter 1:

Catalytic Oxidation of Hydrocarbons

1.1 Introduction

Ostwald proposed that a catalyst is a substance that accelerates the rate of a thermodynamically feasible chemical reaction without itself been consumed in the reaction (1). Catalysis plays an important role in the American chemical manufacturing industry and hence the U.S. economy due to lower operating costs, higher purity products and reduced environmental hazards over other chemical production processes (2). As a result, catalyst based synthesis accounts for more than 20% of all industrial production in the US and 90% of chemical manufacturing processes (3). Catalysts are manufactured for four different markets namely, refining, polymerization, chemicals and environmental, by more than 100 firms worldwide and the market in total is worth in excess of 10 billion dollars according to a public report on catalysis and biocatalysis technology published in 1998 by the National Institute of Standards and Technology in the U.S. (2).

Catalytic systems can be classified into three main categories: heterogeneous, homogeneous and enzymatic (4). Homogeneous catalysts are in the same phase as the reactants, e.g. the gas phase oxidation of sulphur dioxide by nitric oxide. Enzyme catalysts play a crucial role in metabolic processes. Heterogeneous catalysts are usually solid surfaces and are phase separated from the gas and/or liquid reactants surrounding them (4). Heterogeneous catalysts are often the most convenient to use due to ease of separation of the catalyst and the reactants and products. The main environmental application of heterogeneous catalysts is in motor vehicle emission control, which will be discussed later. Other important industrial heterogeneous catalytic processes are shown in Table 1.1. The catalyst alters the rate of the reaction by providing an alternative reaction mechanism with lower activation energy than the non-catalytic reaction (5).

Industrial process	Reaction	Catalyst	WAP * (million tones) (Ref)
SYNTHESIS			
Ammonia	$N_2 + 3H_2 \leftrightarrow 2NH_3$	Iron	140 (6)
Nitric acid	$4\ NH_3 + 5O_2 \leftrightarrow 4NO + 6H_2O$ $2NO + O_2 \leftrightarrow NO_2$ $2NO_2 \leftrightarrow N_2O_4$ $3N_2O_4 + 2H_2O \leftrightarrow 4HNO_3 + 2NO$	Pt/Rh gauze	60 (6)
Sulphuric acid	$2SO_2 + O_2 \leftrightarrow 2SO_3$	V_2O_5	>140 [6] (6)
Ethanoic acid	$CH_3OH + CO \rightarrow CH_3COOH$	Rh or Ir	6 (6)
Methanol	$CO + 2H_2 \leftrightarrow CH_3OH$ $CO_2 + 3H_2 \leftrightarrow CH_3OH + H_2O$	$Cu/ZnO/Al_2O_3$	$2.1*10^5$ (7)
PETROL SYNTHESIS			
Reforming	$C_6H_{14} \rightarrow C_6H_{12} \rightarrow C_6H_6$	Pt/Al_2O_3	(6)
Cracking	$C_7H_{16} \rightarrow C_3H_6 + C_4H_8$	zeolites	500 (6)
Isomerization	$C_5H_{12} \leftrightarrow$ 2-methylpentane $C_4H_{10} \leftrightarrow$ iso-C_4H_{10}	Pt/Al_2O_3 $AlCl_3$ and HCl	(6)
Hydrotreatment	$SC_4H_4 + H_2 \rightarrow C_4H_{10} + H_2S$	$CoS\text{-}MoS_2$	(7)
Polymerization - Ziegler-Natta	$C_2H_4 \rightarrow$-CH_2-CH_2-$(CH_2$-$CH_2)_n$-	$AlEt_3$ and $TiCl_4$	17.9 (8)

* WAP = World annual production (million tones of product).

Table 1.1: Important industrial catalytic reactions compiled from references quoted within table.

1.2 Heterogeneous Catalysis

The heterogeneous catalytic reaction process can be divided into 5 fundamental steps (4) (see Fig 1.1), namely:

1. Transport of reactant to the catalyst;

2. Adsorption of the reactant on the catalyst surface. At least one reactant must be chemisorbed for catalytic reaction to occur;

3. Reaction on the catalyst between two chemisorbed species or between one chemisorbed species and a reactant in the gas or liquid phase;

4. Desorption of the products from the catalyst surface;

5. Transport of the products through the gas phase away from the surface of the catalyst.

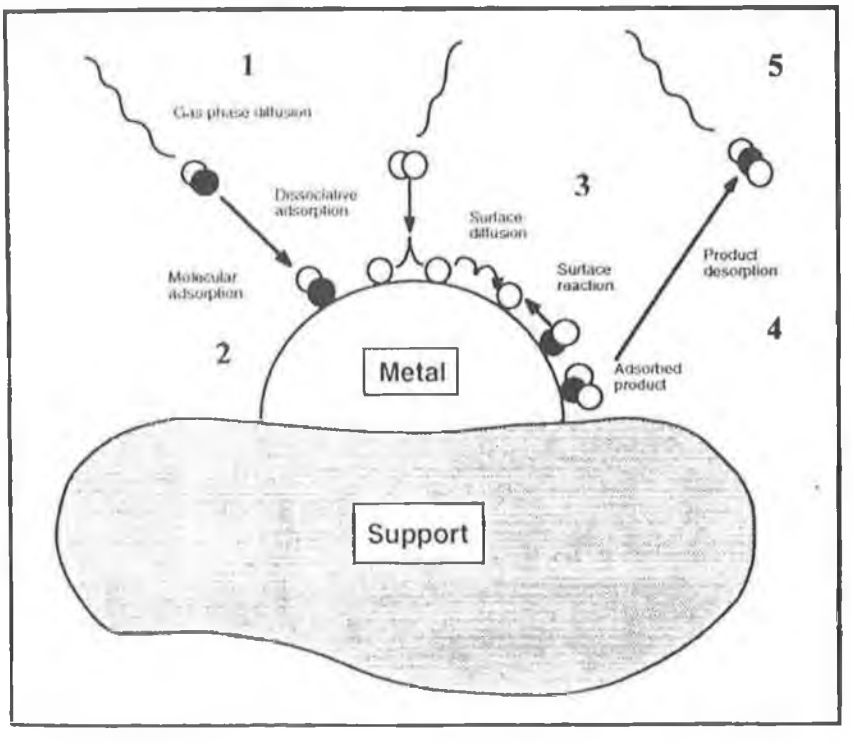

Fig 1. 1: Steps during a catalytic reaction (9).

Steps 2, 3 and 4 are chemical, involving electronic movement (4). Each of these steps has its own activation energy (5). The rates of step 2 and step 3 are influenced respectively by the total surface area of the catalyst and by the concentration of the various adsorbed species on the catalyst surface. The catalytic pathway has an activation energy for the formation of an intermediate surface complex, which is significantly less than that for the homogeneous uncatalysed reaction. Since the activation energy appears as an exponent in the rate equation, a small decrease in the activation energy has a marked influence on the reaction rate. The two key steps of adsorption and mass transport are now considered in more detail.

1.2.1 Adsorption

Step 2 in Fig 1.1 was adsorption of the reactant on the catalyst surface. Adsorption can be subdivided into two types: **physisorption** and **chemisorption.**

Physical adsorption or physisorption involves forces of molecular interaction such as Van der Waals forces (4), where no significant change in the electronic orbital pattern of the species involved is observed. Physical adsorption is completely reversible, equilibrium between the adsorbate and fluid phase is established very rapidly, there is no activation energy involved in the elementary step of adsorption from the gas phase and it is relatively nonspecific. The molar heats of adsorption, i.e. the heat released when a mole of substance is transferred from the gaseous to absorbed state, are usually in the range found for heats of liquidisation or vaporization i.e. 8-20 $kJmol^{-1}$. Physical adsorption is always exothermic and becomes multilayered at P/P_o values of approx 0.1 to 0.3 (5). P/Po is the relative pressure where P is the partial pressure of the vapour in the system and Po is the vapour pressure that would exist above a pure liquid at the same temperature.

Physical adsorption measurements of typically N_2 are used to determine the overall surface area, the average pore size and pore size distribution of a catalyst (5). Isotherms, i.e. plots of volumes adsorbed versus relative pressure at constant temperature, can be classified into five types as shown in Fig 1.2 (4).

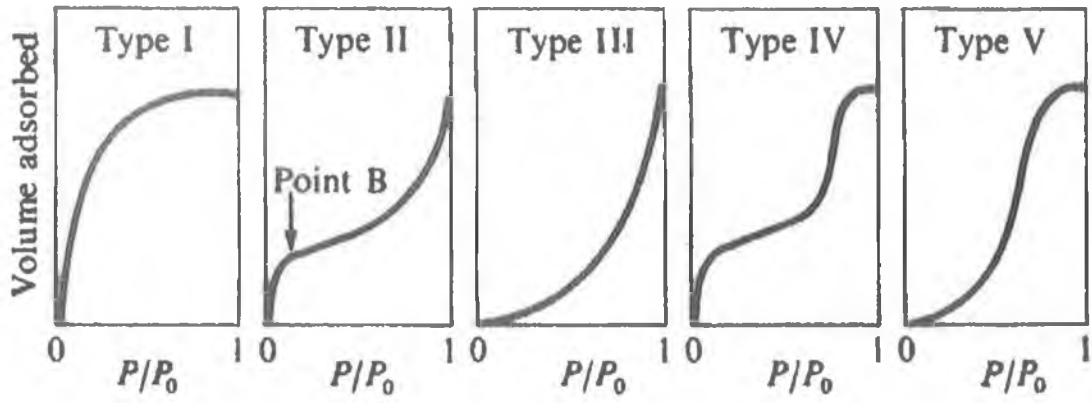

Fig 1.2: Typical types of adsorption isotherms (4).

Type I and II isotherms represent adsorption on micropores and nonporous structures (5). Type III occurs on surfaces where forces of adsorption are relatively weak and where no point corresponding to complete monolayer coverage is exhibited. Type IV is observed on porous materials with filling of pores. Type V is similar to type III at low pressures but condensation in pores occurs at higher partial pressures. Type I, II and IV are most commonly seen experimentally.

Evaluation of specific surface area from adsorption isotherms involves evaluation of the monolayer capacity and calculation of the specific area using the cross-sectional area of the adsorbate molecule (10). Evaluation of the monolayer capacity is determined using the BET equation. The equation was derived by Braunauer, Emmet and Teller and is shown below;

$$\frac{P}{x(P_o - P)} = \frac{1}{x_m C} + \frac{C-1}{x_m C} * \frac{P}{P_o} \qquad \text{(equation 1)}$$

where P = pressure, P_o = saturation pressure, C is a large constant , x_m is the monolayer quantity and x is the quantity adsorbed at pressure P (10). The monolayer quantity refers to the quantity of the adsorbate that can be accommodated in a completely filled, single layer of molecules (a monolayer) on the surface of the solid. It can be expressed in various units, the most common being cm^3 at STP per gram of solid.

This equation was derived assuming that the surface was an array of equivalent adsorption sites, each site being capable of adsorbing one molecule. When a molecule from the gas phase hits an empty adsorption site, it condenses there for a certain time interval and then evaporates. This condensation-evaporation cycle was first postulated by Langmuir but was only applied to monolayer coverage. The BET equation was derived based on the assumption that the condensation – evaporation cycle could also occur on second and higher molecular adsorption layers and that within each layer, dynamic equilibrium exists i.e. the number of molecules evaporating per second is equal to the number of molecules condensing per second on the layer immediately below. Other assumptions included that the heat of adsorption in all layers above the first is equal to the latent heat of condensation and the evaporation-condensation constants (i.e. frequency of oscillation of the adsorbed molecule divided by the condensation coefficient for molecules from the gas phase striking the molecules of a layer) in all layers above the first are identical.

Using the BET equation, a plot of $\frac{P}{x(P_o - P)}$ vs $\frac{P}{P_o}$, should give a straight line with slope of $\frac{C-1}{x_m C}$ and intercept of $\frac{1}{x_m C}$, thus allowing determination of x_m. Knowing the cross- sectional area of the adsorbed molecule, then allows calculation of the total surface area of the surface.

In general, type II isotherms are linear between relative pressures of about 0.05 and 0.35 (10). However as pointed out by Sing and Gregg (10), exceptions to this are demonstrated by the work of Isirikyran and Kiselev on graphitised carbon black where BET plots are only linear up to a relative pressure of 0.1. Optimum conditions for determining the monolayer accurately included type II isotherms with a relatively high value of C (in excess of 50) and hence having a sharp knee and a well-defined point B (see Fig 1.2). Point B is the point at which the linear portion begins and the level of adsorption at point B represents the monolayer capacity. The calculation of the specific surface area involved the use of the cross-sectional surface area of the adsorbed molecule (A_m). For nitrogen, A_m was calculated from the liquid density which assumes normal liquid packing of the adsorbate on the surface of the solids. Criticisms of the BET equation include the fact that the model assumes that the surface is energetically

homogeneous (10). However, in practice most surfaces are heterogeneous. The model also took account of vertical interactions between adsorbed molecules but neglected horizontal interactions, which can became significant at high surface coverages. It also assumed that the heat of adsorption in the multilayer was equal to the heat of condensation. However in a bulk liquid, molecules have 12 neighbours while in the BET model, adsorbed molecules only have two "vertical neighbours". Despite these limitations, comparisons of this technique with results determined by electron microscopy studies indicated that the BET method using N_2 adsorption led to a good estimate of surface area for non-porous solids (10).

If the solid surface is porous (mesopores present), the type II isotherm can be modified to a type IV isotherm (11). Porosity enhances surface area and pores are classified according to size. Pores of less than 1.5nm are micropores, whereas pores greater than 100nm are macropores. Mesopores have an average pore width between those values. Type IV isotherms resemble type II isotherms at low relative pressures but at higher relative pressures, adsorption in the mesopores leads to multilayer formation, until at a certain pressure, a sharp increase in the volume adsorbed is observed. This is caused by the onset of capillary condensation or pore filling. The plateau at very high relative pressures is reached when mesopore filling is complete. Hysteresis loops are also associated with Type IV isotherms, whereby evaporation of the adsorbate after saturation occurs at a pressure lower than that of capillary condensation. Hysteresis arises due to the difference between the pore filling and pore emptying mechanisms due to the shape of the pores. The Kelvin equation (equation 2) is used to calculate the radius of a pore, r, from the relative adsorption pressure P/Po at which the capillary condensation starts (7):

$$(r - t) = \frac{0.4078}{\log(P / P_o)} \qquad \text{(equation 2)}$$

where t is the statistical thickness of the adsorbed multilayer in nm and can be calculated from equation 3 at each partial pressure.

fragments on the surface. The strength of adsorption can be experimentally determined from the molar enthalpy of adsorption (4).

Bond (4) proposed that the catalytic activity of a surface and the strength of reactant adsorption on the surface were related as follows; "in a unimolecular reaction the catalytic activity is inversely related to the strength of chemisorption of the reactant, providing that adsorption is sufficiently strong for the adsorbate to achieve high surface coverage". This is represented by the "volcano curve" in Fig 1.3 (12).

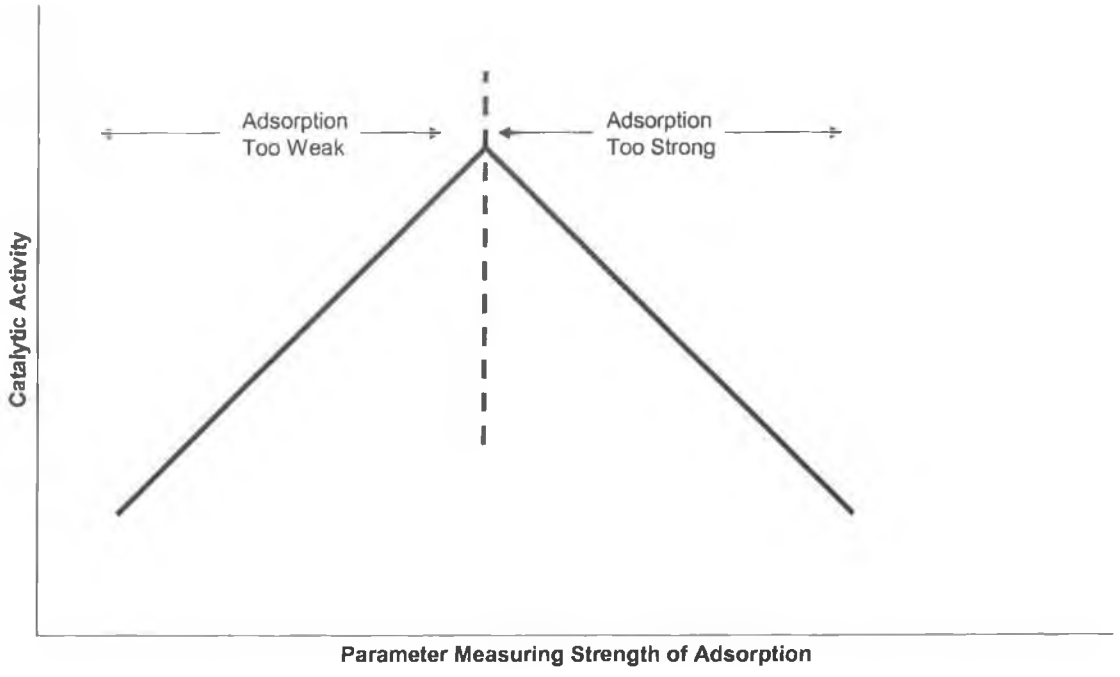

Fig 1.3: Catalytic activity as a function of strength of adsorption (12).

If the reactant is strongly bound to the surface, the activity declines either because the other reactant molecules cannot adsorb at the surface or the adsorbate molecules are immobilized on the surface. If the reactants are weakly bound, then activity will also be very low as the lifetime of the adsorbate may be too short for the reaction or only a small fraction of the surface is covered (4).

1.2.2 Mass Transport

Mass transfer is the physical process where reactants pass through the fluid phase surrounding the catalyst to the active sites on the catalyst surface and the products are transported from the catalyst (4)- see steps 1 and 5 in Fig 1.1. Mass transfer may be

internal where reactants move from the catalyst surface to the inside of the catalyst pore or external involving migration to the catalyst surface. Slow mass transfer is most likely to occur at interfacial boundaries and within pores and may limit the overall rate of the reaction. When steps 1 and 5 in Fig 1.1 are the slowest steps, the overall reaction rate is diffusion limited i.e. the rate is determined by the arrival of the reactants or departure of products.

It is important to know when external mass transfer limitations are occurring since it means that the catalyst is operating at less than its maximum capacity. The following experimental factors may indicate external diffusion limitations outside the particles (4):

- The rate of a catalytic reaction is not accurately proportional to the catalyst weight;
- Improving the movement of the gas phase raises the rate;
- The temperature co-efficient is low, i.e. Increasing the temperature doesn't increase the reaction rate significantly or as predicted by the Arrhenius equation and the rate is proportional to $T^{1/2}$, hence low apparent activation energy (10-15 $kJmol^{-1}$) are observed.

1.2.3 General Factors affecting catalytic activity and selectivity

Activity and selectivity are very important parameters in catalysis and refer to the rate of conversion of reactants to products and the degree to which one reaction is favoured compared to other thermodynamically possible reactions respectively. A commonly used index to allow comparison of catalytic activity is the temperature required for the reaction under consideration to reach an arbitrary degree (or rate) of conversion (13) or alternatively to measure the reaction rate at a certain temperature. However activity may decrease over time due to: poisoning, fouling, thermal deactivation, gas/ vapour solid reactions and/or mechanical failure (14) (see Table 1.2 for summary).

Of all the deactivation mechanisms shown in Table 1.2, fouling of a surface by carbon deposits and/or coke is most common for supported metals and can reduce catalyst activity dramatically. Carbon is formed from the splitting of CO and can exist in

various forms, namely, α-carbon, β-carbon and graphite. These are formed at different temperatures and differ in terms of reactivity, structure and morphology (14). α-carbon is in the form of an adsorbed atomic carbon, which can be subsequently converted into the β-carbon (a polymeric carbon film) at below 500°C. Above this temperature, crystalline graphite platelets and films are formed. Coke refers to condensed or high molecular weight hydrocarbons and is formed from the cracking of olefins, benzene or polynuclear aromatics on acid sites on oxide catalysts. The extent and rate of coke formation is dependent on hydrocarbon structure, reaction conditions (i.e. temperature), acid strength and pore structure.

Type	**Mechanism**	**Species responsible**	**Effects**
Poisoning	Strong chemisorption of contaminant species in gas phase	Group 5A and 6A Halogens, alkali Molecules with multiple bonds Unsaturated HC	Block adsorption sites Modify nearest metal atoms Cause reconstruction of surface
Fouling	Physical deposition of species from fluid phase on catalyst surface	Carbon – alpha, Beta and graphite Coke	Adsorption onto acidic sites Blocking of catalyst pores and active sites
Thermal Deactivation (Sintering)	Reduction of surface energy achieved by reduction in surface area. Surface diffusion and particle coalescence	Elevated temperatures > 500°C	Growth in catalyst crystallites Reduction in porosity Loss of support surface area
Gas/vapour solid reactions	Reaction of vapour phase with catalyst	Carbonyls, oxides, sulphides and halides	Production of inactive bulk and surface phases Production of volatile compounds
Solid-solid Reactions	Transformations from active to non active		

Table 1.2: Various mechanisms of deactivation of catalysts (as taken from ref 14).

Specific activity of a catalyst is affected by sintering depending on whether the reaction is structure sensitive or structure insensitive (14). For structure - sensitive reactions, e.g. ethane hydrogenolysis, ethane steam reforming and methane combustion over supported Pd and Pt catalysts (15), the catalytic activity depends on surface area of catalyst and the size of the metal crystallites. Catalytic activity per unit surface area is independent of changes in the metal crystallite size in structure sensitive reactions, e.g. CO hydrogenation on supported cobalt, nickel, iron and ruthenium (14).

1.3 Environmental Catalysis

Interaction of hydrocarbons with oxygen in the presence of a catalyst can result in either selective oxidation or complete oxidation depending on the catalyst and conditions used. In complete oxidation or combustion, the main products were carbon dioxide and water below 500°C although CO, H_2 and lower alkanes have also been formed above that temperature (16). Catalytic combustion of alkanes can be described by the following reaction:

$$C_nH_{2n+2} + (3n+1/2)O_2 \rightarrow n\ CO_2 + (n+1)\ H_2O.$$

In selective or partial oxidation, complete combustion is prevented and the intermediate oxidation products, which have the same carbon skeleton as the starting hydrocarbon, are formed. Three key types of selective oxidation reactions are observed and the starting hydrocarbon is normally an olefin or aromatic (4):

(1) Formation of oxygenated products without carbon-carbon bond fission, e.g. the oxidation of ethane to oxirane using a silver catalyst at approx 247°C.

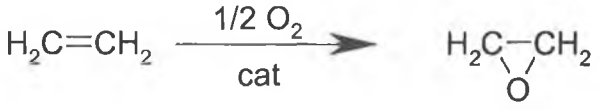

(2) The oxidative removal of hydrogen to form carbon-carbon double bonds (oxidative dehydrogenation) e.g. the dehydrogenation of butene to 1,3-butadiene using a manganese-iron spinel catalyst.

(3) Formation of nitriles or oxygenated species with carbon-carbon bond fission e.g. the formation of acrylonitrile from propene using a promoted bismuth molybdate catalyst ($Bi_2MoO_2Bi_2O_3MoO_3$) at 397°C- 497°C.

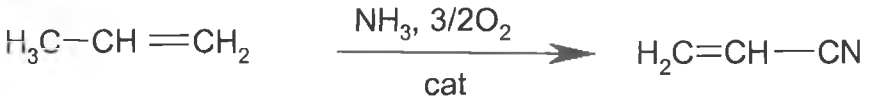

Catalytic combustion or complete oxidation plays an important role in the abatement of atmospheric pollution caused by various industries and automobile exhausts, e.g. NO_x, SO_x, CO and hydrocarbons (17). The combustion of methane, which is formed as a by-product in many industrial processes as well as being emitted from natural gas fueled vehicles and gas power plants, is of interest due to its significant greenhouse effect. Significant amounts of unburned hydrocarbons, carbon monoxide and nitrous oxides were emitted to the atmosphere from car exhausts (18). 40% of key air toxics emitted in urban areas come from motor vehicles (19) and motor vehicles contribute to 2/3 of CO emissions, more than a third of NO_2 and more than one-quarter of volatile organic compounds (VOC) (20). The levels of exhaust gas emissions are summarized in Table 1.3. Increasing awareness of pollution caused by various industries and automobile exhausts have prompted the introduction of stringent regulations on the emission of NO_x, SO_x and other greenhouse gases. For example by 2005 catalytic converters must have conversions in excess of 98% for a ULEV (Californian Ultra low emission vehicle) and in excess of 99% for SULEV (Californian Super Ultra low emission vehicle) with very fast light-off times in the region of 10-20 seconds (21). This will require a ten and four fold decrease in NO_x and hydrocarbon emissions respectively if Californian SULEV legislation is to be met.

Car exhaust emissions are hazardous as hydrocarbons and carbon monoxide react in the presence of sunlight to form ground level ozone, which is a major constituent of smog (18). The basic reactions for removal of CO and hydrocarbons in the exhaust are oxidation to CO_2, while the NO_x is reduced to N_2 and water. An automotive catalyst promotes the following reactions at lower temperatures than a thermal process, using a three way catalyst (twc):

Oxidation

$C_yH_n + (1+n/4)O_2 \rightarrow yCO_2 + n/2\ H_2O$

$CO + ½\ O_2 \rightarrow CO_2$

$CO_2 + H_2O \rightarrow CO_2 + H_2$

Reduction

$NO + CO \rightarrow 1/2\ N_2 + CO_2$

$NO + H_2 \rightarrow 1/2\ N_2 + H_2O$

$(2 + n/2)\ NO + C_yH_n \rightarrow (1+n/4)N_2 + yCO_2 + n/2\ H_2O$

Model Year	**grams per mile** **Carbon Monoxide**	**Hydrocarbons**	**Nitrogen Oxides**
Pre-1968 (Uncontrolled)	90.0	15.0	6.2
1970	34.0	4.1	-
1972	28.0	3.0	-
1973-74	28.0	3.0	3.1
1975-76	15.0	1.5	3.1
1977	15.0	1.5	3.1
1980	7.0	0.41	2.0
1981	3.4	0.41	1.0
1994-96 (Tier 1)	3.4 (4.2)	0.25 [a] (0.31)	0.4(0.6)
2004 (Tier 2) [b]	1.7 (1,7)	0.125[a] (0.125)	0.2 (0.2)

- Not applicable

Note: Figures in parenthesis apply to a useful life of 100,000 mile or ten years beyond the first 50,000 miles.

[a] Non –methane hydrocarbons

[b] The U.S. Environmental Protection Agency (EPA) could delay implementation until 2006.

Table 1.3: Progression of U.S exhaust emissions standards for light-duty gasoline-fuelled Vehicles (grams per mile) (22).

This simultaneous oxidation and reduction can be achieved in a narrow air/fuel ratio range (15:1) around the stoichiometric values. The TWC gas catalyst typically consists of 1-2g of platinum and 0.2-0.3 g of rhodium (23) dispersed on a thin layer of a porous material. This thin layer is typically in the form of a washcoat supported on a ceramic monolith or honeycomb surface and is composed mainly of high surface area alumina, which as been surface treated with cerium and zirconium oxides.

Ceria has a number of roles in TWC. These include:

- improvement in the dispersion of noble metals (24,25), by reducing aggregation of the noble metals in the catalyst;
- promotion of the water shift reaction over noble metal particles (26);
- stabilisation of γ-form and hence surface area of the alumina support (27);
- improving oxygen storage capacity (28).

The final role is the most important one since it ensures that the optimum gas composition required for efficient conversion is maintained. This is achieved via interconversion of Ce^{4+} and Ce^{3+} ions, enabling the adsorption of O_2 when operating conditions are lean and releasing oxygen when the fuel ratios are higher. High emission levels of hydrocarbons are found especially during the cold start period when the engine is not sufficiently warmed up, i.e. in the first 2 minutes of operation. In order to meet these regulations and reduce hydrocarbon cold start emissions, new technologies involving catalytic and engine design have been developed. From a catalytic perspective, the use of a close coupled catalyst was investigated. This involved the positioning of the close coupled catalyst adjacent to the exhaust manifold (less than 1 foot from the engine) and attached directly to the outlet of the exhaust manifold (29), so that the catalyst warmed up faster. This was used in conjunction with a conventional three way catalyst "under the floor" of the car, which was placed further upstream from the close-coupled catalyst. Hence the close-coupled catalyst was the first catalyst component that the exhaust gas encountered and the close coupled catalyst was exposed to high temperature exhaust gas immediately exiting the engine after it had warmed up. The close coupled catalyst presented in two patents by Heck (29,30) had no oxygen storage component (e.g. ceria) present but a high concentration of Pd, which removed

relatively high amounts of hydrocarbons and significant amount of CO. The ceria was omitted to reduce the exothermic oxidation of CO and hence prevent excess oxidation and overheating of the close coupled catalyst. Another reason for its omission was to avoid the detrimental reaction between ceria and Pd that may occur at high temperatures (30). Unreacted CO and other pollutants were then passed to the upstream underfloor three way catalyst (which had a OSC component). However this resulted in very high operating temperatures (1050°C) to which the close coupled catalyst was exposed and hence catalysts used must have significant thermal stability (21). Other strategies involve developing catalysts that work efficiently at lower temperatures, coating the catalysts onto metallic substrates, which are then electrically heated, and coating the catalysts onto substrates with very thin walls. The latter two strategies are to ensure that the catalyst heats up faster.

Catalytic combustion has been employed as an alternative to thermal combustion due to its greater efficiency, lower operating temperatures and reduced thermal NO_x emissions (31). In thermal combustion, flame temperatures up to between 1500 and 2000°C have been observed (15). At these temperatures, nitrogen and air react to form nitrogen oxides. Since the oxidation reactions involve homogeneous gas-phase radicals, operation control can be difficult. Another advantage of catalytic combustion is the wide range of fuel/air ratios that can be used. In thermal combustion, the feed composition must be within certain limits. If the fuel concentration is too high, there is a risk of explosion while a low fuel concentration causes unstable combustion flames. In contrast, stable combustion has been achieved catalytically at lean fuel mixtures.

The relationship between the reaction rate and the gas temperature of a combustion catalyst is described by Fig 1.4 (15). In region A and B, or the low temperature regions, the rate of combustion is controlled by the rate of reaction at the catalyst surface. The conversion rate increases exponentially with a rise in temperature. In region C or the medium temperature region, mass transfer from the bulk gas to the catalyst's active surface dominates the reaction rate. This mass diffusion becomes rate limiting and suppresses the increase in catalytic activity. In region D or the high temperature region, homogeneous combustion in the bulk gas phase begins simultaneously with the surface reaction and the reaction rate increases very sharply.

The various different classes of catalysts used for the combustion of alkanes have been reviewed extensively by Choudhary et al (17) and are summarized in Table 1.4. As noted by Choudhary et al (17), the majority of work on combustion catalysis has involved noble metal catalysts, mainly Pt and Pd.

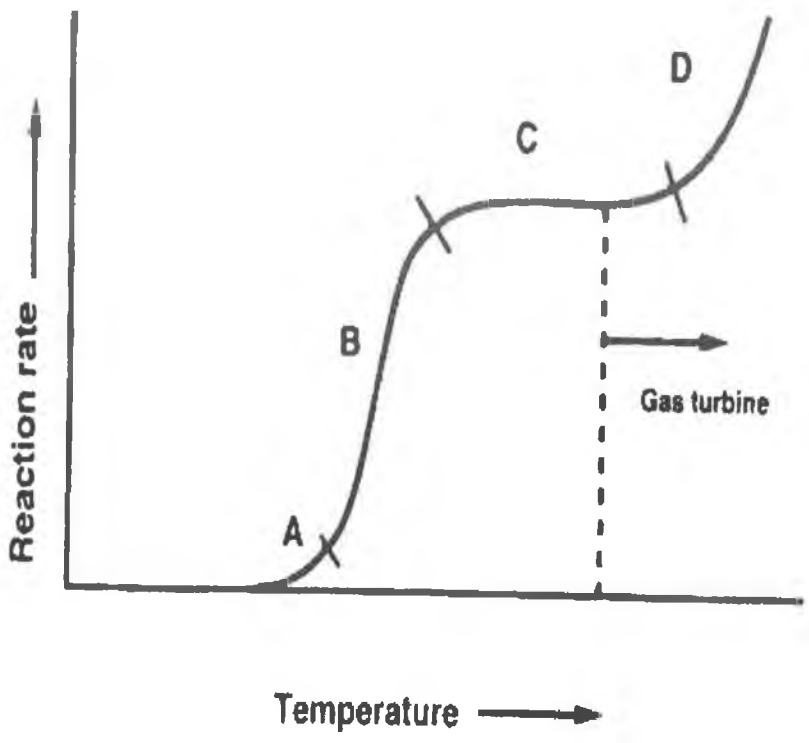

Fig 1.4: Typical rate curve for catalytic combustion (15).

Advantages of noble metal catalysts are their high intrinsic activity, which is related to their ability to activate H_2, O_2, C-H and O-H bonds and greater resistance to sulphur poisoning (32). Problems encountered with the operation of platinum and palladium catalysts include loss of platinum surface area in catalytic reforming and conversion of palladium to an inactive oxide at temperatures of 707-827°C in an oxidizing environment. Another significant disadvantage is the high cost and decreasing reserves of noble metals. Metal oxides are far cheaper and more available than noble metals, although they have significantly higher light-off temperatures. In this thesis, oxidation over metal oxides (simple and mixed) only will be discussed in the following sections, with primary focus on complete oxidation. Single metal oxides will be considered first followed by mixed metal oxides (supported metal oxides, perovskites and hexaaluminates), which have been further classified into smaller groups.

Class	Examples	Organic reactant
Noble metals	Pd/ZrO_2	methane
	Pd/Al_2O_3	methane
	Pd/SiO_2	methane
	PdO/CeO_2	CO
	Pd foil	Ethane, methane, propane butane
	Pt foils	Ethane, methane, propane and n-butane
	Pt/Al_2O_3	Propane, propene
Metal oxides	Co_3O_4, MnO_2, CuO, Mn_3O_4,Cr_2O_3	Propane, methane
Mixed metal oxides	Perovskites	methane
	Hexaaluminates	
	Zirconia doped with Mn, Co, Cr and Fe	Methane, propane
	Co supported on zirconia	Methane

Table 1.4 : Summary of the various classes of combustion catalysts reported in a review by Choudhary et al (17).

1.3.1 Oxidation over Single Metal Oxides

Metal oxides consist of two distinct sites - a positive charge associated with the metal cation and a negatively charged site associated with the oxygen ion. Golodets (33) subdivided the oxides into three different categories based on the heats of formation of metal oxides from the metal in the presence of oxygen (see Table 1.5).

$-\Delta H^{o}_{298K}$ (kcal/atom O g)$^{-1}$	**Metal**	**Oxide**
< 40	Pt, Pd, Ru, Rh, Ir , Au	Unstable oxides
40-65	Cu, Co, Fe, Ni, Re, Pb and Cd	Moderately stable
>65	Mo, Mn, Na, Zr, Al, Ce and Cr	Stable oxides

Table 1.5: Different categories of metal oxides based on the heat of formation (ΔH^{o}_{298K}) values.

This classification is important because it implied that metals with unstable oxides existed as metals under combustion or excess oxygen conditions and the oxidation mechanism of the hydrocarbon on such a surface would only involve molecular oxygen from the gas stream (12). For some oxides such as Co_3O_4 (34) and Mn_3O_4 (35), lattice oxygen has been shown to be involved in the total oxidation of propane and propylene through IR spectroscopy studies.

Moro-oka and Ozaki correlated the heats of formation of the oxide with rates of reaction for the oxidation of propylene (36) and isobutene, ethylene, acetylene and propane (37) in air. The heat of formation was divided by the number of oxygen atoms in the oxide to give an indication of strength of the metal-oxygen bond and was designated ΔH_o. It was found in both studies that the larger the heat of formation of the oxides, the less active was the catalyst (as determined by rates at 300°C). This is illustrated in Fig 1.5. This indicated that the slow or rate determining step of the reaction depended on the ΔH_o of the catalyst. As ΔH_o increased, the catalyst became increasingly covered with oxygen while the hydrocarbon coverage decreased. Hence the rate determining step shifted from the chemisorption of oxygen at low ΔHo to a surface reaction between the adsorbed oxygen and hydrocarbon at higher ΔH_o (37).

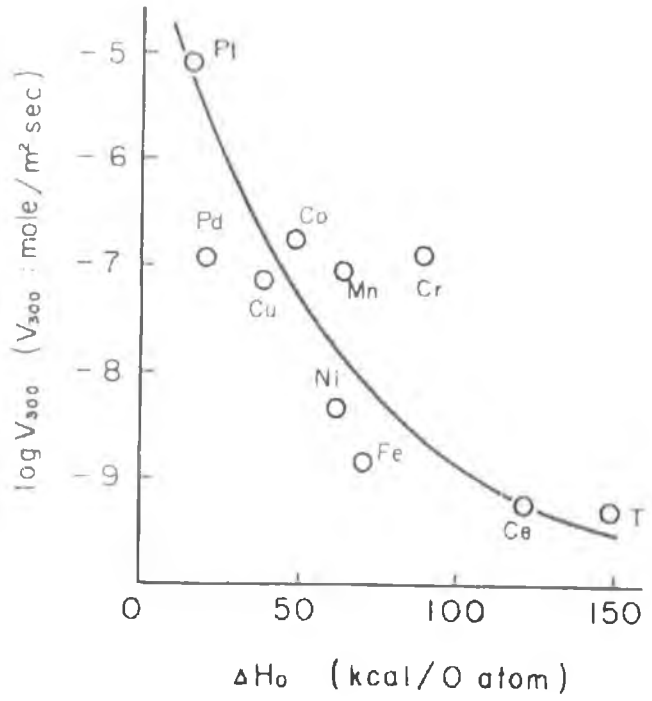

Fig 1.5: Correlation of the catalytic activity V_{300} with ΔHo in the oxidation of propane (37).

Other techniques that have been used to estimate the mobility of oxygen on the catalyst surface (and hence the metal-oxygen bond strength) are heats of chemisorption of oxygen on reduced surfaces (q_s), desorption of oxygen from an oxidised surface (33) and isotopic exchange (38). Oxides with high heats of chemisorption of oxygen (q_s) indicated very strongly bound oxygen and these oxides have the most stable configurations in the d-shell of the cation e.g. d^0, d^5 or d^{10}, while less stable configurations were associated with oxides with lower q_s values. Low values of q_s were observed for NiO, MnO_2, Co_3O_4, Cr_2O_3. Doornkamp et al (38) found that the higher the metal-oxygen bond strength, the lower the exchange rate of dioxygen with one or two oxygen atoms of the oxide and that maximum exchange rates were observed for Co_3O_4, MnO_2, CuO, and NiO, indicating greater oxygen mobility on these surfaces.

A qualitative correlation between semiconductivity and q_s has also been proposed whereby high, medium and low values of q_s correspond predominantly to insulators, n-type semiconductors and p-type semiconductors respectively (33). Accordingly, Bond (4) has classified metal oxides into three groups based on their electrical conductivity; namely n-type semiconductors, p-type semiconductors and insulators. In n-type oxides

electrical conductivity occurs due to an excess of electrons in the lattice while the p-type oxides conduct electrons by means of positive holes caused by electron deficiency in the lattice. In general, p-type oxides have cations with accessible higher valence states and gain oxygen on heating in air. Examples include NiO, CoO, Cu_2O, SnO, PbO and Cr_2O_3 (4), Mn_2O_3 and Mn_3O_4 (39), and Co_3O_4 (40). For n-type semiconductors, an accessible lower oxidation state is necessary and on heating in air oxygen is lost with accompanying reduction of cations to anions; examples are ZnO, Fe_2O_3, TiO_2, CdO, V_2O_5, CrO_3 and CuO (4). However as Bond concluded (4), semiconductivity may be only a rough guide to catalytic activity in the case of transition metal oxides due to variable valency of transition metals and non-stoichiometry throughout the bulk, and different oxidation states between the bulk and surface. For example in the case of CuO, both Cu(I) and Cu(II) sites have been detected on the surface after simple evacuation treatments at 10^{-5} torr in an IR cell (41).

At 300°C in excess oxygen, maximum specific catalytic activities (SCA) for the oxidation of methane were observed for Co_3O_4, MnO_2, NiO and CuO powders by Boreskov (42). In his extensive review, Golodets (33) concluded from studies of oxidation of various paraffins that highest activity was usually exhibited by Co_3O_4, MnO_2, Cr_2O_3, NiO, moderate activity by CuO, Fe_2O_3, ZnO, and low activity for V_2O_5, MoO_3, WO_3, ThO_2 and ZrO_2. Arnone et al (43) found similar activation energies for the oxidation of methane on Mn_3O_4, Co_3O_4, Cr_2O_3 and Fe_2O_3, despite the fact that Fe_2O_3 is a n-type semiconductor according to Bond (4). Yao (44) observed increasing specific rates of oxidation of carbon monoxide in order

ZrO_2<NiO,Cr_2O_3<Fe_2O_3<MnO_2<CuO<Co_3O_4<Pt (wire)<Pd (wire)

Increasing rate

Moro-oka et al (37) reported on the catalytic properties in the oxidation of propane in a mixture of 2 vol% hydrocarbon, 50vol% oxygen and 48 vol% nitrogen. The rate of oxidation of propane was first order w.r.t propane concentration and independent of oxygen concentration.

Based on the reaction rate at 300°C, the following series in order of increasing activity can be established.

$$ThO_2 < CeO_2 < Fe_2O_3 < NiO < MnO_2 < CuO < Pd < Cr_2O_3 < Co_3O_4 < Pt$$

Increasing rate

This is in broad agreement with Yao (44) with the exception of NiO and Cr_2O_3.

1.3.2 Oxidation Mechanisms

Satterfield (5) summarises three types of mechanisms for catalytic oxidation reaction: namely,

- Langmuir-Hinshelwood - An adsorbed oxygen reacts with chemisorbed hydrocarbon
- Rideal - Eley - One adsorbed oxygen reacted with gas phase organic reactant.
- Mars-van Krevelen – A redox mechanism where the catalyst surface oxidises the hydrocarbon and then is re-oxidised by molecular oxygen from gas phase as shown in the following two steps (45)

  (a) Aromatic + oxidized catalyst → oxidation product + reduced catalyst
  (b) Reduced catalyst + oxygen → oxidised catalyst

The Mars-van Krevelen will now be discussed in more detail. Incorporation of oxygen into the lattice was observed for the Mars-van Krevelen mechanism for the oxidation of aromatics over vanadium oxide in a fluid bed reaction (45). The best kinetic fit was found when it was assumed that the oxygen came from the lattice in the form of O^{2-}. The loss of oxygen resulted in oxygen vacancies and subsequent reduction of the metal cation to maintain overall electrical neutrality. Chemisorption of oxygen on the reduced metal cations and reoxidation of the catalyst then occured. This mechanism was proved by kinetic analysis. Reaction constants of the second step (b, above) were found to be identical for various aromatics, indicating that the reoxidation of the reduced catalyst was a common step. Isotopic studies have shown that when lattice oxygen was

involved, two different oxygen sites were involved in the reaction (46). One site was where the gaseous oxygen was activated exclusively and the reaction site where active oxygen was added to the carbon atom. Rapid migration of the activated oxygen to the reaction site through the bulk of the oxide was then required for the mechanism to operate. Hence lattice vacancies would play an important role in facilitating the migration of the oxide ion through the bulk (46). The formation of lattice vacancies will be discussed further in section 1.5.

The Mars-van Krevelen mechanism has been represented in Fig 1.6:

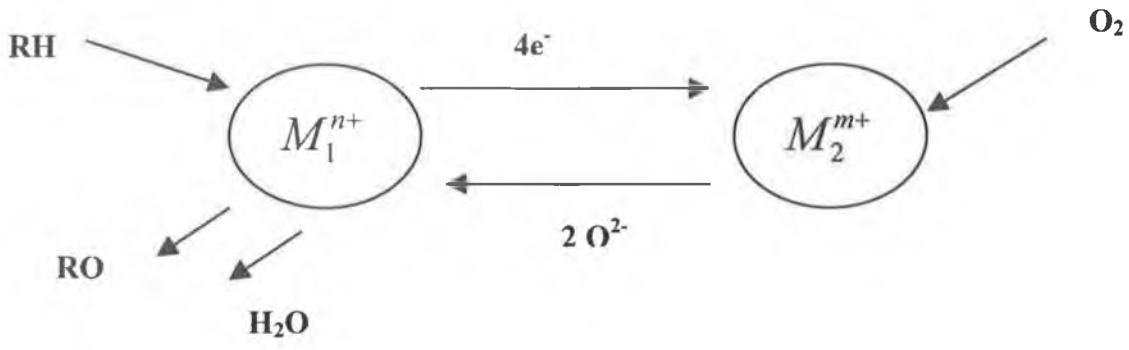

Fig 1.6 Representation of the Mars-van Krevelen mechanism where R represents an alkyl group (47), where M_1 and M_2 are metal cations.

Bond (4) proposed that as a result of the differences in electrical properties of oxides, different mechanisms of oxidation of CO exist. On p-type oxides, adsorbed O^- reacted with adsorbed carbon monoxide while on n-type oxides, carbon monoxide reacted with two oxide ions in the surface (lattice O^{2-}). Baldi et al (39) demonstrated a difference in the total oxidation mechanism of propane between a p-type semiconducting manganese oxide and a n-type semiconductor iron oxide. It was found that for Mn_3O_4 and Mn_2O_3, an initial selectivity to propene of zero increased to a maximum at 1% conversion followed by further decrease. For Fe_2O_3, a high selectivity to propane was observed at 0.1 % conversion and was followed by a decrease. It was proposed that for both oxides, the rate determining step i.e. the activation of the C-H bond and involvement of lattice oxygen (step 1 in Fig 1.7), was the same and then two paths were possible after that,

step 2 and 3 (Fig 1.7). Step 2 was faster when the oxide was rich in Mn and step 3 (via propene) was favored over iron rich oxides.

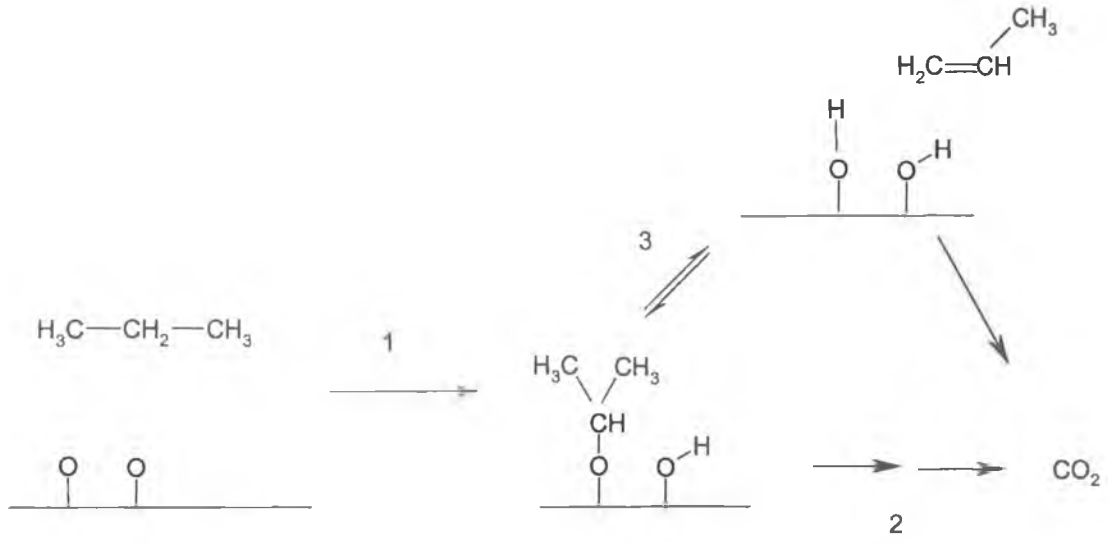

Fig 1.7 Oxidation mechanism of propane over manganese and iron oxides (39).

Hence the activity of the catalyst for total oxidation depends on the type of oxygen involved in the reaction. The formation of different types of molecular or atomic negative ions occured by stepwise reduction of the oxygen molecule (47). In many cases the activation of oxygen not only involved adsorbed states but also incorporation into the oxide lattice according to the scheme (Fig 1.8):

O_2 (g) + e- $\rightarrow$ O_2^- (surf)

O_2^- (surf) + e- $\rightarrow$ $2O^-$ (surf)

$2O^-$ (surf)+ e- $\rightarrow$ O^{2-} (s)

Fig 1.8 Activation of oxygen, where O_2^- (surf) represents surface superoxide or molecular radical ion, O^- (surf) represents a surface oxide radical ion and O^{2-} (s) represents an oxygen incorporated into the lattice of the solid oxide (47).

The different properties of the various adsorbed oxygen species are described in Table 1.4. O^- has only been detected by EPR and was more reactive than O_2^- (48) but it disappeared on increasing temperature (42). Superperoxide species have been observed

on the surface of reduced ceria (49). They have been formed by via interaction of two O^{2-} as well as by a gain of an electron by the superoxide species.

Ion	Binding energy ($kJmol^{-1}$)	Distance between Atoms (Å)	$v(O_2)$ cm^{-1}	Temp (°C)
O_2^+	640	1.12		
O_2	494	1.21	1580	27-127
O_2^- (superperoxide)	394	1.26	1097	< 177
O_2^{2-}(peroxide)		1.49	802	

Table 1.6 : Properties of dioxygen and its ions, where binding energy represents the energy evolved due to the binding of an electron to the oxygen ion, v (O_2) represents the frequency of vibration in the IR spectrum and the temperature is the temperature range from which the oxygen species desorbs from the surface (42).

Sokolovskii (50) concluded that the weaker the oxygen bonding to the surface the more efficient complete combustion was and that the following characteristics were observed for total oxidation as deduced from Fig 1.9

- A high rate of primary oxygen activation to form a high concentration of highly reactive surface states (O_s) – commonly O^- and O_2^- ;
- large number of coordination sites available that can easily donate and accept electrons (3d elements with unfilled d shell);
- slow transformation into the lattice to form lattice oxygen (O_r).

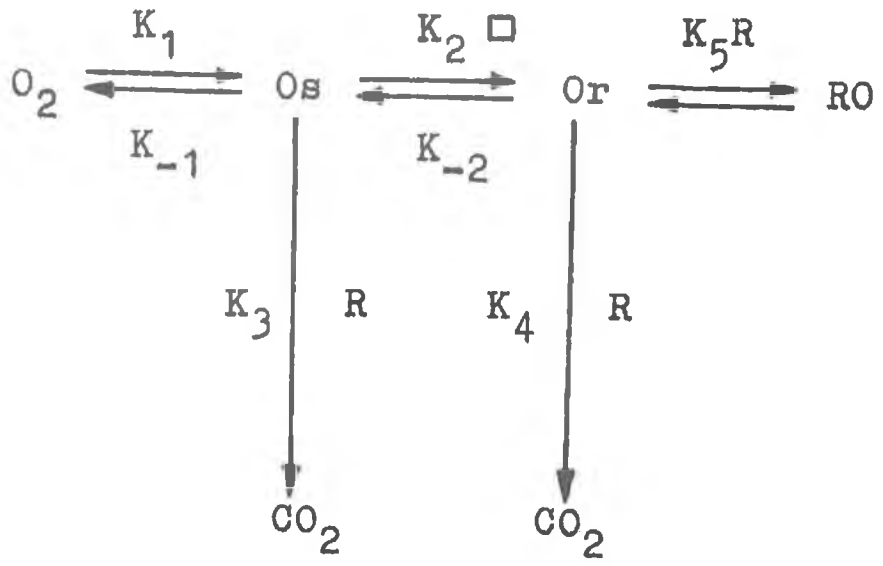

Fig 1.9 Scheme for the primary activation of dioxygen where O_r is the oxygen of the catalyst lattice and the vacancy in the oxygen lattice of the catalyst is represented by □ (50).

Boreskov (42) also concluded that the strength or state of the oxygen bond was important and that weakly bound oxygen was involved in total oxidation. The correlation observed by Moro-aka et al (36) would also support that conclusion. However the formation of carbonate-formate intermediates detected by the monitoring of oxidation rections by IR have suggested the presence of a Mars-van Krevelen type mechanism for alkane oxidation.

At low and high temperatures two alternative mechanisms have been proposed for the oxidation of paraffins over CuO: stepwise and concerted (42). Stepwise mechanism involved two oxygen atoms bound simultaneously to the catalyst, which required the breakage of the O-O bond and hence high temperatures. The concerted mechanism occurred where dioxygen and molecules of oxidized substance were involved simultaneously in an active complex on the catalyst surface. At 200°C in the concerted mechanism region the reaction rate was determined by the decomposition of the formates and there was a weak dependence on the structure of the hydrocarbon. At 300-400°C in the stepwise mechanism the rate determining step was the reaction between the oxidized substance and the catalyst. The rate of hydrocarbon oxidation increased with the number of C atoms and decreasing C-H bond energy; hence methane was the most unreactive molecule. This is illustrated in Fig 1.10 for the combustion of methane.

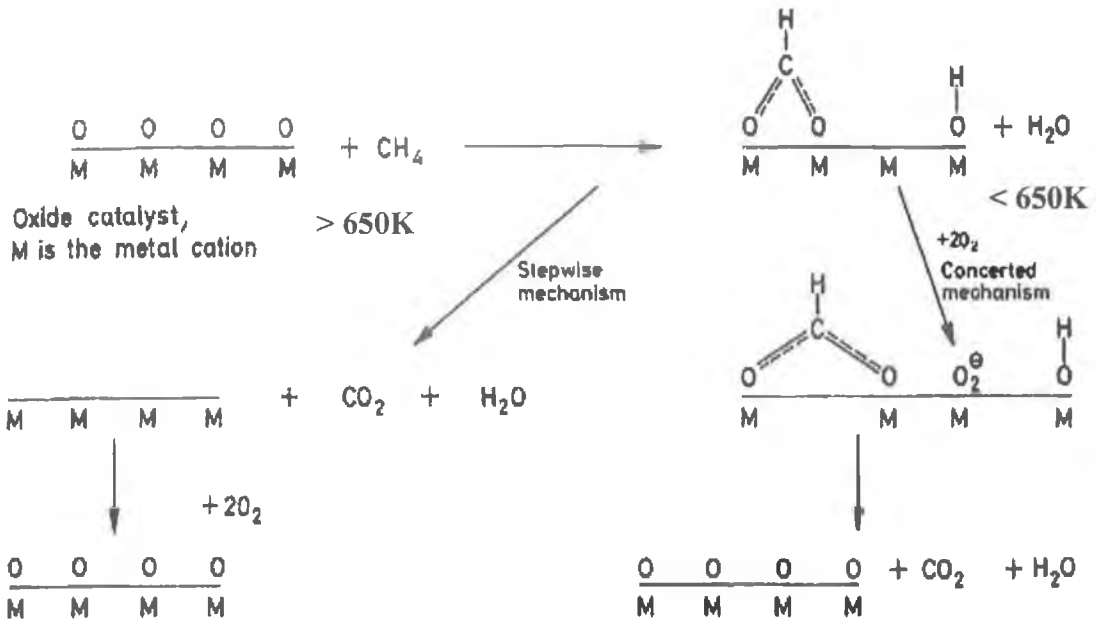

Fig 1.10 Oxidation of methane over a metal oxide, showing the stepwise and concerted mechanisms (42).

For the oxidation of CO, reduction-oxidation mechanisms have been observed on CeO_2 (51), CuO (52), Cu_2O (52) and Co_3O_4 (40). The rate of CO oxidation over CuO (52) was found to agree with the bulk reduction of CuO to Cu, indicating a redox cycle between 0 and 1 as follows:

$$O^{2-}{}_{lc} + O_2(Oads) + CO_{ads} \rightarrow CO_2 + O_2(O_{ads}) + 2e^-$$

where $O^{2-}{}_{lc}$ represents a lattice oxygen and O_2(Oads) represents neutral adsorbed species of dioxygen (O_2) and/or neutral atomic oxygen (O)

The catalytic rate of CO oxidation over Cu_2O agreed with the bulk reduction of CuO* to Cu_2O. The copper valence changed from +1 to +2 initially and then cycled between +2 and +1 during catalytic process. Table 1.7 summarizes the adsorbed species present on CuO and Cu_2O after reduction in carbon monoxide followed by oxidation in air.

Oxide	Treatment	Sample after treatment	Adsorbed species
Cu_2O	none	Cu_2O	O_{2ads}^-
Cu_2O	Oxidation in air	Metastable CuO *	O^-
Metastable CuO *	Reduction in CO	Cu_2O	O_2^-, O^-
CuO	none	CuO	O_{2ads} and/or O
CuO	Reduction in CO	Cu	none

Table 1.7: Adsorbed species present on the surface of various copper oxides and the effect of alternative reduction and oxidation on the structures of CuO and Cu_2O.

A similar mechanism for CO oxidation has been proposed by Breyesse et al (51) on ceria surfaces, see Fig 1.11

$$CO\ gas \leftrightarrow CO\ ads$$

$$CO\ ads + O^{2-}_{\square} \rightarrow CO_2 + \square^{2-}$$

$$CO_2\ ads \leftrightarrow CO_2\ (g)$$

$$O_{2\,(g)} + 2\square^{2-} \rightarrow 2O^{2-}_{\square}$$

Fig 1.11: CO oxidation mechanism over CeO_2 (51), where $O^{2-}_{\square}$ and $\square^{2-}$ represent lattice oxygen and oxygen vacancy in lattice respectively.

Using Co_3O_4 (40) however, a redox reaction occured at room temperature by oxidation of CO and reduction of Co^{3+} to Co^{2+} or even Co^+. The CoO formed on reduction was very unreactive. The activity of Co_3O_4 was related to the instability of Co^{3+} ions that tend to be reduced to lower valent states (40).

The oxidation of alkenes and alkynes occur at lower temperatures than alkanes but similar mechanistic features have still been reported. In the total oxidation of propylene, lattice oxygen reacted with the adsorbed hydrocarbon (53). The surface state of the metal oxide i.e. the reduction state determined whether the adsorbed oxygen reacted with another adsorbed oxygen or with neighbouring lattice oxygen. At low temperatures (150-225°C) total and selective oxidation reactions took place via the Mars-van Krevelen mechanism. Total oxidation with adsorbed oxygen only takes place

at high temperatures when the surface was strongly reduced. IR studies by Baldi et al (35) and Finnichio et al (54) on the combustion of alkanes have come to similar conclusions as follows:

- Nucleophilic species (O^{2-}) ions on oxidized cationic sites were involved in both partial and total oxidation at low temperatures (54,35) in a Mars-van Krevelen type scheme.
- Hydrocarbons were activated by C-H cleavage of the weakest C-H bond (35);
- Discrimination between partial and total oxidation depended on whether the desorption of the partial oxidation product was faster or slower than its overoxidation (35);
- The weakest C-H bond was activated at a reducible cation oxide anion couple (35) ;
- The higher the temperature required, the deeper the oxidation of the first detectable surface species (35);
- CO_2 arose from the combustion of acetates and formates (35).

For the more reactive Co_3O_4 (55), propane was activated at both the center carbon and terminal carbon. In Fig 1.7, the center carbon of propane was activated.

1.3.3 Oxidation over Mixed Oxide Surfaces

This section will discuss the combustion of hydrocarbons and carbon monoxide over mixed oxides. Mixed oxides have been divided into three sections: supported oxides, perovskites and hexaaluminates.

1.3.3.1 Supported Oxides

Supported oxides consist of catalytically active metal oxides incorporated onto a support, typically non transition metal oxides. The catalytically active component consisted of various noble metals or some transition metal oxides and is supported on metal oxides (TiO_2, Al_2O_3, MgO, ZrO_2 and SiO_2) and on activated carbons. These

oxides have been considered as suitable support materials due to the following desirable characteristics (5):

- Inertness ;
- desirable mechanical stability under reaction conditions ;
- high surface area ;
- porosity with average pore sizes greater than 5nm ;
- low cost ;
- high melting points ;
- low volatility.

The support is used to increase the surface area of catalytic material (56), reduce the volatility of the catalytically active component (57), decrease sintering and improve thermal and chemical stability of catalytic material and to govern the useful lifetime of the catalyst (56).

Supported catalytic materials have been prepared by deposition techniques such as impregnation, ion exchange and grafting. These represent liquid solid interfaces, gas solid interfaces and solid-solid interface respectively. Impregnation involves the addition of a solution of a suitable metal salt to the support material and is very versatile in terms of type of solvent and range of loadings (58). Ion-exchange involves ionisation of the surface hydroxyl groups of the support followed by attachment of the desired ion to the hydroxyl group by electrostatic forces. This method is generally only suitable for low loadings (58).

One of the main problems of oxide supports reported was the sintering of and consequential reduction in surface area of the oxide supports at high temperatures. Temperatures involved are dependent on the intrinsic properties of the material such as melting points and phase transformations (59). For example the latter played a key role in the deactivation of alumina ($\gamma \rightarrow \alpha$ at 1100°C) and titania (anatase $\rightarrow$ rutile transition at ca 700°C). The main mechanisms reported for supported oxides are the diffusion of metal oxides and vaporisation (57). Addition of additives to the supports can inhibit sintering as illustrated in Table 1.8.

Support	Additives	Typical SA (m^2g^{-1})	Calc Temp (°C)	Melting points (°C)	Reference
γ-Al_2O_3	none	250-350	500	2072	5, 59
	none	<10	1100	nc	61
	BaO (2.7wt %)	32	1200	nc	60
	La_2O_3 (5 mol %)	50	1100	nc	61
SiO_2 gel	none	700	nc	nc	5
MgO	none	22	nc	2852	5
ZrO_2	none	51	nc	2700	5
TiO_2	Al_2O_3 (20 mol %)	318	450	1840	62
	none	100	450	nc	62

Table 1.8: Properties of commonly used supports with and without additives where SA represents surface area measured by the BET method and Calc Temp represents the temperature of calcination.

Zirconia is reported as a particularly effective material due to:(63)

- Strong interaction with the active phase;
- High thermal stability and improved chemical inertness compared to other classical supports;
- Acidity, basicity, reducing and oxidising abilities;
- Superacidic properties possible on addition of sulfate ions (62).

However its disadvantages include lower surface area for commercially available samples compared to that of alumina and more expensive than other supports (5). However as will be discussed in section 2.1, the surface area can be increased by altering the preparation method or the addition of dopants to zirconia.

This section will discuss the reactivity and characteristics of active transition metals, namely Co, Mn and Cu, supported on zirconia due to their importance to the rest of the thesis and the fact that they have been reported to be amongst the most active (33) among single metal oxides. In a general review by Spivey (12), it was pointed out that

noble metals (Pt, Pd) had a higher activity for total oxidation of hydrocarbons than metal oxides but were less resistant to poisoning and more expensive. Hence they had have been widely investigated for many pollution control applications, while comparatively little literature has been published on the combustion of hydrocarbons using zirconia as a support for transition metal oxides.

In the case of copper, the oxidation of carbon monoxide (64, 65) and methanol synthesis (66) have been mainly investigated. Studies have shown that copper supported on zirconia (CuO/Z) and yrittia-zirconia (CuO/YSZ) were more active for the oxidation of CO than those supported on alumina despite a lower surface area (64,65). For Cu/Zr, the higher activity was attributed to a beneficial synergy between the zirconium oxide and the highly dispersed copper oxide species, which promoted the reduction of Cu^{2+} to active Cu^{+} species. In the latter (CuO/YSZ), a surface oxygen vacancy of the support formed an interfacial active centre consisting of Cu^{+} and surface oxygen vacancy.

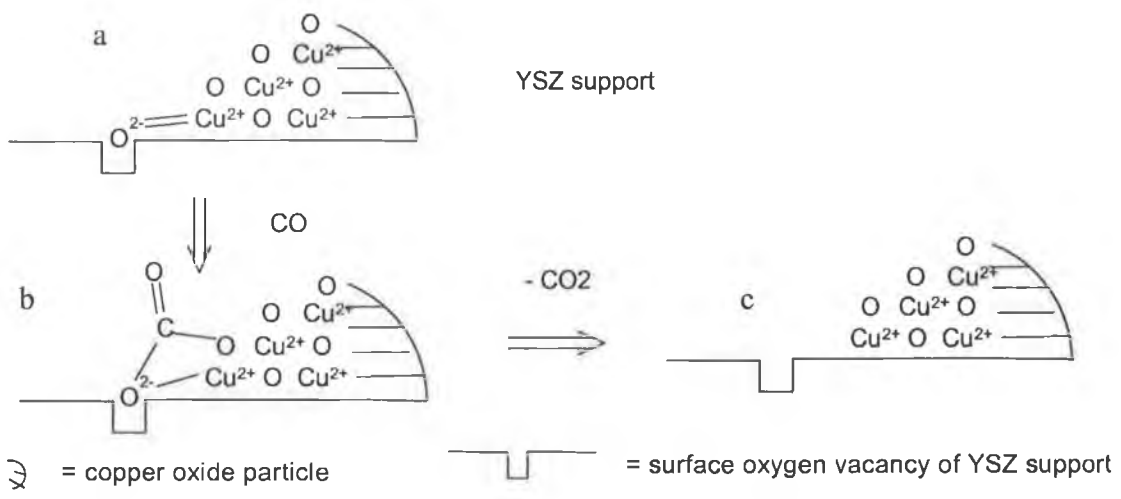

Fig 1.12:Oxidation of CO on CuO/YSZ where (a) represents the active site, (b) is adsorption of carbon monoxide and (c) is desorption of carbon dioxide (65).

This provided a second reaction pathway as shown in Fig 1.12 involving chemisorbed oxygen which was responsible for the observed high activity and light-off behaviour which was absent for the alumina support. Temperature programmed reduction was used to understand the light-off behaviour of the zirconia supported catalysts. The

temperature programmed reduction (TPR) data for the catalysts (Cu/Z and Cu/YSZ) in comparison to CuO/Al_2O_3 are shown in Table 1.9 (64, 65).

Sample	TPR peaks (°C) α	β	γ	Reference
8 wt% CuO/Z	174	192	225	64
1.5 wt% CuO/YSZ	156 (α_1), 175 (α_2)	>200	>225	67
7.5 wt% CuO/Al_2O_3		215	230	67

Table 1.9: TPR data for supported CuO/ZrO_2, CuO/YSZ and CuO/Al_2O_3 where α, β, γ are arbitrary symbols used to distinguish between the different types of peaks at various temperatures in the TPR profile and α_1 and α_2 are sub peaks of α peak.

The light-off behaviour is related to the α peaks (65) and the data shows clearly the improved light-off behaviour of Zr based over alumina based supports. This is due to the to highly dispersed CuO formed by an induction effect from the zirconia support. The α_1 peak was reported to be due to the removal of the oxygen ions in the oxygen vacancy depicted in Fig 1.12 (a). At ca 700°C, copper aluminate ($CuAl_2O_4$) may form resulting in deactivation of the Cu/Al_2O_3 catalyst has been reported (68).

In the case of cobalt, Xiao et al (69) and Tiernan et al (70) found that cobalt supported on zirconia was more active than cobalt on Al_2O_3, TiO_2 and MgO and had an activity for the combustion of methane comparable to that of supported noble metals (70). The formation of inactive spinal cobalt aluminate ($CoAl_2O_4$) above 550°C on alumina supported catalysts (69,70,71) has been noted. A very strong interaction between the cobalt ions and high surface area alumina was indicated by Solid Insertion Probe –Mass Spectrometry that resulted in lower activity of the catalyst (70). This is a thermal analysis technique that follows the decomposition of the precursor as a function of temperature and will be discussed in more detail in Chapter 2. The high activity was attributed to a strong interaction and synergy between Co_3O_4 was highly dispersed over the zirconia support, strong interaction and synergy between them reason for activity (69). The CH_4 combustion activities (as measured in references 69 and 70) are

compared to noble metal catalysts in Table 1.10, note the high activity of 15% Co/ZrO_2 catalyst calcined at a relatively low temperature of 400°C.

Calcination at 1000°C of 5% Co/ZrO_2 resulted in a severe loss in activity. This was attributed to a reduction in surface area to 1.5 m^2g^{-1} after heat treatment at 1000°C (69). Milt et al (72) concluded that the severe loss in activity for methane combustion after 150 hours on stream of a 1.9 wt % cobalt on zirconia catalyst was due to the disappearance of cobalt from the surface and its migration into the lattice. The incorporation of lanthanum into the zirconia maintained a higher fraction of cobalt at the surface and hence deactivation on stream was reduced although not totally alleviated.

Sample (wt %)	**BET SA (m^2g^{-1})**	**T_{50}(°C)**	**Calc temp (°C)**	**Reference**
Co/ZrO_2 (1)	52.3	460	600	69
$CoZrO_2$ (10)	50.9	480		
Co/ZrO_2 (15)	48.5	470		
Co/ZrO_2 (5)	4	490	600	70
Co/ZrO_2 (15)	nd	395	400	
Co/Al_2O_3 (5 + 15)	191	>500	600	
Pt/Al_2O_3 (0.5)		470	630	
Pd/Al_2O_3 (0.5)		330	630	

Table 1.10: CH_4 combustion activities and BET surface areas (SA) for various cobalt supported oxides in comparison to Pt and Pd supported on alumina. All samples were prepared by impregnation. T_{50} represents temperature at which 50 % conversion of methane occurs and n.d is not determined.

1.3.3.2 Perovskites

Perovskites represent a type of mixed metal oxide ABO_3 where the central atom A is coordinated to 8 B atoms at the corners and 12 oxygen (X) atoms at the midpoint of the

cell edges. It has been represented as a ccp array of A and B atoms with the B atoms occupying the octahedral holes and is shown in Fig 1.13.

A large number of cations can occupy A or B sites in this structure provided that the radii of A and B are greater than 0.90 Å and 0.51Å respectively and that for a given B cation, the radius of A (r_a) is restricted by the following equation (73):

$$0.75 < (r_a + r_o)\sqrt{2}(r_b + r_o) < 100$$

where r_b and r_o represent radii of B and O respectively.

Properties of the B ion and its oxygen neighbours can be altered by the choice of A (73). The A ion is generally catalytically inactive and usually a lanthanide cation while the B cations are generally active for oxidation catalysis and is a transition metal (74). The relatively large distance separating the B cations meant that reactant molecules only interacted with single sites. Perovskites have generally been prepared by the following methods: decomposition of metal acetates and/or nitrates (75), reaction of nitrates with citric acid to form amorphous citrates of metal (76,77,78,79), low temperature decomposition of nitrates using glycerol (81) and flame-hydrolysis (80). However as shown in Table 1.11, compounds prepared by acetate decomposition have low surface areas (<5 m^2g^{-1}) which decreased to below $1m^2g^{-1}$ after calcination at 1200°C (75). Higher surface areas have been observed for samples prepared via the citrate methods. Leanza et al (80) reported extremely high surface areas after calcination at high temperatures using a novel flame hydrolysis method where the precursor solution of acetate salts and citric acid was nebulised into a H_2 and O_2 flame to achieve a finely powdered solid.

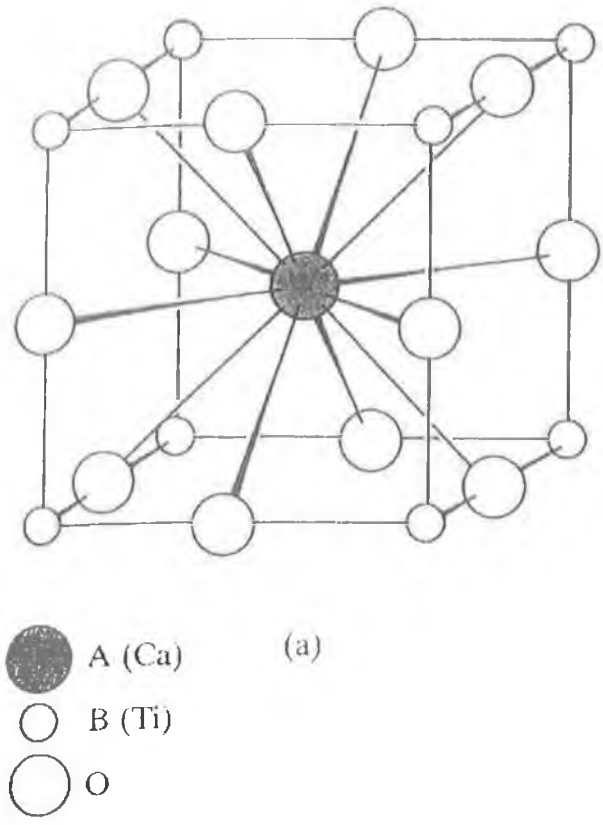

Fig 1.13 Representation of a perovskite structure (92).

Two types of oxygen species and oxidation mechanisms have been identified on perovskites depending on reaction temperature (75). At low temperatures (<450°C), reaction involves weakly adsorbed or surface oxygen, while at higher temperatures, the reaction by lattice oxygen becomes more dominant. These were referred to as the suprafacial and intrafacial mechanisms respectively. The two types of oxygen species (i.e. surface oxygen and lattice/bulk oxygen) have been detected by TPD (81) as an α peak and β peak respectively. The low temperature α peak depended primarily on the substitution degree of the A cation with a cation of a different valency. The higher temperature β peak depended on cation B and its reduction to a lower oxidation state.

At low temperatures, the oxidation rate of methane combustion is half order w.rt. to partial pressure of oxygen and first order w.r.t methane partial pressure, indicative of weakly bound oxygen species which are in equilibrium with gaseous dioxygen. Increasing temperatures result in a decrease in the surface coverage of the weakly bound

oxygen and at high temperatures, the oxidation rate is zero order w.r.t oxygen partial pressure and first order w.r. t. methane partial pressure (75).

For unsubstituted perovskites, the activity for combustion has been reported to be primarally controlled by the physiochemical properties of the B –site cation rather than the relatively small effect of the A – site cation. Arai et al (75) observed that Mn and Co in the B cation site along with La in the A cation site are the most active for methane combustion and are comparable in activity to 1 wt% Pt on alumina. $LaMnO_3$ has been reported to be more active than $LaCoO_3$ since lanthanum stabilises manganese in its higher oxidation state (+4) in equilibrium with Mn +3 (79). The creation of cation vacancies, excess oxygen and nonstoichiometry were associated with $LaMnO_3$. Catalytic activity was dependent on the reducibility of manganese (79), stability of mixed valence states, stabilisation of unusual oxidation states and mobility of oxygen ions and point defects i.e. A cation vacancies, B cation vacancies and anion vacancies (73). However in contrast, Arai et al (75) observed that $LaCoO_3$ reached 50% conversion of methane at a lower temperature than $LaMnO_3$.

Partial substitution of the cations in the A site has been reported to result in a drastic modification of the catalytic properties of these compounds and the degree of partial substitution plays a significant role in defining the catalytic activity of the perovskites. The activities for methane combustion and textural properties are represented in Table 1.11. For $LaMnO_3$ perovskites prepared by different methods, more active catalysts for methane combustion were characterised by higher bulk oxygen mobility related to a higher concentration of structural defects (82), which should have an effect on the intrafacial mechanism, which requires abstraction of lattice oxygen. Increases in activity have also been associated with non-stoichimetric compounds such as $LaMn_{0.9}O_3$ where manganese is deficient (74) and $La_{0.9}FeO_{2.85}$ (81). The increased activity for the latter was attributed to a greater density of active sites and greater mobility of surface oxygen species while for the former, increase in specific surface area and Mn^{4+}/Mn^{3+} ratio were responsible. Of all the perovskites tested by Arai et al (75) the most active for methane oxidation i.e. lowest T_{50} was $La_{0.6}Sr_{0.4}MnO_3$. Most of the studies have observed that doping at optimum levels has a beneficial effect on catalytic activity.

Catalyst							
$La_{1-x}A_xBO_3$			T_{50} (°C)	SA (m^2g^{-1})	Calc (°C)	Preparation Technique	Ref
B site	A site	x					
Co	0	0	525	3	850	Acetates	75
	Ba	0.2	535	5.1			
	Sr	0.2	518	4.7			
	ce	0.2	499	3.1			
		0	466	17.9	1600-1800	Flame-hydrolysis	80
	Ce	0.1	438	24			
	Eu	0.1	462	18.3			
Mn	Sr	0	579	4.6	850	acetates	75
		0.4	482	3.3			
		0.2		45	740	citrate	77
	Eu	0.1	nd	26	740	Citric acid	77
	Ce	0.1	nd	20	700	citrates	
	Ce	0.1	nd	32	750	Citric acid	77
Fe		0	571	3.1	850	acetates	75
1 wt% Pt/Al_2O_3			518	146	500	impregnation	

Table 1.11: Effect of doping of the La sites of perovoskites on activities for combustion of methane where T_{50} = temperature at which 50% conversion of methane was achieved. The preparation techniques used involved decomposition of appropriate metal acetates at indicated temperature.

However in some studies, partial substitution in certain cases proved detrimental to the catalytic activity. In the case of $LaMnO_3$, substitution of La with cerium slowed the rate of perovoskite phase formation, increased the surface area and the amount of oxygen desorbed below 410°C (76). However, the changes in methane activity didn't correlate as predicted with the change in these parameters. Only an increase in activity was observed for x = 0.1, while above that lower activities per surface area at 550°C were observed. Also it appears that there is a limit on the value of x depending on the dopant

used and several studies have reported that partial segregation of binary oxides such as CeO_2 (80) and Sm_2O_3 (79) occurred when x was greater than 1 (79,80) so that a two phase system was formed. Leanza et al (80) attributed the increase in activity on doping of 10% of Ce^{4+} for La^{3+} in $LaCoO_3$ to the formation of Co^{2+} species and a subsequent creation of associated active sites/or the decrease in concentration of anionic vacancies to compensate for the partial substitution of Ce^{4+} cations for La^{3+} cations. The former was the most likely reason. The decrease in anionic vacancies led to a decrease in the T_{max} in the alpha peak in the TPD of preadsorbed oxygen.

In general, it has been reported that low oxygen mobility favours the suprafacial mechanism, while high ionic mobility favours the participation of bulk oxygen and hence the intrafacial mechanism is preferred (83). Both the α and β peaks are crucial to describing catalytic activity, with the α peak indicating the concentration of surface oxygen vacancies and the latter also an indication of catalyst reducibility and oxygen mobility. A low temperature β peak indicates easy reducibility and enhanced redox properties which is connected with the concentration of oxygen vacancies. Hence the predominant mechanism was the intrafacial one, while a low suprafacial activity was confirmed by the presence of a weak oxygen desorption peak

1.3.3.3 Hexaaluminates

As mentioned Section 1.4.1, alumina undergoes a phase transition to low surface α-alumina at high temperatures. The addition of Ba, Sr and La to alumina results in formation of either one of two layered structures, β- alumina and magnetoplumbite, shown schematically in Fig 1.14 (59). Both structures consist of alternative stacking of a spinal block with close packed layer of oxygen and a mirror plane along the c direction. In the mirror plane, there are less oxygen ions and hence they are more loosely packed compared to the spinal structures. Hence the preferred direction for O diffusion and desorption is perpendicular to the c direction i.e. through the mirror plane. Grain growth along this occurs, forming thin particles, which are unstable (84). In this structure, the anion layers of the β-alumina cannot rearrange to the α phase due to the blocking effect of the alkali metals (85).

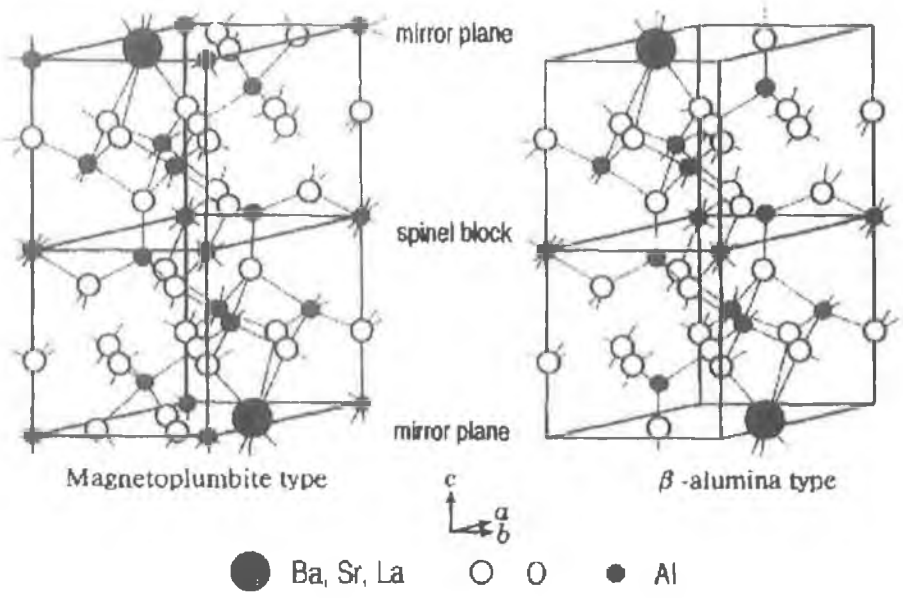

Fig 1.14 Crystal structures of hexaaluminates (59).

The general formulas of the barium (BHA) and lanthium hexaaluminates (LHA) are $BaAl_{12}O_{19}$ and $LaA_{11}O_{18}$ respectively. They have been prepared by (a) co-precipitation of nitrates with bases such as ammonium hydroxide (86,87), ammonium carbonate (87,88) and (b) alkoxide hydrolysis in a sol-gel method (85,89,90). Both supercritical drying (SCD) (86,90) and oven drying (CD) (86) for both methods have been investigated. An increase in the activity of the BHA for methane combustion have been achieved by the substitution of Al^{3+} with transition metals, Mn (85,90), Cu (89) and Co (90). The activities of various unsubstituted and substituted hexaaluminates are reported in Table 1.12, where x refers to the degree of substitution or number of an aluminium cation (s) replaced with a transition metal.

For both BHAs and LHAs, a limit was observed on the number of foreign cations that can be introduced without destabilising the structure and consequent formation of a second phase. These are three Mn^{3+}, four Fe^{3+} (85) and between one and two Cu^{2+} ions (89). A similar affect was observed for La-hexaaluminates ($LaB_xA_{12-x}O_{19}$) where above $x = 2$, formation of $LaMnO_3$ was observed (86).

$AB_xAl_{12-x}O_{19}$							
A	**B**	**x**	**T_{50} (°C)**	**SSA (m^2g^{-1})**	**Calc °C/h**	**Preparation Method**	**Ref**
Ba	0	0	800	14.5	1600/5	Sol-gel, SCD	90
	Mn	1	600	16.3	1600/5	Sol-gel, SCD	90
	Mn	1	640	35	1100	Precipitation	88
	Co	1	660	13.9	1600/5	Sol-gel, SCD	90
	Co, Mn	1	670	14.3	1600/5	Sol-gel, SCD	90
	0	0	770	11	1200/24	Sol-gel, CD	85
	Mn	1	610	20			85
	Mn	2	560	14			85
	Fe	1	635	14			85
	Fe	2	605	12			85
	Fe, Mn	2	560	15			85
La	0	0	nc $T_{10} = 620$	49	1200/4	Precipitation, SCD.	86
	Mn	0.1	nc $T_{10} = 450$	28	1200/4	Precipitation, SCD.	86

Table 1.12: Methane combustion activities and specific surface areas (SSA) for hexaaluminates prepared by various authors where T_{50} represented the temperature required for 50% conversion of methane and nc = not cited. SCD and CD refer to supercritical drying and conventional drying respectively.

Mn was shown to be more active than Co in BHA where a volcano type relationship between catalytic activity and difference of standard formation enthalpies of tri-valent and divalent metal oxides was established (31). Mn was located at the summit with the highest activity as indicated by the lowest T_{10} (temperature at which 10% conversion occurred). Aging had no significant effect on activity or surface areas further confirming the high thermal stability of these compounds. An increase in surface area was observed on increased substitution of Mn for barium in BHA when sol-gel method (85) and co-precipitation using ammonium carbonate (87) were used in their synthesis. BHA samples substituted with up with 3 Mn cations showed better activity and thermal

stability than the unsubstituted one (89). Copper substituted samples resulted in a lower surface area and this was the reason for the lower activity when compared to Mn. Precipitation of BHA with ammonium hydroxide increased the surface area compared to precipitation using ammonium carbonate (87). For LHAs, a decrease in surface area was observed on increasing Mn content and was attributed by the authors to an increase in anion vacancies and migration of nearby Al^{3+} anions (86). Increased surface areas were noted by Yan and Thompson for a similar system (90). For both LHA and BHA, supercritical drying increased the surface area of hexaaluminates compared to conventional drying (86,90).

1.4 Ceria, Zirconia and Modified Zirconia Catalysts.

The literature on the use of cerium and ceria-zirconia mixed oxides will be discussed in detail, as cerium is a key part of the work to be discussed in later chapters. As mentioned in section 1.3, cerium plays a key role in the effective operation of the twc catalyst, mainly due to its oxygen storage capacity. Ceria can be doped with rare metals such as Zr, Pr and Tb to form solid solutions (91), but doping with zirconia has been most widely investigated and ceria-zirconia mixed oxides are now widely used as oxygen storage components in catalytic converters. An introduction to crystal structures and to those in particular of ceria, zirconia and ceria-zirconia mixed oxides will be presented in the next section because of the relevance to the system studied in this thesis, in particular due the effect of crystal structures on catalytic characteristics. This will then be followed by a detailed discussion of the oxygen storage capacity and associated redox properties of the aforementioned compounds. Finally, the applications of the ceria-zirconia mixed oxides as well as zirconia doped with other transition metals as combustion catalysts will be presented.

1.4.1 Crystal structures of CeO_2, ZrO_2 and mixed CeO_2-ZrO_2.

Crystal structures are formed from close packing of atomic layers. Each crystal is derived from a basic building block (known as a unit cell) that repeats itself over and over in a regular way (92). The unit cell of a three dimensional lattice is a parallelepiped (three sets of parallel faces) defined by 3 distances a, b, c and three interaxial angles α, β, γ. There are 7 different crystal classes with different symmetry requirements. These

are cubic, hexagonal, tetragonal, orthorhombic. rhombohedral, monoclinic and triclinic. In a cubic system, a, b and c are equal and all interaxial angles are 90°. In a tetragonal system, all the angles are still 90° as in the cubic structure but one of the cell edge lengths is elongated, resulting in only two of the sides being equidistant. Finally in a monoclinic system, none of the side lengths are equal and only two of the interaxial angles are 90°.

However there are also 4 different types of unit cells:

The primitive unit cell, denoted P, has only one lattice point.

A body centred unit cell (I) has a lattice point at each corner and one at the center.

The face centred unit cell (F) has a lattice point at each corner and one in the center of each face.

The face centred unit cell (A, B or C) has a lattice point at each corner and one in the center of opposite faces.

By applying these 4 different types of unit cells to the seven crystal structures, 14 different Bravais lattices are deduced. In each of these lattices the symmetry of the unit cell is maintained. These are illustrated in Fig 1.15. There are two types of crystal space within a close packed structure. Six atoms, three in one layer and three in another surround an **octahedral** hole. Four atoms surround a **tetrahedral** hole with centers at the corners of a tetrahedron (see Fig 1.16)

Miller indices are used to label the lattice planes in Bravais lattices. They are usually written (h,k,l) where h, k and l are integers, positive, negative or zero (93). They can be calculated by expressing the intercept of the plane in the x, y and z axis in multiples of the unit cell dimensions (a, b and c) and taking the reciprocals of these intercepts. The intercept along a direction gives h, the intercept along the b gives k and the intercept along the c gives l.

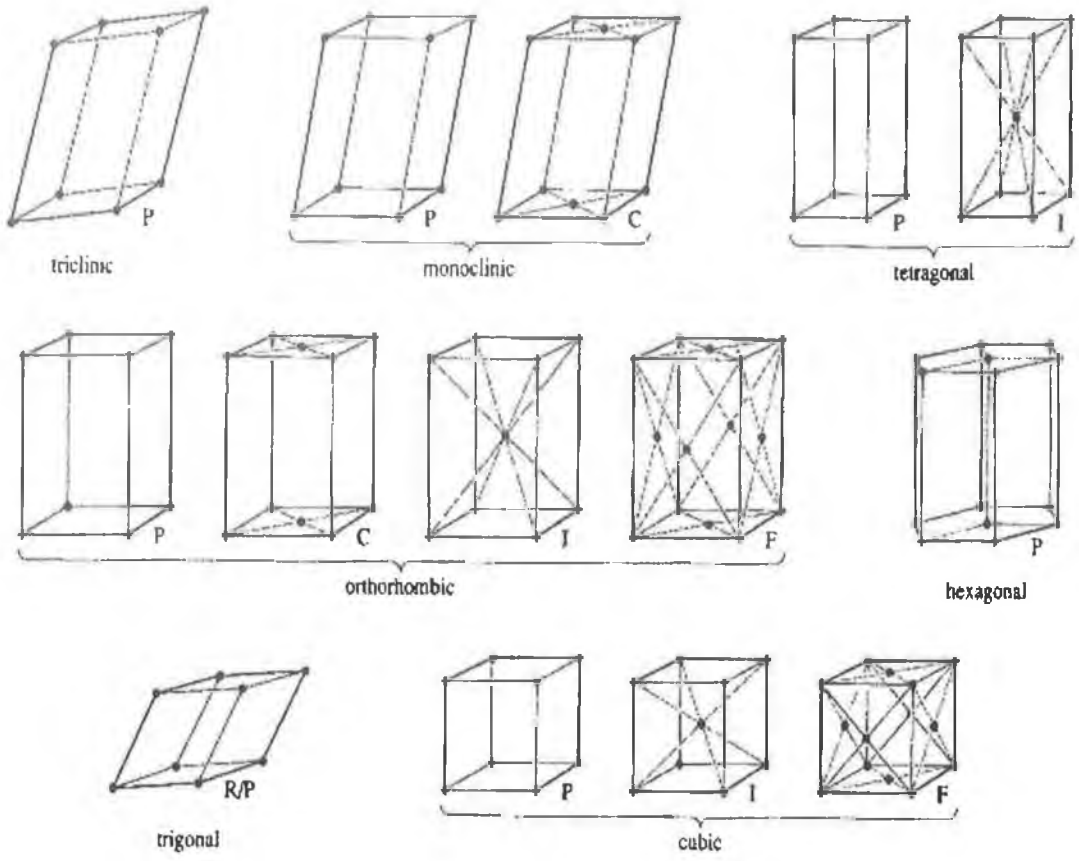

Fig 1.15: The 14 Bravais Lattices (92).

Ceria has been viewed as a fluorite crystal structure with a lattice constant of 0.541nm (94). The lattice constant is the length of the side of the unit cell represented in Fig 1.17. The fluorite structure is derived from the CaF_2 crystal structure but this structure can also be adapted where the anions are oxygen ions. A schematic of a fluorite structure of general formula is AO_2 shown in Fig 1.17, where A can be U, Th and Ce. It has been represented as an array of cations forming a face centred cubic lattice with oxygen ions occupying the tetrahedral interstitial sites or alternatively as a cubic close packed array of oxygen anions with each alternative octahedral hole occupied by a cerium atom. In any case, each cerium site was surrounded by eight oxygen ions that formed the corners of a cube and each oxygen anion was surrounded by 4 cations in a tetrahedron.

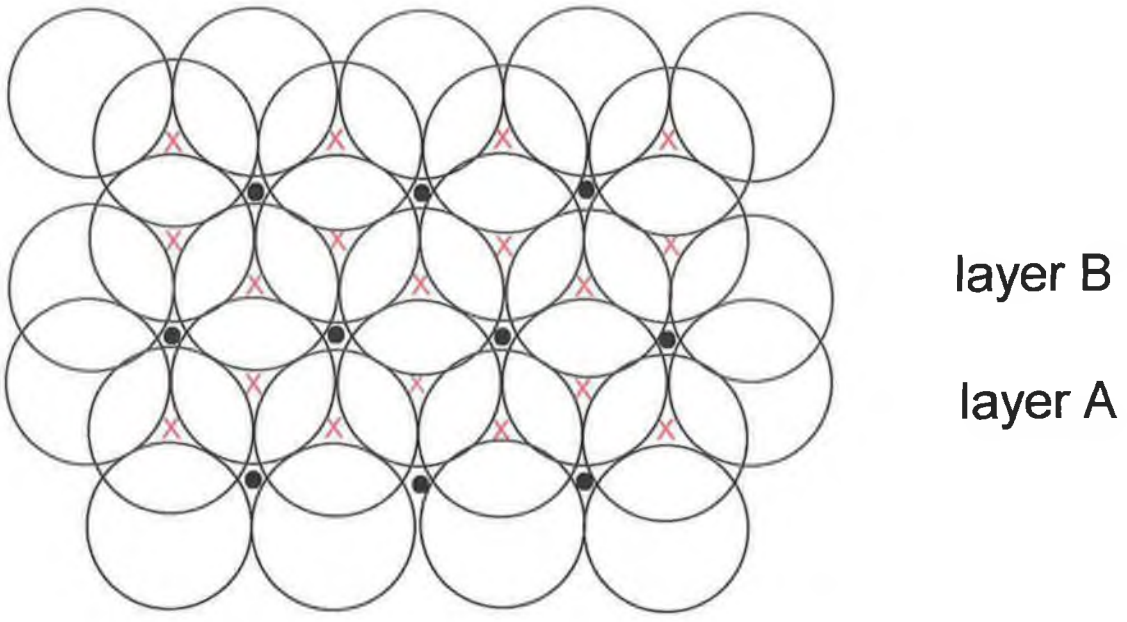

Fig 1.16: Two layers of close packed spheres with a X and ● marking the tetrahedral and octahedral holes respectively (92).

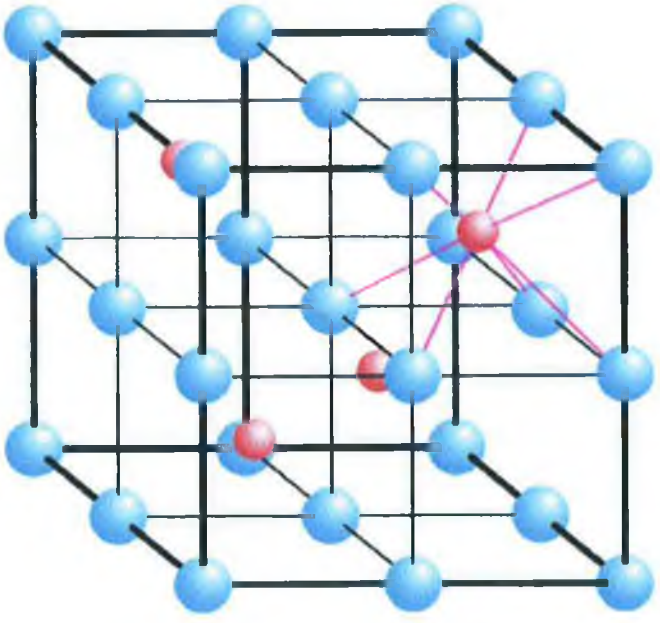

Fig 1.17: The fluorite (AO_2) oxide structure. The red spheres represent the A cation sites and the blue spheres the oxygen sites (95).

Zirconium dioxide has a high melting point, low thermal conductivity and high resistance to corrosion (96). Three crystalline forms of zirconia are known to exist: the monoclinic which is stable up to 1200°C, the tetragonal which is stable up to 1900°C and the cubic which is stable above 1900°C (see Fig 1.18). Each of these may exist in a metastable, stabilized or strained state, all of which are non-equilibrium states. Furthermore, the metastable tetragonal phase is stable up to 650°C.

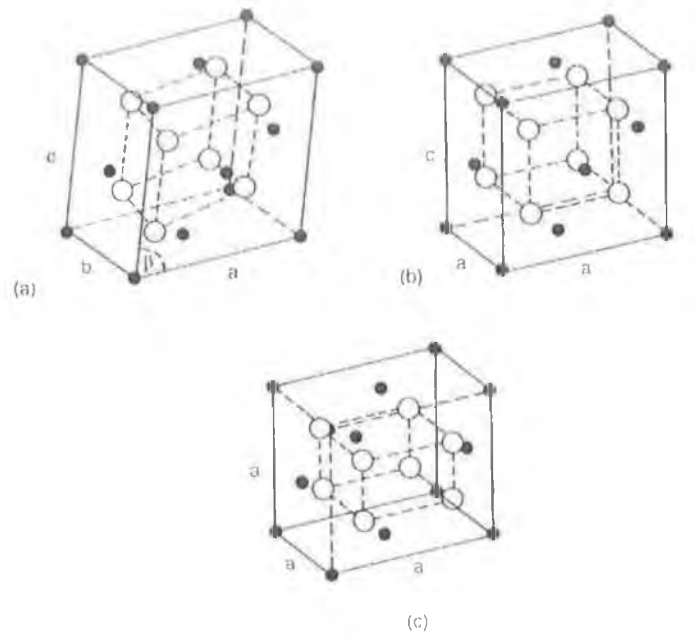

Fig 1.18 Structure of (a) monoclinic (b) tetragaonal (c) cubic ZrO_2 where the open and closed circles represent oxygen anions and zirconium cations respectively (97).

Cubic zirconia has the same fluorite structure as ceria, while tetragonal zirconia has a distortion of the cubic structure obtained by displacement of alternating pairs of oxygen atoms up and down the z axis (98). Hence it is viewed as a layer structure, where two types of bonding between the zirconium cation and the oxygen anions are observed (99). For the monoclinic, there are two non-equivalent oxygen sites: O_I are three fold coordinated in a planar configuration and O_{II} are four-fold coordinated in a distorted tetrahedron. Instability of tetragonal zirconia and cubic phases has been attributed to the small size of the Zr^{4+} ion which is unfavourable for 8-fold coordination (99). This results in oxygen overcrowding and strain in the cation network. Each polymorph has a

different space group and different raman spectrum have been recorded - each as summarised in Table 1.13.

Phase	Space group [98]	Coordination [98]			Bond lengths (Å)	
		Zr	O_I	O_{II}	Zr-O_I	Zr-O_{II}
Tetragonal (t)	Fm3m	8	4	4	2.10	2.35 [99]
Metastable tetragonal (t')	Fm3m					
Cubic	$P4_2/nmc$	8	4	4		
Monoclinic (m)	$P2_i/c$	7	3	4	2.03, 2.05 2.14	2.14 2.23 [100] 2.15, 2.23

Table 1.13: Structural parameters of the different crystal structures of zirconia. (References given as superscripts).

Stabilisation of the metastable tetragonal phase at low temperatures has been attributed to its higher surface energy and smaller particle size (101,102). Tichit et al (101) postulated that the size below which the tetragonal phase was stable was 100Å while a much higher value of 300Å was proposed by Garvie (102). On heating, the crystallites grew with a reduction in excess surface energy until a critical size was reached above which only the monoclinic phase was observed by XRD (102). The tetragonal phase was stabilised by a small average crystallite size, large specific surface area and excess surface energy compared to a single crystal. The following structures as a function of temperature have been proposed by Ali and Zaki (103) (see Fig 1.19). The final transformation to monoclinic was enhanced on subsequent cooling to room temperature (103). The cubic, tetragonal and monoclinic phases have been reported to exist within the critical particle size ranges of 50-140Å, 100-220 Å and 190-420 Å respectively. Another reason proposed for the stabilisation of the metastable tetragonal phase was the slow kinetics of the metastable tetragonal and cubic to monoclinic transformation since major structural changes were required to go from the 8 to 7 fold coordinated Zr ions.

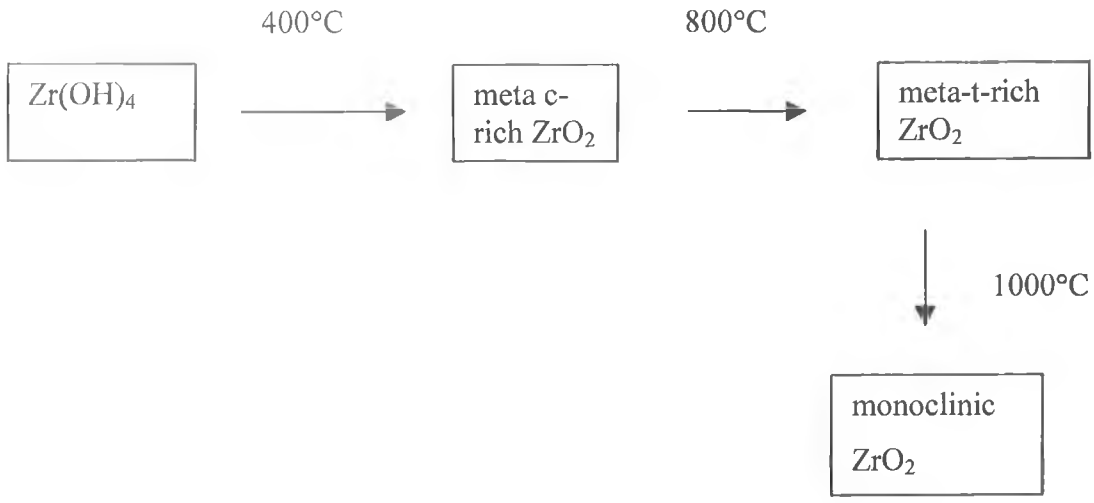

Fig 1.19:Temperature dependence of different structures of zirconia where meta is metastable, t is tetragonal and c is cubic (103).

The addition of both lower valent dopants, Y^{3+} (104), Ca^{2+} (92) and tetravalent dopants Ce^{4+} (104) and Ge^{4+} (99) to zirconia have also been reported to stabilise the cubic and tetragonal phases. A solid solution is formed when as solute atoms are added to the host material the crystal structure is maintained and no new structures are formed (105). A solute is defined as an element or compound present in minor concentrations.

Point defects (see Fig 1.20) are introduced as a solid solution is formed. These can be divided into **Substitutional** or **Interstitial**. In the former, solute atoms replace the host atoms. In the latter, solute atoms fit into the interstitial spaces in the atomic lattice of the host. Factors that affect the extent to which the solute dissolves into the host atoms are:

- **Atomic Size**: to form the solid solution, a difference in atomic radii between the two atom type of less than ± 15% is required, otherwise new phases will be formed due to significant lattice distortion.
- **Electrochemical Factor**: The greater difference in electronegativity of the two atoms the less likely the formation of a solid solution.
- **Crystal structures**: For complete solid solubility, crystal structures of the metals must be the same.

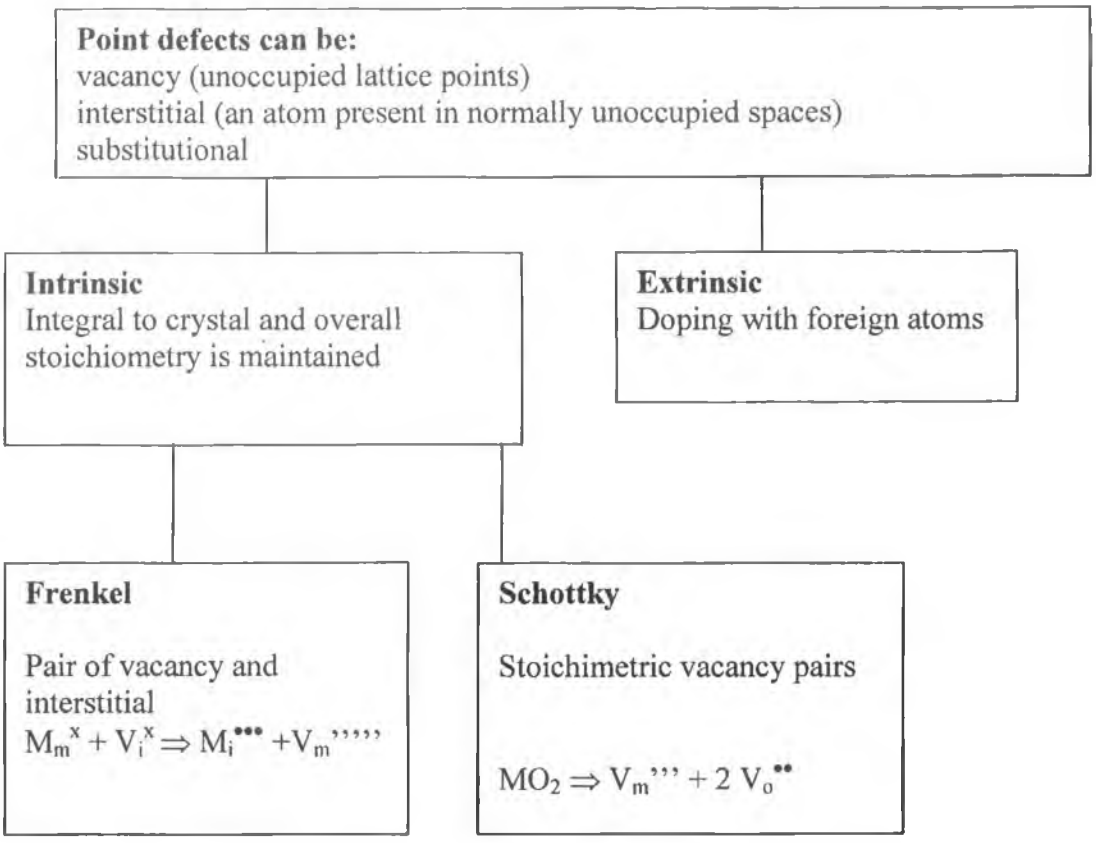

Fig 1.20: Classification of point defects (106). Point defects have been classified relative to perfect atomic lattice by Kroger notation which uses the symbol $species_{(site)}^{(charge)}$ where the charge is represented by number of dots (·) for positive charge and primes (') for negative charge and x for neutral. Species are the atomic species symbol or V for a vacancy, while the site is the perfect crystal lattice site on which the defect is formed or i = interstitial site.

Frenkel defects are caused by the movement of a metal cation from its lattice position to a unoccupied interstitial position, while Schottky defects relate to a pair of vacant sites, anion and cation vacancies. When solute or dopant cations have lower valency than the host, oxygen vacancies via the following reaction are created (107):

$$M_2O_3 + ZrO_2 \rightarrow 2M_{Zr}' + V_o^{\bullet\bullet} + 3\,O_o^x$$

where M represents the trivalent cation, M_{Zr}' is the trivalent cation on the zirconium cation site with a excess negative charge, $V_o^{\bullet\bullet}$ is an oxygen vacancy with two positive charges and O_o^x is an oxygen ion on its normal lattice position and is neutral.

The oxygen vacancies created have been reported to stabilise the cubic phase by relieving the oxygen overcrowding present in the structure (99). The larger the size of the dopant the more effective it is to stabilise a structure with 8 fold coordination. For zirconia doped with yrittia and cerium, the tetragonal → monoclinic phase transformation depends on the amount of stabiliser present and was attributed to the ultrafine or very small nature of the particles (104). The particle size effect has also been reported to be the reason for the stabilisation of the tetragonal phase via doping with ceria (108). A maximum grain size of 2.4 nm was also required to retain the pure tetragonal phase. But other authors have also concluded that this was not the only factor affecting this transformation (104).

The structures of the ceria-zirconia solid solutions have been reported to depend on composition and temperature. The structures of the solid solutions are the same as those reported in Table 1.14 with t and t' detected by XRD (109,110). The main difference between the two is the orthogonality (c/a ratio). A larger value of 1.018 has been reported for the tetragonal phase compared to 1.010 for the metastable phase t' (110). A second metastable tetragonal phase (t") was detected by raman spectroscopy (111), which had the same space-group as the t and t' phases but had an axial ratio of 1, equal to that of the cubic phase. Hence it could not be distinguished from the cubic phase by XRD but only by raman spectroscopy. The t' and t" phases however have been distinguished from each other by XRD from splitting of the peak at 70° of the former as shown in Fig 1.21 (111).

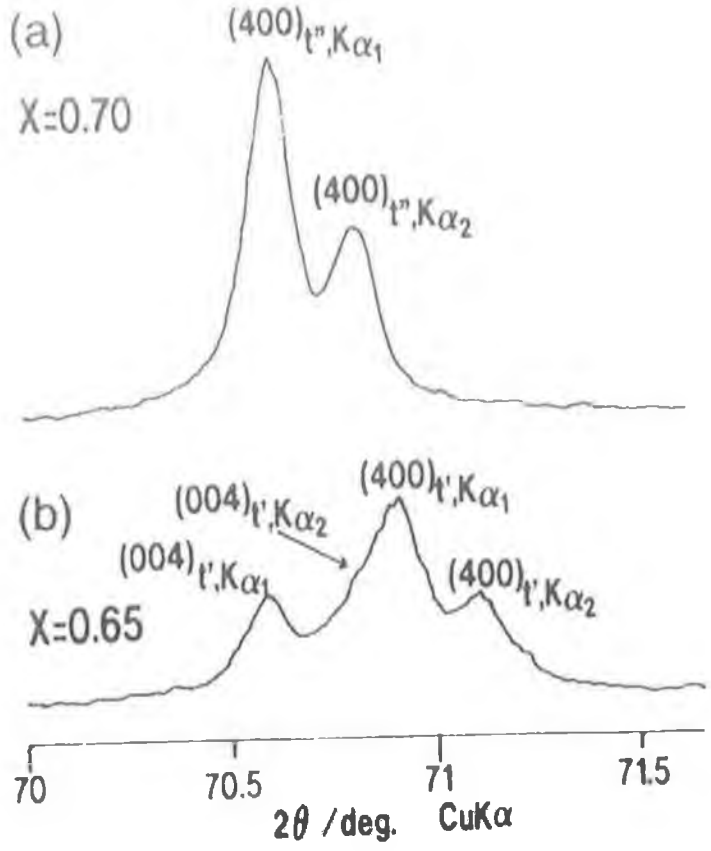

Fig 1.21 XRD of t'-ZrO_2 and t" – ZrO_2 of (b) $Ce_{0.65}Zr_{0.35}O_2$ and (a) $Ce_{0.70}Zr_{0.3}O_2$ (111).

The various phases of ceria-zirconia mixed oxide as a function of preparation method and cerium content reported in various studies are detailed in Table 1.14. In general above 70% mol% of cerium, the cubic structure corresponding to that of ceria has been observed (99). Whether this was classified as the c or t" in Table 1.14 depended on whether XRD or raman was used. Hence, the c and t" phase will be referred to herein as a cubic phase.

Preparation Method	Temperature (°C)	% CeO_2	Phases detected	ref
Firing oxide mixtures	≤ 1200	0-4	m	112
		8-12	m and t	112
		11-20	t	100,113
		30-40	t, t' and c (minor)	100,113
		50	t'	100
		65	t'	100
		70-80	t ''	100
		90	c	100
		60-100	c	100,113
Sol-gel	≤ 600	16	t-$Ce_{0.16}$ $Zr_{0.84}$ O_2	114
		50	c and t (minor)	114
		60	c and t (minor)	114
Co-precipitation	≤ 600	67	c	125,115
		75	c-$Ce_{0.75}$ $Zr_{0.25}$ O_2	114
		80	c	116

Table 1.14: The phases reported by various authors for ceria-zironia mixed oxides using different preparation methods, where m, t and c are monoclinic, tetragonal and cubic respectively, t' is the metastable tetragonal phase and minor indicates presence of minority phase.

The phase diagram for low cerium levels is shown in Fig 1.22 (97). At 0-4 mole %Ce, the monoclinic phase is formed up till approx 1200°C. Between 8 and 15 mol % Ce, the percentage of tetragonal to monoclinic phase present depends on the temperature of the system. At 5% CeO_2 a tetragonal form was formed at 1100°C and on quenching was transformed into a metastable monoclinic phase (m) (112). Hence any discrepancies in crystal structure for low cerium contents in Table 1.14 can be attributed to slight differences in temperatures used in synthesis or treatment of the sample following firing at high temperatures i.e. rapid or slow cooling to room temperature.

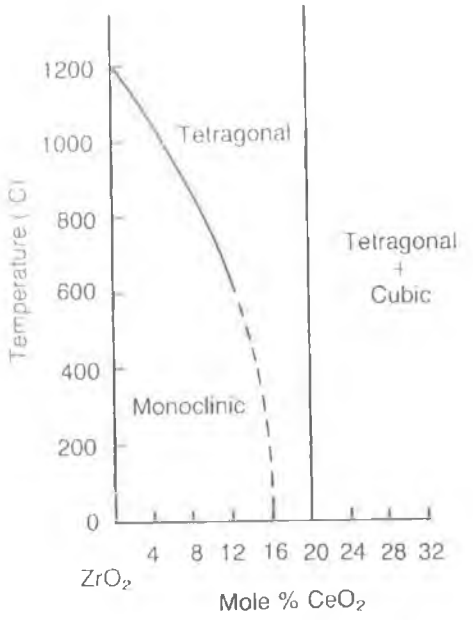

Fig 1.22 Phase diagram of CeO_2-ZrO_2 up to 32 mole % CeO_2 (97)

At 30% and 40% cerium addition, both stable and metastable tetragonal phases with cubic phase as the minority has been observed, with the amount of t' increasing for the latter composition (100). The formation of the cubic or tetragonal phase depends on the synthesis method, especially in ceramics. In ceramics, CeO_2 and ZrO_2 were fired at temperatures in excess of 1400°C and then quenched to maintain the homogeneity of the sample and then annealed in air at 627°C to reoxidise the sample (110). This was performed because partial reduction of Ce^{4+} to Ce^{3+} occurred at the high temperatures used in the firing process. The cubic phase was observed for the samples containing 30-90 mol % CeO_2 on firing and quenching, since the cubic phase is stabilised by oxygen deficiency associated with the reduction. On annealing in air the samples containing 30-65% CeO_2 transformed to the t' phase. This dependence on preparation parameters is especially true for $Ce_{0.5}$ $Zr_{0.5}$ O_2 (50 mol%) solid solution due to its position in the phase diagram. When quenching followed by annealing was performed, the t' and c' (cubic) phases were observed for that composition. Use of a non-quenching or slow cooling rate resulted in formation of the t' phase (100). The presence of the t'' phase in another study (117) using a non-ceramic preparation method for the same composition was attributed to formation of small crystallites.

Another study by Fornasiero et al (118) highlighted the importance of the preparation method on the structures of the resulting oxides for a $Ce_{0.60}Zr_{0.40}O_2$ solid solution. Oxides with surface areas of 50 and 1 m^2g^{-1} were prepared using the citrate and ceramic method respectively. The former had a cubic structure with a minority t" phase detected, while the latter had a tetragonal structure since it was best fitted to the $P4_2/nmc$ space group. Hori et al (119) compared two methods of preparation and their effect on phases formed and particle size. Cubic $Ce_xZr_yO_2$ solid solutions were prepared by co-precipitation with up to 50% mol Zr while at higher concentrations tetragonal solutions were formed. General preparation methods are given in Chapter 2.

1.4.2 OSC and Redox Properties of Ceria

The most important role played by ceria in the three way catalyst is the extension of the working "window" for the air/fuel ratio (28) across which the catalyst can reduce NO_x and oxidise CO and hydrocarbons at the same time. In the oxidative atmosphere, the CeO_2 species dominates while in the reducing environment Ce_2O_3 or CeO_{2-x} exists due to the low redox potential between Ce^{3+} and Ce^{4+} (120). Hence CeO_2 enables oxygen storage during the fuel-lean oxidation cycle (through reaction of CeO_{2-x} with O_2, NO and H_2O) and oxygen release during the fuel- rich part of the cycle to help oxidise CO and hydrocarbons and restore CeO_{2-x} according to the equation below;

$$2CeO_2 \Leftrightarrow Ce_2O_3 + \tfrac{1}{2} O_2$$

The quantities of oxygen that can be reversibly provided to and removed from the gas stream are called the Oxygen Storage Capacity (OSC) (121).

The value of OSC of a particular system depends on the experimental techniques and conditions used to determine it. Characterisation of the redox state is performed via quantative analysis of the oxygen released, oxygen vacancies or number of Ce^{3+} ions formed. Yao and Yao proposed three different techniques to measure OSC (121). The first method (a) involved oxygen chemisorption on a prereduced catalyst and indicated the number of the sites available for oxygen transfer on the catalyst surface during the actual operation of the catalyst. The second technique (b) measured the amount of oxygen transferred in a pulse regime simulating the oscillations, which the exhaust gas

may experience. This was measured in two ways: (i) the total amount of carbon monoxide oxidised in a series of CO pulses until no more oxidation was observed (OSCC or oxygen storage capacity, complete) or (ii) the amount of CO oxidised in one pulse following an oxygen pulse (OSC). The pulse method results were affected by pre-treatment temperature, pulsing temperature and partial pressure of carbon monoxide. A general decrease in the oxygen storage capacity was observed when the pre-treatment temperature (in a flow of helium followed by oxygen) was increased from 600 and 800°C for unsupported ceria and noble metals on ceria (121). With increasing temperature of pulsing a larger proportion of the available oxygen is being used since the adsorption of oxygen is an activated process. An increase in the CO partial pressure led to a large increase in both OSC and OSCC in the study (121).

The third widely used technique (c) is temperature-programmed reduction (TPR), which is used to establish the total amount of transferable oxygen during reduction (up to 900°C or less). In this case the sample is exposed to a constant stream of the reducing agent as the sample is heated up a certain reduction temperature, at a specified linear heating rate, instead of individual pulses of hydrogen. The value of OSC (μmol O_2/μmol CeO_2) for a given sample can vary depending on the technique used, as illustrated in Table 1.15 (121).

Sample (wt %)	**TPR**	**O_2 chemisorption @ 500°C**	**Pulse @ 500°C**	
			OSC	**OSCC**
CeO_2/Al_2O_3 (20)	0.22	0.06	0.0017	0.0087

Table 1.15: OSC values (μmol O_2/μmol CeO_2) obtained for a supported ceria sample at 500°C using temperature programmed reduction (TPR), oxygen chemisorption and pulse measurements (OSC and OSCC). (121).

The largest value was observed for TPR since it represents both surface and bulk reduction.

The presence of two peaks in the TPR of ceria with hydrogen (121, 122, 123, 124) and carbon monoxide (125,126) has been extensively reported. The two peaks have been attributed to the presence of two types of oxygen ions in ceria (121). A surface capping oxygen anion, which attaches to a surface Ce^{4+} in an octahedral coordination was ascribed to a reduction peak at ca. 500°C. A bulk oxygen anion, which is bonded to two Ce^{4+} ions in the bulk ceria, was found to be reducible at ca. 750°C. Using CO, the reduction peaks in the range 400-500 and 800-900°C have been reported depending on conditions used. The low temperature peak was affected by surface area (121,123), while the high temperature peak is intrinsic to the material and was observed regardless of surface area. The area of the low temperature peak was smaller for a ceria sample with surface area of $1 m^2g^{-1}$ compared to a sample with surface area of 10 m^2g^{-1}. The influence of surface area on reduction profile is illustrated in Figure 1.23 (121). For high surface area CeO_2 samples with surface areas of 44 and 35 m^2g^{-1}, a difference in the shape of the low temperature peak was observed but its location remained constant (127).

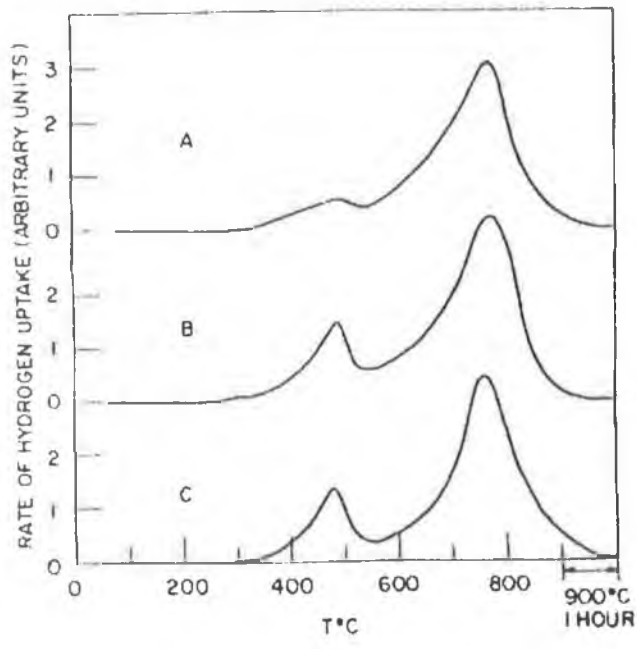

Fig 1.23 Rate of H_2 uptake as a function of temperature in the TPR of CeO_2 samples. (a) CeO_2 (1), BET area : $1 m^2g^{-1}$. (b) CeO_2 (2), BET area : $10 m^2g^{-1}$ (c) same as in (b) but reoxidised at 200°C after the previous reduction (121)

Giordano et al (127) investigated the reduction mechanisms of two ceria samples (HSA and LSA) with surface areas of 44 and 3 m^2g^{-1} respectively. For the HSA sample, two peaks were observed at 500°C and 827°C, while only one peak at 827°C was observed for the LSA sample. A significant surface area loss was observed during the TPR conditions for the HSA at approx 327-777°C and for temperatures higher than 777°C, the behaviour of the HSA sample was analogous to that of the LSA sample. The difference in the TPR profiles of LSA and HSA ceria was related to the sintering of the latter and the simultaneous reduction of ceria nanocrystallites in the HSA sample. Subsequently the nanocrystallites were transformed into bulk ceria, the reduction of which was responsible for the second peak in both samples. Hence surface (removal of surface oxygen) and bulk reduction occurred successively. For reduction of CeO_2 with CO (128), a similar mechanism with the formation of surface oxygen vacancies has been proposed. Lattice oxygen diffuses onto the surface and an oxygen vacancy diffuses from the surface to the inner part of a particle. The structures of both CeO_2 and Ce_2O_3 are such that addition or removal of oxygen atoms involved minimal rearrangement of the cerium cations (129). Detailed quantum mechanical calculations have indicated the following model for the formation of an oxygen vacancy in ceria (129). As an oxygen atom was removed from the surface, two electrons were simultaneously localised on two cerium atoms in the immediate surrounding of the vacancy with the conversion of Ce^{4+} into Ce^{3+}.

Theoretical calculations showed that the energy required for the reduction of Ce^{4+} to Ce^{3+} with the formation of oxygen vacancies is lower for the surface than for the bulk (130). In a series of metal oxides (viz, CeO_2-Al_2O_3, MgO, ZrO_2, γ-Al_2O_3 and SiO_2), ceria had the greatest surface and bulk oxygen mobilities with diffusion co-efficients of $5700*10^{-19}$ m^2 s^{-1} and $50*10^{-23}$ m^2s^{-1} respectively (131). The oxygen diffusion wasn't related to the metal-oxygen bond strength but due to the presence of anion vacancies.

Impregnation of palladium on ceria resulted in disappearance of the first reduction peak on the TPR profile and the appearance of a new feature below 100°C, due to both reduction of PdO and surface reduction of ceria (122). The TPR profiles before and after impregnation of palladium are shown in Figs 1.24-1.25. In general, promotion of reduction of metal oxides by the addition of the noble metal dopants was achieved by an

increase in the number of nucleation sites or provision of a higher concentration of active hydrogen (132). Another study (133) also reported on the beneficial addition of noble metals to ceria, namely an increase in OSC since the metals acted as portholes for the migration of oxygen onto the support.

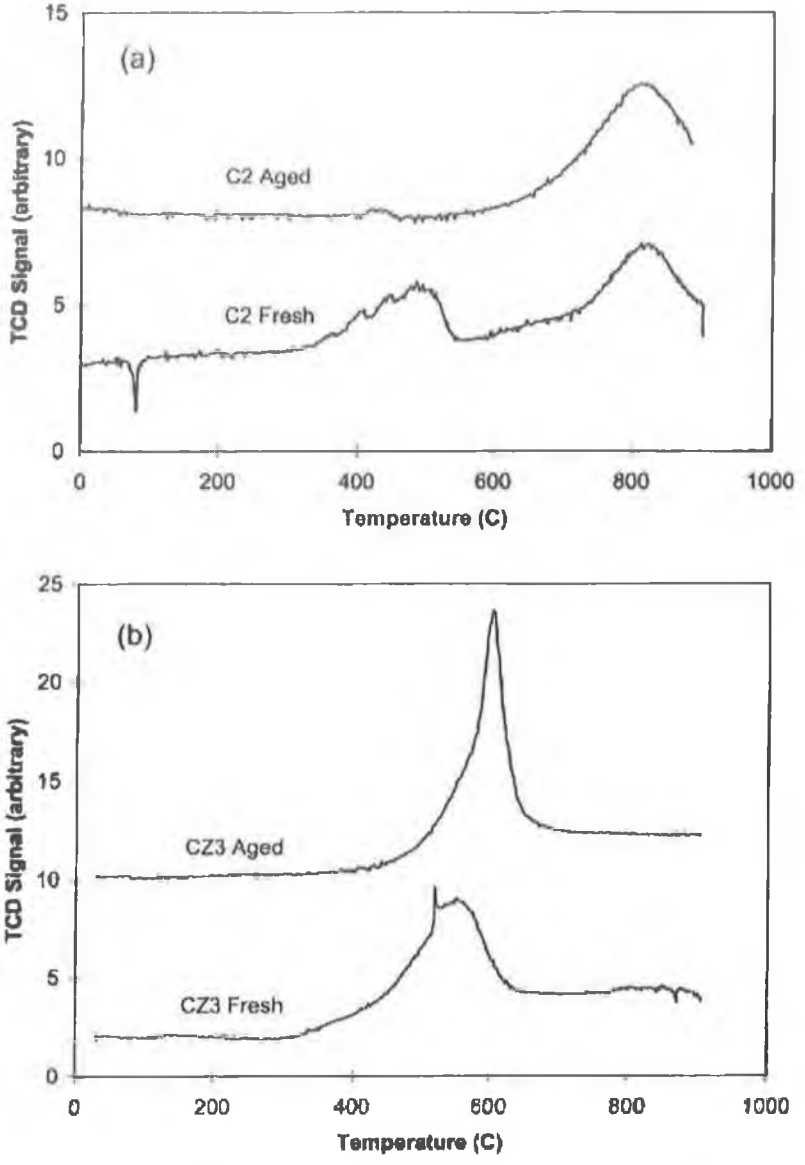

Fig 1.24: TPR profiles of fresh and aged 70: 30 wt % CeO_2-ZrO_2 (CZ3) and CeO_2 (C2) before addition of palladium (122).

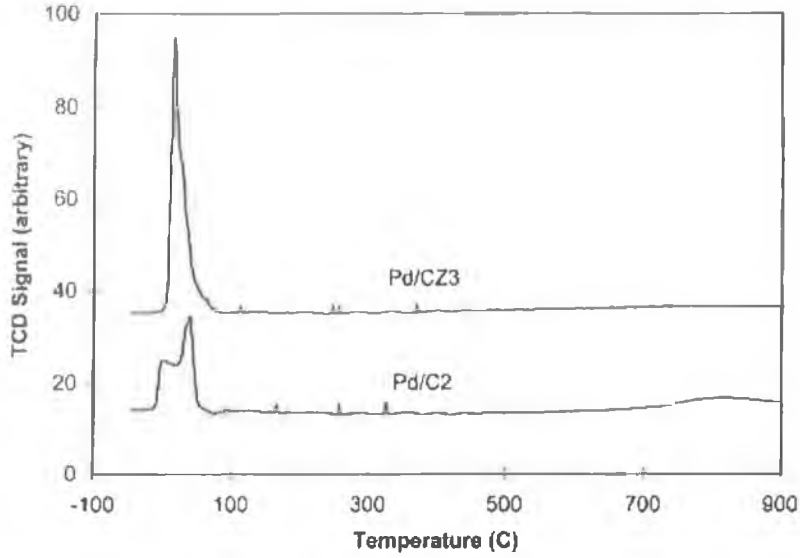

Fig 1.25:TPR profiles of fresh 70: 30 wt % CeO_2-ZrO_2 (CZ3) and CeO_2 (C2) after impregnation of 0.5 wt% Pd (122).

Consecutive TPR experiments reported by Fally et al (123) showed that the low temperature reduction temperature was eliminated due to sintering. A similar effect was also observed for aging at 1000°C and 1050°C under air (122,124) and redox conditions (122). Under hydrothermal aging (134), a three way catalyst containing ceria showed less reduction at 500°C than a fresh non-aged sample. Samples were aged at 1000°C in the presence of water and then subjected to a oxidation treatment in oxygen at 500°C followed by a reduction with CO at 500°C. XPS measurements were taken after each treatment to characterise the oxidation state of cerium present by comparison to XPS spectra of CeO_2 and Ce_2O_3 standards. The fresh sample was completely oxidised to CeO_2 and then partially reduced to 30% CeO_2: 70 % Ce_2O_3. Separate experiments showed that the reason for only partial reduction of the oxidised fresh sample was reoxidation of the sample during sample transfer by background oxygen present in the XPS reactor although the possibility that only surface reduction was observed wasn't ruled out. However for the aged sample, only reduction to 70% CeO_2: 30% Ce_2O_3 of the oxidised sample was observed. A decrease in activity for CO oxidation was also found, leading the authors to conclude that the dominant deactivation mechanism was the decrease in the supply of oxygen from ceria, which therefore is no longer available for CO oxidation. Other studies have also reported on the poor thermal stability of ceria whereby at high temperatures, an increase in crystallite size (134,135,136) and decrease in surface area occurred. The influence of a reducing atmosphere on the thermal

stability of high surface area ceria ($115m^2g^{-1}$) was investigated (137). The sample was treated for 2 hrs under hydrogen ($3.6h^{-1}$) or carbon monoxide ($0.6h^{-1}$) in the temperature range 400 to 850°C at 8°C min^{-1}. Under hydrogen, the surface area dropped to approx $14m^2g^{-1}$ between 397 and 597°C. Under vacuum, air ($3.61h^{-1}$) or carbon monoxide, a similar decrease occurred between 627 and 727°C. Under carbon dioxide, temperatures higher than 727°C were required to observe a net decrease in surface area. Under water vapour (613 Pa), the specific area was reported to be $67m^2g^{-1}$ after heating at 697°C. Hence compared to air or water, the thermal stability under hydrogen was very poor but improved under carbon dioxide.

In all atmospheres the first step of sintering was the loss of microporous surface (137). After this sintering of the particles, growth of crystallites occurred. The vacancies created by reduction by hydrogen were deemed to favour oxygen mobility and hence sintering since sintering occurs due to the migration of oxygen vacancies in the bulk. Under the carbon monoxide atmosphere, the polydentate carbonate species were formed which were stable and were eliminated from the bulk at higher temperature and hence the thermal stability under carbon monoxide compared to hydrogen was high. The high partial pressure of carbon dioxide stabilized the carbonate species and prevented their desorption. Hence the surface area was preserved since elimination of the carbonate species formed on the ceria promotes loss of surface area. Jen et al (122) concluded that this loss in surface area resulted in a limitation in the ability of ceria to supply oxygen from the bulk below 800°C. Another study (136) reported a correlation between increase in crystallite size and decrease in CO and C_2H_4 conversion in a commercial three way catalyst containing cerium oxide, Pt and Rh while Su et al (25) concluded that sintering was the most likely reason for a large loss of OSC in catalysts containing cerium oxide or nickel oxide.

1.4.3 OSC and Redox Properties of Ceria-Zirconia Mixed Oxides

Oxygen storage capacity can also be increased by the presence of point defects: both intrinsic and extrinsic. Point defects and the methods by which OSC have been measured have been discussed in detail in sections 1.4.1. and 1.4.2 respectively.

Numerous studies have reported that the OSC of cerium-zirconium mixed oxides are greater than that of ceria using pulse methods TPR (126,138), Ce^{3+} content (138,139,140) and FTIR (138). However the OSC value of the mixed oxides depended on the reduction temperature (500, 700 and 1000°C) and the composition (138). After reduction to 500°C in a TPR experiment, followed by oxidation with oxygen pulses at 427°C, a maximum amount of transferable oxygen (OSC) was observed for a 80 mol % cerium sample. An increase in the reduction temperature to 700 and 1000°C shifts the maximum OSC to a 50 mol % cerium content sample.

The following trends in OSC in ceria-zirconia mixed oxides have been observed and some of the OSC values reported, surface areas and reduction characteristics for ceria-zirconia mixed oxides of various compositions are summarised in Table 1.16, while the effect of aging on the OSC values are reported in Table 1.19. The oxygen storage capacity values quoted are after reduction of the sample in TPR experiment to either 500°C (138) or 700°C (126) or exposure to the sample to pulses of CO and O_2 at 400°C (125) and 500 °C (122). Hence the values from each study should not be directly compared to each other but the trends within each study noted.

- OSC of ceria was increased by zirconium substitution. However OSC was not only proportional to the zirconium content since the OSC process was related to the $Ce^{4+} \rightarrow Ce^{3+}$ redox, whose number decreased as the zirconium content increased (140). Hence no OSC was observed for zirconia. High and constant OSC values were observed for zirconium contents of 20-50 mol % (139, 140) and 20-40% (122, 125).

- Low and high OSC values were associated with the tetragonal and fluorite structure respectively (113, 114). OSC was strongly influenced by the presence of the cubic structure as compared to the tetragonal one (113). This was due to increased oxygen mobility in the former structure.

Sample	% Ce	Phases *	BET SA (m^2g^{-1})	TPR peaks (°C)	OSC ^ (μmol O/g cat)	Ce^{3+} (%)	Ref
CZ-100	100 [a]	ng	100	517,895	135	9	138
CZ-80/20	80 [a]			555	435	35	
CZ-68/32	68 [a]			560	425	39	
CZ-50/50	50 [a]			563	400	47	
CZ-15/85	15 [a]			383,572	180	12	
CZ100	100 [b]	c	ng	500,800	210	ng	122
CZ70/30	70 [b]	c	ng	580	590	ng	
Pd/CZ100	81 [b]	ng	ng	100,800	360	ng	
Pd/CZ70/30	79 [b]	ng	ng	100	970	ng	
CZ100	100	c	25	ng	74	ng	125
CZ68/32	68	c	40	450	200	ng	
CZ63/37	63	c	40	470	219	ng	
CZ50/50	50	t	45	480	175	ng	
CZ15/85	15	t	25	570	40	ng	
CZ 0/100	0	m	10			ng	
CZ100	100 [a]	c	75	400,900	186	ng	126
CZ100	100 [a]		37	ng	62	ng	
CZ67	67 [a]	c	26	460	543	ng	
	67 [a]		10	ng	558	ng	

Table 1.16: OSC values for some ceria-zirconia mixed oxides (CZ) alone and impregnated with 2 wt % palladium, along with surface area calculated by BET method (BET SA) and peak maximum in TPR measurements, and amount of Ce^{3+} ions formed (%) after reduction to 773K. ^ see text regarding measurement of OSC for each study and ng represents data not given. * Phases were determined by XRD where m, t and c are the monoclinic, tetragonal and cubic phases respectively, [a] is mol % CeO_2 and [b] is wt % CeO_2.

- OSC of a mixed oxide with 67mol % Ce was 4 times that of ceria despite a lower surface area (126). No direct correlation between surface area and OSC was reported (114, 123,126). Fornasiero et al (113) also showed that for even very low surface area samples in the region 1-2 m^2g^{-1}, appreciable OSC (9.4 mLg^{-1}) was detected.

- Addition of palladium increased the OSC of both ceria and a 70:30 wt % CeO_2:ZrO_2 sample (see Table 1.16) (122).

- OSC varied for different supports of the same composition (122) and was sensitive to preparation parameters and particle size (118). For example, Jen et al (122) found that for 2 wt% palladium impregnated on supports with the same composition (70 % Ce) namely CZ2 and CZ3 and redox aged at 1050°C, OSC values (at 350°C) ranged from 570 μmol for CZ3 to 390 μmol for CZ2. Both compounds after impregnation had identical surface areas of 7 m^2g^{-1}. The difference in the OSC values arose from initial rates of CO_2 production after pulses of CO, a larger initial rate being observed for the CZ3. The differences in OSC were attributed to differences in the support itself and their specific processing rather than Pd-support interaction and Pd particle sizes. Fornasiero et al (118) observed for the same sample, Rh loaded $Ce_{0.60}Zr_{0.40}O_2$, the OSC value varied depending on surface area and particle size. A OSC value of 17.4 mL O^2g^{-1} was observed for a sample with a particle size of 6 nm compared to 8.4 for a sample with a particle size in excess of 90 nm.

In order to help understand the increase in OSC associated with certain mixed oxide compositions and preparation methods, the oxides have been investigated using TPR and structural studies such as EXAFS and neutron diffraction. The majority of studies using TPR have shown that the introduction of zirconium shifted the temperatures of reduction to lower values and resulted in the formation of a single peak (113, 123,138) on the TPR profiles (see Table 1.16 and Fig 1.26). The only exceptions to this was $Ce_{0.5}Zr_{0.5}O_2$ with a surface area of 64 m^2g^{-1} which was reported to have two peaks at 607 and 737°C respectively (117,141,142). Fornasiero et al (141) attributed the presence of the two peaks to two reduction processes occurring in the bulk of the mixed

oxide. The higher surface area sample was more reducible compared to lower surface area samples and hence the increased reducibility increased the concentration of charged defects. At a certain temperature, clustering of the defects occurred which decreased the rate of ionic transport in the bulk and further bulk reduction was shifted to higher temperatures. Hence bulk diffusion was limiting the diffusion of ions in the bulk.

The percentage reduction (amount of Ce^{3+} formed) also increased with zirconium content (138) and the mixed oxides regardless of surface area had higher reduction % than ceria alone (123) (see Table 1.16). Hydrogen uptake values calculated from the TPR profiles of $Ce_{0.5}$ $Zr_{0.5}$ O_2 were much higher than that estimated for surface reduction of ceria alone (141). For ceria and $Ce_{0.67}$ $Zr_{0.37}$ O_2 impregnated with equivalent amounts of Pt,Rh, Pd, Ru, and Ir, 1 and 5 oxygen layers respectively were involved in the OSC process (133). From theoretical OSC values for ceria, oxygen storage was limited to the surface, while for the mixed oxide, both surface and bulk oxygen storage occurred (125).

Hence in general, on introduction of Zr^{4+}, oxygen mobility in the bulk was increased by creation of structural defects (143). Bulk reduction was promoted and reduction occurred simultaneously in the bulk and the surface (140,141,143). This illustrated in Fig 1.26. In line with OSC values, a high degree of reduction between 327 and 427°C was observed for mixed oxide samples with 40-60% CeO_2 and the maximum of this peak for the cubic $Ce_{0.5}Zr_{0.5}O_2$ was 70°C lower than for the tetragonal phase (113). Maximum OSC was observed for the cubic sample and OSC increased with an increase in reducibility (140). Addition of Rh, Pt and Pd promoted the reduction of the support - see Table 1.16 (122). The peak temperature of the support reduction decreased from 377-677°C to about 177°C for Rh and Pt-loaded samples (141).

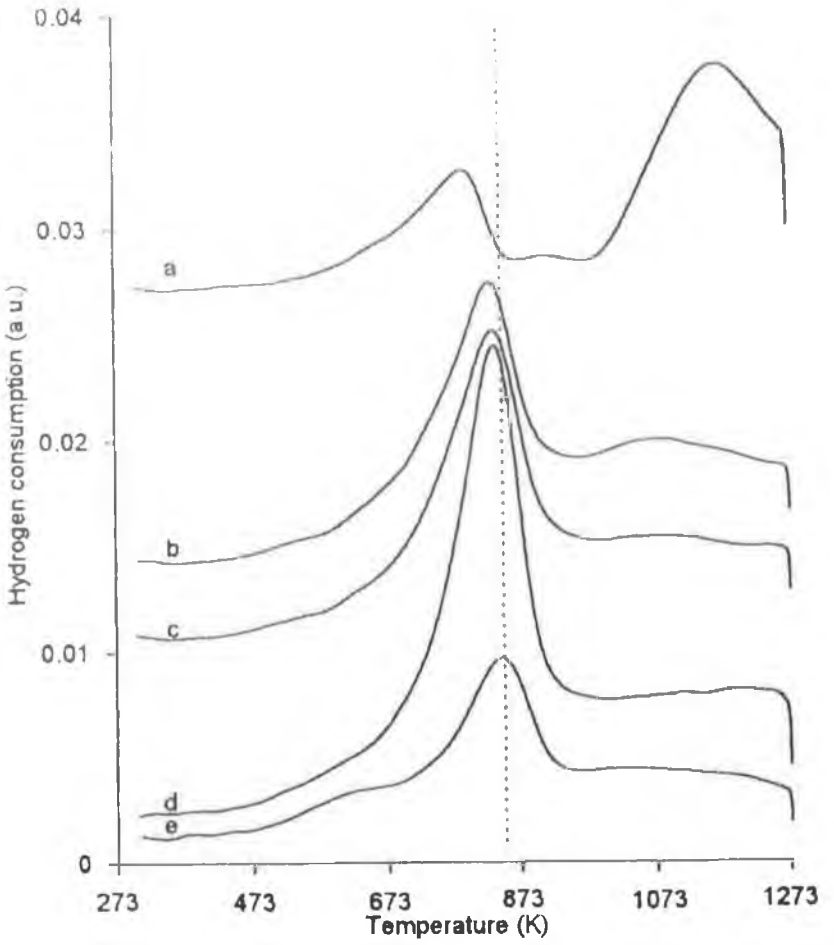

Fig 1.26: TPR profiles of (a) CZ 100/0, (b) CZ-80/20-HS, (c) CZ-68/32-HS, (d) CZ-50/50-HS, (e) CZ-15/85-HS where HS represents high surface area (138).

Isotope studies have shown that introduction of zirconium into the ceria lattice increased the rate of $^{18}O_2$ isotopic exchange (125) and that the exchange process up to 600°C involved surface oxygen ions and 3 bulk oxygen layers. $Ce_{0.63}Zr_{0.37}O_2$ was the most reactive of the samples studied for exchange reactions. Other samples studied were ceria-zirconia mixed oxides of the general formula $Ce_xZr_{1-x}O_2$ with x =1, 0.68, 0.50, 0.15 and 0. It was speculated that surface oxygen ions were superoxides or peroxides, with the presence of the former being confirmed in later study (144). A parallel between the amount of superoxides formed and the OSC (as measured by the pulse method) was observed. The superoxides were formed by interaction between gaseous oxygen and oxygen vacancies adjacent to the reduced cerium sites. Superoxides formed on the mixed oxide were more stable than for ceria and disappeared in the latter case on revacuation treatment.

Structural studies of ceria-zirconia mixed oxides with EXAFS showed the following results:

- An increase in ZrO_2 content led to a progressive shortening of the Ce-O bond length, 99, 100) due to the decrease in the cell parameter. Reported values for the mixed oxide have been 2.30Å (99) and 2.295 – 2.330 Å (100) compared to 2.35Å for pure ceria (99).

- Cerium preferred to keep its ideal fluorite situation also in mixed oxides (99,100) hence a coordination number of 8 for cerium was observed. This decrease in the Ce-O bond should make the removal of oxygens bonded to cerium atoms harder, but at same time, Zr-O bond distances increased as the cerium content increased.

- Disorder in oxygen sublattice was generated on substitution of cerium with zirconium (118). Some oxygen ions were pushed away from the zirconium cation to a distance further than the length of the first Zr coordination shell (100,118) or non-bonding distance, to relieve the overcrowding and stress on the 8 coordinated zirconium atom.

- As a result a tetragonal distortion was generated and t' phase formed was formed (100).

- Distortions in oxygen sublattice depended on the particle size, precursor (118) and composition (100). These are summarised in Table 1.17.

- The displacement of the oxygen ions far from zirconium was responsible for the improved reduction behaviour of ceria-zirconia mixed oxide due to their high disorder (118).

Sample	SA	CN* Zr-O	Radius (Å)	Ref
$Ce_{0.6}Zr_{0.4}O_2$	<1	4 2	2.134 2.328	118
$Ce_{0.6}Zr_{0.4}O_2$	50	5 2	2.132 2.323	
$Ce_{0.6}Zr_{0.4}O_2$	2	5 2	2.132 2.29	
t-$Ce_{0.2}Zr_{0.8}O_2$	ng	4 4	2.09 2.31	100
t' – $Ce_{0.5}Zr_{0.5}O_2$	ng	3 2	2.12 2.32	
t ''-$Ce_{0.5}Zr_{0.5}O_2$	ng	4 2	2.12 2.34	
t '' – $Ce_{0.6}Zr_{0.4}O_2$	ng	4 2	2.13 2.33	
c-$Ce_{0.8}$ Zr 0.2 O_2	ng	4 2	2.17 2.33	

Table 1.17 : Surface areas (SA), coordination number of Zr (CN) and Zr-O bond length (Radius) of various compositions of ceria-zirconia mixed oxides as determined by EXAFS studies. Phases were identified by XRD and raman where t and t' are the tetragonal and metastable tetragonal phase, t'' and c are the cubic phases and ng referes to data not given.

Mamontov et al investigated the relationship between oxygen storage capacity by TPR and the concentration of vacancy interstitial oxygen defects in a ceria and 70:30 % CeO_2: ZrO_2 solid solution, the structure of which is shown in Fig 1.27 (126). The creation of vacancies in the tetrahedral sites of the cubic structure by movement of interstitial ions to octahedral sites has been reported previously and the interstitial oxygen ions were believed to be the active species that provided the necessary oxygen mobility in pure ceria (145). It was found that on heating to 800°C, the number of oxygen vacancies was found to be equal to the number of interstitial ions for ceria, while an 8% difference between the two was observed for the solid solution (126). Hence the movement of the interstitial ions in the latter created non-stoichiometry and net oxygen deficiency. A dramatic reduction in OSC at 760-800°C on aging of ceria was correlated with a decrease in oxygen defect concentration. For the mixed oxide, oxygen defect concentration remained constant, as did oxygen storage capacity in the same temperature range. Hence the interstitial ions and oxygen vacancies were crucial

to the oxygen storage capacity. The smaller ionic radius of zirconium made it difficult for the vacancies to recombine with the interstitial ions.

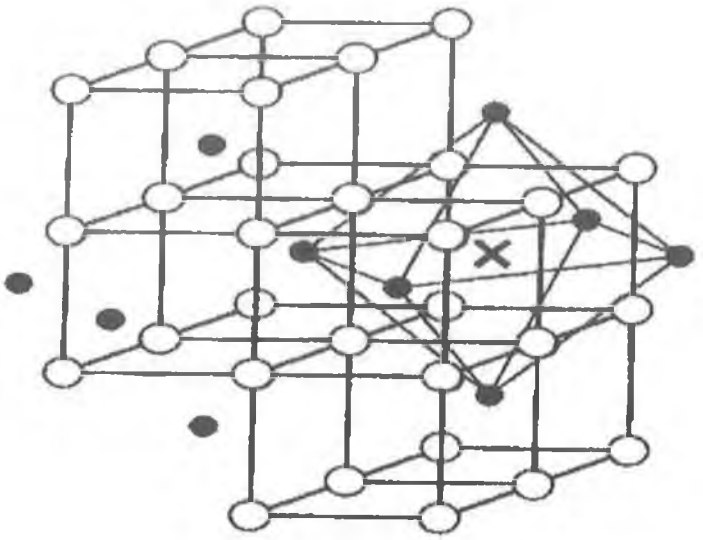

Fig 1.27: Fluorite structure of ceria and ceria-zirconia solid solutions, where the open circles refer to oxygen ions and the cations are the small filled circles. x represents an octahedral site (126).

The effect of redox cycling and aging in air on both textural and redox properties of cerium-zirconium mixed oxides has been investigated. In general redox cycling involves reduction of the sample in hydrogen followed by cooling to 427°C in helium and reoxidation with pulses of oxygen or flowing oxygen three (139) or four times (146). Promotion or preservation of reducibility by redox cycling has been reported to be a general property of high surface area mixed oxides (117,123,139) regardless of surface area. The effect of redox cycling on the reduction characteristics and textural properties of different mixed oxides is summarised in Table 1.18. The structure of the redox cycled mixed oxide samples changed with composition and treatment. On recycling 2 and 3 times, shoulders appeared on the low temperature side of the main peak (139). These extra features were favoured by an increase in zirconium content.

sample	SA (m^2g^{-1})	% Ce^{3+} fresh	% Ce^{3+} recycled	TPR peaks (°C) * Fresh	TPR peaks (°C) * recycled	Ref
CZ100-HS	100	38	39	517,897	857	123, 139
CZ100-LS	20	40	38			123
CZ80/20-HS	111(16)	55	56	557	517,592	123, 139
CZ80/20-LS	15 (13)	56	56			123
CZ 68/32HS	100(28)	66	67	557	522,572	123, 139
CZ 68/32-LS	23 (20)	66	66			123
CZ50/50-HS	106(22)	87	67	562	527,567	123, 139
CZ50/50- LS	21 (17)	73	78			123
CZ15/85-HS	95(53)	92	93	382,572	387,517	123, 139
CZ 50/50	64	62	54	557,607,737	391,472,566	141

Table 1.18: Effect of redox cycling experiments on temperatures of reduction and amount of Ce^{3+} formed on reduction (%) . Numbers in parentheses represent the BET surface areas (SA) after redox cycling, while LS and HS means low and high surface area respectively.

Despite a loss in surface area, total OSC by TPR and the availability of bulk and surface oxygen were unaffected by redox cycling of mixed oxide. The reduction % i.e. amount of Ce^{3+} cations formed was much higher for the low surface (LS) samples than the corresponding high surface (HS) samples after aging. The increase in reducibility was explained by a surface with a higher reactivity and a stable highly reduced state at temperatures as low as 280°C (123)

The redox behaviour of low surface area (LS) $Ce_{0.68}Zr_{0.32}O_2$ ($23m^2g^{-1}$) under re-oxidation conditions has also been examined and the results are shown in Fig 1.28 (147). TPR-MS traces for water were used to show the effect that the alternate mild and high temperature reoxidation treatments had on the redox behaviour of the mixed oxide previously reduced at 950°C. The two treatments resulted in very different but reversible redox behaviours. Before running the TPR-MS experiments, the oxide sample was oxidised either under mild oxidation (MO) or high temperature conditions (HTO). Both oxidation treatments were similar in that the sample was heated in a 5%

O_2/He mixture to either 550°C or 950°C respectively. A high temperature reduction treatment (SR) consisted of heating the MO pre-treated LS oxide under hydrogen to 950°C followed by a further MO reoxidation treatment. The resulting sample is referred to as SR and trace (b) in Fig 1.28 corresponds to the TPR-MS of that reduced sample. An increase in reducibility was observed. HTO of the SR sample led to a severe loss of reducibility as indicated by trace (c) in Fig 1.28. Oxidation of the sample resulting from the TPR-MS experiment in Fig 1.26 (c) according to the HTO treatment resulted in a shift towards lower reduction temperatures by 200K in the subsequent TPR-MS [Fig 1.28 (d)]. Fig 1.26 (g-j) demonstrates that the TPR-MS effects due to successive application of MO and HTO treatments are reversible since the behaviour can be reproduced in a cyclic fashion.

The effect of redox cycling and aging in air on OSC values and surface areas at 1050°C has also been investigated by Jen et al (122) and results are summarised in Table 1.19. Aging in air at > 900°C decreased the OSC of mixed oxides, both alone (140) and impregnated with palladium (122). However, the decrease in OSC on aging under redox conditions (alternating a 1 mol % CO/He and 0.5 mol % O_2 mixture every 10 minutes) was much greater for the ceria sample than the mixed oxide sample, both impregnated with palladium (see Table 1.19). Air aging at the same temperature decreased OSC more than redox aging.

Other studies have reported that the addition of zirconia to ceria stabilises surface area after high temperature treatments. The addition of zirconium retarded crystallite growth of the ceria matrix up till 770°C (148), with addition of 50 and 33 mol% ZrO_2 showing the best resistance to surface area loss up till 1000°C. Mamontov et al (126) also concluded that zirconium inhibited surface diffusion and surface area loss at high temperatures.

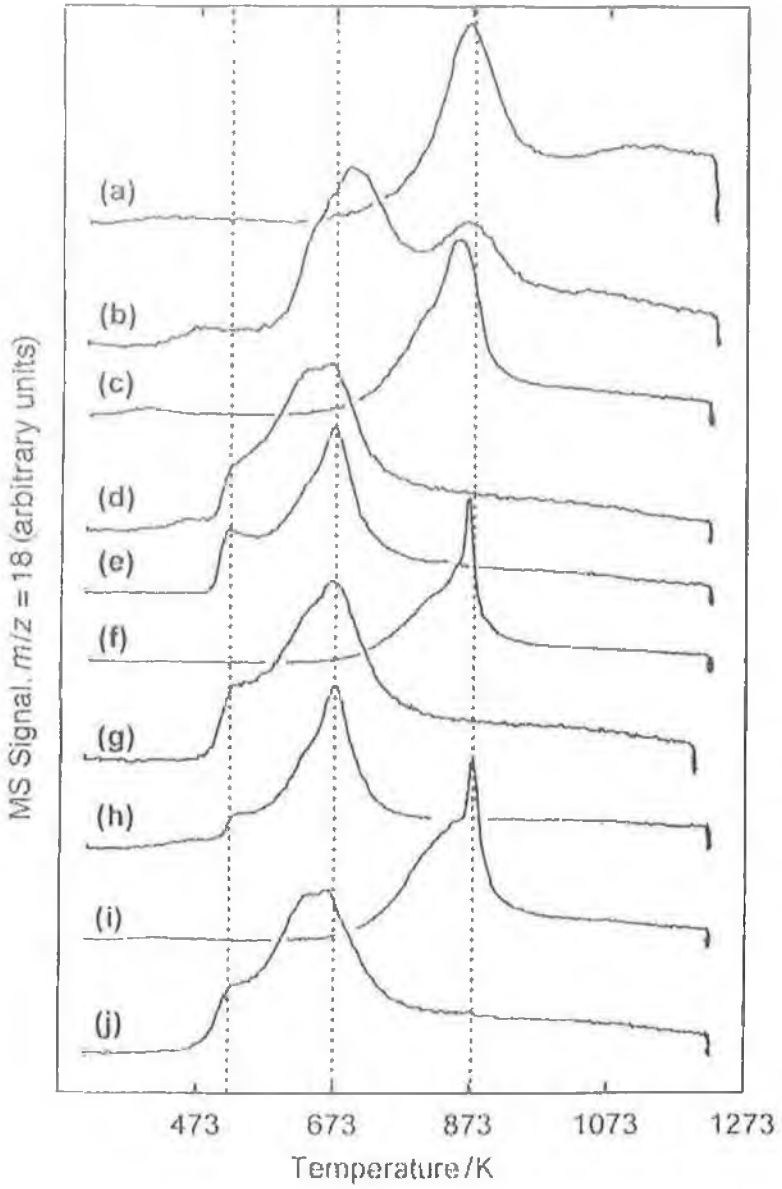

Fig 1.28: Influence of the pre-treatment conditions on the reducibility of a Ce/Zr mixed oxide(CZ-68/32-HS). TPR –MS traces corresponding to the sample pretreated as follows (a) fresh oxide sample(b) SR pre-treatment (c) HTO (d) MO (e) HTO (f) MO (g) MO (h) MO (i) HTO (j) MO (147). SR, HTO and MO refers to high temperature reduction treatment, high temperature oxidation and mild oxidation, for details see text (147).

sample	Wt % CeO_2	SA (m^2g^1)	Treatment (temp/°C)	OSC * @		OSC ~ @	Ref
				350°C	500°C	400°C	
CZ100	100	ng	none	100	210		122
2% Pd CZ100	100	81	none	270	360		
2% Pd CZ100	100	4	Redox (1050)	4	50		
CZ 70/30	70	ng	none	140	590		
2%Pd CZ70/30	70	79	none	890	970		
2% Pd CZ70/30	70	7	Redox (1050)		680		
2% Pd CZ70/30	70	5	Air (1050)	350	624		
CZ100	100	ng	none			0.2	140
		26	Air (900)			0.025	
CZ80	80	ng	none			0.225	
		30	Air (900)			0.100	
CZ68	68	ng	none			0.260	
		47	Air (900)			0.100	
CZ50	50	ng	none			0.320	
		48	Air (900)			0.080	

Table 1.19: Effect of air and redox aging on the OSC values and surface areas (SA) of ceria-zirconia mixed oxides, alone and impregnated with a noble metal. * OSC (µmol O/g) (was measured by exposure of sample to a alternate CO and O_2 pulse at 350 and 500°C ~ OSC (mmol O_2/g) was measured by exposure of sample to alternate CO and O_2 pulse at 400°C.

1.4.4 Other Modified Transition Metal Zirconia Catalysts

The concept of using zirconia as a support where the zirconia is already in the oxide form and the active metal oxide is impregnated on it has already been discussed in section 1.4.2. However Choudhary et al (149) found that a manganese-zirconia mixed oxide prepared by co-precipitation were more active for the combustion of methane than the corresponding impregnated sample. The reasons for this were stabilization of the cubic form, more mobile lattice oxygens and an increase in surface area. Despite their high activity as reported by Choudhary et al (149), relatively few publications have appeared on manganese, copper and cobalt doped zirconia. The effect of general doping of zirconia has been discussed previously in section 1.4.1. The doped zirconia samples below have been prepared by both co-precipitation and sol-gel and their structural parameters are summarized in Table 1.20, compiled from various references. Addition of up to 20 wt% Cu resulted in formation of substitutional vacancies (see section 1.4.1) due to smaller size of Cu^{2+} cations (150). The lattice parameter (i.e. the length of the side of the unit cell) calculated from the main diffraction peaks of the cubic phase decreased on increasing copper content (150). Up to 20 mol % of Cu (150) and 10% of Mn (152, 153) resulted in the formation of a solid solution, with the presence of a single phase detected in the XRD. Above these values (dissolution limits), precipitation of an additional second phase of CuO (150) and Mn_2O_3 (152) was observed. The dissolution limit observed for Mn by Fernandez Lopez et al (152, 153) was independent of the method used i.e. sol-gel or co-precipitation but was lower than that observed by Choudhary et al (149). In the latter a single cubic phase was maintained up to a Mn/Zr mole ratio of 0.67. For the sol-gel method performed at a very low or high pH, pure tetragonal phase was the only phase observed. Increase in the calcination temperature resulted in the progressive formation of Mn_2O_3, Mn_3O_4 and monoclinic ZrO_2 for samples prepared by the sol-gel method (153).

Transition metal (Me)	Me content	Preparation Method	SA/Calc temp (m^2g^{-1}) / °C	Structures	ref
Cu	2-20 ~	Sol-gel	2-8 /600	c-ZrO_2	150
Cu	1 ^	Modified sol-gel -acidic -basic	 79.5 /600 30.7 /600	 t-ZrO_2 t + m-ZrO_2	151
Mn	0.05 *	Co-precipitation	70 /600	c + m ZrO_2	149
	0.11		72 /600	c-ZrO_2	
	0.25		90 / 600	c-ZrO_2	
	0.43		71 / 600	c-ZrO_2	
	0.67		66 /600	c-ZrO_2	
	1		63/600	m + c ZrO_2, MnO_2	
Mn	0.1 #	Co-precipitation	7 / 600	t-ZrO_2	152
		Sol-gel	13 / 600	t-ZrO_2	153
	0.2 #	Co-precipitation	6 /600	t-ZrO_2	152
		Sol-gel	61/ 600	t-ZrO_2	153
	0.5 #	Co-precipitation	56 / 600	t-ZrO_2	152
		Sol-gel	61 / 600°C	t- ZrO_2, Mn_3O_4, Mn_2O_3	153
	0.8 #	Co-precipitation	61 @ 600°C	t-ZrO_2, Mn_2O_3	152
	0.9 #	Co-precipitation	66 @ 600°C	Mn_2O_3	152

Table 1.20: Stuctural parameters of modified zirconia where t represents tetragonal, m monoclinic and c cubic. The transition metal content was indicated in various ways dependent on the study where ~ represents mol % of Cu, * molar ratio (Mn)/(Zr), ^ wt % of Cu and # is the Mn versus Zr atomic composition for mixed oxides of the general formula $Mn_xZr_{1-x}O_2$.

Another study (154) found that ZrO_2 structure affected the nature of the manganese species present as shown in Table 1.21. In oxidizing environment, manganese entered the monoclinic phase as Mn^{3+} and Mn^{4+} and the cubic and tetragonal phases as Mn^{3+} and Mn^{2+}.

Sample	**wt % Mn**	**Temperature (°C)**	**Structure**			**Mn $^{n+}$**
			% m	**%t**	**%c**	
ZrO_2 (cp)	0	700	99	1		
ZMn (imp)	0.2	900		100		2+,3+
ZMn (cp)	0.5	850	71	29		
		1000	100			4+, 3+
		1350	100			4+, 3+
ZMn (cp)	1	1350	100			4+, 3+
YSZMn (imp)	0.2	1350			100	2+, 3+

Table 1.21: Effect of structure of zirconia (Z) and yrittia-stabilised zirconia (YSZ) on the oxidation state of the Mn species where m, t and c are the monoclinic, tetragonal and cubic phases, cp and imp are the co-precipitation and impregnation techniques respectively used for the preparation (154).

Castro et al (151) also highlighted the effect of modifying the sol-gel method by adding sulphuric acid or ammonium hydroxide to the alkoxide precursor followed by addition of water. The decrease in surface area for the former was attributed to increased alkoxide hydrolysis due to higher water content of the hydroxide.

Of the studies summarized in Table 1.20, only a few of the catalysts have been tested in the oxidation of hydrocarbons and carbon monoxide. The optimum activity measurements are summarized in Table 1.22.

Sample	T_{50} (°C) CH_4	C_4H_{10}	rate CH_4 * C_4H_{10} [a]	structure	Ref
Mn/Zr 0.11	490	nd	0.104	c ZrO_2	149
0.25	450	nd	0.126	c ZrO_2	
0.43	525	nd	0.097	c ZrO_2	
0.67	550	nd	0.079	c	
1	560	nd	0.025	m & c ZrO_2,MnO_2	
Mn (0 mol%)	nd	380	0.98	m	155
Mn (5 mol%)	nd	293	6.35	c + m	
Mn (10 mol%)	nd	207	19.4	c	
Mn (20 mol%)	nd	172	26.85	c	
Mn (30 mol%)	nd	187	24.60	c	
Mn (50 mol%)	nd	237	13.22	c + MnO_2	

Table 1.22: Combustion activities and structures for manganese-zirconia mixed oxides where rate was expressed in * mmol m^{-2} h^{-1} and [a] µmol g^{-1} s^{-1} and T_{50} = temperature required for 50% conversion of methane and butane. c and m reperesent cubic and monoclinic phases respectively as determined by XRD and nd represents not determined.

The good activity for manganese-zirconia oxides for both methane (149) and butane combustion (155) was attributed to the presence of the cubic structure which had more reactive lattice oxygen. Catalysts containing the cubic phase of zirconia were more active than catalysts containing the mixed cubic and monoclinic phases of zirconia (149). While all samples containing manganese showed a decrease in reduction temperatures compared to zirconia the largest shift was observed for cubic containing sample. Deterioration in activity for butane oxidation was observed on complete transformation from the cubic to monoclinic phase at 800°C (155). Another study (156) on manganese-zirconia indicated that the cubic phase is stabilized by the presence of Mn^{4+} up till 973K and Mn^{2+} after reduction above 700°C. Thermal analysis studies indicated that optimum amounts of manganese (0.1-0.3 mol) decreased the enthalpy and temperature of crystallization and this was the reason for the stabilization of the cubic

phase at low temperatures (157). The cubic structure obtained depended on an optimum amount of manganese. Maximum activity for the combustion of methane was also observed for a 20 mol % CuO/ZrO_2 prepared by a sol-gel method, with 95% conversion at 400°C (150). A steady increase in catalytic activity as the copper content was increased from 1 to 20 mol % was observed, indicating that the activity was related to CuO present in lattice positions as well as CuO on the surface/subsurface layer of cubic zirconia. The incorporation of redox Cu^{2+} into cubic zirconia along with the increase in oxygen mobility due to the formation of oxygen vacancies were the reasons given for the high activity of the 20 mol% CuO/ZrO_2 sample

References

(1) Oswald, W. Z., *Physik Chem.* **15,** 705 (1984).

(2) Catalysis and Biocatalysis Technologies 1998 White Paper "Leveraging resources and targeting performance" www-15.nist.gov/atp/97wp-cat.htm

(3) www.oit.doe.gov/chemicals/visions_catalysis.shtml

(4) Bond, G . C., *"Heterogeneous Catalysis: Principles and Applications"*, Clarendon Press, Oxford, 1987.

(5) Satterfield, C. N., *"Heterogeneous Catalysis In Practice"*, McGraw and Hill, New York, 1980.

(6) www.schoolscience.co.uk/content/5/chemistry/catalysis/catsch3pg2.html

(7) Schloten, J. J. F., in *"Catalysis : An Integrated Approach to Homogeneous, Heterogeneous and Industrial Catalysis"* (Moulijn, J. A., van Leeuwen, P. W. N. M. and van Santen, R. A., eds.), Studies In Surface Science and Catalysis, Vol. 79, 419-437, Elsevier, Amsterdam, 1993.

(8) Lee, J. D., *"Concise Inorganic Chemistry"*, Van Nostrand Reinhold Co, New York, 1977.

(9) Bowker, M., *"The Basis and Applications of Heterogeneous Catalysis"*, Oxford University Press, New York, 1998.

(10) Sing, K. S. U., Gregg, S. I., *"Adsorption, Surface Area and Porosity"*, Academic Press, London, New York, 1967.

(11) Campbell, I. M., *"Catalysis at Surfaces"*, Chapman and Hall, London NY, 1988.

(12) Spivey, J. J., *Ind. Eng. Chem. Res.* **26**, 2165 (1987).

(13) Thomas,J. M., Thomas, W.J., *"Principles and Practice of Heterogeneous Catalysis"*, VCH, New York, 1997.

(14) Bartholomew, C. H., *Appl. Catal., A* **212,** 17 (2001).

(15) Zwinkels, M. F. M., Järås, S. G. and Menon, P. G., *Catal. Rev .Sci. Eng.* **35,** 319 (1993).

(16) Germain, J. E., *"Catalytic Conversion of Hydrocarbons"*, Academic Press, NY, 1969.

(17) Choudhary, T. V., Banerjee, S., Choudhary, V. R., *Appl. Catal., A* **234,** 1 (2002).

(18) Heck, M. R., Farrauto, R. J., *Appl. Catal., A* **221,** 443 (2001).

(19) "*Technical Support Document : Control of Emissions of Hazardous Air Pollutants from Motor Vehicles and Motor Vehicles Fuels*," EPA Document No: EPA-420-R-00-023, December 2000.

(20) Pickrell, D., *Transportation Research Part. A* **33,** 527 (1999).

(21) Kašpar, J., Fornasiero, P., Hickey, N., *Catal. Today* **77,** 419 (2003).

(22) CONCAWE (Conservation of Clean Air and Water in Europe) 1994. Motor Vehicles Emission Regulations and Fuel Specifications 1994. Report 4/94, Brussels.

(23) Kummer, J. T., *J. Phys. Chem.* **90,** 4747 (1986).

(24) Su, E. C., Rothschild, W. G., *J. Catal.* **99,** 506 (1986).

(25) Su, E. C., Montrueil, C. N., Rothschild, W. G., *Appl. Catal.* **17,** 75 (1985).

(26) Kim, G., *Ind. Eng. Chem. Res. Dev.* **21,** 267 (1982).

(27) Harrison, B., Diwell, A., Hallett, C., *Plat. Met. Rev.* **32,** 73 (1988).

(28) Herz, R. K., *Ind. Eng. Chem. Res. Dev.* **20,** 451 (1981).

(29) Hu, Z., Heck, R. M., Rabinowitz, H. N., USP 6, 044, 644 (2000).

(30) Hu, Z., Heck, R. M., Smaling, R. M., Amundsen, A. R., USP 6, 497, 851 (2002).

(31) Eguchi, K., Arai, H., *Catal. Today* **29,** 379 (1996).

(32) Kesselring, J. P., "*Advanced Combustion Methods*" , Wiley, New York, 1986.

(33) Golodets, G. I., "*Heterogeneous Catalytic Reactions Involving Molecular Oxygen*", Elsevier, Amsterdam, 1983.

(34) Finocchio. E., Busca. G., Lorenzelli. V., Willey, R. J., *J. Catal.* **151,** 204 (1995).

(35) Baldi, M., Finocchio, E., Milellab. F., Busca, G., *Appl. Catal., B* **16,** 43 (1998).

(36) Moro-oka. Y., Ozaki, A., *J. Catal.* **5,** 116 (1966).

(37) Moro-oka,Y., Morikawa,Y., Ozaki, A., *J. Catal.* **7,** 23 (1967).

(38) Doornkamp, C., Clement, C., Ponec,V., *J. Catal.* **182,** 390 (1999)

(39) Baldi, M., Sanchez Escribano,V., Gallardo Amores, J. M., Milella, F., Busca, G., *Appl. Catal., B* **17,** L175 (1998).

(40) Busca, G., Guidetti, R., Lorenzelli, V., *J. Chem. Soc., Faraday Trans.* **86,** 989 (1990).

(41) Busca, G., *J. Mol. Catal.* **43**, 225 (1987).

(42) Boreskov, G. K., "*Catalytic Oxidation Of Dioxygen*", (Anderson, J. R, Boudart. M., eds.), Catalysis, Science and Technology, Vol.3, 40-137, Springer-Verlag, NY, 1982,

(43) Arnone, S., Bagnasco, G., Busca, G., Lisi, L., Russo, G., Turco, M., in "*Natural Gas Conversions V*" (Parmaliana, A., Sanfilippo, D., Frusteri, F., Vaccari,A., Arena, F., eds.), Studies in Surface Science and Catalysis, Vol.119, 65-70, Elsevier, Amsterdam, 1998.

(44) Yao, Y. Y., *J. Catal.* **39,** 104 (1975).

(45) Mars, P., van Krevelen, D. W., *Chem. Eng. Sci.* **3,** (1954).

(46) Moro-oka,Y., Ueda, W., Lee, K-H., *J. Mol. Catal. A: Chem.* **1,** 3954 (2003).

(47) Giamello, E., *Catal. Today* **41,** 239 (1998).

(48) Sojka, Z., Che, M. *C., R. Acad. Sci.* **3,** 163 (2000).

(49) Li, C., Domen, K., Maruya, K., Onishi, T., *J. Catal.* **123,** 436 (1990).

(50) Sokolovskii, V. D., *Catal. Rev. Sci. Eng.* **32,** 1 (1990).

(51) Breyesse, M., Guenin, M., Claudel, B., Latreille, H., Veron, J., *J. Catal.* **27,** 275 (1972).

(52) Nagase, K., Zheng, Y., Kodama, Y., Kakuta, J., *J. Catal.* **187,** 123 (1999).

(53) Doornkamp, C., Clement, C., Ponec.V., *Appl. Catal., A* **188,** 325 (1999).

(54) Finnocchio, E., Busca, G., Lorenzelli, V., Willey, R. J., *J. Catal.* **151,** 204 (1995).

(55) Finnocchio, E., Busca, G., Lorenzelli, V., Escribano, V. S., *J. Chem. Soc., Faraday Trans.* **92,** 1587 (1996).

(56) Pirkanneimi, K., Sillanpaa, M., *Chemosphere* **48,** 1047 (2002).

(57) McCarty, J. G., Gusman, M., Lowe, D. M., Hildenbrand, D. L., Lau. K. N., *Catal. Today* **47,** 5 (1999).

(58) Kung, H.H., in "*Transition metal oxides : surface chemistry and catalysis*" (Kung, H. H., ed.), Studies in Surface Science and Catalysis, Vol. 45 , pages 121-135, Elsevier, Amsterdam : The Netherlands:New York, 1989.

(59) Arai, H., Machida, M., *Appl. Catal., A* **138,** 161 (1996).

(60) Rossignol, S., Kappenstein, C., *Int. J. Inorg. Chem.* **3,** 51 (2001).

(61) Schaper, H., Doesburg, E. B. M., Van Reijan, L. I., *Appl. Catal.* **7,** 211 (1983).

(62) Rajesh Kumar, S., Pillai, S. C., Hareesh, U. S., Mukundan, P., Warrier, K. G. K., *Mater. Lett.* **43,** 286 (2000).

(63) Bhaskar, T., Reddy, K. R., Kumar, C. P., Murthy, M., Chary, K.V. R., *Appl. Catal., A* **211,** 189 (2001).

(64) Zhou, R-X., Jiang, X-Y., Mao, J-X., Zheng, X-M., *Appl. Catal.* **162,** 213 (1997).

(65) Dow, W-P., Huang, T- J., *J. Catal.* **160,** 171 (1996).

(66) Liu, Y., Zhong, B., Peng, S., Wang, O., Hu, T., Ning Xie,Y., Ju, X., *Catal. Today* **30,** 177 (1996).

(67) Dow, W-P., Wang, Y-P., Huang, T- J., *J. Catal.* **160,** 155 (1996).

(68) Marion, M. C., Garbowski, E., Primet, M., *J. Chem. Soc., Faraday Trans.* **86,** 3027 (1990)

(69) Xiao, T-C., Ji, S-F., Wung, H-T., Coleman, K. S., Green, M. L. H., *J. Mol. Catal. A: Chem.* **175,** 111 (2001).

(70) Tiernan, M. J., Fesenko. E. A., Barnes, P. A., Parkes, G. M. B., Ronane, M., *Thermochim. Acta* **379,** 163 (2001).

(71) Garbowski, E., Guenin, M., Marion, M-C., Primet, M., *Appl. Catal., A* **64,** 209 (1990).

(72) Milt, V. G., Lombardo, E. A., Ulla, M. A., *Appl. Catal., B* **37,** 63 (2002).

(73) Burton, J. J., Robert, L. G., "*Advanced Materials In Catalysis*", Academic Press, New York, 1977.

(74) Spinnichi, R., Delmastro, A., Ronchetti, R., Tofanari, A., *Mater. Chem. Phys.* **78,** 393 (2002).

(75) Arai, H., Yamada, T., Eguchi, K., Seiyana, T., *Appl. Catal.* 265 (1986).

(76) Alifanti, M., Kirchnerova, J., Delmon, B., *Appl. Catal., A* **245,** 231 (2003).

(77) Marchetti, L., Formi, L., *Appl. Catal., B* **15,** 179 (1998).

(78) Ciambelli, P., Cimino, S., De Rossi, S., Lisi, L., Minelli, G., Porta, P., Russo, G., *Appl. Catal., B* **29,** 239 (2001).

(79) Ciambelli, P., Cimino, S., De Rossi, S., Faticanti, M., Lisi, L., Minelli, G., Pettiti, I., Porta, P., Russo, G., Turco, M. , *Appl. Catal., B* **24,** 243 (2000).

(80) Leanza, R., Rossetti, L., Fabbrini, L., Oliva, C., Forni, L., *Appl. Catal., B* **28,** 55 (2000).

(81) Spinicci, R., Tofanari, A., Delmastro, A., Mazza, D., Ronchetti, R., *Mater. Chem. Phys.* **76,** 20 (2002).

(82) Oliva, C., Forni, L., *Catal. Comm.* **1,** 5 (2000).

(83) Forni, L., Rossetti, I., *Appl. Catal., B* **38,** 29 (2002).

(84) Machida, M., Sato, A., Kijima, T., Inoue, H., Eguchi, K., Arai, H., *Catal. Today* **26,** 239 (1995).

(85) Artizzu-Duart, P., Millet, J. M., Guilhaume, N., Garbowski, E., Primet, M., *Catal. Today* **59,** 163 (2000).

(86) Wang, J., Tian, Z., Xu, J., Xu, Y., Xu, Z., Lin, L., *Catal. Today* **83,** 213 (2003).

(87) Jang, B. W.-L., Nelson, R. M., Spivey, J. J., Ocal, M., Oukaci, R., Marcelin, G., *Catal. Today* **47,** 103 (1999).

(88) Berg, M., Järås, S., *Catal. Today* **26,** 223 (1995).

(89) Artizzu-Duart, P., Brullé, Y., Gaillard, F., Garbowski, E., Guilhaume, N., Primet, M., *Catal. Today* **54,** 181 (1999).

(90) Yan, L-C., Thompson, L. T., *Appl. Catal., A* **171,** 219 (1998).

(91) Trovarelli, A., de Leitenburg, C., Dolcetti, G., *Chemtech* 32 (1997).

(92) Smart, L., Moore, E., "*Solid State Chemistry : An Introduction*", Chapman and Hall, London, 1995.

(93) Weller, M., "*Inorganic Materials Chemistry*", Oxford University Press, Oxford,1994.

(94) Fukui, K., Namai, Y., Iwasawa, Y., *Appl. Surf. Sci.* **188,** 252 (2002).

(95) Skinner, S. J., Kilner, J. A., *Mat. Today* **6,** 30 (2003).

(96) Yamaguchi, T., *Catal. Today* **20,** 199 (1994),

(97) Lee, W. E., "*Ceramic Microstructures : Property Control by Processing*", Chapman and Hall, London, 1994.

(98) Zhao, X., Vanderbilt, D., *Phys. Rev. B: Condens. Matter* **65,** 1 (2002).

(99) Ping, Li., Chen, I-Wei., Penner-Hahn , J. E., *J. Am. Ceram. Soc.* **77,** 1281 (1994).

(100) Vlaic, G., Di Monte, R., Fornasiero, P., Fonda, E., Kašpar, J., Graziani, M., *J. Catal.* **182,** 378 (1999).

(101) Tichit, D., El Alami, D., Figueras, F., *J. Catal.* **163,** 18 (1996).

(102) Garvie, R. C., *J. Phys. Chem.* 1238 (1964).

(103) Ali, A. A. M., Zaki, M. I., *Thermochim. Acta* **387,** 29 (2002).

(104) Lin, J-D., Duh, J-G., *J. Am. Ceram. Soc.* **81,** 853 (1998).

(105) Callister, W. D., "*Materials Science and Engineering*", John Wiley and Sons, New York, 1997.

(106) McHale, A. E., "*Phase Diagrams and Ceramic Processes*", Chapman and Hall, New York, 1998.

(107) Zacate, M. O., Minervini, L., Bradfield, D. J., Grimes, R. W., Sickafus, K. E., *Solid State Ionics* **128,** 243 (2000).

(108) Quinelatoa, A. L., Longob, E., Perazollic, L. A., Varela, J. A., *J. Eur. Ceram. Soc.* **20,** 1077 (2000).

(109) Yashima, M., Morimoto, M., Ishizawa, N., Yoshimura, M., *J. Am. Ceram. Soc.* **76,** 1745 (1993).

(110) Yashima, M., Morimoto, M., Ishizawa, N., Yoshimura, M., *J. Am. Ceram. Soc.* **76,** 2865 (1993).

(111) Yashima, M., Arashi, H., Kakihama, M., Yoshimura, M., *J. Am. Ceram. Soc.* **77,** 1067 (1994).

(112) Yashima, M., Takashina, H., Kakihana, M., Yoshimura, M., *J. Am. Ceram. Soc.* **77,**1869 (1994).

(113) Fornasiero, P., Di Monte, R., Ranga Rao, G., Kašpar, J., Meriani, S., Trovarelli, A., Graziani, M., *J. Catal.* **151,** 168 (1995).

(114) Rossignol, S., Madier, Y., Duprez, D., *Catal. Today* **50,** 261 (1999).

(115) Colon, G., Valdivieso, F., Pijolat, M., Baker, R. T., Calvino, J. J., Bernal, S., *Catal. Today* **50,** 271 (1999).

(116) Terribile, D., Trovarelli, A., Llorca, J., de Leitenburg, C., Dolcetti, G., *Catal. Today* **43,** 79 (1998).

(117) Fornasiero, P., Balducci, G., Di Monte, R., Kašpar, J., Sergo, V., Gubitosa, G., Ferrero, A., Graziani, M., *J. Catal.* **164,** 173 (1996).

(118) Fornasiero, P., Fonda, E., Di Monte, R., Vlaic, G., Kašpar, J., Graziani, M., *J. Catal.* **187,** 177 (1999).

(119) Hori, C. E., Haryani, P., Simon Ng , K. Y., Brenner, A , More, K., Rahmoeller, K. M., Belton, D., *Appl. Catal., B* **16,** 105 (1998).

(120) Kagaku-Binran, Koeshen II: Japanese Chemical Society, Ed:Maruzen Tokyo, 1984, pII-476.

(121) Yao, H. C., Yu Yao,Y. F., *J. Catal.* **86,** 254 (1984).

(122) Jen, H-W., Graham, G. W., Chun, W., McCabe, R. W., Cuif, J-P., Deutsch, S. E., Touret, O., *Catal. Today* **50,** 309 (1999).

(123) Fally, F., Perrichon, V., Vidal, H., Kaspar, J., Blanco, G., Pintado, J. M., Bernal, S., Colon, G., Daturi, M., Lavalley, J. C., *Catal. Today* **59,** 373 (2000).

(124) Bozo, C., Guilhaume, N., Garbowski, E., Primet, M., *Catal. Today* **59,** 33 (2000).

(125) Madier, Y., Descorme, C., Le Govic, A. M., Duprez, D., *J. Phys. Chem. B* **103,** 10999 (1999).

(126) Mamontov, E., Egami, T., Brezny, R., Koranne, M., Tyagi, S., *J. Phys. Chem. B* **104,** 11110 (2000).

(127) Giordano, F., Trovarelli, A., De Leitenburg, C., Miona, M., *J. Catal.* **93,** 273 (2000).

(128) Ozawa, M., Loong, C-K., *Catal. Today* **50,** 329 (2001).

(129) Skorodumova, N. V., Simak, S. L., Lundqvist, B. I., Abrikosov, L. A., Johansson, B., *Phys. Rev. Lett.* **89,** 1 (2002).

(130) Sayle, T., Parker, S., Catlow, C. R. A., *J. Chem. Soc., Chem. Commun.* 977 (1992).

(131) Martin, D., Duprez, D., *J. Phys. Chem.* **100,** 9429 (1996).

(132) Hurst, N. W., Gentry, S. J., Jones, A., McNicol, B. D., *Catal. Rev. Sci. Eng.* **24,** 233 (1982).

(133) Bedrane, S., Descorme, C., Duprez, D., *Catal. Today* **75,** 401 (2002).

(134) Schmieg, S. J., Belton, D. N., *Appl. Catal., B* **6,** 127 (1995).

(135) Rosemond, E., Essayem, N., Frety, R., Perrichon,V., Primet, M., Galasc, S., Chevner, M., Gauthier, C., Mathis, F., in "*Catalysis and Automotive Control IV*" (Kruse, N., Frennet, A., Bastin, J.-M., eds.), Studies in Surface Science and Catalysis IV, Vol. 116, 137-146, Elsevier, New York, 1998.

(136) Irusta, S., Boix, A., Vassallo,J., Miro, E., Petunchi.J, in "*Catalysis and Automotive Control IV*" (Kruse, N., Frennet, A., Bastin, J.-M., eds.), Studies in Surface Science and Catalysis IV, Vol. 116, 175-184, Elsevier, New York, 1998.

(137) Perrichon,V., Lacchir, A., Abouarnadasse, S., Touret, O., Blanchard, G., *App. Catal., A* **129,** 69 (1995).

(138) Daturi, M., Finocchio, E., Binet, C., Lavalley, J., Fally, F., Perrichon, V., Vidal, H.,Hickey, N., Kašpar, J., *J. Phys. Chem. B* **104,** 9186 (2000).

(139) Vidal, H., Kašpar, J., Pijolat, M., Colon, G., Bernal,S., Cordón, A., Perrichon,V., Fally, F., *Appl. Catal., B* **27,** 49 (2000).

(140) Finnocchio, E., Daturi, M., Binet, C., Lavalley, J. C., Fally, F., Perrichon, V., Vidal, H., Kašpar, J., Graziani, M., Blanchard, G., in "*Science and Technology in Catalysis 1998*" Studies in Surface Science and Catalysis,Vol. 121, 257-262, Tokyo: Kodansha; Amsterdam; New York; Elsevier, 1999.

(141) Fornasiero, P., Balducci, G., Kašpar, J., Meriani, S., Di Monte, R., Graziani, M., *Catal. Today* **29,** 47 (1996).

(142) Fornasiero, P., Kašpar, J., Sergo, V., Graziani, M., *J. Catal.* **182,** 56 (1999).

(143) González-Valasco, J. R, Guittiérrez-Ortiz, M. A., Marc, J. L., Botas, J. A., Pilar González-Marcos, M., Blanchard, G., *Appl. Catal.*, B **22,** 167 (1999).

(144) Descorme, C., Madier, Y., Duprez, D., *J. Catal.* **196,** 167 (2000).

(145) Mamontov, E., Egami, T., Brenzy, R., Koranne, M., Tyng, S., *J. Phys. Chem. Solids* **61,** 1345 (2000).

(146) Ozawa, M., Kimura, M., Isogai, A., *J. Alloys Compd.* **193,** 73 (1993).

(147) Baker, R. T., Bernal, S., Blanco, G., Cordón, Ana M., Pintado, J. M., Rodriguez-Izquierdo, Jose M., Fally, F., Perrichon, V., *Chem. Commun.* 149 (1999).

(148) Colon, G., Valdivieso, F., Pijolat, M., Baker, R. T., Calvino, J. J., Bernal, S., *Catal. Today* **50,** 271 (1999).

(149) Choudhary, V. R., Uphade, B. S., Pataskar, S. G., *Appl. Catal., A* **227,** 29 (2002).

(150) Dongare, M. K., Dongare, A. V., Tare, V. B., Kemnitz, E., *Solid State Ionics* **152,** 455 (2002).

(151) Castro, L., Reyes, P., De Correa, C. M., *J. Sol-gel. Sci. Tech.* **25,** 159 (2002).

(152) Fernández-López, E., Sánchez-Escribiano, S., Resini.C, Gallardo-Amores, J. M., Busca, G., *Appl. Catal., B* **29,** 251 (2001).

(153) Fernández-López, E., Sánchez-Escribiano, S., Resini.C, Gallardo-Amores, J. M., Busca, G., *Solid State Ionics* **4,** 951 (2002).

(154) Occhiuzzi, M., Cordischi, D., Dragone, R., *Phys. Chem. Chem.* Phys. **5,** 4938 (2003).

(155) Keshavaraja, A., Ramaswamy, A. V., *Appl. Catal., B* **8,** L1 (1996).

(156) Keshavaraja, A., Ramaswamy, A., *J. Mater. Res.* **9,** 837 (1994).

(157) Keshavaraja, A., Jacob, N. E., Ramaswamy, A. V., *Thermochim. Acta* **254,** 267 (1995).

Chapter 2:

Preparation and Characterisation Techniques used

2.1 Introduction

In this chapter, the literature on the general preparation of bulk oxides is reviewed, with emphasis on the preparation of zirconia and ceria-zirconia mixed oxides. In addition, the background and experimental procedures for each technique used to characterise and test the catalysts prepared in this thesis, are discussed in the Experimental Section (2.3). Details of exact preparation conditions used to prepare catalysts for this work are given in the relevant sections (Zr-Ce, section 3.1, Zr-Mn, section 4.1 and Zr-Co and Zr-Cu, section 5.1).

2.2 General Preparation Methods

Intimate blending techniques for the preparation of multicomponent oxides involve the use of co-preciptiation, ball-milling and sol-gel techniques (1). Ballmilling has been rarely used for the preparation of multicomponent catalysts due to the high temperatures and long reaction times involved. Hence both co-precipitation and sol-gel techniques will be discussed in greater detail. Co-precipitation and sol-gel techniques employ precursor compounds such as carbonates, bicarbonates, hydroxides, nitrates and oxalates that decomposed at low temperatures in air or oxygen hence minimising sintering of the oxide. For low temperature synthesis, a solid containing the metal precursors is extracted from solution, dried and calcined. According to Kung (1), the crystallographic forms, morphology, composition and surface structure of the final powder differs depending on the method used.

2.2.1 Precipitation and Co-precipitation

Zirconia has been prepared by precipitation by the following reactions (2,3):

$ZrOCl_2 + 2NH_4OH \rightarrow ZrO(OH)_2 + 2NH_4Cl$ @ 80°C

$ZrO(OH)_2 \rightarrow ZrO_2$ calcination

In co-precipitation, a precipitating agent is added to a solution containing the precursor compounds. Since the precursor is normally in aqueous form, the solution chemistry of

the zirconium ion and precursor has been investigated. A tetranuclear $(Zr_4(OH)_8(H_2O)_{16})^{8+}$ ion has been identified in solutions of $ZrOX_2.8H_2O$ where X = Cl, Br and I (4), the structure of which is depicted in Fig 2.1.

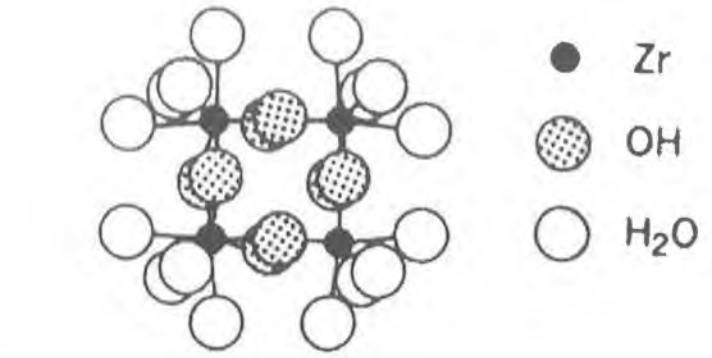

Fig 2.1: Schematic representation of tetranuclear $(Zr_4(OH)_8(H_2O)_{16})^{8+}$ ion (4).

Polymerisation of the tetranuclear cation on heating and/or addition of base resulted in formation of amorphous hydrated oxyhydroxide of general formula $ZrO_{2-x}(OH)_{2x}.yH_2O$ where $x \leq 2$ and $y = 1$ (5) or $ZrO_x(OH)_{4-2x}.yH_2O$ (6). The x value depended on experimental condition. For example, the formation of an oxyhydroxide with $x = 1$ or $ZrO(OH)_2$ has been reported (2,7). As the sample became drier, the value of x decreased. The following scheme has been proposed (see Fig 2.2) (5). At 80°C, release of adhered H_2O occurred, followed by dehydroxylation at 140°C and formation of amorphous zirconium oxide between 200 and 400°C. At 500°C, the amorphous zirconium oxide crystallised in a tetragonal or monoclinic phase, depending on the composition of the original starting material. The transformation from the metastable tetragonal to the monoclinic phase occurred upon further heating from 600 - 800°C. The monoclinic form was prepared at 500°C from the rapid addition of an aqueous solution of potassium fluorozirconate to concentrated ammonium hydroxide at room temperature.

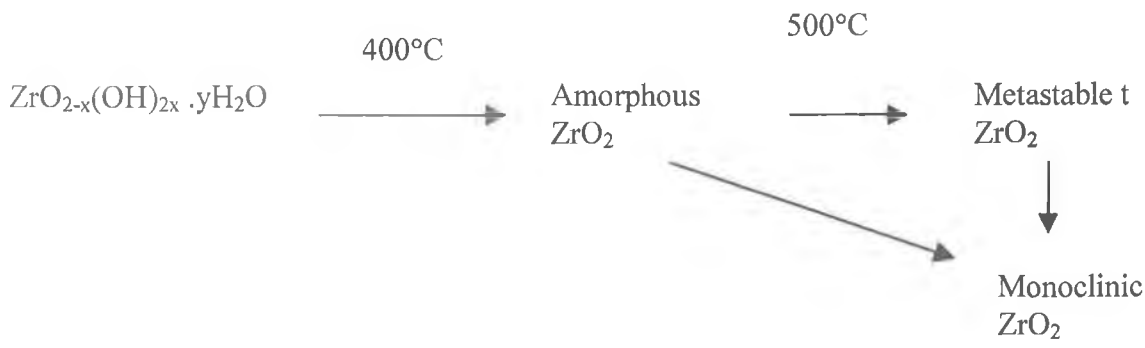

Fig 2.2:Changes in zirconium oxyhydroxide on heating (5), where t represents tetragonal zirconia.

The crystallisation of zirconium has been detected by thermal analysis such as differential thermal analysis (DTA). An exothermic peak has been observed in many thermal decomposition studies of zirconia and modified zirconia (see cited references in Table 2.1). It has been ascribed to crystallisation of amorphous zirconium oxide into tetragonal or monoclinic phases (2,5,8,9). The temperature of this crystallisation peak has been affected by pH, addition of additives and in some studies on the conditions of preparation (see Table 2.1).

An increase in pH increased the surface area of uncalcined samples (6). Critical particle size also was a function of pH where below pH 6 and above pH 10 larger crystals were formed and in the intermediate pH, crystals of size 120-170Å were reported. Two different types of preparation methods were used in the study (6):

(i) Constant pH method where precursor solution was added to base;

(ii) Non steady pH method where base was added dropwise to the precursor solution.

The former method gave surface areas 30-60% higher than the latter, keeping all other variables constant.

Sample	Additive	pH	Peak temp of exotherm (°C)	Reference
ZrO_2	none	4	470	2
		9	452	
ZrO_2	Cu (2mol%)	nd	462	10
	Cu(17mol%)	nd	551	
	Cu(30mol%)	nd	No peak	
Sulphated-ZrO_2	none	1	No peak	11
	Cu	1	545	
	Fe	1	577	
NH_4OH-ZrO_2	none	9	430	11
	Cu	9	447	
ZrO_2	none	8	467	7
	Mn (0.1) *	8	603	
	Mn (0.3) *	8	687	

Table 2.1: Summary of the effect of various transition metal oxides on the DTA (Differential thermal analysis) profile of ZrO_2. nd represents not determined, indicating that no pH value was given in the corresponding study. The pH values quoted is the final pH established with the addition of ammonia during precipitation (ref 2,9) while in ref 11, final pH of 1 or 9 was reached by the addition of sulphuric acid or ammonium hydroxide to the precursor solution respectively. *concentration of Mn (mol) in parenthesis.

Particle size of precipitates has also been found to be dependent on the precipitate solubility in the medium in which it was being formed (12). Temperature, reaction conditions and rate at which the reactants were mixed also had an impact (12). Precipitation has been reported to occur in three steps, superstaturation, nucleation and growth. Supersaturation can be approached by increasing concentration and pH or decreasing the temperature (13). Once within the supersaturation region, precipitation has been reported to occur readily and the particles develop in two sequential steps:

nucleation and particle growth (12). The former occured when a minimum number of ions, atoms, or molecules unite to form a stable second phase and particle growth follows. In the latter, growth occurred on existing nuclei. The size of the precipitated crystal decreased as supersaturation increases. If nucleation is the predominant process, a precipitate with a large number of small particles is formed, while growth is characterised by a small number of large particles (12). The rate of nucleation and particle growth has been reported to be related to a single parameter called relative supersaturation which can be defined by the following equation:

$$\text{Relative supersaturation} = \frac{Q - S}{S}$$

where Q is the concentration of the solute and S is the equilibrium solubility. When relative supersaturation is high, nucleation exceeds particle growth and the precipitate is colloidal. At low supersaturation, particle growth may be greater and a crystalline solid was more likely.

Srinivasan et al (9) found that the time taken to reach pH values in the range 7-9 and at 10.4 had a significant effect on the structures formed. Rapidly precipitated samples contained predominantly monoclinic phase while slow precipitation (8 hours) yielded tetragonal phase. For pH >10.5, both rates of addition yielded tetragonal phase. The same study also concluded that at room temperature, the cation added with the base (ammonium, sodium and potassium) or anion associated with the precursor had no effect on the crystal structure. The extent of polymerisation in the zirconyl precursor ($ZrCl_4$ vs $ZrOCl_2.8H_20$) was reported to be the significant factor. However, Tichit et al (14) observed that the starting salt had an effect on surface area with higher surface areas obtained using the oxychloride salt, while nitrate salt led to gels with denser particles compared to the oxychloride.

The digestion temperature, precipitating agent and time of digestion have all been reported to play a crucial role on both surface area and crystal structure as shown in Table 2.2. Digestion refers to a step in the preparation process that occurs after complete addition of the base to the precursor solution i.e. precipitation.

A portion of precipitate was removed immediately and washed (undigested or 0 hours) and the rest was left to digest, in its mother liquor, at a certain temperature for various lengths of time. After the respective times, the samples were then removed and vacuum filtered (15). At the same temperature and pH, increasing digestion time dramatically increased surface area and percentage of tetragonal phase (15,16). However depending on the base used and pH, different optimum digestion times have been reported: 12-24 hours for KOH and NaOH (15) and 72 hours for ammonium hydroxide (16). In the latter, pH 9 was maintained. In the study by Chuah and Jaenicke (15), pH 14 was maintained and for undigested samples (0 hours) a mixture of two phases (monoclinic and tetragonal) were formed. This is in contrast to results by Srinivasan et al (9), who at the same pH, observed pure tetragonal phase at room temperature. Increase in digestion temperature only gave moderate increase in surface area but greatly increased the amount of tetragonal phase when the temperature was increased from 50 to 80°C (16).

Digestion temp (°C)	**Digestion time (hours)**	**Structure (%)**	**Precipt agent**	**SA/Calc temp (m^2g^{-1})/°C**	**Ref**
100	12-24	t	NaOH	250 /500	15
	12-24	m + t	KOH	200 /500	
25	0	m + t	NaOH	43 /500	
	0	m + t	KOH	40 /500	
25	48	m	NH_4OH	164 /600	16
	72	t	NH_4OH	240 /600	
80	48	t (40)	NH_4OH	190 /600	

Table 2.2: Effect of digestion temperature and time on structures and surface areas (SA), where m and t are monoclinic and metastable tetragonal respectively and Precipt agent is the base used.

Chuah and Jaenicke (15) also observed that digested samples of the NaOH series had higher surface areas than those from the KOH series. Digestion also had a significant effect on thermal stability in terms of surface area and the amount of tetragonal phase

present. Digested samples retained a surface area of $170m^2g^{-1}$ after calcination at 800°C and the % tetragonal phase remained constant at approx. 75-85% when the zirconia was calcined up to 1000°C (15). After calcination at 1100°C, the monoclinic phase became predominant, especially for digestion times of less than 48 hours. Samples prepared via longer digestion times in the KOH series still retained 70% tetragonal phase. For undigested samples, 100% monoclinic phase was observed by 900°C. Reasons cited for improved thermal stability were the formation of stronger network at the higher temperature and longer digestion time (15). With the latter, thickening of the neck occurred to a greater extent. With the higher temperature, the rate of collisions of the particles increased leading to aggregation of the particles. Further deposition of the oxide occurred preferentially at the junction of the two particles and the neck area was thickened. Other suggestions for the effect of digestion time on thermal stability were formation of purer and less defective crystals, which reduced surface diffusion and intercrystallite growth and sintering (15,16). As the calcination temperature was increased, degree of transformation to the monoclinic phase increased (16,17). Neck growth is shown in Fig 2.3.

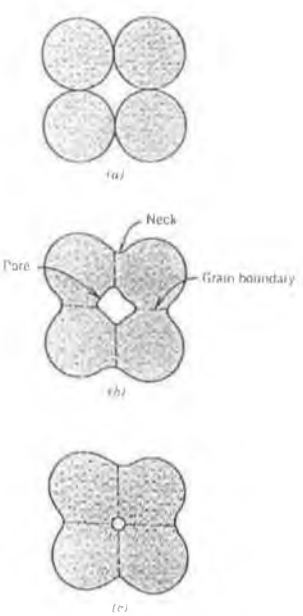

Fig 2.3:For a powder compact, microstructural changes that occur on firing (a) powders particles after pressing. (b) particle coalescence and pore formation as sintering begins and (c) as sintering proceeds, the pores change size and shape (18).

2.2.2 Sol-gel method

A sol has been described as a colloidal suspension of solid particles in a liquid and contains particles with sizes in the range 1-1000 nm. A gel has been defined as a semi solid material in which the solid gel network enscapulates the liquid phase (alcohol) (19). In the sol-gel process, a sol is prepared and then grown in size to form a gel. Most commonly used raw materials in sol-gel chemistry are alkoxides although metallic salts such as oxalate, acetate, citrate can also be employed (20). The transformation of a sol to a gel has been reported to take place via hydrolysis and condensation of the alkoxide precursor (19). Hydrolysis reaction is represented as

$$\text{-M-OR} + H_2O \rightarrow \text{-M-OH} + \text{R-OH} \qquad \text{Hydrolysis}$$

For metal alkoxide precursors ($M(OR)_x$), R represents an alkyl group

In the condensation reaction, the two partially hydrolysed molecules join together with the liberation of water or an alcohol. Those reactions are represented as follows (19):

$$\text{-M-OR} + \text{-M-OH} \rightarrow \text{-M-O-M-} + \text{R-OH} \qquad \text{condensation}$$
$$\text{-M-OH} + \text{-M-OH} \rightarrow \text{-M-O-M-} + H_2O \qquad \text{condensation}$$

Monomers have been reported to condense to form rings and create 3-D colloidal particles. Linear, branched or particulate polymeric species are produced during the growth process (20). Further particle growth has been reported on these nuclei to proceed by an Ostwald ripening mechanism whereby particles grow in size and smaller particles precipitate onto larger or higher molecular weight segments.

The key controlling factors for the textural and chemical properties of the calcined oxides have been reported as the ratio of the rate constants of hydrolysis and condensation, which are affected by the following:

- **Nature of organic portion (R group)**: rate constant for hydrolysis decreased as the size of the alkoxy ligand increased (19).
- **Drying methods**: The gels formed have been dried by evaporative drying or supercritical drying (19). The latter has the advantage that partial collapse of the network structure and loss of surface area is minimised. This was because the supercritical drying removed the liquid-solid interface that developed when solvent was removed from the pores of the gel. This is achieved by using a drying temperature and pressure that exceeds the critical pressure of the solid. Inevitable shrinkage of the gel by evaporative drying can be minimised by use of a solvent with a lower surface tension (20).
- **Digestion conditions**: Digestion of the gel in the mother solution at constant pH and higher temperature increased surface area and decreased crystallite size of calcined ZrO_2 and improved thermal stability at 1000°C (21). Below 1000°C, no phase transformation to the monoclinic phase was observed for the digested samples. Optimal digestion time of 192 hours was observed with an increase in surface area up to that point. Increase in thermal stability was attributed to formation and stabilisation of a strengthened porous network via increased neck formation between particles.
- **Water/alkoxide ratio.** The effect of this parameter depended on whether the gel was digested or not (21). For undigested samples, the water alkoxide ratios of 2, 16 and 32 had no significant effect on surface area. For digested samples at optimal digestion time, increased water/alkoxide ratio increased the surface area. The increase in surface area was attributed to the dominance of the nucleation mechanism in the higher water/alkoxide ratio, which resulted in formation of smaller particles.
- **pH** : Digestion at pH 1 and 3 decreased the surface area compared to pH 9 for digested and undigested samples and resulted in formation of mixtures of tetragonal and monoclinic phases (21). Digested samples had a more uniform structure with many small amorphous particles linked to form a sponge-like network. In the presence of excess water, hydrolysis of zirconium hydroxide was fast and the nucleation mechanism predominated over particle growth. Uniform spherical shaped particles were observed with each sphere being a single crystal for digestion at pH 1 and 3. Under acidic conditions, the solubility of zirconia

was high and particle growth occurred due to continuous dissolution and redistribution. The surface areas and structures are represented in Table 2.3, using the data reported in reference (21).

Another study (19) found that in silica-zirconia mixed oxides, an increase in the prehydrolysis ratio (i.e. mol H_2O/mol Si) ratio during prehdyroysis of silica reduced the surface area and affected the hydrolysis reaction itself. At lower prehydrolysis rates, much of the silicone precurser was unhydrolysed. At high ratios, cross linking occurs between the hydrolysed dimers. The hydrolysis reaction can be catalysed by the addition of an acid or base (22). The mechanism of hydrolysis and the structure of the linear molecules formed have also been found to be dependent on pH.

Sample	**pH**	**Digestion time (hours)**	**SA* (m^2g^{-1})**	**(H_2O)/ ^ ($M(OR)_4$)**	**% t ~**
ZrO_2	1	0	20	32	9
		24	22		65
		192	70		28
	3	0	27	32	8
		24	52		71
		192	58		59
	9	0	20		7
		96	190		100
		192	380	32	amor
		192	300	16	amor
		192	280	2	amor

Table 2.3: Effect of variations in preparation parameters on ZrO_2 prepared by the sol-gel method where * surface area as determined by the BET method, ^ the water/alkoxide ratio and % t the tetragonal phase. amor represents amphorous structure (21).

Metal salts can also be used to reduce the number of alkoxides in the system provided they are soluble in alcohol (22). Examples include citrates, acetates, formates, tartarates

and nitrates. Rossignol et al (23) have prepared cerium zirconium oxides from two different zirconium precursors using the sol-gel and co-precipitation methods. Zirconyl chloride and zirconium nitrate were used in the co-precipitation method while zirconium n-propoxide and cerium nitrate was used in the modified sol-gel method. They concluded that the specific area of the calcined oxides was independent of the mode of preparation and the percentage of ceria. However the zirconium precursor used had an influence on the structures formed. The structures formed have been already detailed in section 1.4.1 in Table 1.14.

Ceria-zirconia mixed oxides have also been prepared by mixing cerium nitrate and zirconium oxychloride salt solution with urea (24). Urea is used for the homogeneous generation of hydroxide ion via the following equation (12):

$$(H_2N)_2CO + 3H_2O \rightarrow CO_2 + 2NH_4^+ + 2OH^-$$

The precipitating agent appeared gradually and homogeneously throughout the solution via the slow chemical reaction described above. Possibly because of the homogeneous nature of the preparation, the authors have described it as a sol-gel method.

In general, the sol-gel method has been reported to provide superior control of the texture, composition, homogeneity and structural properties of the final solids. However the main barrier to scale up to industrial scale is the increased viscosity of the reaction medium in which the sol-gel chemistry occurs (20), since a semi solid structure is formed.

2.3 Catalyst Characterisation and Testing Techniques

2.3.1 Activity Determination

The apparatuses used to determine the activity for combustion of propane and methane are illustrated in Fig 2.4 and Fig 2.5 respectively. Catalytic tests were carried out at atmospheric pressure in a continuous flow reactor by monitoring the level of combustion of methane and propane as a function of temperature. The flow reactors used for both gases were very similar except for the incorporation of a 4-port switching valve and extra mixing coil in the propane activity unit (see Fig 2.4 and 2.5). The advantage of the switching valve was that the reaction mixture could be passed directly to the gas chromatograph (GC) and thereby by-passing the sample to check the "baseline concentration" of propane. The purity of the methane and propane (supplied by Air Products) was in excess of 99.9% and 97% respectively.

The activity test involved passing a stoichiometric mixture of gas (either propane or methane) in air over the sample. The flow rates of air and reactant gas to be used for the analysis under stoichiometric conditions were determined from the following equations:

$$CH_4 + 2O_2 \rightarrow CO_2 + 2H_2O$$

$$C_3H_8 + 5O_2 \rightarrow 3CO_2 + 4H_2O$$

Assuming an oxygen concentration of 20% in air, the gas flow rates given in Table 2.4 were used.

	Propane	**Methane**
Hydrocarbon: air ratio	1:25	1:10
Flow rate of propane (cm^3min^{-1})	2	3
Flow rate of air (cm^3min^{-1})	50	30
Total flow rate (cm^3min^{-1})	52	33

Table 2.4 Gas flow rates of propane/air and methane/air mixtures.

Flow rates of the hydrocarbon and air were measured using a bubble flow meter and controlled using mass flow controllers with ranges of 0-5cm^3min^{-1}(gas) and 0-100 cm^3min^{-1} (air). The gas mixtures were sampled and analysed using a GC with a 0.5 ml and 1 ml sampling loop respectively.

0.3g of the catalyst sample, located on a sintered disc in a quartz u-tube, was heated stepwise to specific temperatures between 20 and 600°C using a furnace supplied by Lenton Thermal Designs Systems Ltd. Insulating wool was packed around the top of the furnace to prevent heat loss during analysis. At each temperature, the sample was left to stabilise for 10 minutes. Then the concentration of hydrocarbon reactant and reaction products in the effluent stream was monitored at each temperature for at least 15 minutes using in situ GC (FID detector) until equilibrium was established. Equilibrium was considered to be established when at least two reproducible hydrocarbon peaks were observed, the difference in their areas being normally less then 5 %. At some temperatures, considerably longer then 15 minutes was necessary for equilibrium to be attained. The instrumental conditions for the GC analysis for both reactant gases are given in Table 2.5.

Typically, activities were measured at room temperature, 100°C and then the temperature was increased in 25 or 50°C increments once 10% conversion was reached. Hence, the temperatures at which catalytic activity was monitored changed from one sample to another. For methane, typically no activity was observed below 300°C. Measurements at each temperature were performed at least twice or until consecutive peak areas agreed within 5%. Propane and methane conversions were calculated by comparing the peak area at a certain temperature to that in the by-pass loop and that at room temperature respectively. The final temperature reached for analysis depended on both the sample and the gas used since propane is more reactive than methane under these conditions. In general, samples were heated to a temperature at which all the methane or propane introduced was destroyed, or to a maximum temperature of 600°C. For methane, the final temperature was 600°C, while for propane, the final temperature varied depending on the activity of the sample. For the materials described in Chapter 3, the samples were heated up to final temperatures in the range 400-500°C, while for the materials described in Chapter 4, final temperatures were lower in the range 250-325°C.

After the first analysis run with the methane or propane gas mixture to maximum conversion or 600°C (Run 1), the samples were then cooled to room temperature and the experiment repeated (Run 2).

Reactant Gas	**Propane (C_3H_8)**	**Methane (CH_4)**
Instrument	Pye Unicam 4550	Schimadzu GC-14A
Detector	Flame Ionisation Detector Thermal Conductivity Detector	Flame Ionisation Detector
Column type (s)	4 mm ID, 6 mm OD, packed	4 mm ID, 6mm OD, packed
Column Packing	Porapak Q (FID) Porapak Q (TCD)	Porapak Q (FID)
Carrier Gas	He (normal grade; Air products)	N_2 (normal grade; AirProducts)
Flow rate	0.7 kg/cm^3	1.25 kg/cm^3
Temperatures (FID) Column Injector Detector	 200 °C 150 °C 200 °C	 150 °C 150 °C 200 °C

Table 2.5: GC instrumental conditions for gas analysis. Temperatures of column, injector and detector refer to those used for the FID. The Pye-Unicam 4550 GC incorporated two separate columns both packed with Porapak O for each detector used.

Two separate measurements of a sample from the same batch, ZrMn50-cp-b and ZrMn100-cp, were recorded for methane and propane combustion respectively to estimate the experimental errors involved in each procedure, the results of which are recorded in Table 2.6. For methane the errors for T_{10}, T_{50} and T_{90} values are relatively small, with the smallest error observed for T_{50}. On the other hand, T_{10} values for propane fluctuated significantly but again the smallest error was observed for the T_{50} values.

	Methane			Propane		
	T_{10} (°C)	T_{50} (°C)	T_{90} (°C)	T_{10} (°C)	T_{50} (°C)	T_{90} (°C)
Sample 1	333	366	443	122	217	244
Sample 2	325	364	432	201	211	224
Mean	329	365	437.5	161	214	234
Error	4	1	8	39	3	10

Table 2.6: Estimation of errors in determination of methane and propane using repeat measurements of fresh ZrMn50-cp-b and ZrMn100-cp respectively where T_{10}, T_{50} and T_{90} refer to temperatures of 10, 50 and 90% of methane and propane conversion.

The detection of permanent gases, O_2 and CO_2 using a thermal conductivity detector (TCD) was only carried out at a few specific temperatures. This was due to the much longer analysis time required compared to the hydrocarbon detection. GC conditions to detect CO_2 involved programming the GC oven temperature to rise at 10°C/min from 47 to 200°C, after 5 minutes hold at 47°C. Using the TCD at each temperature wasn't practical since the column temperature had to be cooled down to below 50°C from 200°C for each injection and hence it was difficult to cool the oven sufficiently after each injection. Using the TCD and the porapak Q column only CO_2 could be detected. The limit of detection for CO was lower than room temperature using the aforementioned column and any CO present could not be separated from the air peaks in the TCD. Hence CO_2 was the only detectable carbon product under the experimental conditions used.

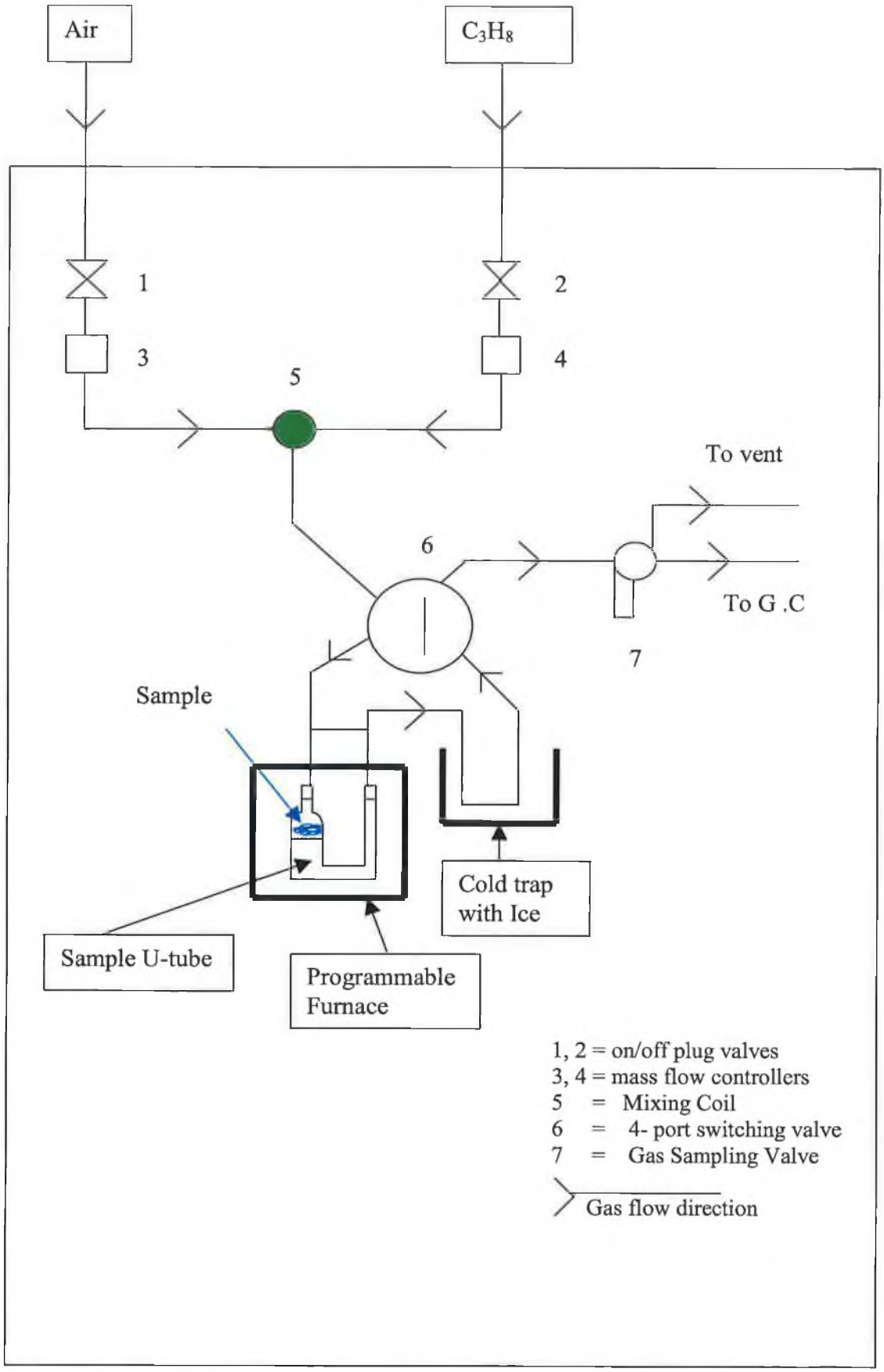

Fig 2.4 Flow diagram of propane activity unit

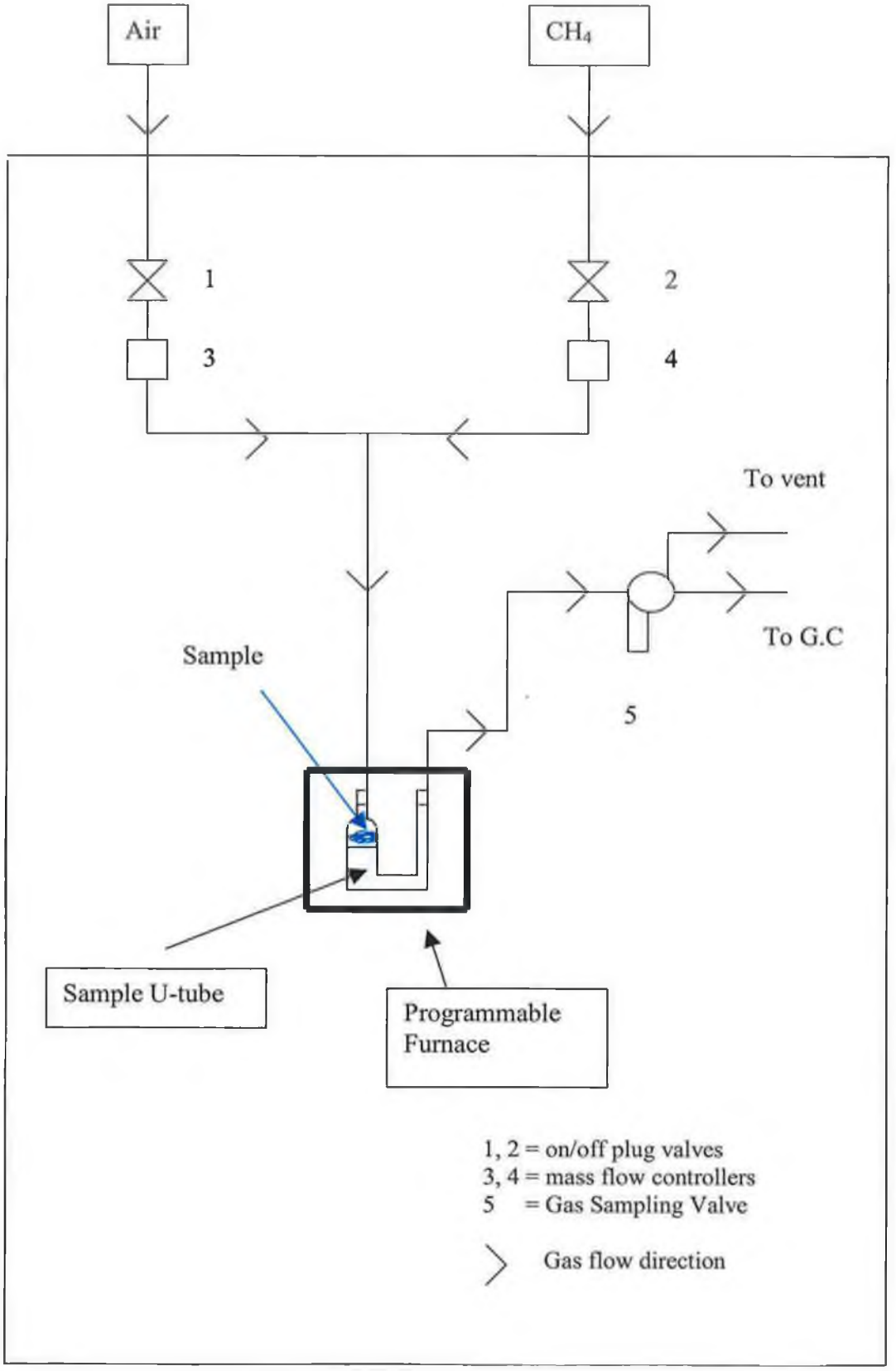

Fig 2.5 Flow diagram of methane activity unit

2.3.2 Temperature Programmed Reduction – Mass Spectrometry (TPR-MS)

Background

Temperature programmed reduction is used to characterize metal oxide catalysts. TPR has been used to give qualitative information on the oxidation state of the reducible species present (25). During TPR, the following reduction reaction is monitored as a function of temperature (26):

$MO_n + H_2\ (g) \rightarrow MO_{n-1} + H_2O\ (g)$

where MO_n is the metal oxide.

In the experiment, an inert sweep gas, containing a modest concentration of the reducing agent, is passed over the sample located in a sample holder in a programmable furnace. The concentration of reducing agent or reaction product in the effluent gas is monitored using a thermal conductivity detector (TCD) or mass spectrometry (MS). As the temperature of the furnace is increased at a constant rate, the hydrogen uptake or water production is measured as a function of sample temperature. A TCD has been most commonly used to measure hydrogen consumption by monitoring the hydrogen content of the gas mixture passed over the sample (25). Mass spectrometry has also been used to detect reaction products and offers the advantage of being able to detect hydrogen consumption and water production simultaneously (27). The temperatures at which the maximum amount of water is formed or hydrogen taken up, have been used to identify the species, while quantitative information (concentration of the species) has been found from the peak areas (28).

Metal oxide reduction is a solid gas reaction and the rate of reduction can be represented by equation 2.1 (25):

$$\frac{d\alpha}{dT} = \frac{A_o}{\beta} \exp \frac{-E}{RT} * f(\alpha) \qquad \text{Equation (2.1)}$$

where α is the degree of reduction

$f(\alpha)$ is a function, dependent on the reaction mechanism

A_o is the exponential factor

β is the heating rate

E is the apparent activation energy

R is the universal gas constant

T is the temperature

The apparent activation energy for reduction can be calculated from the Kissinger equation, which was derived from equation 2.1 (25) and can be represented as;

$$\ln\left(\frac{\beta}{T_{max}^2}\right) = -\frac{E}{RT_{max}} + \ln\left(\frac{A_o R}{E}\right) + c \quad \text{Equation (2.2)}$$

where β is the heating rate,

c is a constant

T_{max} is the temperature of maximum reduction

R is the universal gas constant

E is the apparent activation energy

A_o is the exponential factor.

Applying equation 2.2, a plot of the LHS term versus $1/T_{max}$ yields a straight line with a slope of –E/R.

Experimental Detail

A schematic diagram of the TPR-MS apparatus used is shown in Fig 2.6. Approx 20 mg of the catalyst was placed in a cylindrical silica tube on a glass wool plug. The silica tube was then enclosed in a nichrome wound minifurnace. The sample temperature was measured using a thermocouple placed in the sample. A 5%H_2/He gas mixture was continuously passed over the sample at a flow rate of 50 ml/min. The furnace temperature was increased linearly at a rate controlled by a Eurotherm temperature programmer. The heating rate was imputed on the PC using software developed by the Centre for Applied Catalysis in Huddersfield (27), which was in turn connected to the temperature programmer via a serial interface. Various linear heating rates of between 1 and 20°C/min were used to heat the sample from room temperature

to 900°C. The effluent gas stream flowed directly into the source chamber of a magnetic sector mass spectrometer (VG micromass 7070HS mass spectrometer). This was made possible by the use of a jet separator, which removed the carrier gas molecules and preserved the high vacuum conditions in the ion source of the MS. A MID (multiple ion detector) was used to directly monitor the following ions: m/z=18 (H_2O) m/z=17 (H_2O), m/z=1(H_2) and m/z=2 (H_2), as the sample was heated up to 900°C. Due to the jet separator used and the low molecular weight of hydrogen, the hydrogen intensities were quite weak compared to the water signals. Hence TPR profiles presented in the thesis are shown as a function of the evolution of the water signal only, except for strongly reducing samples and all peak positions were determined using water evolution. Hence the method is not quantative for H_2 uptake.

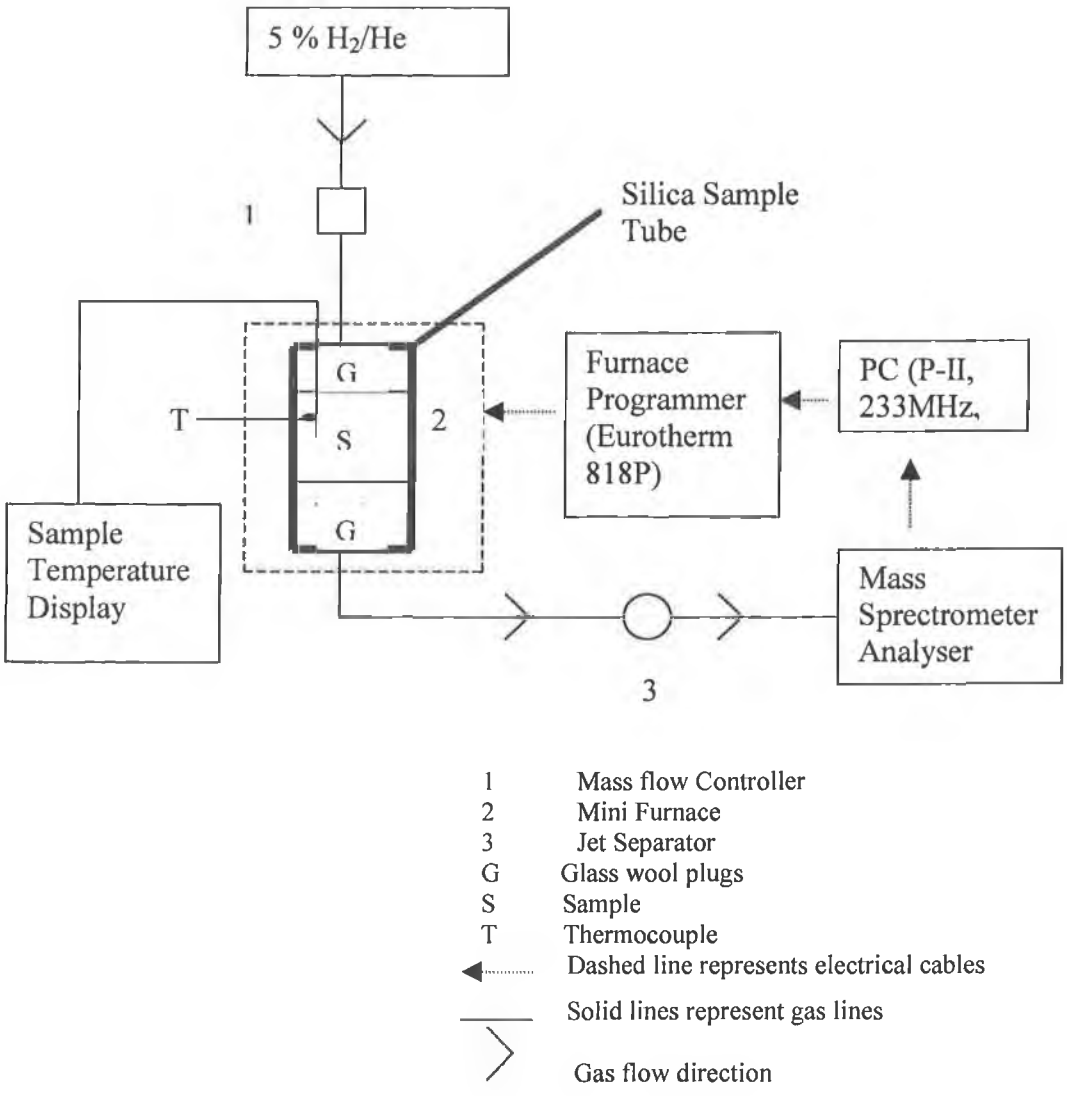

Fig 2.6 Temperature Programmed Reduction-Mass Spectrometry apparatus

2.3.3 Evolved Gas Analysis (EGA)

Background

In evolved gas analysis, the sample is heated linearly under vacuum and the gas species evolved are monitored as a function of temperature. This technique has been used to study the preparation of supported catalysts and the degree of active phase interaction with the support for catalyst systems such as titania supported vanadia (29), ceria supported chromia (30) and ceria and titania supported chromia catalysts (31). In order to investigate the samples prepared in this thesis, Solid Insertion Probe –Mass Spectrometry (SIP-MS) was used to study the decomposition of the catalyst precursor species. To date, only one study (27) has investigated the application of the SIP-MS technique for catalyst preparation. Advantages of using this technique are small sample size, thus reducing temperature gradients across the sample, high vacuum pressure that prevents back reaction of the products with the reactants and increased sensitivity.

Experimental Detail

As shown in Fig 2.7 (a) the SIP consists of a cylindrical microfurnace at the end of a stainless steel rod (32). In the experiment, the sample (approx 10 mg) was placed in the sample cavity of the Solid Insertion Probe (SIP) (see Fig 2.7 (a)). No pretreatment of the sample was performed except for initial drying of the sample during its preparation. The sample cavity was sealed and the SIP was placed directly into the source chamber of the mass spectrometer using a series of airlock valves (see Fig 2.7 (b). The sample temperature was measured using a thermocouple located at the base of the sample holder. Hence the thermocouple was in direct contact with the sample itself. The SIP was then heated from room temperature to 900°C at a linear heating rate of 10°C/min using a thermocoax winding. The required experimental conditions were set on the furnace programmer, connected to the computer via an RS232C serial interface, which controlled the power applied to the SIP thermocoax winding (see Fig 2.7 (b)) (32). The mass spectrometer (Micromass 7070HS) was operated in "peak select" mode along with an MID (multiple ion detector). Direct measurement of selected m/z values yielded the evolved gas profiles as function of temperature for the following ions: m/z = 17 (OH), m/z = 18 (H_2O), m/z = 28 (N_2), m/z = 30 (NO + NO_2), m/z = 32(O_2), m/z = 44

(N_2O) and m/z = 46 (NO_2). The ions were monitored alternatively for 500ms each while the furnace temperature was increased every 1000ms (32).

The heating conditions and data acquisition were performed by software developed in the Center for Applied Catalysis in Huddersfield on a PC. Voltages corresponding to the relative concentrations of the species being measured were acquired from the Multiple Ion Detection unit via an analogue-to-digital converter (32). These values and the sample temperature were processed on the PC to yield evolved gas profiles i.e. sample temperature versus intensity of selected ions. Typical results obtained are given in sections 3.3.2.2 and 4.3.2.2.

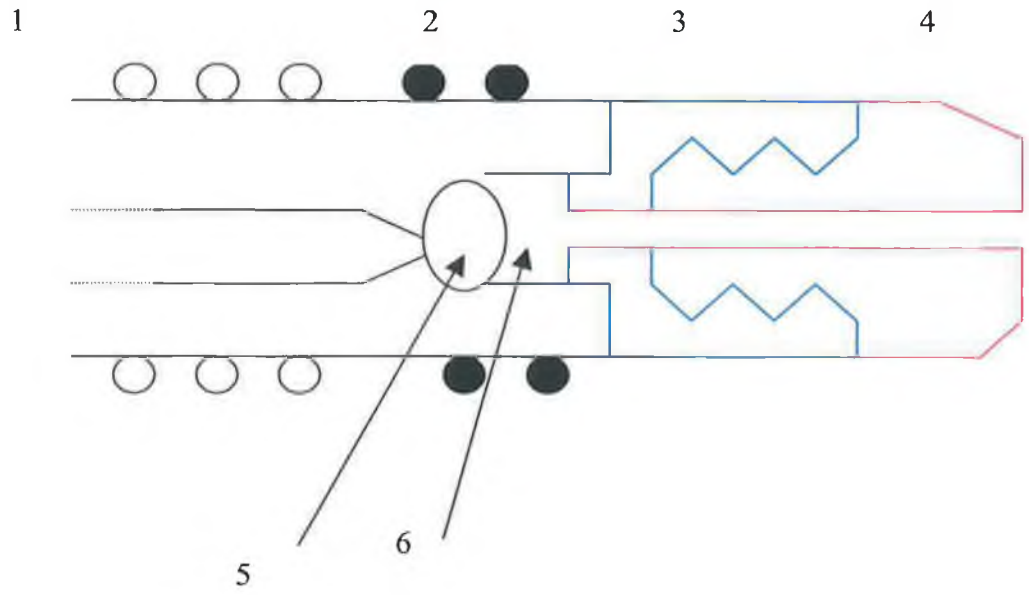

Fig 2.7 (a) Cross section of solid insertion probe (SIP): 1, Watercooling coil ; 2, Thermacoax heating Element; 3, Nichrome Plug; 4, Ceramic Tip; 5, Thermocouple; 6 Sample Cavity (32).

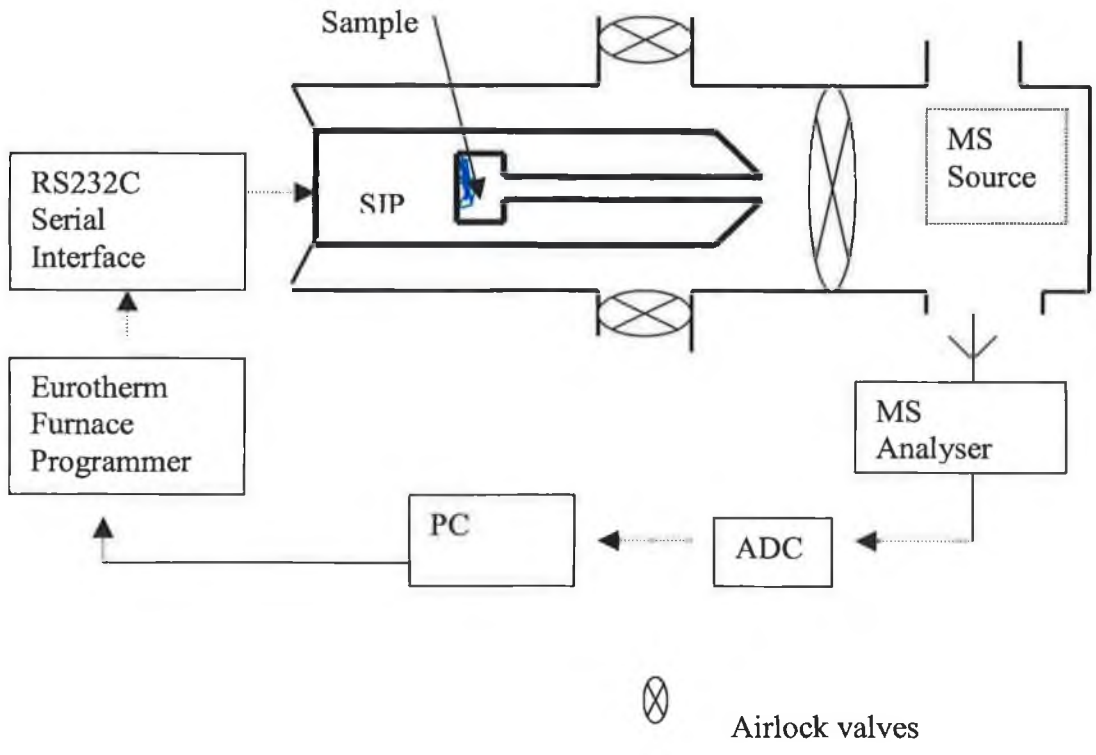

Fig 2.7 (b) Overall Schematic of SIP-MS.

2.3.4 TGA-SDTA (Thermogravimetric Analysis – Single Point Differential Thermal Analysis)

Background

In thermogravimetry (TG) the mass of a sample is monitored as a function of sample temperature. TG curves have been reported to be affected by a number of factors including heating rate, furnace atmosphere, sample holder, amount of sample and particle size (33). In this case, the sample was weighed continuously using a parallel guided balance (34). This method meant that positioning of the sample had no effect on the measurement. Differential thermal analysis (DTA) measures the temperature difference between a substance and reference material as a function of temperature while both are subjected to the same controlled temperature program. The difference in the response of the sample under study to the temperature program i.e. physical and chemical changes in the sample, are monitored. Exothermic and endothermic peaks were detected where the temperature of the sample rose above and fell below that of the reference material respectively. The reference temperature was calculated mathematically using the well defined model of an empty pan (34). The sample temperature was measured using a sample temperature sensor (R type thermocouple) directly attached to the sample holder. Hence the instrument allowed simultaneous observation of the mass and temperature changes of the sample.

Experimental Detail

Simultaneous thermogravimetry (TG) and differential thermal analysis (DTA) were performed in a Mettler-Toledo TGA/SDTA 851 module. A schematic of the fully automated system is shown in Fig 2.8. Samples (approx 40 mg) were weighed into a 70 μL aluminium oxide crucible, which was then loaded into the TGA-SDTA using a TS0801RO Automatic Sample Robot. The samples were then heated from room temperature to 600°C at 10°C/min in air (50 ml/min). The data from the TG and STDA were then analysed using the Star base software for windows NT. The software package also allowed the input of the various experimental conditions and sample weights.

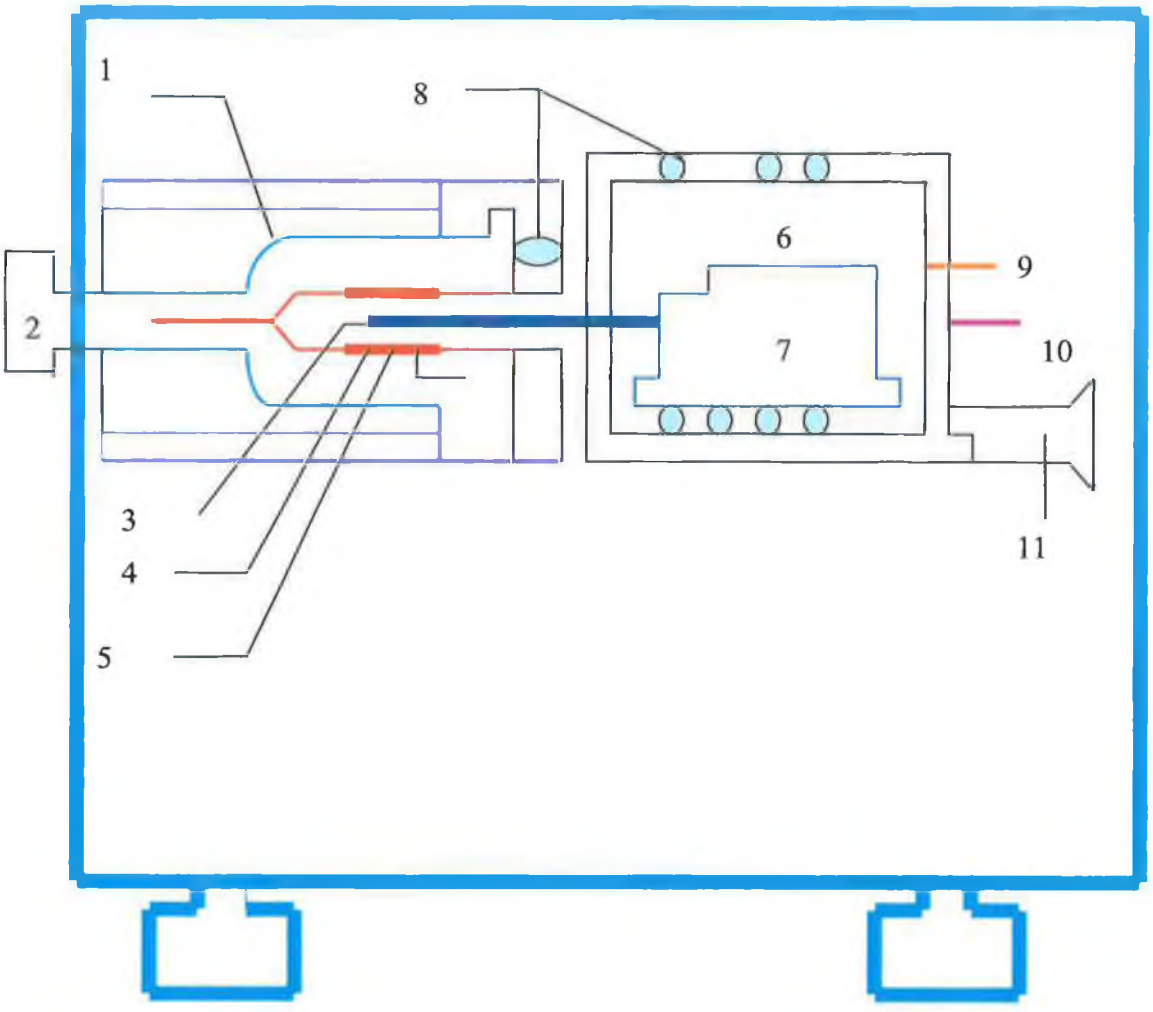

Key to illustration:

1. Fused silica jacket
2. Gas outlet stopcock
3. Sample temperature sensor
4. Furnace heater
5. Furnace temperature sensor
6. Thermostated balance chamber
7. Parallel guided ultramicro balance
8. Cooling
9. Protective gas inlet
10. Reactive gas inlet
11. Vacuum connection

Fig 2.8 Schematic of Mettler Toledo TGA/STDA 851 (34)

2.3.5 X-Ray diffraction (XRD)

Background

In XRD, powdered samples are exposed to monochromatic x-radiation and the angles at which diffraction occurs are determined using a diffractometer. A typical diffractometer operated in a Bragg-Brentano method is represented in Fig 2.9. Here, the X-ray tube and the detector are situated on the same diffractometer circle and the sample is then rotated by an angle $\Delta\theta$ about the diffactometer ring center. This is then followed by detector rotation about the same axis by the angle $2\ \Delta\theta$.

The coherent beam of monochromatic x-rays were generated by striking a pure anode of metal with high energy electrons in a sealed vacuum tube. Soller slits (series of parallel plates) were used to create a parallel beam of X-rays that were directed at the sample.

Interaction of the x-rays with the sample created diffracted beams which have been related to the interplanar spacings (d_{hkl}) according to Braggs Law as follows:

$$n\lambda = 2\ d_{hkl} \sin\theta$$

where λ is the x-ray wavelength, n is an integer and θ is half the 2θ value or the angle of the observed diffraction. The interatomic spacing (d_{hkl}) refers to the magnitude of the distance between two adjacent and parallel planes of atoms.

Experimental Detail

The water supply for the X-ray tube was turned on followed by the power to the instrument. The sample holder consisted of a aluminum or copper plate with a hole in the middle. One side of the hole was covered with one sided adhesive tape. The sample was crushed into a fine powder and then placed in the above cavity where it was pressed into a flat disc using a glass slide. This was then mounted onto the sample holder of a Sietronics X-ray Diffractometer. The instrumental and experimental conditions used are summarised in Table 2.7.

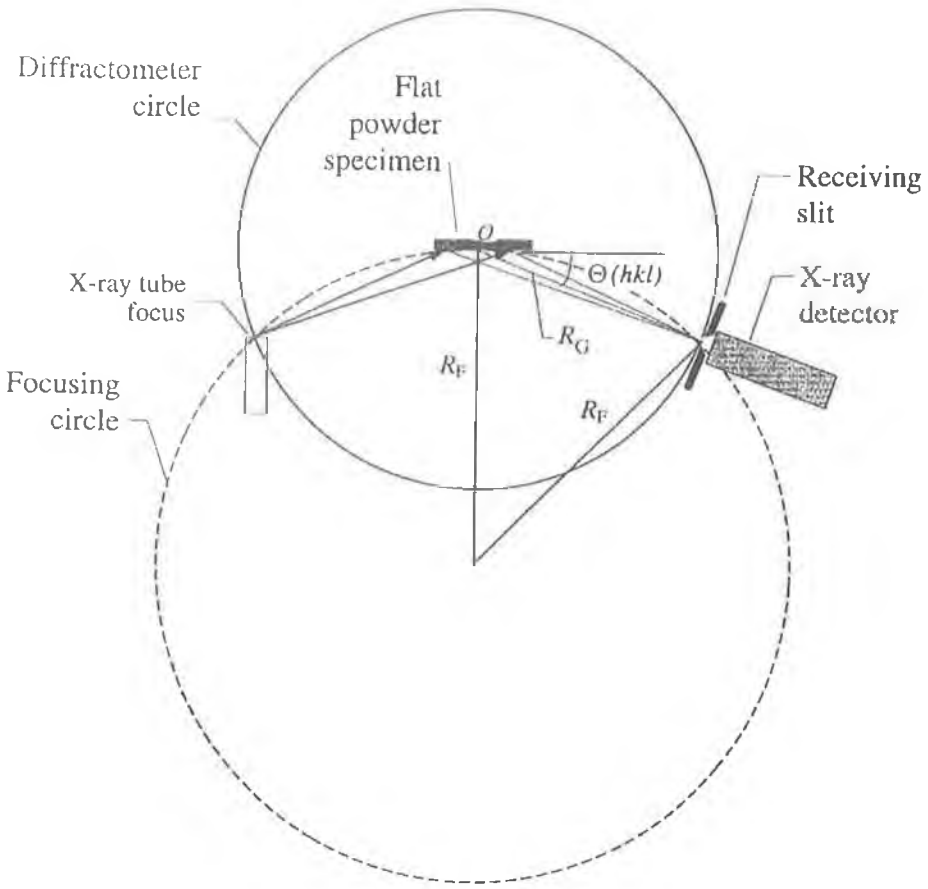

Fig 2.9:Schematic of typical XRD powder diffractometer operated in Bragg-Brentano method (35), where O and R_G are the rotation axis and radius of the diffractometer circle, R_F is the variable radius of the focusing circle and Θ (θ) is the incident angle.

Peak heights of the diffraction maxima was related to the intensity of those diffractions in the spectra and x-ray data was recorded in terms of intensitiy (y-axis) vs2θ (x-axis). The raw data was processed by a computer program to yield interplanar spacings. Phase identification was made by comparing peaks and peak intensity to standard data provided by the International Center for Diffraction Data.

Instrumental conditions	
Radiation	Cu Kα (λ= 1.5418Å)
Anode Current	30 mV
Acclerating Voltage	20 KeV
Inital 2θ (°)	10
Final 2θ (°)	90
Step size (°)	0.05
Scan speed	1°/min

Table 2.7: Instrumental used for Sietronics X-Ray Diffractometer.

2.3.6 Surface areas

Background

Measurement of the total surface area of the catalyst can be achieved via physisorption of a suitable adsorbate (36). Of the many gases readily available, adsorption of nitrogen at 77K is used widely. The BET theory has been discussed in detail in section 1.2.1 and has been widely used to calculate the monolayer capacity from the linear portion of the isotherm.

Total surface area was determined by BET gas adsorption method at the temperature of liquid nitrogen (77K). At these temperatures, N_2 condenses onto the surface of the solid sample and the volume for monolayer coverage can be determined. Once this value is known, the surface area can be calculated by multiplication of the number of molecules in the monolayer by the average area of each nitrogen molecule.

Experimental surface area measurements were determined via N_2 adsorption at 77K using a Gemini Micrometrics II 2375 instrument, as shown in Fig 2.10. Specific surface areas were determined using a multipoint BET method based on the amount of N_2 adsorbed at 77K between relative pressures of between 0.05 and 0.30. In this method, the pressure difference between two sample tubes, one with sample and one empty tube (balance tube), was monitored using a differential pressure transducer as the analysis

gas was metered into both tubes simultaneously (37). The pressure difference is caused by adsorption of the gas by the sample, which results in a decrease in pressure in the sample tube. The rate of analysis gas delivery is then matched exactly to the rate at which it is being adsorbed by the sample and a constant pressure of analysis gas over the sample is maintained.

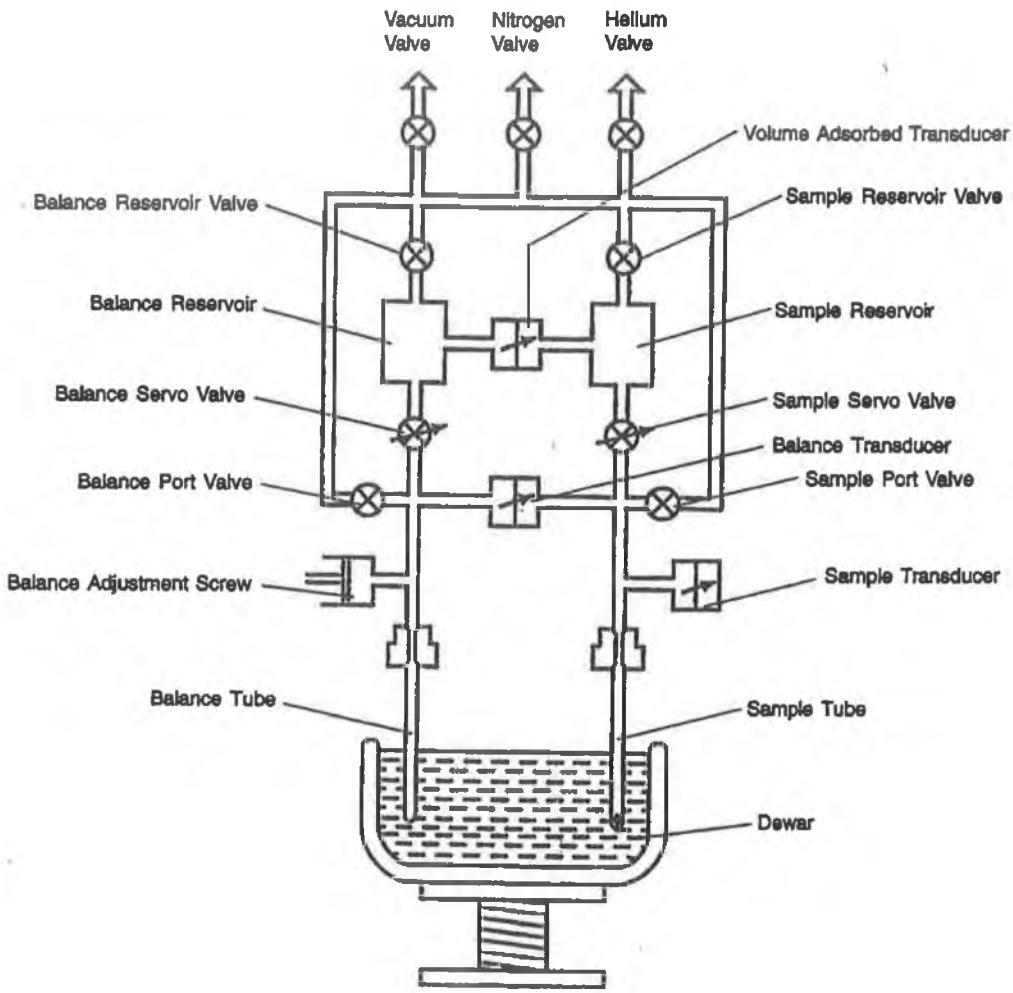

Fig 2.10: Schematic of Micrometrics Gemini Instrument (37).

Experimental Detail

Between 0.1 and 0.2 g of a sample was weighed into a sample tube and heated at 200°C overnight in a furnace under air. The sample was then re-weighed and the final sample weight was then used to calculate the sample surface area in m^2g^{-1}. The sample tube

was placed in the sample port of the instrument. Both balance and sample tubes were evacuated to zero pressure at a rate of 500 mmHg/min and immersed in a dewar of liquid nitrogen. The analysis gas (5 vol/vol % N_2/He) was then metered into the sample tube and the balance tube at the same time. The instrument was operated in scan mode where the gas pressure is raised at a constant rate based on the pressures used and length of analysis. The volumes of gas adsorbed at each pressure (P) in the sample tube were recorded and automatically converted to s.t.p conditions. Using gas volumes between relative pressures (P/P_o) of 0.05 and 0.30 and a saturation pressure (P_o) of 760 mmHg, the BET equation (detailed in Appendix A and section 1.3.1.1) was applied.

References

(1) Kung, H. H., in " *Transition Metal Oxides: Surface Chemistry and Catalysis"*, (Kung, H. H., eds.,) Studies in Surface Science and Catalysis Vol.45 ,121-135 , Elsevier, Amsterdam, 1989.

(2) Kaddouri, A., Mazzocchia, C., Tempesti, E., Anouchinsky, R., *J. Therm. Anal.* **53,** 97 (1998).

(3) Yamaguchi, T., *Catal. Today* **20,** 199. (1994),

(4) Cotton, F. A., Wilkinson, G., "*Advanced Inorganic Chemistry*", Interscience, N.Y, 1988

(5) Sato, T., Ozawa, F., Nakumura, T., Watanabe, H., Ikoma, S., *Thermochim. Acta* **34,** 211 (1979).

(6) Tichit, D., El Alami, D., Figueras, F., *App. Catal., A* **145,** 195 (1996).

(7) Keshavaraja, A., Jacob, N. E., Ramaswamy, A. V., *Thermochim. Acta* **254,** 267 (1995).

(8) Livage, J., Doi, K., Mazières, C., *J. Am. Chem. Soc.* **51,** 349 (1967).

(9) Srinivasan, R., Harris, M., Simpson, M., De Angelis, R. J., Davis, B. H., *J. Mater. Res.* **3,** 787 (1998).

(10) Dongare, M. K., Dongare, A. V., Tare, V. B., Kemnitz, E., *Solid State Ionics* **152,** 455 (2002).

(11) Castro, L., Reyes, P., De Correa, C. M., *J. Sol-gel. Sci. Tech.* **25,** 159 (2002).

(12) Skoog, D. A., West, D. M., "*Fundamentals of Analytical Chemistry*", Saunders College Pub, Fort Worth, 1996.

(13) Perego, C., Villa, P., *Catal. Today* **34,** 281 (1997).

(14) Tichit, D., El Alami, D., Figueras, F., *J. Catal.* **163,** 18 (1996).

(15) Chuah, G. K., Jaenicke, S., *Appl. Catal., A* **163,** 261 (1997).

(16) Calafat, A., in "*Preparation of Catalysts VII*", (Delmon, B., Jacobs, P. A., Maggi, R., Martens, J. A., Grange, P., Poncelet, G., eds). Studies in Surface Science and Catalysis, Vol.118 , 837-843, Elsevier, New York, 1998.

(17) Mercera, P. D. L., Van Ommen, J. G., Doesburg, E. B. M., Burggraaf, A. J., Ross, J. R. H., *App. Catal.* **57,** 127 (1990).

(18) Callister, W. D., "*Materials Science and Engineering*", John Wiley and Sons, New York, 1997.

(19) Miller, J. B., Ko, E. I., *Catal. Today* **35,** 269 (1997).

(20) Jecloux, A. J., Pirard, J. P., *J. Non Cryst. Solids* **225,** 146 (1998).

(21) Chuah, G. K, Liu, S. H., Jaenicke, S., Li, J., *Microporous Mesoporous Mater.* **39,** 381 (2000).

(22) Jones, R. W., "*Fundamental Principles of Sol-Gel Technology*", Brookfield, VT, The Institute of Metals, 1989.

(23) Rossignol, S., Madier, Y., Duprez, D., *Catal. Today* **50,** 261 (1999).

(24) Thammachart, M., Meeyoo, V., Risksomboon, T., Osuwan, S., *Catal. Today* **68,** 53 (2001).

(25) Schlolten , J. J. F.,in "*Catalysis : An Integrated Approach*" (Van Santen, R.A, Van Leeuwen. P. W. N. M, Moulijn, J. A., Averill, B. A., eds.), Studies in Surface Science and Catalysis. Vol 123 , 525-538, Elsevier, Amsterdam, 19

(26) Kung, H. H., in " *Transition Metal Oxides: Surface Chemistry and Catalysis*", (Kung, H. H., eds.,) Studies in Surface Science and Catalysis Vol.45 ,91-109 , Elsevier, Amsterdam, 1989.

(27) Tiernan, M., Fesenko, E. A., Barnes, P. A., Parkes, G. M. B., Ronane, M., *Thermochim. Acta.* **379**, 163 (2001).

(28) Monti, D. A. M., Baiker, A., *J. Catal.*, **83**, 323 (1983).

(29) Nalbandian, L., Lemonidou, A. A., *Thermochim. Acta.* **419,** 149 (2004).

(30) Viswanath, R. P., Wilson, P., *Appl. Catal., A* **201**, 23 (2000).

(31) Wilson, P., Madhusudhan Rao, P., Viswanath, R. P., *Thermochim. Acta* **399,** 109 (2003).

(32) Tiernan, M. J., Barnes, P. A., Parkes, G. M. B., *J. Phys. Chem. B.*, **103,** 6944 (1999)

(33) Wendlandt, W. M., "*Thermal Analysis*", New York, John Wiley and son, 1985

(34) Mettler Toledo DTA/STDA Product Brochure, 2004.

(35) Aslanov, L. "*Crystallographic Instrumentatio* " (Howard, J. A. K., ed.), Oxford University Press, Oxford, 1998.

(36) Sing, K., *Colloids and Surfaces A* **187,** 3, 2001.

(37) Micrometrics II 2375 Handbook, Equipment Description, 1996

Chapter 3:

Preparation and Investigation of Ceria-Zirconia Mixed Oxide Combustion Catalysts.

3.1 Introduction

As shown in the literature survey, ceria and ceria-zirconia mixed oxide materials have been widely studied for redox, oxygen storage and structural characteristics that affect their general use as three way catalysts. Doping of ceria with zirconia is reported to improve its thermal stability (1) and oxygen storage capacity (2). The oxygen storage capacity of these materials has been investigated in particular since this property is important in car automotive exhaust catalysts (3). However relatively few publications on the catalytic activity of the mixed oxides alone, i.e. in the absence of a noble metal component for the combustion of hydrocarbons have appeared in the literature.

Table 3.1 summarizes the characterization and activity data determined for selected ceria, zirconia and ceria-zirconia mixed oxides for the oxidation of propane and methane, taken from the literature.

Sample	**Method**	**T_{50} (°C)**		**SA (calc temp) m^2g^{-1} (°C)**	**Ref**
		CH_4	**C_3H_8**		
$Ce_{0.8}Zr_{0.2}O_2$	Co-prep	542		29 (927)	4
CeO_2	Co-prep	662		6	
ZrO_2	Co-prep	697		10	
CeO_2	Co-prep		485	52 (550)	5
$Ce_{0.8}Zr_{0.2}O_2$	Co-prep		458	93	
CeO_2	Co-prep	607		29.5	6
CeO_2	Urea	725		102 (500)	8
$Ce_{0.75}Zr_{0.25}O_2$	Urea	540		108	
$Ce_{0.50}Zr_{0.50}O_2$	Urea	590		116	
$Ce_{0.25}Zr_{0.75}O_2$	Urea	605		120	

Table 3.1: Activities of selected literature mixed oxide samples where T_{50} represents temperature at which 50% conversion of methane or propane was reached. SA is the specific surface area as determined by the BET equation, calc temp is temperature of calcination and co-prep and urea represents co-precipitation and urea hydrolysis preparation methods respectively.

Zamar et al (4) found that $Ce_{0.8}Zr_{0.2}O_2$ was an effective catalyst for methane combustion (see Table 3.1) and that the activity was comparable to that of Pt/CeO_2 under the same reaction conditions. The increase in oxidation activity for the mixed oxides over CeO_2 and ZrO_2 was attributed to the higher oxygen mobility at lower temperature and the lower reduction temperature of Ce^{4+}. The mixed oxides were also more active than ceria for propane combustion (5); out of a series of ceria-zirconia mixed oxides with various cerium contents, namely 50, 65, 80 and 92 mol %, maximum activity was observed for $Ce_{0.92}Zr_{0.08}O_2$. For the oxidation of propene over high surface area mixed oxides supplied by Rhodia (7), it was found that the higher the cerium content, the more active the catalyst. For a series of catalysts $Ce_{0.15}Zr_{0.85}O_2$, $Ce_{0.5}Zr_{0.5}O_2$, $Ce_{0.68}Zr_{0.32}O_2$, $Ce_{0.80}Zr_{0.20}O_2$ and CeO_2, T_{50} values of 554, 512, 502, 493 and 479°C respectively were obtained. Hence the most active of all the catalysts studied was ceria while of the mixed oxides, a minimum T_{50} value was observed for $Ce_{0.80}Zr_{0.20}O_2$. Zirconia presented the lowest activity of all the samples studied with only 4.8% of propene converted at 500°C. Pengpanich et al (8) found that for the catalytic combustion of methane, conversion decreased with an increase in zirconium loading and that the mixed oxides were more active than pure ceria or zirconia, despite similar surface areas. Redox and structural properties played a more important role in the catalytic activity than BET surface area. The most active catalyst was the $Ce_{0.75}Zr_{0.25}O_2$, similar to the favorable composition found for propene (7) and CO (9) combustion. Kinetic studies indicated that the reaction rate was generally first order and zero order w.r.t methane and oxygen respectively. Bozo et al (10) observed that the introduction of Zr^{4+} ions into the ceria lattice didn't have a marked effect on the light-off temperature (T_{50}) for the combustion of methane with values varying from 572°C for ceria to 593°C for Ce/Zr 47/53.

Rossignol et al (11) reported that the preparation method had an effect on the oxygen storage capacity and structure of ceria-zirconia mixed oxides ($Zr_{1-x}Ce_xO_2$). The two methods used to prepare a range of compositions from x = 0 to 1 were (i) precipitation of zirconium and cerium nitrates by aqueous ammonium hydroxide and (ii) sol-gel hydrolysis of zirconium n-propoxide and cerium nitrate. In terms of oxygen storage capacity (OSC), it was found that a maximim OSC value was obtained at different compositions, depending on the method used. Samples prepared by the sol-gel method had the highest OSC for $0.75 \leq x \leq 0.98$, while for co-precipitated samples, a plateau was

observed above x = 0.50. From structural studies using XRD, modified sol-gel samples with x_{ce} = 50 and 60, $Zr_{0.25}$ Ce $_{0.75}O_2$ (cubic) and minor tetragonal zirconia phase were identified. For x = 0.75, $Zr_{0.25}Ce_{0.75}O_2$ was the only phase observed while for higher cerium contents x = 0.90 and 0.98, cubic ceria was observed. In contrast for the co-precipitated samples, a mixture of cubic ceria and tetragonal zirconia was observed for all cerium contents when $x \geq 0.5$. The two preparation techniques have been discussed in detail in chapter 2. It has been reported that the sol-gel method allows greater control of the texture, composition, homogeneity and structural properties of the final solids (12).

Hence, while the hydrocarbon oxidation activity of ceria-zirconia has been investigated to date in the literature as well as the effect of preparation method on structural and redox properties of these materials, no study has been performed to compare the combustion activity of these oxides prepared by different methods. Since Rossignol et al (11) reported that the sol-gel technique allowed the preparation of stable oxides with high oxygen mobility, the sol-gel method employed in the current work is very similar to that reported by Rossignol (11).

In this chapter, the effect of the preparation method on catalytic properties of ceria-zirconia mixed oxides and their activity for the oxidation of propane and methane is detailed. A series of mixed oxide catalysts were prepared by both the co-precipitation and sol-gel techniques. Within each preparation method, some preparation parameters are varied and the effect of this on textural properties will be discussed. The effect of high temperature aging treatments for selected samples was also determined. Temperature programmed reduction was also used to examine the reducibility of selected samples and SIP-MS has been employed to identify the species being evolved during calcination.

3.2 Experimental

3.2.1 Catalyst Preparation

Two different methods of preparation similar to those of Rossignol et al (11) were used to prepare a range of ceria-zirconia mixed oxides with cerium contents of 10, 30, 50, 70 and 85 mol %, namely co-precipitation and sol-gel.

Co-precipitation method (cp): Appropriate amounts of cerium nitrate tetra-hydrate (Aldrich, 97%) and zirconyl chloride octahydrate (Fluka, 99%) were dissolved in 25 mL of water. (see Table 3.2). 10 ml of ammonium hydroxide solution (35% or 18.7M) was added at room temperature, under constant stirring and the precipitate left overnight. For selected samples, pH titration curves were performed by monitoring the pH with a pH meter after addition of known amounts of base to the precursor solution using a burette. The precipitate was then filtered and washed with distilled water until the filtrate was clear of chloride ions (washings were clear when drops of silver nitrate were added). The filtrate was dried overnight at 45°C and then overnight at 110°C. The oxide was formed by calcination in a static air furnace at 600°C for 6 hours.

Sol-gel method (sg): 10 ml of a solution of 70 % (w/v) zirconium n-proproxide in propanol (Aldrich) was mixed with 20 ml of isopropanol. This solution was then added dropwise to 10 ml of aqueous cerium nitrate solution (see Table 3.3 for concentrations) under constant agitation. A precipitate was formed, left overnight, then filtered and dried at 60°C for one hour and overnight at 110°C. It was then calcined at 600°C for 6 hours.

Pure ZrO_2 (ZrCe0-cp and ZrCe0-sg) samples were prepared by the above co-precipitation and sol-gel methods in the absence of cerium nitrate. A third sample of pure ZrO_2, (ZrCe0–Aldrich) was purchased from Aldrich. Two pure cerium oxide samples were tested – namely ZrCe100-cp prepared by co-precipitation using only cerium nitrate and ZrCe100- Aldrich purchased from Aldrich.

The calcined products from both techniques and those purchased from Aldrich are referred to as fresh samples. Fresh samples were then aged at 800°C for 8 hours and are

referred to as "aged samples". All calcinations and aging procedures were performed in static air in a muffle furnace.

Sample	Calculated mol% Ce	Wt (g) $ZrOCl_2.H_2O$	$Ce(NO_3)_3.6H_2O$	Vol NH_4OH (ml) ^	SA (m^2g^{-1})
ZrCe0-Aldrich	0	N/a	N/a	N/a	5
ZrCe0-cp-1	0	10.02	0	10	34
ZrCe10-cp-1	10	10.00	1.50	10	15
ZrCe30-cp-1	30	10.00	5.77	10	22
ZrCe50-cp-1	50	10.00	13.46	10	10
ZrCe50-cp-1a	50	10.00	13.46	20	20
ZrCe50-cp-2	50	5.01	6.75	12	34 *
ZrCe50-cp-2b	50	5.06	6.81	45	35 *
ZrCe70-cp-1	70	10.00	31.45	10	7
ZrCe85-cp-1	85	10.00	76.36	10	22
ZrCe100-cp-1	100	10.01	0	10	63 *
ZrCe100-Aldrich	100	N/a	N/a	N/a	30

Table 3.2: Preparation conditions for all samples (ZrCeX-cp-y) prepared by co-precipitation where X =mol % (mol of ce/(mol of zr + mol ce)*100), cp is co-precipitation method and y represents different type of procedure used. 1 refers to the concentration used based on 10g of Zr precursor while 2 refers to half that concentration. a or b denotes the addition of 20 or 45 mL of NH_4OH respectively. SA is the specific surface area as determined by the BET method after calcinations at 600°. *Note for 3 samples, reproducibility was tested by retesting each result once. For all 3 samples, the values were within ± 3 m^2g^{-1} of each other. ^ will be referred to as ammonium hydroxide in text herein.

Sample	Calculated Mol % Ce	$Zr(OC_3H_7)_4$ (ml)	$Ce(NO_3)_3.6H_2O$ (g)	SA (m^2g^{-1})
ZrCe0- sg	0	10	0	34
ZrCe10-sg	10	10	1.6376	37
ZrCe50-sg	50	10	9.2795	44
ZrCe70-sg	70	10	21.6507	47
ZrCe85-sg	85	5	26.2919	50

Table 3.3: Preparation conditions for samples (ZrCeX-sg) prepared by sol-gel technique where X is the calculated mol % ([mol of ce/(mol of zr + mol ce)] *100) , sg is the sol-gel technique and SA is the specific surface area as determined by the BET method after calcination at 600°C.

3.2.2 Catalyst Characterisation

Uncalcined oxides were characterised using simultaneous SDTA-TG and SIP-MS. Powders calcined at 600°C were characterised using XRD, TPR-MS, BET and tested for methane and propane oxidation activity. All the above-mentioned techniques used have been detailed in chapter 2. The techniques used to study each sample are summarised in Table 3.4.

3.3 Results and Discussion.

3.3.1 Characterisation of fresh samples: SA and pH titrations.

The surface areas of the fresh samples are given in Table 3.2 and 3.3. The highest surface area was observed for ceria prepared by the co-precipitation method. All the mixed oxides prepared by the co-precipitation method had lower surface areas than that of ceria and no clear trend was observed between cerium content and surface area. Surface area increased with Ce content up to 30 mol% cerium and then decreased at higher cerium contents with the exception of ZrCe85-cp-1. For the sol-gel samples, a small linear increase was observed on increasing cerium content. The surface areas of all the mixed oxide samples prepared by the modified sol-gel method were significantly higher than those prepared by the co-precipitation method.

Sample	CH_4 Act	C_3H_8 Act	SIP-MS	TPR-MS	TG-SDTA	XRD
ZrCe0-cp	√	√	√		√	√
ZrCe10-cp-1		√				
ZrCe30-cp-1						
ZrCe50-cp-1	√	√	√	√	√	√
ZrCe70-cp-1		√				
ZrCe85-cp-1		√				
ZrCe100-cp-1		√	√			√
ZrCe100-Aldrich	√	√		√		√
ZrCe0- sg	√	√	√			√
ZrCe10-sg		√				
ZrCe50-sg	√	√	√	√		√
ZrCe70-sg		√				√
ZrCe85-sg		√				√

Table 3.4: Summary of characterisation techniques performed on each sample, where CH_4 act and C_3H_8 act represent methane and propane combustion studies.

Rossignol et al (11) described the sol-gel technique as modified but gave no specific reason for this. In comparison to some other sol-gel techniques used, it could be modified in the sense that only one alkoxide precursor was used instead of two reported in some studies (13). The higher surface areas for the modified sol-gel samples are in agreement with other studies on preparation methods e.g. of alumina (14), zirconia (15) and manganese-zirconia (16), where it was shown that porosity of both alumina and zirconia was greatly affected by the method used.

For alumina, the porous volume was 20% higher for the sol-gel sample than a conventional co-precipitated sample and in the former, pores with smaller diameters (below 50Å) contributed to the cumulative pore volume (14). For sol-gel and precipitated zirconia samples (15), the mean pore diameters were below 50Å and between 10-150Å respectively and a narrow pore distribution was observed for the

former. In general, Fernandez-Lopez et al (16) found that mixed oxides prepared by the sol-gel method gave higher surface areas than co-precipitated ones. In a general review, Perego and Villa (17) reported that the sol-gel method offered better control over pore volume, surface area and pore size distribution. Chuah et al (15) proposed that in the sol-gel method, formation of the precipitate was controlled on a molecular scale and particle size was determined by the rate of hydrolysis of the alkoxide and subsequent condensation of the hydroxide formed. Nucleation predominated over particle growth in the presence of excess water and resulted in the formation of small particles (15). Hence, using zirconium propoxide as the starting material instead of zirconyl chloride, increased the surface area from 250 m^2g^{-1} to 380m^2g^{-1}.

The procedures followed in our study were based on those reported by Rossignol et al (11, 18). In contrast to our results and those by Chuah (15), Rossignol et al (11) found that the mode of preparation had no effect on the surface areas of the oxides with higher surface areas than the current study (approx 50 m^2g^{-1}) being observed for both co-precipitated and sol-gel samples. The same study (11) also found that there was no correlation between cerium content and surface area and that ZrO_2 prepared by sol-gel method had a lower surface area than the co-precipitated sample with surface areas of 21 and 34 m^2g^{-1} respectively.

The amount of ammonium hydroxide used was based on a paper by Rossignol et al (11) whose preparation procedure was based on the addition of 12 ml of concentrated ammonium hydroxide (14.7 M) to 40 ml of a cerium and zirconium precursor solution. However the final pH and the concentration of precursor solution used was not detailed. Hence the effect of precursor concentration and pH was examined for a ZrCe50-cp sample. ZrCe50-cp-1a was prepared by the addition of 20 ml of ammonium hydroxide and its surface area was compared directly to ZrCe50-cp-1, which was prepared with 10 ml of ammonium hydroxide. The final pH was not determined for the preparation of ZrCe50-cp-1 but was extrapolated from the pH curve obtained for ZrCe50-cp-1a since all other preparation conditions used were identical for both samples. The concentration of both zirconyl oxychloride and cerium nitrate were decreased by a half and two different volumes of ammonium hydroxide were added to prepare two oxide samples, namely 12 ml (ZrCe50-cp-2) and 45 ml (ZrCe50-cp-2b). The pH of the former was continuously monitored up to 12 ml of base, while for the latter the pH was monitored

from 15 ml to 45 ml. The pH titration curves determined for ZrCe50-cp-1a, ZrCe50-cp-2 and ZrCe50-cp-2b are shown in Fig 3.1.

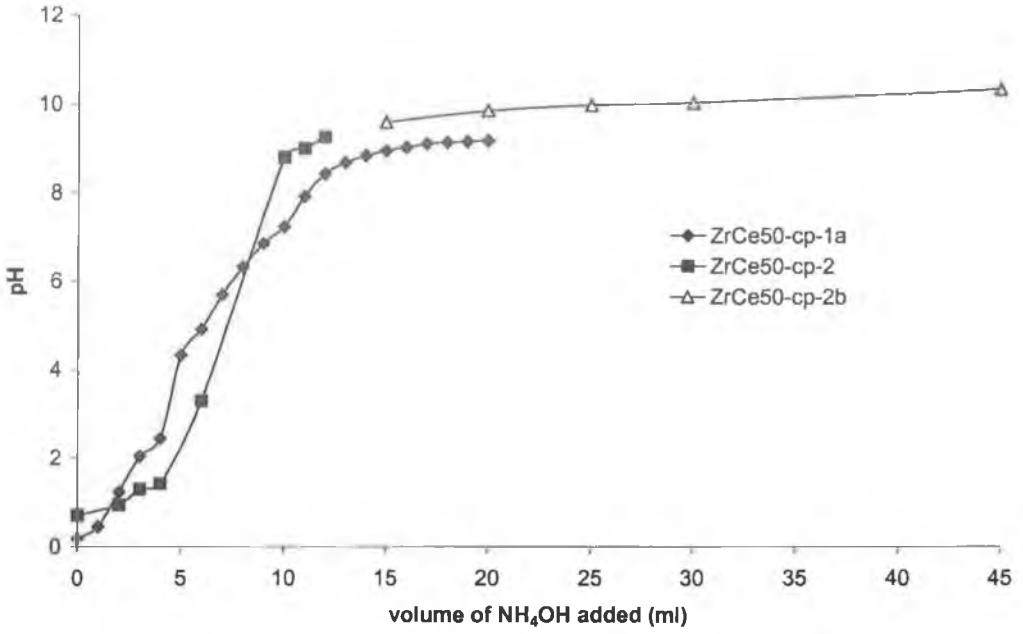

Fig 3.1 pH titration curves of ZrCe50-cp-1a, ZrCe50-cp-2 and ZrCe50-cp-2b.

Studies on the 50 mol% cerium sample showed that the final pH reached for a given amount of ammonium hydroxide depended on the concentration of the cerium and zirconium precursor solution On decreasing the concentration of both cerium and zirconium precursors by half and addition of 2 ml extra of ammonium hydroxide, the surface area of the calcined oxide was increased from 10 to 34 m^2g^{-1} (compare samples ZrCe50-cp-1 and ZrCe50-cp-2 in Table 3.2). For more concentrated solutions (ZrCe50-cp-1b), addition of 10 ml of ammonium hydroxide resulted in a pH of approx 7 while for a solution with half that concentration (ZrCe50-cp-2), addition of the same amount of ammonium hydroxide yielded a final pH of 8.9. For the former, 20 ml of ammonium hydroxide was required to reach a pH of 9. Once a pH of 9 was reached addition of further amounts of ammonium hydroxide only increased the pH by a relatively small amount and no subsequent increase in surface area was observed.

Other authors have reported on the effect of initial concentrations and pH on surface area. Bruce et al (19) found that on increasing initial cerium concentration from 0.005M to 0.05M, the surface area decreased from 200 to 2 m^2g^{-1}. The method used involved the addition of cerium ammonium nitrate to ammonium carbonate along with

bubbling of CO_2 through the mixture. The final pH reached was 7 and the same concentration and volumes of ammonium carbonate were used for all cerium concentrations. The authors (19) concluded that the reason for the remarkable sensitivity of final surface area to initial cerium concentration was not clear and that other papers had reported a similar method but without any indication of any concentration-dependence of surface area. Tichit et al (20) found that on increasing pH (from 4-12), surface areas for pure zirconia increased after drying at 110°C. At final pH of 4, 6, 8, 10 and 12, surface areas of 19, 58, 150, 191 and 217 m^2g^{-1} respectively were reported. Another study (21) also reported that increase in pH from 8 to 11 increased the surface area and decreased crystallite size.

The pH has also been reported to have an effect on the final phase composition of zirconia, the degree of hydrolysis of the zirconium precursor and the structure of zirconium complexes found in solution (22). Two batches of hydrous zirconia were produced by addition of ammonia to achieve final pH values of 4.5 and 9.5. At the lower pH the monoclinic phase was dominant while at the higher pH, the tetragonal form was observed. Prior to addition of a base, the cyclic tetramer species $(Zr(OH)_2.4H_2O)_4^{8+}$ described in section 2.1.1, is the dominant species in zirconium oxychloride solutions. On increase in pH via addition of base, hydrolysis of the four water groups surrounding each Zr atoms occurs to form reactive hydroxy groups. The hydroxy groups can then react with water molecules of other tetrameric ion species in a condensation reaction to form hydroxyl (OH) bridges between the metal cations via loss of four water molecules (20). Further condensation produced oxobridges or –M-O-M- bonds and a polymer network is formed. It has been reported that at different pH values various zirconium monomer species exist, all with various concentrations of hydroxy groups (22). At pH values below 7, water molecules are mainly coordinated around the zirconium atom. At pH 7, two of the water molecules are replaced by hydroxyl groups that can polymerize with other hydroxyl groups. At pH 7-10, all of the water molecules surrounding the Zr atom are replaced by hydroxyl ions and further polymerization can occur. Table 3.5 shows the pH values reported by various authors to prepare zirconia, manganese oxides and manganese-zirconia mixed oxides. In general a minimum pH of 8 is required for precipitation.

Oxides prepared	Base used	Final pH	Reference
Manganese-zirconia	$(CH_3)_4NH_4OH$	8	23
Manganese-cerium	1N NaOH	10	24
Manganese oxide	NH_4OH	8.5, 9.5	25
zirconia	NH_4OH	10.4	26
zirconia	NH_4OH	9	27
zirconia	NH_4OH	9.4	28
zirconia	NaOH	14	15
zirconia	NaOH	10	29

Table 3.5: Various pH values reported in the literature for the preparation of zirconia and selected mixed oxides and the precipitating agents used to achieve each pH.

In our studies a minimum pH of 9 was required to achieve a significant increase in the surface area of the oxide. Above this value, in the case of the less concentrated solutions, no change in surface area was observed. The majority of the mixed oxide samples were prepared with 10 ml of ammonium hydroxide and a pH of 7 was observed in the case of ZrCe50-cp-1. As observed in Table 3.5, at least a pH of 8 was used in typical literature preparations of oxides, suggesting that the low surface areas observed in this work were due to the pH used. The concentrations of the initial precursor solution also played an important role, with the pH values obtained depending on the amount of precursor used. For example doubling the amount of ammonium hydroxide used to reach a pH of 9 increased the surface area two-fold. Decreasing the concentration by half and using approximately the same amount of ammonium hydroxide increased the surface area three-fold.

3.3.2 Thermal and structural studies on fresh samples

3.3.2.1 TG-SDTA

Simultaneous TG-SDTA experiments were performed on ZrCe0-cp-1 and ZrCe50-cp-1 as outlined in chapter 2, the results are shown in Figs 3.2 and 3.4 respectively. The data reported consists of the SDTA data on the left-hand vertical axis where the change in the temperature of the sample compared to a reference is plotted as a function of sample

temperature. On the right hand axis, the TG data, showing the change in weight of the sample as a function of the sample temperature, is represented. The TG data can be presented in either weight (mg) or as a percentage of the initial weight at ambient temperature. The latter is used in all TG data reported in this thesis and is used to determine weight losses (%) over certain temperature ranges. The derivative of the TG curves (DTG) allows the determination of the rate of weight change as a function of temperature and is useful in determining the temperatures at which changes in mass occur for overlapping or poorly resolved events. While DTG was performed on all the data presented, only the TG curves are actually shown. An example of a DTG curve in relation to a TG curve is shown in Fig 3.3.

DTG of ZrCe0-cp-1 (Fig 3.2 and 3.3) indicates a broad endothermic peak in the range 60 to 135°C with a maximum at 89°C. There is also a second peak observed between 150 and 230°C, centered at 183°C. SDTA (Fig 3.2) shows a similar profile with endotherms in the same temperature range, indicating dehydration of the sample since the SDTA profile is accompanied by weight loss. An exothermic peak at 433°C on the SDTA trace without weight loss is observed which indicates a crystalline transition (30). The exotherm has been reported to be due to rapid crystallization and coalescence of primary particles, with corresponding loss of surface area. The total weight loss calculated from the TG curve from 25 to 600°C is 17.20%. Tichit (20) proposed that peaks observed above 70°C were due to release of crystalline water from the oxychloride and that physically adsorbed water was desorbed from zirconia in the temperature range 30 to 71°C depending on the pH of the preparation method and that the final precipitates after heating were of general formula $ZrO_x(OH)_{4-2x}.yH_2O$ or $ZrO_2.xH_2O$. In Fig 3.2, a weight loss of 1.2% was observed up till 60°C and if this is subtracted from the total weight loss to remove the effects of physically adsorbed water, the weight loss is 16.37%. Using the weight loss above 60°C, the composition of the ZrCe0-cp-1 (assuming starting formula as (20)) equates to $ZrO_2.H_2O$ where x = 1.34. The value is greater than 1 which would be observed for $ZrO(OH)_2$ or $ZrO_2.H_2O$ and less then 2 which would be expected for $Zr(OH)_4$ or $ZrO_2.2H_2O$. It has been proposed that of the two possible zirconium hydroxide species, $ZrO(OH)_2$ or $Zr(OH)_4$, the latter is not stable at room temperature (31) and if heated, aged or boiled, transformation into the former oxy hydroxide species occurs. The oxy hydroxide species contains two hydroxy groups per zirconium ion and is reasonably stable. Tichit et al (20) also observed that

the compositions of the gels prepared by precipitation lay between $ZrO_2.1.23H_2O$ and $ZrO_2.1.86H_2O$. Hence the precipitated hydroxide is of a structure intermediate between $ZrO(OH)_2$ and $Zr(OH)_4$ and suggests polymerization of the cyclic-tetramer species.

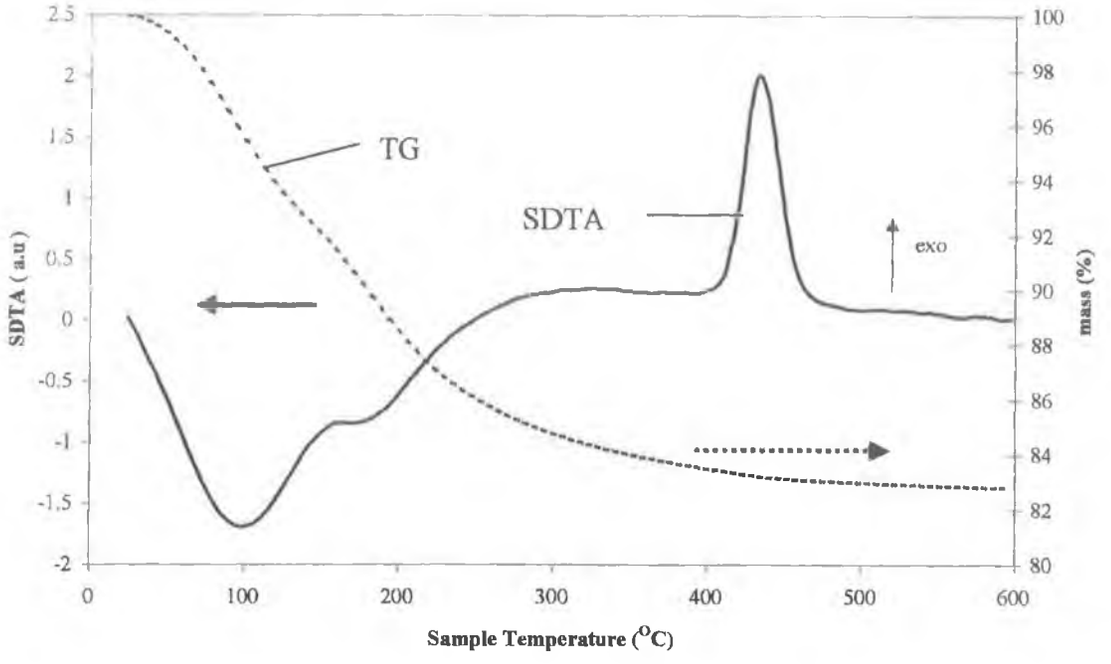

Fig 3.2 Simultaneous TG-SDTA of ZrCe0-cp-1 (sample weight : 40.27mg)

Fig 3.4 shows the simultaneous SDTA-TG of ZrCe50-cp-1. DTG of ZrCe50-cp-1 shows a very broad endothermic peak from 50 to 280°C with a smaller peak at approx 300°C. A gradual mass loss (approx 10%) in the TG (Fig 3.4) up to 300°C was followed by a smaller, sharper mass loss between 350 and 400°C. The SDTA profile (Fig 3.4) shows an endothermic peak between 30 and 175°C, which then continues into a broad exothermic peak with a maximum at approx 300°C. Another smaller endothermic peak at 376°C in the SDTA accompanied by weight loss is observed. An exothermic peak albeit it more defined and smaller was observed by Rossignol et al (11) between 240 and 260°C in co-precipitated ceria-zirconia sample with 50 mol% of cerium and it was attributed to decomposition of residual nitrates. No exothermic peak up to 500°C corresponding to crystallization was observed on the dried sample by Rossignol et al (11) and was attributed to the presence of a minor tetragonal ZrO_2 phase, along with the ceria phase.

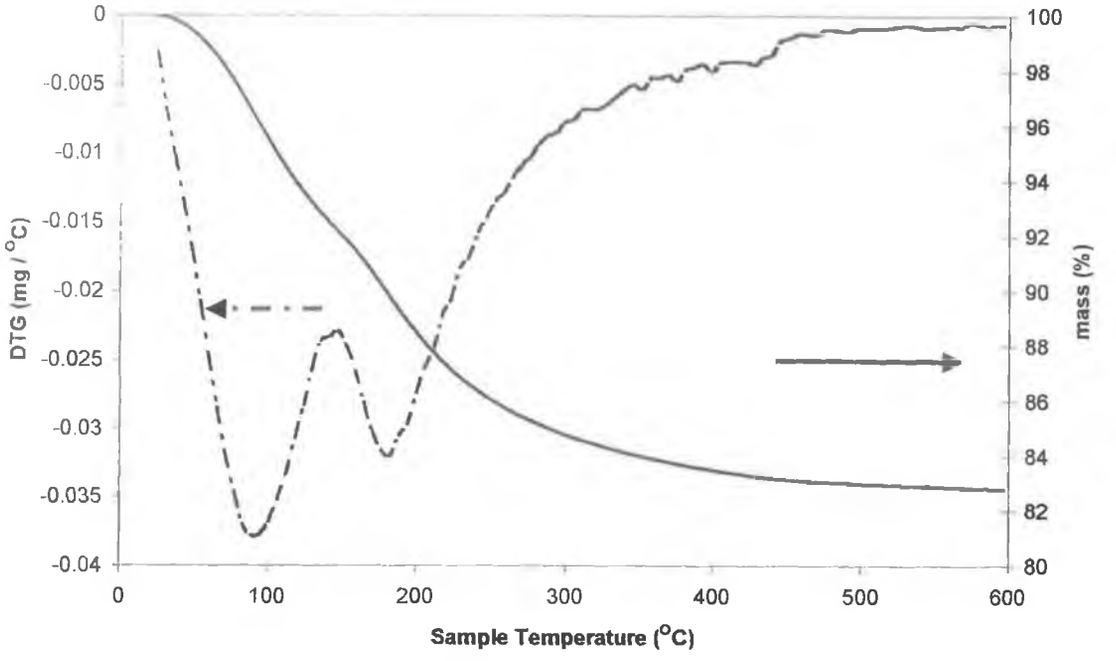

Fig 3.3:TG and corresponding DTG data for ZrCe0-cp-1.

Similarly, in the preparation of Ce_{12} Zr $_{0.88}$ O_2 via a citric acid method, no clear exothermic peak for crystallisation of the solid solution was observed, which according to the authors was possibly masked by the strong exothermic effect at about 400°C (32).

The presence or absence of the exothermic peak observed in pure zirconia could not be determined conclusively for ZrCe50-cp-1 due to the presence of the large exothermic peak attributed to decomposition of the nitrates. In the SIP-MS of ZrCe50-cp-1, evolution of nitrate species was observed from approx 250°C up until 600°C. It has been reported in the literature that doping of zirconia with transition metals such as Mn (31), Cu (33,34) and Fe (33,35) shifts the exothermic peak due to crystallization of zirconia to higher temperatures e.g. incorporation of 0.3 mol of manganese into zirconia increased the temperature of crystallisation from 467 to 687°C, while addition of copper and iron to zirconia prepared by the sol-gel method, increased the temperature of the exothermic peak from 430°C for unpromoted zirconia to 447 and 455°C for 1 wt % Cu and Fe respectively. Doping of zirconia with iron increased the temperature of the crystallization peak in the DTA from 405°C for pure zirconia to 690°C for a sample doped with 30 mol % Fe_2O_3 (35). The beneficial addition of anions has also been reported by Srinivasan et al (36) who observed that the sulfating of zirconia shifted the exothermic peak from 450°C for unsulphated zirconia to 622°C on heating in air. Some

studies have observed that the exothermic peak is due to crystallization into the cubic and tetragonal phases (31,36,35) while another study has attributed it to crystallization into the tetragonal and monoclinic phases (33). However other studies have shown that the tetragonal phase is stable at high temperatures and the monoclinic phase is observed during cooling after crystallization (37,38). Hence another possibility is that the exotherm of ZrCe50-cp-1 was shifted to higher temperature above 600°C or that the hydrous oxide formed after drying was already crystalline.

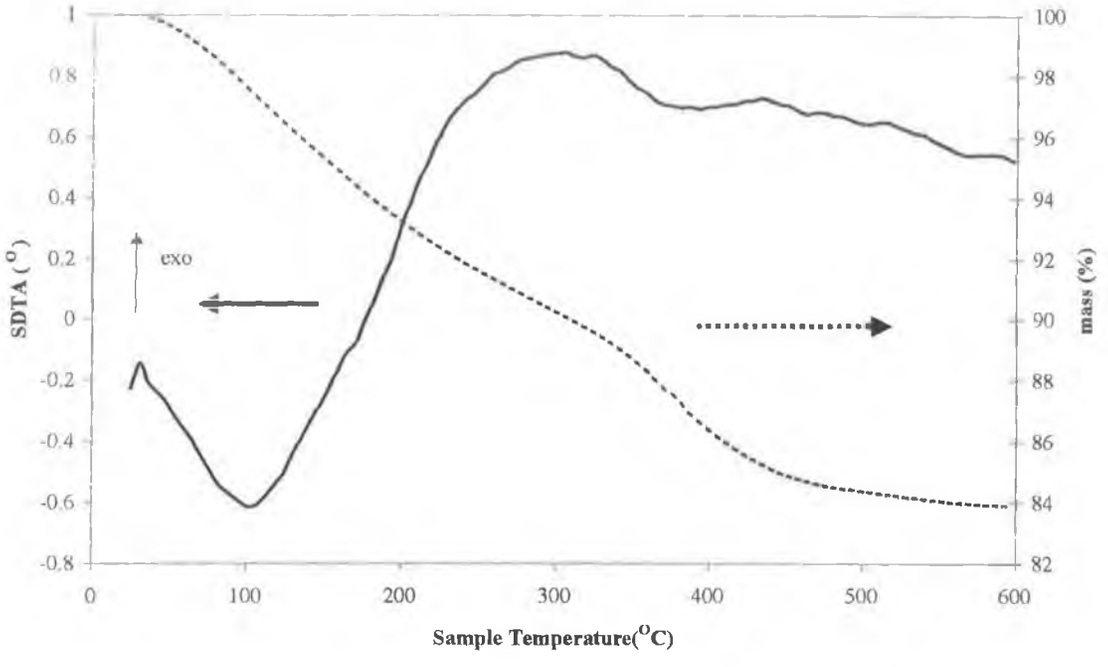

Fig 3.4 Simultaneous TG-SDTA of ZrCe50-cp-1: sample weight : 40.10 mg

3.3.2.2 SIP-MS

SIP-MS experiments were performed as outlined in chapter 2 on the dried precipitates formed after precipitation and the results are shown in Figs 3.5 to 3.9. The SIP-MS data represents the intensity of different gaseous ions evolved as a function of sample temperature as the sample is heated at a constant linear heating rate under vacuum. The ions monitored for each sample are indicated in the legend of the corresponding figure. For ZrCe0-cp-1 (see Fig 3.5), small and large peaks at approx 90°C and 159°C corresponding to the evolution of water (m/z = 18) and hydroxyl groups (m/z = 17) are observed and can be attributed to the dehydration of zirconium oxide hydrate or hydroxide.

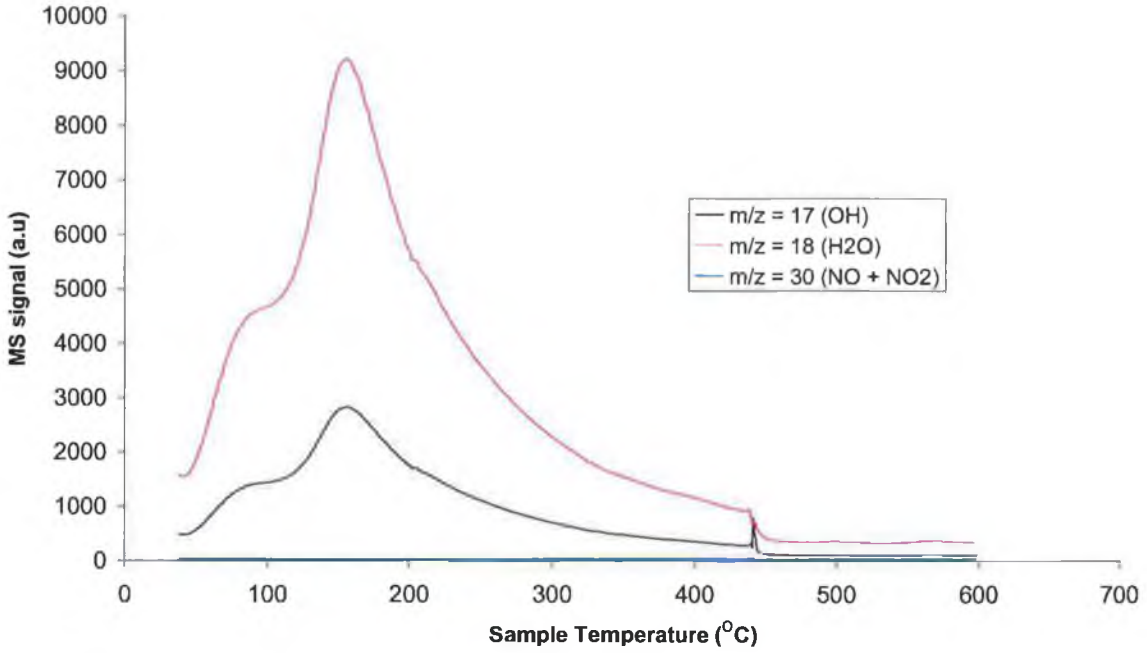

Fig 3.5: SIP-MS of ZrCe0 –cp-1

For cerium oxide (see Fig 3.6), the m/z = 18 trace associated with the evolution of water and the dehydration of the hydroxides shows a small peak at 137˚C with shoulder at 285˚C. The total peak stretches from 70 to 300˚C with the high initial signal for water associated with physically adsorbed water due to the high surface area of the sample. A similar but less intense signal was observed for the evolution of the hydroxyl ion due the scarcity of the OH that is formed from fragmentation of H_2O. Nitrate evolution (NO + NO_2) began at approx 250˚C with shoulder at 287 ˚C and maximum at 361˚C. It then continued until 600˚C while a peak at 287˚C is observed for N_2O. Hence the majority of the m/z = 30 trace is due to the evolution of NO_x with some N_2O being given off at the beginning. The presence of the nitrate indicates that not all the precursor was reacted with the ammonium hydroxide to form cerium hydroxide

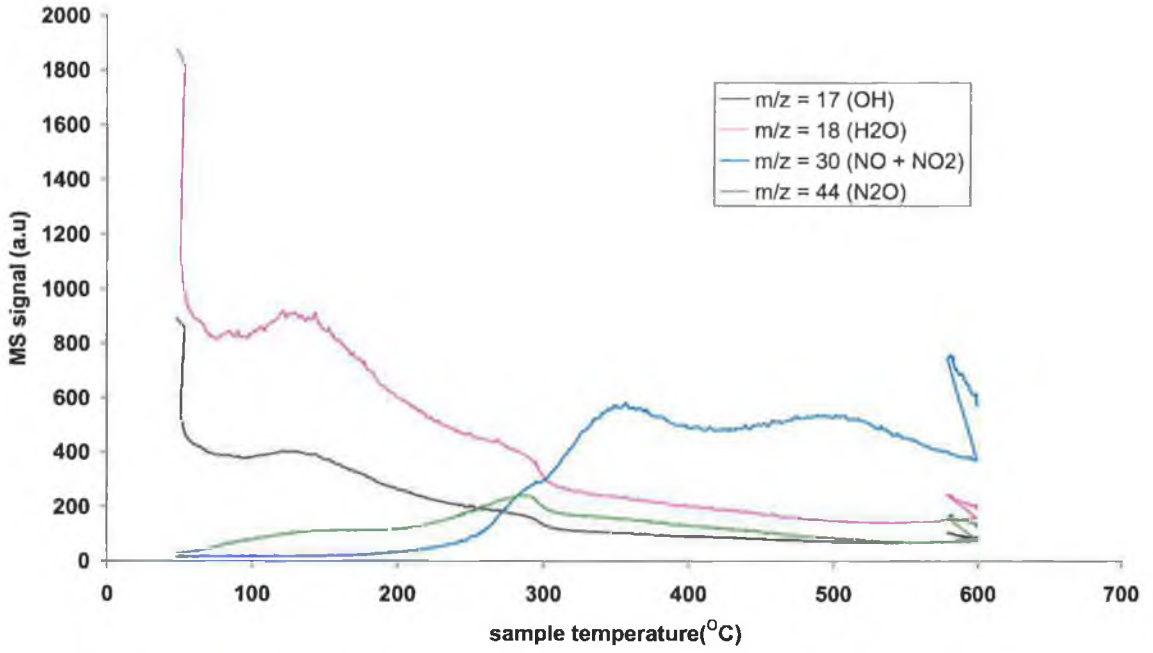

Fig 3.6: SIP-MS of ZrCe100-cp-1.

The SIP-MS of ZrCe50-cp-1 is shown in Fig 3.7. A large peak associated with water with a maximum at 145°C occurred, which indicates dehydration of zirconium hydroxide and/or cerium hydroxide. The signal extends from approx 70 to 460°C with shoulders at 280°C and 334°C. A very wide peak associated with the m/z = 30 trace which can be associated with NO, NO_2 and N_2O was also observed. Evolution of that fragment begins at 200°C with a first maximum at 260°C and second at 420°C. For N_2O, peaks at 282°C and 403°C are observed. By 462°C, evolution of N_2O is complete while significant evolution for NO and NO_2 is observed up till 560°C. According to literature (39), NO, N_2O and NO_2 give parent ion intensity (i.e. ion currents in amperes for the ions formed by electron impact) at mass numbers 30, 44 and 46 of 91, 62 and 22 respectively. N_2O and NO_2 then fragment to contribute to the m/z = 30 peak with relative intensities of 19.5 and 59.25 respectively of the total intensity of the m/z =30 peak. Below 427°C, the partial pressures of oxides of nitrates are as follows N_2O>NO>NO_2 while above 427°C, NO>N_2O>NO_2. Hence above 427°C, nitrates decompose mainly to give NO. The presence of the nitrate peaks, which are similar to those reported for ceria, indicates the presence of unreacted cerium nitrate in the uncalcined sample, which is then evolved on heating.

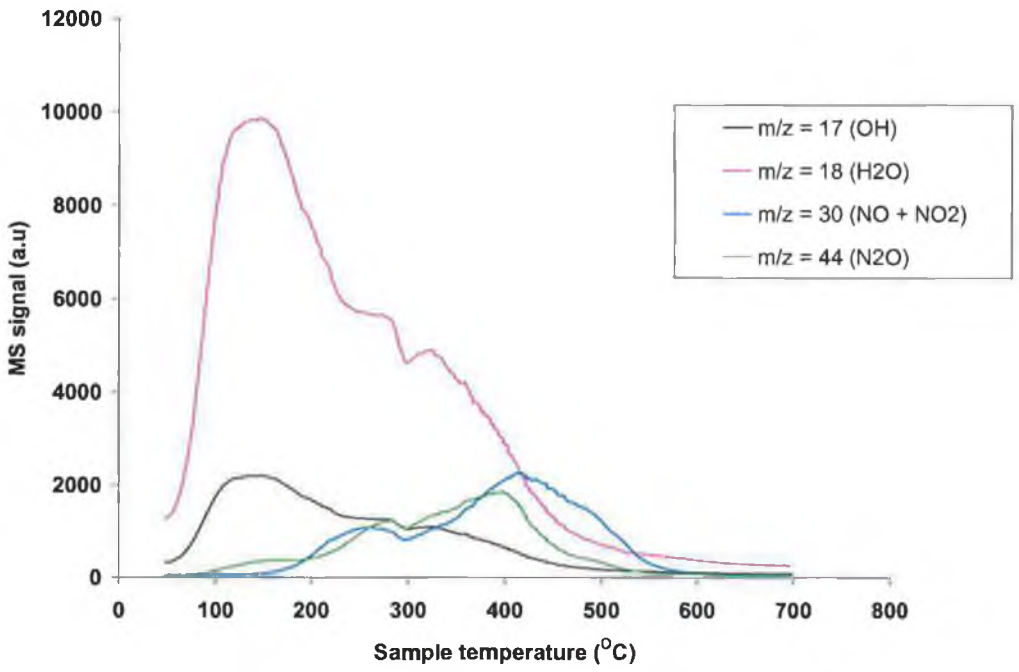

Fig 3.7 : SIP-MS of ZrCe50-cp-1

The SIP-MS data of selected sol-gel samples, namely ZrCe0-sg and ZrCe50-sg, are shown in Figs 3.8 and 3.9 respectively. In the SIP-MS of zirconia prepared by sol-gel, peaks at approx 100°C and 200°C are observed due to desorption of physically adsorbed water and decomposition of zirconium hydroxide or oxide hydrate respectively. For ZrCe0-sg, peaks at approx 100°C and 200°C are observed due to desorption of physically adsorbed water and decomposition of zirconium hydroxide or oxide hydrate respectively. In contrast, the SIP-MS for ZrCe50-sg (Fig 3.9) indicates both the presence of hydroxides and nitrates. Water peaks due to the decomposition of hydroxide are observed at 170°C, while a shoulder was observed between 200°C and 300°C. The m/z =30 trace shows peaks at 200 and 450°C with broad peak between 300 and 400°C.

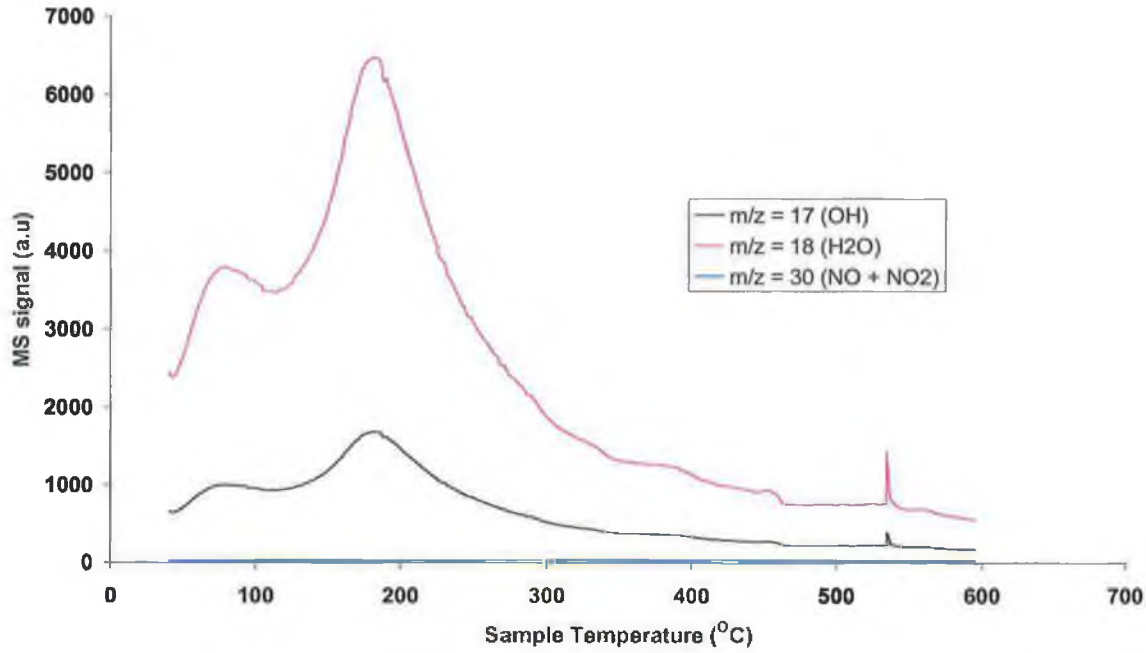

Fig 3.8 SIP-MS of ZrCe0-sg (ZrO_2)

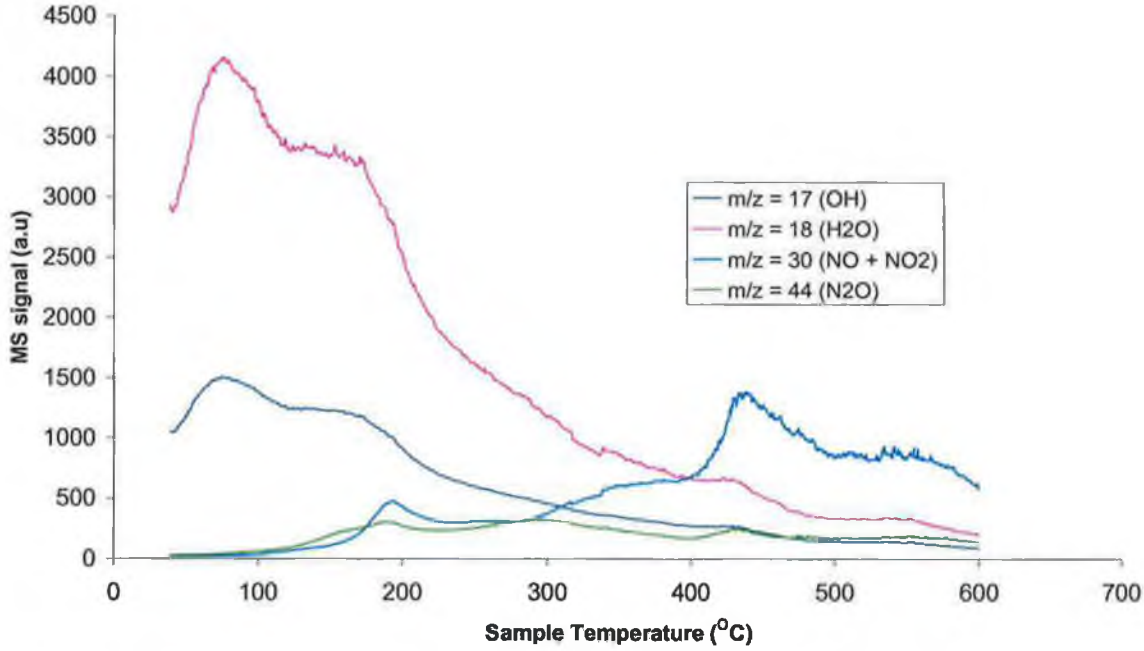

Fig 3.9 SIP-MS of ZrCe50 –sg

3.3.2.3 XRD

The structure of the fresh oxides as determined by XRD are summarized in Table 3.6 and illustrated in Fig 3.10-3.13. It can be seen in Fig 3.10 that the XRD patterns of ZrCe70-sg and ZrCe85-sg show main peaks with visible tailing at about 29, 33, 48 and 56 °, (2θ) which represent indices of (111), (200), (220) and (222) planes respectively of a cubic fluorite structure. By comparison with Fig 3.11 and ICDD file no: 4-0593 for ceria (Table 3.6), a cubic structure corresponding to CeO_2 is indicated. Both ceria samples show the same cubic structure despite differences in surface areas. In contrast for ZrCe50-sg and ZrCe50-cp, wider peaks at higher 2-Theta value are observed. This increase in width for the 50 mol% samples is unlikely to be attributable to a particle size or surface area effect, since in general lower surface area and large particles give sharper and narrower peaks. Both the 50 mol% sol-gel and co-precipitation samples had lower surface areas than ZrCe70-sg and ZrCe85-sg (see Table 3.2 and 3.3). A mixture of phases is indicated in both samples but the noisy baseline makes it difficult to conclusively determine what phases are present.

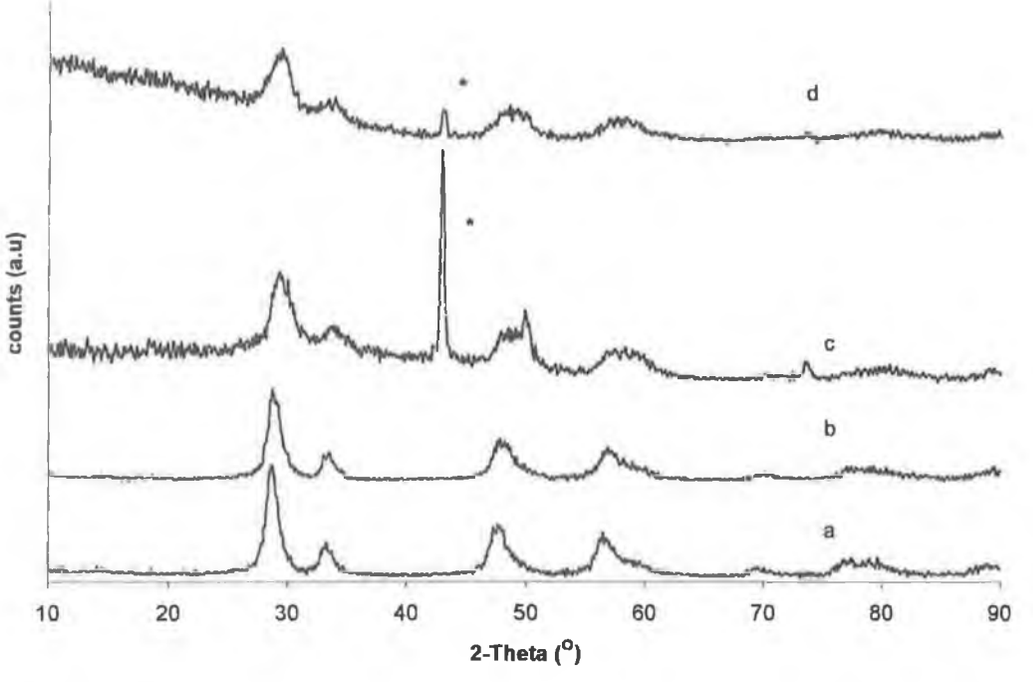

Fig 3.10 XRD patterns for fresh samples calcined at 600°C (a) ZrCe85-sg (b) ZrCe70-sg (c) ZrCe 50-sg (d) ZrCe50-cp-1 where * represents peaks from the copper sample holder.

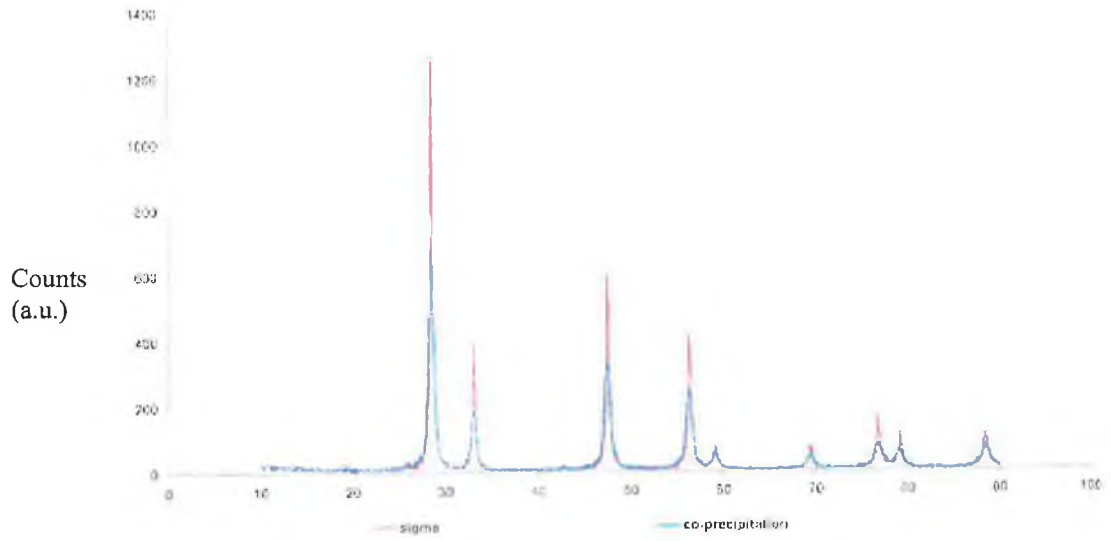

Fig 3.11:XRD of ZrCe100-cp (blue trace co-precipitation) and ZrCe100-Aldrich (red trace sigma).

The XRD of ZrCe50-cp-1 and ZrCe50-sg with an expanded baseline is shown in Fig 3.12 for clarity. The peaks observed at approx 43° are due to the X-Ray beam striking the copper sample holder during analysis of the samples. For ZrCe50-sg, the most intense peaks correspond to d_{hkl} of 3.03-3.06Å. Smaller shoulder peaks at higher d_{hkl} values were also observed (i.e. 3.09 and 3.12 Å), which may correspond to the cubic ceria rich phase. Vlaic et al (40) concluded that the most intense peak for a ZrCe50/50 oxide gave a d_{hkl} of 3.04Å and this corresponded to a tetragonal phase. According to Fornasiero et al (1), the tetragonal phase would be detected by broadening and splitting of the peaks at 47 and 59°. In this work, for ZrCe50-cp-1, a smaller peak was observed with most intense peaks at d_{hkl} 3.03-3.08Å. From Table 3.6, it was observed that ZrO_2 with a low surface area of $5m^2g^{-1}$ had a monoclinic structure. The ZrCe0-Aldrich sample is included for the sole purpose of illustrating the relationship between surface area and the amount of monoclinic phase present. As the surface area increased for ZrCe0-cp and ZrCe0-sg, the fraction of monoclinic phase decreased and the tetragonal phase increased with a mixture of both phases observed. This is in agreement with literature that states that the metastable tetragonal phase is stabilized by smaller particle size (41). The surface areas of the ZrCe0-cp and ZrCe0-sg are similar but the XRD pattern (Fig 3.13) shows that the peak corresponding to the tetragonal phase (2θ =

30.2°) is sharper and narrower in the co-precipitated sample, thus indicating larger tetragonal particles.

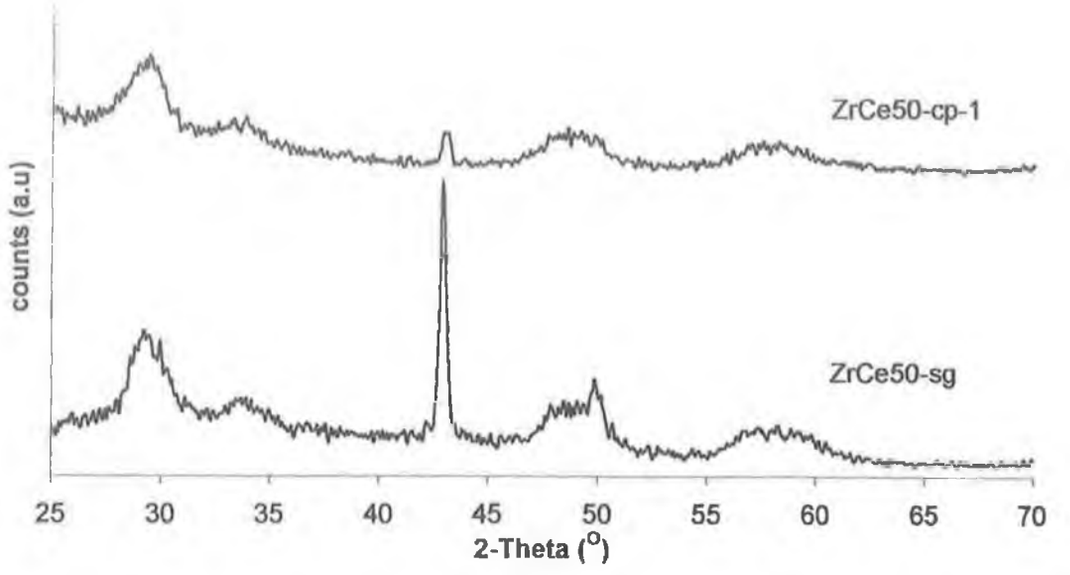

Fig 3.12: Enlargement of XRD spectrum between 25 and 70° for the ZrCe50-cp-1 and ZrCe50-sg samples.

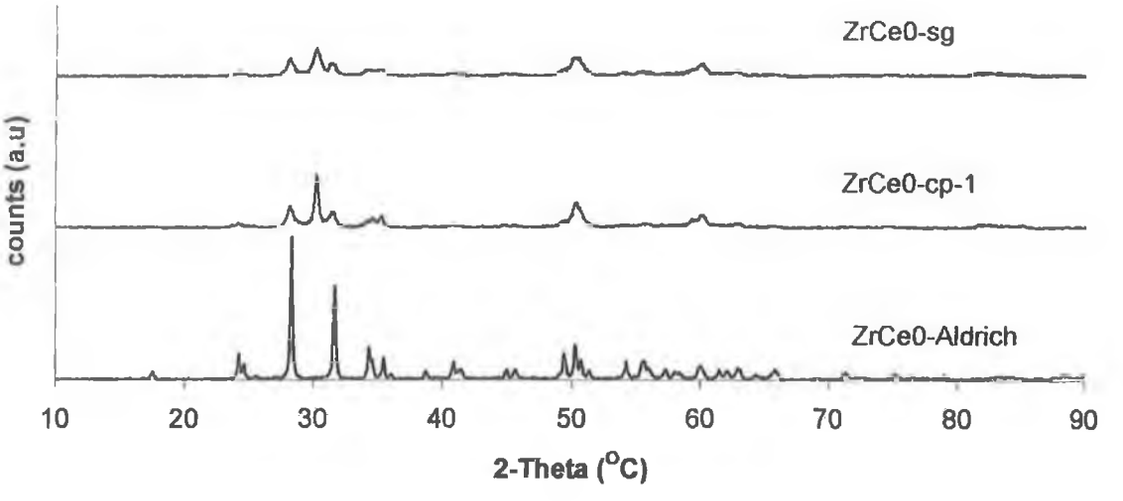

Fig 3.13 XRD patterns of various fresh zirconia samples.

Sample	File no	Main peaks- 2θ (°)	Main Peaks - d_{hkl} (Å)	Relative Intensity(%)	Phase
m-ZrO_2	13-307	Not given	3.16, 2.83, 2.62 1.85	100, 65, 20 18	m
t-ZrO_2	17-923	Not given	2.96, 1.83,1.55, 1.81	100, 65, 45, 35	t
CeO_2	4-0593	Not given	3.12, 1.91, 1.63 2.71	100, 51, 44 29	c
ZrCe0-Aldrich	N/A	28.30, 31.60, 50.25 34.3	3.15, 2.83, 1.82 2.61	100, 65, 24 23	m
ZrCe0-cp-1	N/A	30.20, 50.30, 28.2, 31.35, 60.15, 35.2	2.96,1.81, 3.16, 2.85, 1.54, 2.55	100, 50, 43, 32, 28, 25	m + t
ZrCe0-sg	N/A	30.20, 50.10, 28.15 31.35, 35.25, 60.15 34.15	2.96, 1.82, 3.17, 2.86, 2.54,1.54, 2.63	100, 72, 68, 53, 35, 52 32	m +t
ZrCe50-cp-1	N/A	29.45, 29.25, 29.00 29.75, 30.10, 28.20, 27.95, 33.90, 47.8-50.15*, 57.05-59.55*	3.03, 3.05, 3.08, 3.00, 2.99, 3.16, 3.19, 2.64, 1.90-1.82*, 1.61-1.55*	100, 98, 93, 92, 76, 72, 69, 50, 32-40*, 25-31*.	See text
ZrCe50-sg	N/A	29.20, 29.25, 29.45, 28.85, 28.60, 49.85 47.85 - 49.05	3.06, 3.05, 3.03, 3.09, 3.12, 1.83, 1.90 -1.86,	100, 99, 96, 88, 82, 67, 49-52,	See text
ZrCe70-sg	N/A	28.65, 29.05, 48.05 47.45, 33.45, 56.8	3.12, 3.08, 1.89, 1.92, 2.68, 1.62	100, 88, 44, 38, 36, 45	c
ZrCe85-sg	N/A	28.55, 47.25, 48.10, 56.4, 33.20	3.13, 1.92, 1.89, 1.63, 2.70	100, 49, 45, 43, 38	c

Table 3.6: XRD data for fresh samples prepared by co-precipitation and sol-gel techniques and standard samples of m-ZrO_2, t-ZrO_2 and CeO_2.where m, t and c represents monoclinic, tetragonal and cubic respectively. The main peaks are represented in 2θ and d_{hkl}, the interplanar spacing corresponding to each peak. Relative intensity is the relative intensity of that peak compared to the most intense peak in the diffraction pattern and file no refers to the ICDD file number for that compound. N/A is not applicable and * refers to a group of peaks of low intensity.

3.3.3 Reduction characteristics of fresh samples

In the reduction experiments, the sample was heated at a rate of 10°C/min in a stream of a reducing agent (5%H_2/Ar) and production of water (m/z = 18) was monitored by mass spectrometry as a function of sample temperature. The reduction profiles (TPR-MS) of ZrCe50 samples prepared sol-gel and co-precipitation are compared to a commercial sample of pure CeO_2 (ZrCe100-Aldrich), the results of which are shown in Fig 3.14-3.16. As can be seen from Fig 3.14 and Fig 3.15, both ZrCe50-sg and ZrCe100-Aldrich gave relatively strong signals, the latter being stronger then the former. A very weak signal was observed for ZrCe50-cp-1 (Fig 3.16) and all samples were normalized in order to obtain peak positions (normalized data not shown). The amount of water produced or the amount of hydrogen uptake could not be measured quantitatively due to the jet separator used in the instrument. Peak positions (i.e. temperature corresponding to maximum evolution of water) were quantitatively determined from normalized data and are summarized in Table 3.7. Ceria reduction was the strongest for pure ceria, as indicated by intense evolution of water. Zirconia has been reported in the literature to show no reduction below 1000°C (42) and hence no reduction was expected for pure zirconia samples prepared in this study.

Sample	**Tmax (°C)**
ZrCe100-Aldrich	497 (sh), 548 (sh), 664
ZrCe50-cp-1	474 (sh), 717
ZrCe50-sg	642

Table 3.7 Reduction characteristics of selected samples where T_{max} represents the temperature of maximum reduction and sh represents shoulder peaks

Comparison of these results with literature is quite difficult because the temperature range and the shape of the peak is very dependent on the experimental conditions used (43). The temperature of maximum reduction depends on the concentration of hydrogen, the flow rate of hydrogen, the heating rate used and the mass of the catalyst used. Partial pressures of hydrogen and water can also affect the temperature and mechanism of reduction (44). Gentry et al (43) investigated the specific effects of each

parameter on a zeolite sample. An increase in the flow rate of hydrogen from 10 to 20 cm^3/min lowered the temperature of reduction by 15-30K. This was attributed to the lowering of the degree of conversion of reactants at higher flow rates and an increase in the reactant concentration in the reactor. Increases in the mass of the sample from 50 to 400 mg resulted in the loss of resolution of two separate reduction peaks at lower mass and an increase in T_{max}. Larger masses resulted in more significant temperature and hydrogen concentration gradients within the sample.

As shown in Chapter 1, two peaks for reduction of ceria are observed in 15%H_2 at 10°C/min (3). The first peak, centred at 500°C is due to a surface capping oxygen anion which is attached to a surface Ce^{4+} peak in an octahedral coordination. The latter peak, at 750°C, is due to a bulk oxygen anion which is bonded to two Ce^{4+} ions in bulk ceria. The size of the first peak is lower for the sample with surface area of 1 m^2g^{-1} compared to that of 10 m^2g^{-1}. In the TPR profiles of ceria obtained by Yao and Yao (3), the concentration of hydrogen used was 15%, which can decrease the temperature of reduction by approx 10K for each 1% increase in hydrogen concentration. Fornasiero (45) also observed two peaks for a high surface area ceria sample (196m^2g^{-1}) at 520°C and 828°C. Daturi et al (46) observed two peaks at 517°C and 895°C for a ceria sample with a surface area of approx 100m^2g^{-1}. In general low temperature peaks (below 700°C) were attributed to surface oxide (47), while higher temperature peaks were attributed to nonstoichiometric cerium oxides and bulk Ce_2O_3 (48). In the present study, a single peak was observed for ZrCe100-sigma at 664°C, with a small shoulder at 500°C. The only other study of this ceria sample in the literature (49) reported a main peak at 500°C and a shoulder at 400°C, using temperatures up to 500°C with a much larger amount of catalyst been used (0.3g). The peaks were attributed to surface Ce reduction. Bernal et al (50) observed a very similar TPR-MS profile to the one observed in this study, with a strong reduction peak at 627°C with reduction beginning at around 200°C. The peak at 627°C was attributed to bulk reduction of the oxide to form $CeO_{1.84}$ The oxide with a surface area of 56m^2g^{-1} was prepared by heating high surface area ceria at 550°C in H_2 and reheating in a flow of O_2 at 500°C. In the present study, attempts were made to obtain TPR data for ZrCe100-cp-1, which had a higher surface area of 63m^2g^{-1}. However due to instrumental problems, this was not achieved and hence the following conclusion, based on previous studies, is tentatively suggested.

The main peak observed is that of bulk reduction with the lower temperature peaks representing surface reduction. If the peak represented surface reduction only, the peak area should be smaller to that of the sol-gel sample, which had a higher surface area. Studies have shown that the size of the peak corresponding to surface reduction is dependent on the surface area. Instead the peak area of pure ceria is higher, suggesting that the peak is due to reduction of bulk ceria.

However, in agreement with the majority of the literature, a single broad peak is observed for the mixed oxides. Luo and Zheng (51) reported that the reduction profile of $Ce_{0.5}Zr_{0.5}O_2$ (surface area of $11 m^2g^{-1}$) was characterized by a single peak at 640°C. Their analysis was performed on a 25 mg sample with a heating rate of 20°C/min, which should result in a higher T_{max} than found in our study. The single peak has been reported to indicate that bulk and surface reduction occur simultaneously. However lower temperatures of reduction have been reported. For example Fornasiero et al (45) observed two peaks centred at 577°C and 737°C for high surface area $Ce_{0.5}Zr_{0.5}O_2$ ($64 m^2g^{-1}$). Conditions used were 5% H_2 in argon at 25 ml/min at a linear heating rate of 10°C/min. The flow rate used by the authors is half that used in our study so a lower temperature of reduction should have been observed in our study. The same study also reported that low surface area $Ce_{0.5}Zr_{0.5}O_2$ showed no reduction below 454°C. Daturi et al (46) reported on a single reduction peak at 563°C for high surface area $Ce_{0.5}Zr_{0.5}O_2$ ($100 m^2g^{-1}$). The conditions used were 5% H_2 with no flow rate mentioned at a 10°C/min temperature rise.

In the current study, for the co-precipitated sample, the temperature of reduction (the main reduction peak) was higher than the sol-gel sample. This could have been due to the lower surface area and hence higher particle size of the sample. It has been reported (19) that a decrease in the particle size results in a shift of the reduction peak maximum to lower temperatures. The most important point to make about the TPR profiles is that the sample prepared by the sol-gel method appears more reducible than the co-precipitated sample, suggesting that the Ce^{4+} - Ce^{3+} redox couple is more facile and the lattice oxygens are more labile.

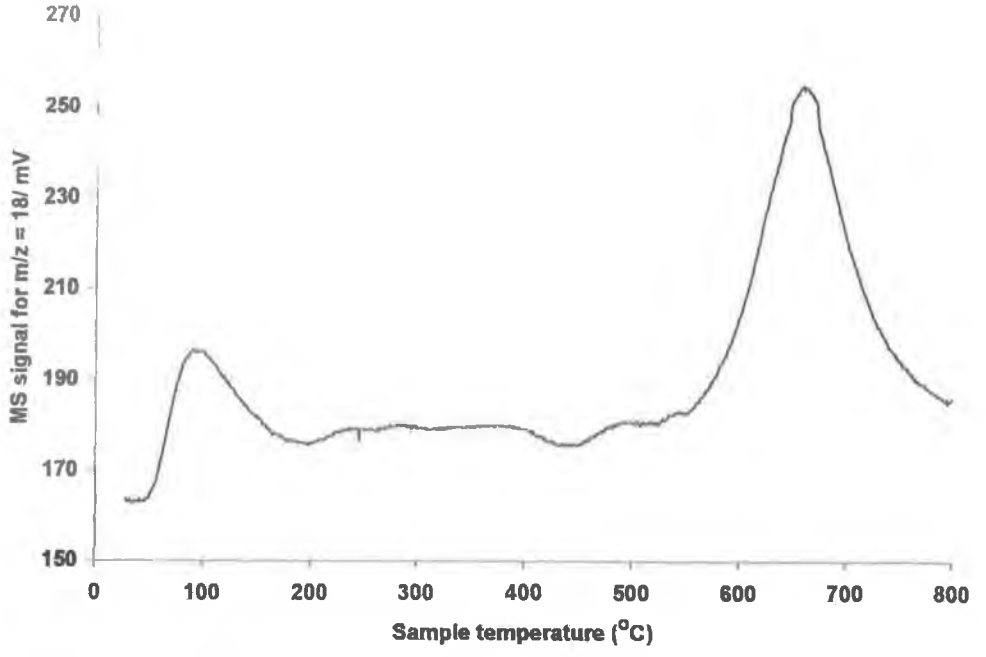

Fig 3.14:TPR-MS profile of ZrCe100-Aldrich at a linear heating rate of 10°C/min.

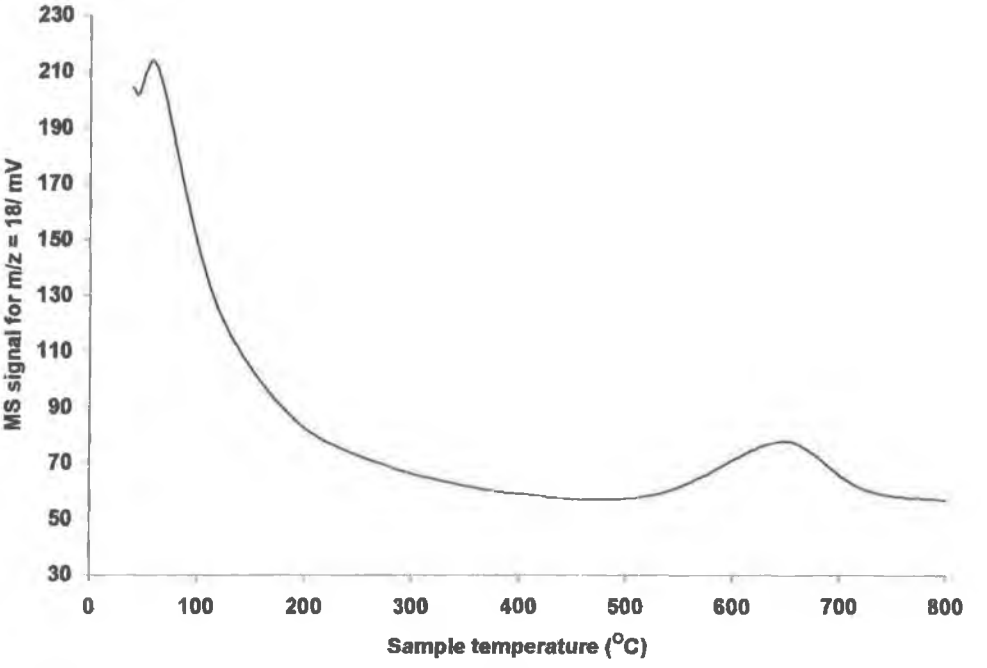

Fig 3.15: TPR-MS profile of ZrCe50-sg at a linear heating rate of 10°C/min.

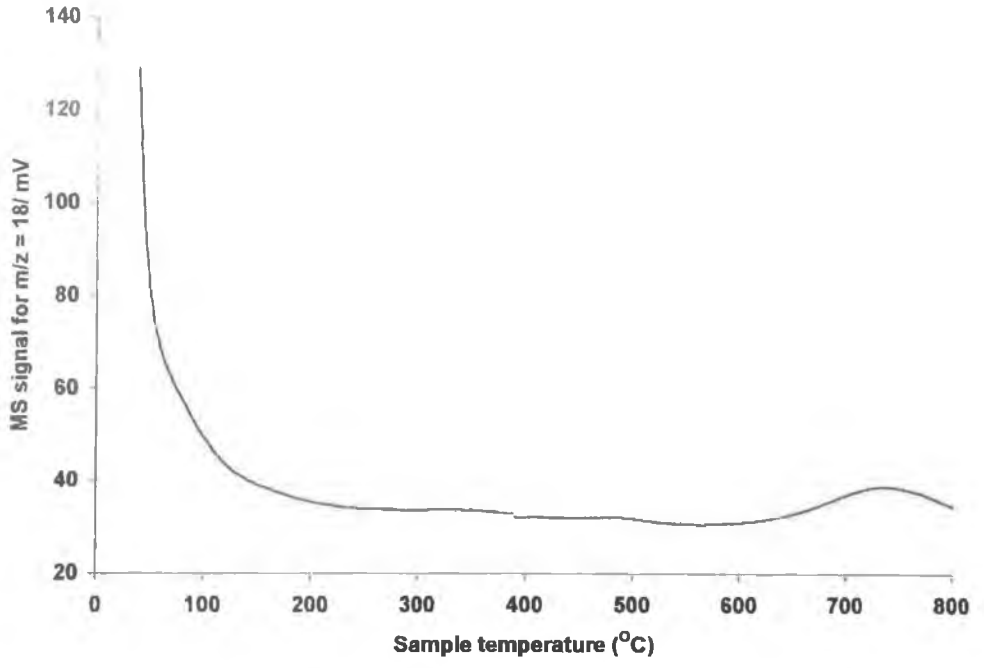

Fig 3.16: TPR-MS profile of ZrCe50-cp-1 at a linear heating rate of 10°C/min.

3.3.4 Oxidation activity for fresh samples

The catalytic activity of the oxides prepared was determined by measuring their activity for the combustion of propane, using the procedure previously described in chapter 2. The activities for propane combustion of the fresh samples are reported in Table 3.8. In order to check for errors in the determination of propane activity, two separate measurements of the same batch of an active manganese oxide sample (preparation method outlined in chapter 4) were performed. A large difference of almost 80°C was observed between T_{10} values on each run, while only a small difference of 6°C was observed between T_{50} values on each run (211 versus 217°C). Firstly it is clear from Table 3.8 that ceria is significantly more active than zirconia in agreement with other studies (7). At 475°C, zirconia has not reached 50% conversion while CeO_2 has reached 100% conversion at 400°C. In general, oxidation activity requires multi-valent metal ions that can take part in oxidation-reduction reactions (52). Ceria shifts very easily between Ce^{4+} and Ce^{3+} while zirconia tends to remain in the Zr^{4+} state. Hence it would appear that the activity found in the mixed oxides is due to ceria in agreement with a previous study (7). In general, the temperatures of 10% conversion (T_{10}) reported in Table 3.8 are lower in run 2 than run 1 (may be an artifact from the experimental

technique), while no change is observed for temperatures of 50% conversion (T_{50}) on going from run 1 to run 2.

sample	SA (m^2g^{-1})	T_{10}(°C)		T_{50} (°C)	
		Run 1	Run 2	Run 1	Run 2
ZrCe0-cp-1	34	432	356	>475	>475
ZrCe10-cp-1	15	429	377	479	487
ZrCe30-cp-1	22	396	343	475	475
ZrCe50-cp-1	10	432	394	500	497
ZrCe70-cp-1	7	396	407	478	473
ZrCe85-cp-1	22	221	188	434	423
ZrCe100-cp	63	143	193	342	353
ZrCe100-Aldrich	30	228	232	378	379
ZrCe0-sg	34	337	nd	>400	nd
ZrCe10-sg	37	358	251	434	434
ZrCe50-sg	44	289	308	421	427
ZrCe70-sg	47	271	259	370	366
ZrCe85-sg	50	250	nd	340	nd

Table 3.8: Activities of catalyst samples where T_{10} and T_{50} represent temperatures at which 10 and 50% conversion of propane was reached. Samples were initially tested (run 1) and then cooled to room temperature and retested (run 2).

For the co-precipitated samples, a much larger variation was observed in the temperatures at which 10% conversion was achieved between run 1 and run 2. With the exception of ZrCe70-cp-1 and ZrCe100-cp, the T_{10} decreased on run 2. A possible reason for this is the elimination of chloride ions still present on the catalyst from the zirconium precursor used. It has been shown that chloride ions can poison catalysts (53). However this study related to noble metals and the calcination procedure used in our study was quite long (6 hrs), which should be sufficient to remove any residual chloride ions. It seemed particularly apparent for zirconia and mixed oxides with low ceria contents, although the reason is not clear. For the sol-gel samples, the variations

between the T_{10} values from run 1 to run 2 were much smaller, with the T_{50} values being within experimental error. The only exception to this is the ZrCe10-sg, which suffers a 100°C decrease in its T_{10} from run 1 to run 2. This may also suggest that the thermal stability of the sol-gel samples is higher than that of the co-precipitated samples after heating in the reaction mixture. The aging behaviour of the samples is explored in a later section.

The samples prepared by sol-gel are more active than the corresponding samples prepared by the co-precipitation method. This may be due to the higher surface areas of the former. It has been reported (54) that the higher the surface area, the greater the amount of surface area accessible to the reactants and the larger the conversion of reactant to product. In the current results, surface area is also seen to have an important effect for example in the case of ZrCe70, the surface area of the sol-gel sample is seven times higher than the co-precipitated sample and there is a difference of 100°C in the temperature at which they reach 50 % conversion of propane. Only a fraction of the surface area determined by the BET technique may be chemically active. This explains why zirconia, with a surface area of 34 m^2g^{-1}, is relatively inactive compared to the mixed oxides.

A general trend between reducibility and activity was observed. The activities of the above samples for oxidation of propane are represented graphically in Fig 3.17. From Fig 3.17 and Table 3.8, the following trend in terms of increasing reducibility (decreasing T_{max} of largest peak) was observed, indicating that ZrCe50-sg was most easily reduced:

ZrCe50-cp-1 < ZrCe100-sigma < ZrCe50-sg.

Significantly higher activities are observed for ZrCe100-Aldrich and ZrCe50-sg, which are also more reducible. A correlation between redox behaviour and activity has been observed by Arnone et al (55) and Pengpanich et al (8) and can be explained as follows: as discussed previously, reduction involves removal of lattice oxygen atoms. The lower the temperature of reduction, the more labile or mobile the lattice oxygen atoms are. The Mars van Krevelen mechanism has been proposed as the mechanism of oxidation

over oxide catalysts (56). This mechanism consists of a redox mechanism involving reaction of lattice oxygen.

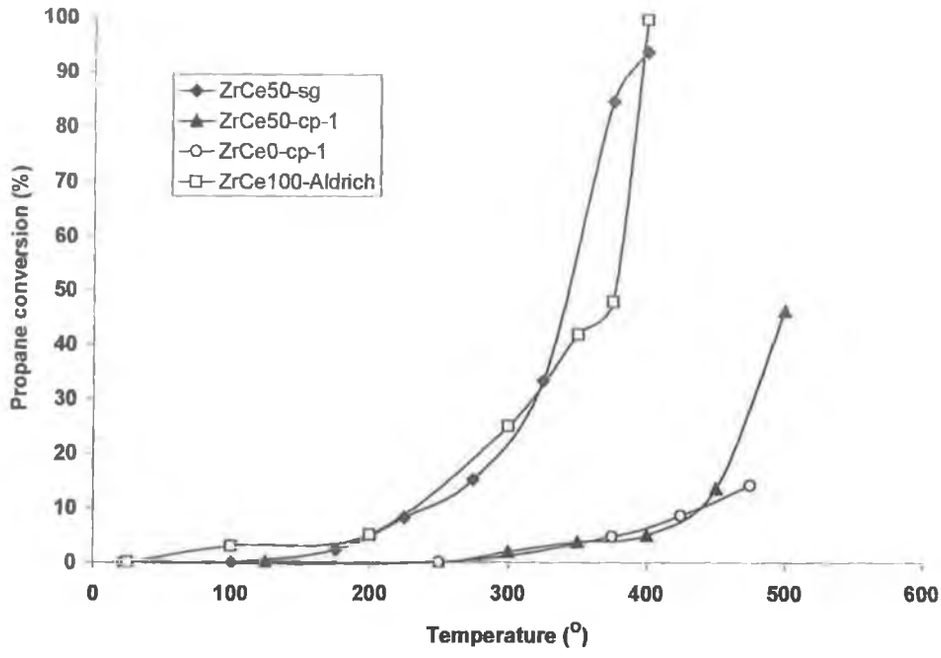

Fig 3.17: Propane oxidation activity for selected ZrCe oxides.

Different activities within each set of preparation conditions were observed within the individual series of catalysts (see Fig 3.18 and 3.19). In the case of the sol-gel samples the activity of the catalyst increased with cerium content i.e. the temperature of 50% conversion decreases as cerium content increases, with the exception of ZrCe50-sg compared to pure zirconia. (see Table 3.8). The latter was only tested up to 400°C and both samples showed similar conversion up to that temperature. The following trend in catalytic activity was deduced based on T_{50} values:

ZrCe85-sg > ZrCe70-sg>ZrCe50-sg> ZrCe10-sg~ZrCe0-sg.

This is in agreement with Pengpanich et al (8) who observed that the catalytic activity for the oxidation of methane decreased with an increase in Zr loading. The same author found that the $Ce_{0.75}Zr_{0.25}O_2$, $Ce_{0.5}Zr_{0.5}O_2$ and $Ce_{0.25}Zr_{0.75}O_2$ were more active than ceria or zirconia alone and the mixed oxides also had slightly higher surface areas. In the case of pure ceria, two samples with different surface areas were investigated in the present study. The sample prepared by co-precipitation had a higher activity and

surface area than the commercial sample obtained from Aldrich. XRD indicated the same cubic structure for both samples. The run 1 activity of ZrCe100-cp is also much higher than run 2, indicating a possible loss of activity and surface area on run 2. The most active sample in terms of T_{50} is ZrCe85-sg with a T_{50} of 340°C and specific surface area of 50 m^2g^{-1}. CeO_2 prepared by co-precipitation has a very similar T_{50} of 342°C but a higher specific surface area of 61m^2g^{-1}. This indicates that despite a lower surface area, the sol-gel sample is as active as ceria and hence the incorporation of zirconia improves their activity, as found in previous studies and something other than surface area is at play. This could be attributed to the introduction of more defects that improves oxygen mobility that is crucial to the oxidation process via the Mars van Krevelen mechanism. However another reason for the increase in activity with relation to pure ceria could be the increased oxygen storage capacity that is associated with mixed oxide. As seen from the literature survey, there is general agreement that OSC of mixed oxides is greater then that of ceria (40, 46, 57). This has been attributed to the incorporation of zirconium into the ceria lattice which creates changes in bond lengths and disorder of oxygen atoms (40).

Fig 3.18 shows that for the fresh sol-gel samples, activity of the sol-gel samples cannot be correlated with surface area alone. Although a linear increase in surface area was observed on increasing the cerium content, activity increased rapidly for the 70 and 85 mol% cerium compared to lower content samples. In agreement with Terribile et al (5) and Pengpamch et al (8), the increase in activity can be related to the cubic structure, that was observed in the XRD of the higher cerium contents. It has been proposed that the cubic structure favours oxygen mobility as compared to the tetragonal structure.

Figure 3.19 illustrates the relationship between surface area, amount of cerium and activity for the co-precipitated samples. In contrast to the sol-gel samples, the activities of co-precipitated samples appear to be surface area dependent, with the same trend being observed for both surface area and activity (Fig 3.19). For the mixed oxides prepared by co-precipitation, the light-off temperature of all mixed oxides were similar with the exception of highest cerium content. They were less active than the pure ceria samples probably due to the significantly lower surface area.

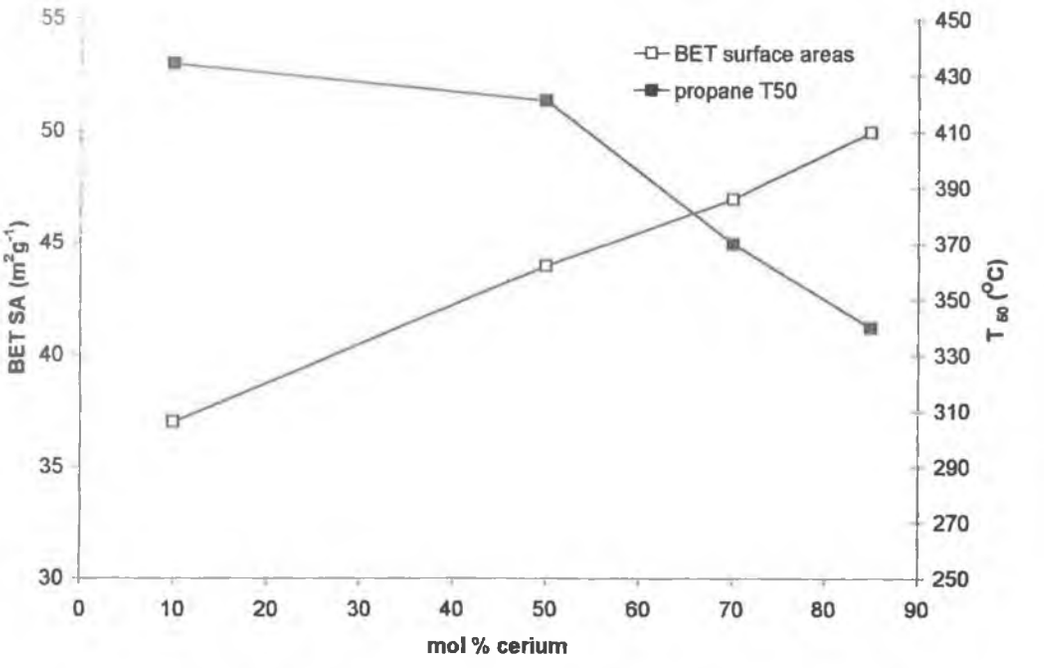

Fig 3.18: Temperature of 50% conversion of propane (T_{50}) and Surface area (BET SA) versus CeO_2 content (mol%) in mixed oxides prepared via the sol-gel method.

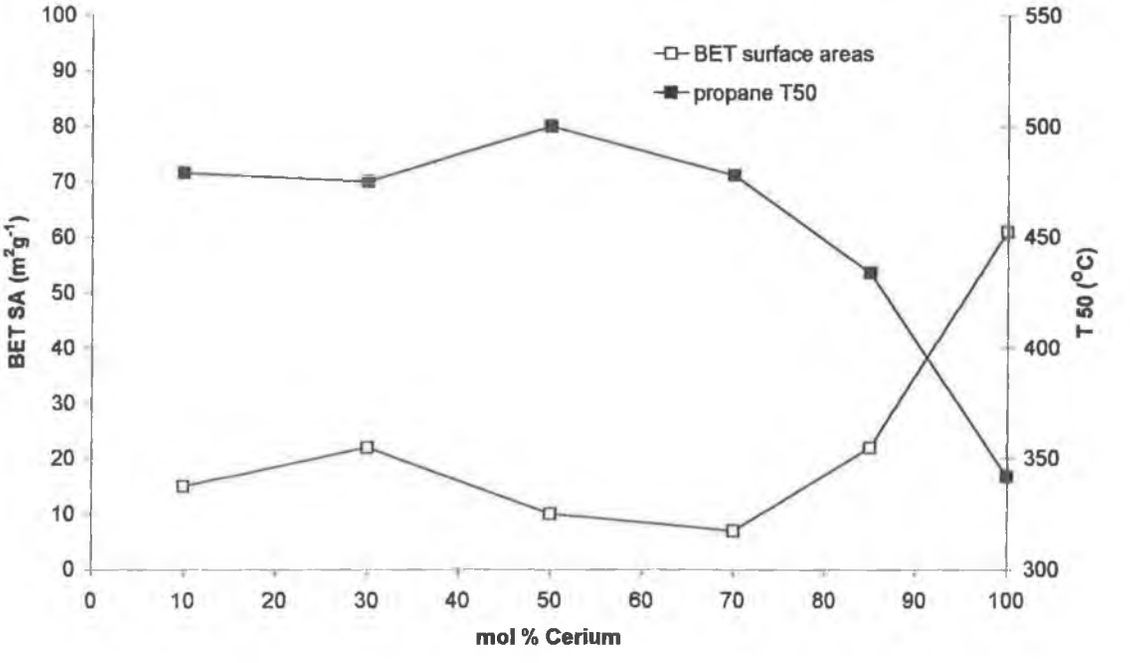

Fig 3.19: Temperature of 50% conversion of propane (T_{50}) and BET surface area (SA) versus CeO_2 content (mol%) in mixed oxides prepared via the co-precipitation method.

The XRD pattern of ZrCe50-cp and ZrCe50-sg were quite similar with no significant differences observed. Hence in order to investigate if the differences in activity were surface area related, reaction rates under differential conditions were determined for both samples for the oxidation of methane (see Table 3.9). The activity of oxides was expressed in terms of surface area using the following equation, similar to that proposed by Milt et al (58).

$$r = X_{CH4} * F_{CH4}/mS \ (\mu mols^{-1}min^{-1}m^{-2}) \qquad (3.1)$$

Where X_{CH4} = conversion of methane (%)

F_{CH4} = flow rate of methane (μmol CH_4 min^{-1})

m = mass of catalyst sample used (g)

S = specific BET area (m^2g^{-1})

Milt et al (58) only applied the equation to calculate reaction rates from conversions of less than 10%. Equation 3.1 was applied to methane results as less variation was observed in the T_{10} values between run 1 and run 2. Results are shown in Table 3.9 and Fig 3.20. The same equation was applied to propane conversion (Table 3.10) since all oxides were tested for propane oxidation. In the latter the equation was extended to conversions between 10 and 50%.

Sample	**r (μmol $min^{-1}m^{-2}$) at**		
	425°C	**500°C**	**550°C**
ZrCe50-sg	0.020 (2)	0.170 (17)	0.456 (45)
ZrCe50-cp-1	0.058 (1.3)	0.133 (3)	0.496 (11)

Table 3.9 : Activities per unit surface area for methane combustion where r represents the reaction rate calculated at different temperatures. The numbers in paranthesis represent the % conversions at those temperatures.

As observed for propane the ZrCe50-sg was significantly more active than ZrCe50-cp for methane combustion, with a T_{10} and T_{50} of 476°C and 556°C for the former. In contrast the latter only reached 10% conversion at 546 and didn't reach 50% conversion within the temperature range used. When the surface area is taken into account as

shown in Table 3.9, ZrCe50-cp-1 is more intrinsically active at 425°C, when conversions are less then 10%. Hence, the low activity of ZrCe50-cp-1 is mainly due to its low surface area.

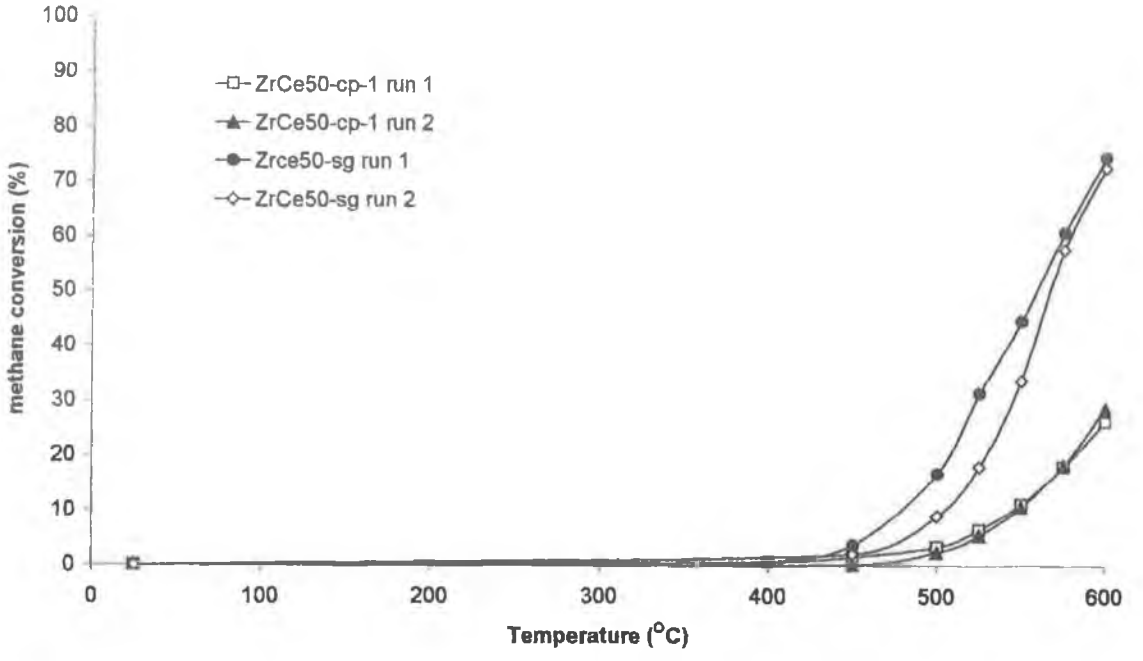

Fig 3.20 : Conversion of methane versus temperature for ZrCe50 prepared by sol-gel and co-precipitation.

Equation 3.1 was also used to calculate reaction rates per surface area for propane combustion, the results of which are shown in Table 3.10. Table 3.10 shows that for sol-gel samples, ZrCe50-sg is more active than ZrCe10-sg at all temperatures except 500°C when activity is expressed per unit surface area. At 300 and 400°C where percentage conversions are below 50%, ZrCe50-sg has higher reaction rate than ZrCe70-sg, indicating that the higher surface area is not the reason for the lower T_{50} of the former. At high conversions, no significant differences were observed. The reaction rates of ZrCe100-cp-1 per unit surface area were the highest of all the oxides at all selected temperatures. Of the mixed oxides prepared by co-precipitation, ZrCe70-cp-1 showed a comparable activity to the sol-gel sample indicating that the high light-off temperature is related to the low surface area of the sample.

Sample	r (μmol $min^{-1}m^{-2}$) at						
	200°C	225°C	300°C	350°C	400°C	425°C	500°C
ZrCe10-sg	0 (0)	0 (0)	0.013 (4)	0.026 (8)	0.071 (22)	0.093 (29)	0.299(100)
ZrCe50-sg	0 (0)	0 (0)	0.038 (14)	0.059 (22)	0.092 (34)	0.149 (55)	0.270(100)
ZrCe70-sg	0.011 (4)	0.014 (6)	0.041 (16)	0.073 (29)	0.235 (93)	0.244 (97)	0.253(100)
ZrCe85-sg	0.004 (5)	0.019 (8)	0.056 (24)	0.141 (59)	0.224 (94)	nd	nd
ZrCe100-cp-1	0.029 (15)	0.034(18)	0.077 (41)	0.096 (51)	0.189(100)	0.189(100)	0.189(100)
ZrCe10-cp-1	0 (0)	0 (0)	(0)	(0)	0.032 (4)	0.075 (9)	0.119 (75)
ZrCe30-cp-1	0.008 (1)	0.011 (2)	0.021 (4)	0.037 (7)	0.059 (11)	0.101 (19)	0.146 (70)
ZrCe50-cp-1	0 (0)	0 (0)	0.024 (2)	0.048 (4)	0.059 (5)	0.111 (9)	0.167 (46)
ZrCe70-cp-1	0.028 (2)	0.028 (2)	0.051 (3)	0.136 (8)	0.187 (11)	0.268 (16)	0.340 (79)

Table 3.10: Activities per unit surface area for propane combustion where r represents the reaction rate calculated at different temperatures. The numbers in paranthesis represent the % conversions at those temperatures.

3.3.5 Effect of aging on activity, surface areas and structure

The fresh samples were then placed in a static air muffle furnace and heated at 800°C for 8 hours. As shown in Fig 3.21, a decrease in surface areas of all oxides is observed on aging, the degree of which depends on the composition and preparation method. On aging, ceria loses 90% of its initial surface area. This poor thermal stability has been reported in the literature and attributed to an increase in crystallite growth at high temperature. The mixed oxides prepared by the sol-gel method are the most thermally stable with losses in surface area of 36%, 26% and 22% for ZrCr50-sg, ZrCe70-sg and ZrCe85-sg respectively. Losses of 70, 57, and 68% were recorded for ZrCe50-cp-1, ZrCe70-cp-1 and ZrCe85-cp respectively. These are also less than ceria, indicating that incorporation of zirconia stabilizes the surface area and minimizes sintering. The stabilization of the surface area of ceria by the incorporation of zirconia has been reported in which the authors concluded that incorporation of zirconia retards crystal growth which is responsible for sintering and the decrease in particle size (59). However in contrast to the above results, they found that the $Ce_{0.80}Zr_{0.20}O_2$ was the least thermally stable in terms of surface area. However their experiments were carried out at a calcination temperature of 950°C in a flowing air stream of argon, oxygen and carbon dioxide.

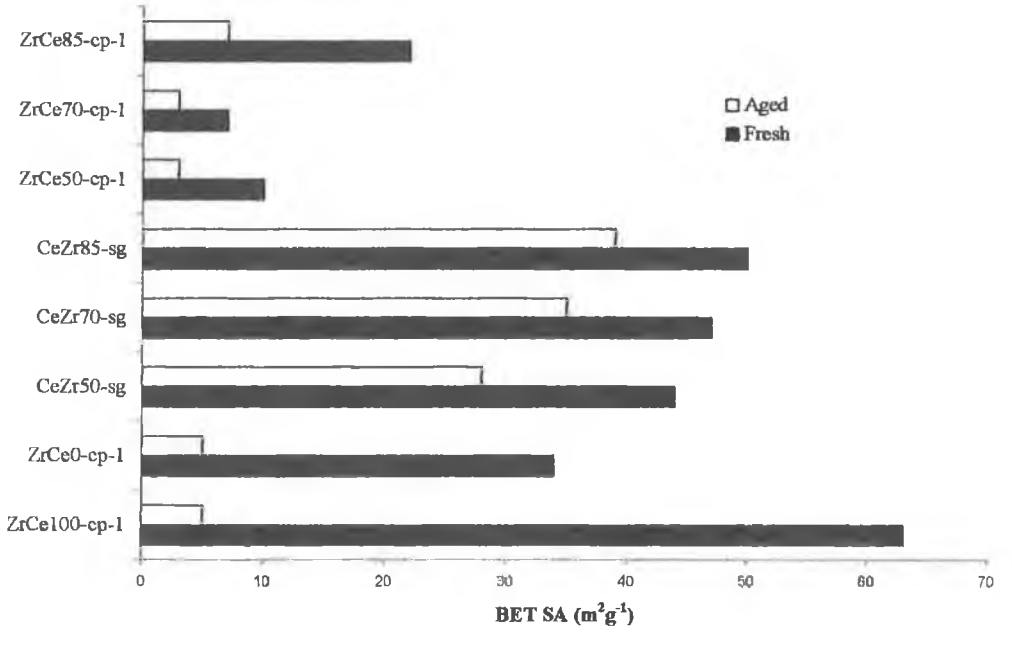

Fig 3.21: Effect of aging on the specific surface areas of fresh (calcined) samples.

The XRD results of selected samples after aging are summarized in Table 3.11 and illustrated in Fig 3.22 (sol-gel samples) and Fig 3.23 (co-precipitation samples). For the mixed oxide samples prepared by both methods, there are no significant changes in structure data on aging, indicating that the mixed oxide retains its structure up till 800°C. A definite but small shift in the 2-Theta angle towards higher values was observed on going from ZrCe50-sg to higher cerium contents, indicating formation of a cubic phase. For ZrCe70-sg, the peak with a d_{hkl} of 3.09Å is removed on aging (see Tables 3.6 and 3.11), while no change was observed for ZrCe85-sg. For ZrCe50-cp, the peaks have a greater intensity but no significant differences were observed.

Sample	**Main Peaks (2θ)**	**Main Peaks-d_{hkl}**	**Relative Intensity (%)**
ZrCe0-cp-1-ag	27.60, 30.85, 49.50, 33.65, 34.7, 29.45	3.23, 2.90, 1.85, 2.66, 2.58, 3.03	100, 75, 47, 33, 28, 19
ZrCe50-cp-1-ag	29.50, 29.30, 28.85, 28.55,28.2,30-33.5,48-49, 58-60.	3.03, 3.05, 3.09, 3.13, 3.17,2.68-2.60, 1.91-1.81, 1.59-1.55	100, 94, 85, 79, 72, 60 -66, 60-70, 58-63.
ZrCe50-sg -ag	29.35, 29.00, 28.65, 49.25, 48.85, 47.9 56.60, 58.8, 59.70	3.04, 3.08, 3.12 1.85, 1.86, 1.90, 1.63, 1.57, 1.55	100, 92, 70 50, 42, 41, 33, 40, 28
ZrCe70-sg-ag	28.55, 47.65, 56.50, 33.40	3.13, 1.91, 1.63 2.68	100, 53, 41, 35
ZrCe85-sg-ag	28.65, 47.70, 56.50 33.25	3.12, 1.91, 1.63, 2.69	100, 53, 46, 35

Table 3.11: XRD data for aged samples prepared by co-precipitation and sol-gel techniques. The main peaks are represented in 2θ and d_{hkl}, the interplanar spacing corresponding to each peak. Relative intensity is the relative intensity of that peak compared to the most intense peak in the diffraction pattern and * refers to a group of peaks of low intensity.

This is all in contrast to pure ZrO_2 prepared by co-precipitation, which is completely transformed to the monoclinic phase on heating to 800°C. This is in agreement with Mercera et al (29) who observed that increasing the temperature increased the degree of transformation to the monoclinic phase and decreased the surface area and total pore volume. The decrease in surface area to 5 m^2g^{-1} hence can be attributed to crystallite growth and accompanying phase transformation.

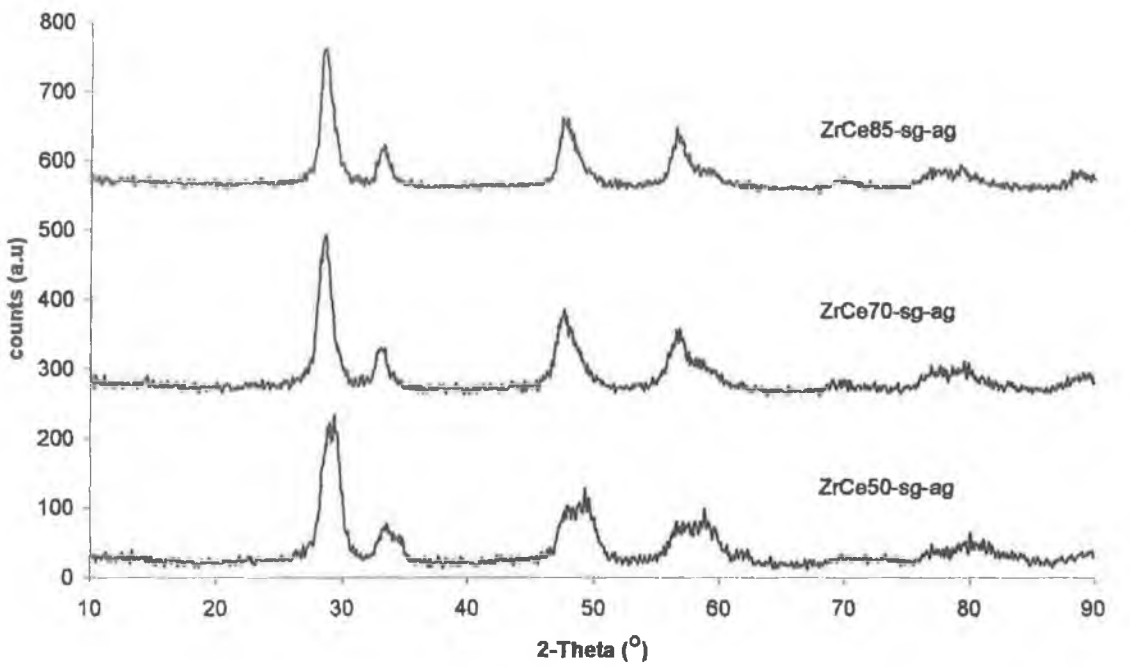

Fig 3.20: XRD pattern of aged samples prepared by sol-gel.

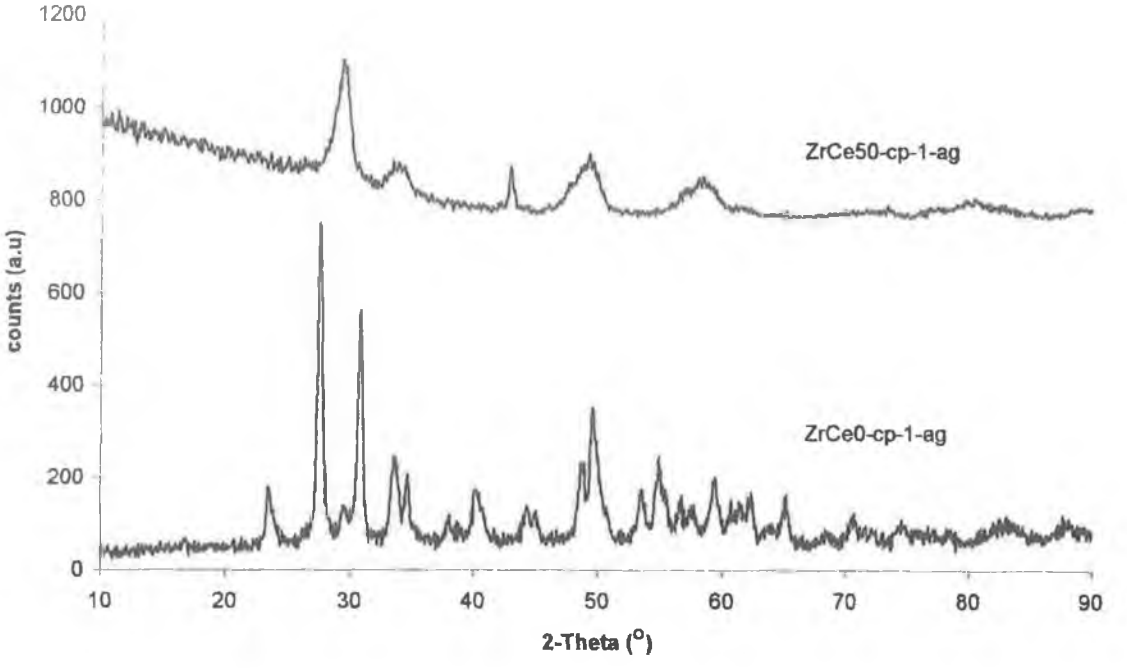

Fig 3.21: XRD pattern of selected aged samples prepared by co-precipitation.

The activities of the selected aged samples are summarized in Table 3.12. The largest decrease in activity was observed for ceria, with an increase of 120°C in T_{50}. The mixed oxides showed a smaller loss in activity with increases of 10, 20 and 60°C in T_{50} values for ZrCe50-sg, ZrCe70-sg and ZrCe85-sg. It appears that the incorporation of zirconium into the ceria lattice stabilizes the activity compared to ceria. This is most likely due to the beneficial effects on the surface area already noted.

sample	**T_{10} (°C)**		**T_{50} (°C)**	
	Run 1	**Run 2**	**Run 1**	**Run 2**
ZrCe0-cp-1-ag	353	nd	>>500	nd
ZrCe50-sg-ag	178	241	433	425
ZrCe70-sg-ag	200	345	389	416
ZrCe85-sg-ag	274	293	405	404
ZrCe100-cp-ag	183	334	457	468

Table 3.12: Activities of aged catalyst samples where T_{10} and T_{50} represent temperatures at which 10 and 50% conversion of propane was reached. Samples were initially tested (run 1) and then cooled to room temperature and retested (run 2).

3.4 Conclusions

The preparation method used has a very important effect on the surface area and catalytic activity of the mixed oxides. SIP-MS indicated the presence of hydroxides in the uncalcined co-precipitated samples while in ZrCe50-cp-1 and ZrCe100-cp-1, both hydroxides and unreacted nitrates were observed. The mixed oxide sol-gel sample (ZrCe50-sg) evolved both hydroxide and nitrate species during heating, as expected from the preparation method. In the TG-SDTA, a glow phenomenon i.e. exothermic reaction where the oxide emits light was observed for pure zirconia, indicated by an exothermic peak at 433°C. This peak was absent for ZrCe50-cp-1, although an unsteady baseline made it difficult to conclude this definitively. The effect could be attributed to masking of the peak by decomposition of nitrate species, increase in the temperature of crystallization to above 600°C or to the fact that oxide was crystalline before calcinations. The mixed oxides prepared by the sol-gel method had higher surface areas and catalytic activity for the oxidation of propane than corresponding samples prepared by a co-precipitation method. In general, the best activity was observed for the ceria-zirconia-mixed oxides prepared by the sol-gel method, which reached 50% conversion in the range 340-434°C. Good activity within the sol-gel samples was correlated with structure rather than surface area, with samples containing the cubic phase being the most active. This phase was found for cerium contents $\geq$ 70%. In comparison, the samples prepared by co-precipitation had T_{50} values in the range 434-490°C. The low surface areas were attributed to the pH and concentrations of the precursor solution used. For both methods, zirconia was the least active while a high surface area ceria sample prepared by co-precipitation was the most active with a T_{50} of 342°C. A correlation was observed between reducibility and catalytic activity, with lower temperatures of reduction for more active samples.

Although pure ceria had the highest surface area initially, it was the least thermally stable. Aging studies at 800°C for 8hrs showed that the incorporation of zirconia stabilizes the surface area of ceria on aging. On aging, the surface area of ceria dropped by 91% while the ZrCe50-sg, ZrCe70-sg and ZrCe85-sg lost 36%, 26% and 22% of their surface areas respectively. The light-off temperatures (T_{50}) of ZrCe50-sg, ZrCe70-sg, ZrCe85-sg and ZrCe100-cp increased by approx. 12, 19, 65 and 120°C respectively for run 1 on aging. This indicates that the ZrCe50-sg and ZrCe70-sg are the most stable

in terms of catalytic activity while ZrCe85-sg and ZrCe100-cp are the least stable. On aging no significant changes were observed in the structures of the mixed oxide, while zirconia was transformed from the tetragonal to the monoclinic. The dramatic structural change was the reason for a severe loss in surface area on aging. A more exhaustive study would have been more conclusive e.g. not all samples were studied by TPR due to the focus on manganese work in this study.

References

(1) Fornasiero, P., Balducci, G., Di Monte, R., Kaspar, J., Sergo,V., Gubitosa, G., Ferrero, A., Graziani, M., *J. Catal.* **164**, 173 (1996).

(2) Vidal, H., Kaspar, J., Pijolat, M., Colon, G., Bernal, S., Cordon, A., Perrichon,V., Fally, F., *Appl. Catal., B.* **27,** 49 (2000).

(3) Yao, H. C.,Yu-Yao, F., *J. Catal.* **86,** 254 (1984)

(4) Zamar, F., Trovarelli, A., De Leitenburg, C., Dolcetti, G., *J. Chem. Soc., Chem. Commun.* 965 (1995).

(5) Terribile, D., Trovarelli, A., De Leitenburg, C., Primavera, A., Dolcetti, G., *Catal. Today* **47,** 133 (1999).

(6) Palmqvist, A. E. C., Johanssom, E. M., Jaras, S. G., *Catal. Letts.* **56,** 69 (1998).

(7) Gonzalez-Valasco, J. R., Guittierrez-Ortiz, M. A., Marc, J. L., Botas, J. A., Gonzalez-Marcos, P., Blanchard, G., *App. Catal., B* **22**, 167 (1999).

(8) Pengpanich, S., Meeyoo,V., Rirksomboon, T., Bunyakiat, K., *App. Catal., A* **234,** 221 (2002).

(9) Thammachart, M., V. Meeyoo, V., Rirksomboon, T., Osuwan, S., *Catal. Today* **68,** 53 (2001).

(10) Bozo, C., Gilhaume, N., Garbowski, E., Primet, M., *Catal. Today* **59**, 33 (2000).

(11) Rossignol, S., Madier, Y., Duprez, D., *Catal Today* **50,** 261 (1999).

(12) Schawrz, J. A, Consteau, C., Consteau, A., *Chem. Rev.*, **95,** 477 (1995).

(13) Miller, J. B., *Catal. Today* **35,** 269 (1997).

(14) Kirszenstztejn, P., Szymkowial, A., Marciniak, P., Martyla, A., Przekop, R., *App. Catal., A* **245,** 159 (2003).

(15) Chuah, G. K., Liu, S. H., Jaenicke, S., Li, J., *Microporous. Mesoporous Mater,* **39,** 381 (2000).

(16) Fernandez-Lopez, E., Sanchez-Escribiano, S., Resini, C., Gallardo-Amores, J. M., Busca, G., *Solid State Ionics* **4,** 951 (2002).

(17) Perego, C., Villa, P., *Catal. Today* **34,** 281 (1997).

(18) Rossignol, S., Gerard, E., Duprez, D., *J. Mater. Chem.* **9,** 1615 (1999).

(19) Bruce, L. A., Hoang, M., Hughes, A. E., Turney, T. W., *Appl. Catal., A* **134,** 351 (1996).

(20) Tichit, D., El Alami, D., Figueras, F., *Appl. Catal., A* **145,** 195 (1996).

(21) Chuah, G. K., *Catal. Today* **49,** 131 (1999).

(22) Chen, S-G., Yin, Y-S., Dao-Ping Wang, D. P., *J. Mol. Struct.*, **690,** 181, (2004).

(23) Choudhary, V. R., Uphade, B. S., Pataskar, S. G., *Appl. Catal., A* **227**, 29 (2002).

(24) Imamura, S., Shono, M., Okamoto, N., Hamada, A., Ishida, S., *Appl. Catal., A* **142**, 279 (1996).

(25) Boyero Macstre, J., Fernandez Lopez, E., Gallardo-Amores, J. M., Ruano Casero, R., Sanchez Escribano, V., Perez Bernal, E., *International Journal of Inorganic Materials*, **3,** 889 (2001).

(26) Srinivasan , R., Harris, M. B., Simpson, S. F., De Angleis, R., Davis, B. H., *J. Mater. Res.* **3,** 787 (1988).

(27) Calafat, A., in "*Preparation of Catalysts VII*", (Delmon, B., Jacobs, P. A., Maggi, R., Martens, J. A., Grange, P., Poncelet, G., eds). Studies in Surface Science and Catalysis, Vol.118 , 837-843, Elsevier, New York, 1998.

(28) Chuah, G. K., Jaenicke, S., Cheong, S. A., Chan, K. S., *Appl. Catal., A* **142**, 279 (1996)

(29) Mercera, P. D. L., Van Ommen, J. G., Doesburg, E. B. M., Burgsaaf, A. J., Ross, J. R. H., *App. Catal.* **57,** 127 (1990).

(30) Livage, J., Doi, K., Mazieres, C., *J. Am. Chem. Soc.* **51**, 349 (1967).

(31) Keshavaraja, A., Jacob, N. E., Ramaswamy, A. V., *Thermochim. Acta* **254,** 267 (1995).

(32) Kakihana, M.,Kato, S., Yashima, M., Yoshimura, M., *J. Alloys. Compd.* **280,** 125 (1998).

(33) Castro, L., Reyes, P., De Correa, C. M., *J. Sol-gel. Sci. Tech.* **25,** 159 (2002).

(34) Dongare, M. K., Dongare, A. V., Tare, V. B., Kemnitz, E., *Solid State Ionics* **152,** 455 (2002).

(35) Štefanić, G., gržeta, B., Musić, S., *Materials Chemistry and Physics* **65,** 216 (2000).

(36) Srinivasan, R., Keogh. R. A., Milburn, D. R., Davis, B. H., *J. Catal.* **153,** 123 (1995).

(37) Mamott, G. T., Barnes, P., Tarling, S. E., Jones, S. J., Norman, C. J., *J. Mater. Sci.* **26,** 4054 (1991).

(38) Srinivasan, R., Davis, B. H., Cavin, O. B., Hubbard, C. R., *J. Am. Ceram. Soc.* **75,** 1217 (1992).

(39) Sayi, Y. S, Yadav, C. S, Shankaran, P. S, Chhapru, G. C, Rhamakumar, K. L, Venugopal, V., *International Journal of Mass Spectrometry* **214,** 375 (2002).

(40) Vlaic, G., Di Monte, R., Fornasiero, P., Fonda, E., Kaspar, J., Graziani, M., *J. Catal.* **182,** 378 (1999).

(41) Garvie, R. C., *J. Phys. Chem.* 1238 (1964).

(42) Bhaskar, T., Reddy, K. R., Kumar, C. P., Murthy, M. R. V. S., Chary, K. V. R., *Appl. Catal., A* **211,** 189 (2001).

(43) Gentry, S. J., Hurst, N. W., Jones, A., *J. Chem. Soc., Faraday Trans.* **75**, 1688 (1979).

(44) Tiernan, M. J., Barnes, P. A., Parkes, G. M. B., *J. Phys. Chem. B* **105**, 220 (2001).

(45) Fornasiero, P., Balducci, G., Kaspar, J., Meriani, M., Di Monte, R., Graziani, M., *Catal. Today* **29,** 47 (1996).

(46) Daturi, M., Finnocchio, E., Binet, C., Lavalley, J., Fally, F., Perrichon, V., Vidal, H., Hickey, N., Kaspar, J., *J. Phys. Chem. B* **104,** 9186 (2000).

(47) Johnson, M. F .L., Mooi, J., *J. Catal.* **103,** 502, (1987).

(48) Shyu, J. Z., Weber, W. H., Ghandhi, H. S., *J. Phys. Chem.* **92,** 4964 (1988).

(49) Tiernan, M. J., Finlayson, O. E., *Appl. Catal., B* **19,** 23 (1998).

(50) Bernal, S., Calvino, J. J., Cifredo, G., Gatica, J. M., Perez Omil, J. A., Pintado, J. M., *J. Chem. Soc., Faraday Trans.* **89,** 3499 (1993).

(51) Luo, M.. Zheng, X. M., *Appl. Catal., A* **189**, 15 (1999).

(52) Zwinkels, M. F., Jaräs, S. G., Menon, P. G., *Catal. Rev. Sci. Eng.* **35,** 319 (1993).

(53) Burch, R., Crittle, D. J., Hayes, M. J., *Catal. Today* **47,** 229 (1999).

(54) Thomas, J. M., Thomas, W. J " *Principles and practice of heterogeneous catalysis*" Weinheim; New York : VCH, 1997

(55) Arnone, S., Bagnasco, G., Busca, G., Lisi, L., Russo, G., Turco, M., in "*Natural Gas Conversions V*" (Parmaliana, A., Sanfilippo, D., Frusteri, F., Vaccari,A., Arena, F., eds.), Studies in Surface Science and Catalysis, Vol.119, 65-70, Elsevier, Amsterdam, 1998.

(56) Bond, G.C., "*Heterogeneous Catalysis: Principles and Applications*", Clarendon Press, Oxford, 1987.

(57) Finnocchio, E., Daturi, M., Binet, C., Lavalley, J. C., Fally, F., Perrichon, V., Vidal. H., Kaspar. J., Graziani. M., Blanchard. G., in "*Science and Technology in Catalysis 1998*" Studies in Surface Science and Catalysis, vol 121, 257-262, Tokyo : Kodansha; Amsterdam; New York; Elsevier, 1999.

(58) Milt, V. G., Lombardo, E. A., Ulla. M. A., *Appl. Catal., B*, **37**, 63 (2002).

(59) Colon, G, Valdivieso, F., Pijolat, M., Baker, R. T., Calvino, J. J., Bernal, S., *Catal. Today* **50**, 271 (1999).

Chapter 4:

Preparation and Investigation of Manganese-Zirconia Mixed Oxide Combustion Catalysts.

4.1 Introduction

In Chapter 3, the activity of ceria-zirconia mixed oxides for the combustion of methane and propane was reported. In the case of samples prepared by the sol-gel method, the incorporation of zirconia into ceria improved the thermal stability after high temperature aging. Despite a lower surface area, a mixed oxide containing 85 mol% of cerium reached 50% conversion of propane at the same temperature as that observed for a high surface area ceria sample. A correlation between reducibility and oxidation activity was indicated, whereby the more active the sample (in terms of temperatures of 50% conversion of the reactant gas) the lower the temperature corresponding to maximum reduction. While the co-precipitation method yielded low surface area samples in comparison to sol-gel, however, it was observed that variations in the preparation conditions used in the precipitation technique had an effect on the surface area of the oxides.

Of the single metal oxides studied, high activity has been reported for Co_3O_4, MnO_2, Cr_2O_3, CuO and NiO (**1,2**). Furthermore, Moro-oka et al (**3**) reported the following series in order of decreasing activity for the oxidation of propane at 300°C

$Pt > Co_3O_4 > Cr_2O_3 > Pd > MnO_2 > CuO > NiO > Fe_2O_3 > CeO_2 > ThO_2$

Hence manganese oxides were more active than cerium oxide. Bulk manganese oxides were found to be active catalysts for the combustion of propane (4,5,6) and CO (1), while co-precipitated manganese - aluminium mixed oxides have also been investigated for propane oxidation (5). It has been suggested that manganese is capable of oxidising methane in the absence of gas phase oxygen and hence acting as an oxygen storage component (7). Chang and McCarty then concluded that manganese oxides have a larger oxygen storage capacity and faster oxygen absorption rates than ceria supported on alumina (8). High oxidation activity requires multi-valent metal ions that can participate in reduction-oxidation reactions (9).

However relatively little work has been done on the oxidation activities of manganese-zirconia mixed oxides. Kesharvaraja et al reported the stabilization of the cubic phase of zirconia by partly substituting Zr^{4+} with Mn^{4+} ions (10,11).

The same group found that manganese-stabilised zirconia was active for the combustion of butane (12). Choudhary et al (13) found that when 20 wt % of transition metals Mn, Co, Fe, Ni, Cu or Cr were incorporated into ZrO_2 bulk structure, Mn-stabilized ZrO_2 showed the highest activity for the combustion of methane. For propane oxidation (14), Co-stabilised zirconia was more active than Mn-stabilised, which however still showed high activity. The same author (15) investigated the combustion of methane over a range of manganese-zirconia concentrations up to Mn/Zr mole ratio of 1 and concluded that the good activity of the mixed oxides was due to the presence of the cubic structure and more reactive lattice oxygen.

In this chapter, the Mn-Zr mixed oxide system is further investigated in terms of surface area and structural properties and also redox characteristics and combustion activity. Previously the co-precipitation method has been used to prepare high surface area sulphated manganese-iron-zirconia mixed oxides (16). This method was used to prepare the manganese-zirconia mixed oxides despite the low surface areas reported in the previous chapter. The effect of changing various experimental parameters and manganese-zirconium ratios on the surface area and structural properties of the mixed oxides was investigated using N_2 adsorption at 77K, TG-SDTA, SIP-MS and XRD. Redox characteristics of selected samples were explored using TPR-MS and the oxidation activity of selected samples for methane and propane combustion was evaluated in order to further explore the link between reducibility and activity indicated in the previous chapter. Finally the effect of high temperature aging at 800°C on various structural and oxidation characteristics was determined.

4.2 Experimental

4.2.1 Catalyst Preparation

The basic procedure used to prepare Mn-Zr mixed oxides with 10, 30, 50, 70 and 85 mol % manganese involved the following:

Appropriate amounts of manganese nitrate tetra-hydrate and zirconyl chloride octahydrate were dissolved in 25 mls of water. 10 mls of ammonium hydroxide (35%) was added dropwise with stirring to precipitate the oxide and the mixture was left overnight without stirring. The precipitate was then filtered and washed with distilled water until the washings were clear of chloride (tested with silver nitrate). The filtrate was then dried overnight at 45°C and 110°C (approx 12-24 hours at each temperature). Finally, the dried powder was calcined in a static air furnace at 600°C for 6 hours, to form the oxide. In general, the synthesis was based on using approx 10 g of zirconyl chloride octahydrate and calculating the corresponding amount of manganese nitrate tetra-hydrate needed to achieve a specified mol % of Mn. The samples prepared by the above method are denoted by the sample ID of the form ZrMnX-cp where X is the calculated mol % Mn and cp denotes that the co-precipitation method was used. Any other samples prepared with a variation in the above preparation method (i.e. precursor concentration, stirring time prior to addition of base or volume of ammonia added) are indicated by the code ZrMnX-cp-y. The preparation conditions used in the preparation of Mn-Zr mixed oxides with various % Mn are summarised in Table 4.1. The term y in the sample ID can be either:

(i) a or b representing a stirring time of 20 or 60 minutes prior to addition of base respectively.
(ii) 1 referring where the concentration precursor concentration is decreased by two-fold using approx 5 g of Zr precursor and 10 ml of ammonium hydroxide.
(iii) 2 where the concentration of precursor was based on approx 10g of zirconium precursor with 40 ml of ammonium hydroxide.

Sample	Stirring time (mins)	Wt (g) $ZrOCl_2.8H_2O$	$Mn(NO_3)_3.4H_2O$	Vol NH_4OH (ml)*	SA ^ (m^2g^{-1})
ZrMn0-cp	0	10.00	0	10	34 ±1
ZrMn0-cp-a	0	10.00	0	10	51 ± 3
ZrMn10-cp	0	10.00	0.89	10	42 ± 1
ZrMn10-cp-a	20	10.00	0.89	10	71 ± 4
ZrMn10-cp-b	60	10.00	0.89	10	113 ± 1
ZrMn30	0	10.00	3.35	10	77 ± 6
ZrMn30-cp-a	20	10.00	3.35	10	109 ± 4
ZrMn30-cp-b	60	10.00	3.35	10	121 ± 1
ZrMn50-cp	0	10.00	7.81	10	115 ± 11
ZrMn50-cp-a	20	10.00	7.81	10	128 ± 9
ZrMn50-cp-b	60	10.00	7.81	10	152 ± 4
ZrMn70-cp	0	10.00	18.14	10	56 ± 1
ZrMn70-cp-1	0	5.50	10.01	10	110 ± 8
ZrMn70-cp-2	0	10.00	18.14	40	88 ± 1
ZrMn85-cp	0	10.00	44.15	10	60 ± 2
ZrMn85-cp-1	0	1.43	10.00	10	60 ± 0
ZrMn100-cp	0	0	10.00	10	10 ± 2

Table 4.1: Preparation conditions and surface area for Mn-Zr mixed oxides with various mol % of Mn. ^ For surface areas determined by the BET method (SA), the values shown are the mean of two measurements of the same sample and the standard deviation between those two separate measurements. For example for ZrMn30-cp, two BET values of 81 and 72 m^2g^{-1} were obtained, yielding a mean value of 77 m^2g^{-1} and a error between those values of 6 m^2g^{-1}. * Ammonium hydroxide used

The aforementioned procedure is referred to herein as the "unoptimised procedure". The 50 mol% Mn system was selected to investigate in detail the effect of preparation method on the resultant surface areas and oxidation activity of the oxides. Table 4.2 summarises the range of preparation method conditions altered i.e. amount of ammonia solution used to precipitate the oxide, the effect of mixing volume (beaker size), rate of addition of the ammonia solution and the mixing time of the zirconyl chloride octahydrate and manganese nitrate tetra-hydrate prior to ammonia addition. The surface areas of the resulting catalysts are given in Table 4.2.

For comparison, Platinum/alumina catalysts and Platinum/ZrMn50-cp were also prepared by impregnation of the support material with excess solution of $H_2PtCl_6.6H_2O$ (Johnson Matthey) in ethanol. The appropriate amount of chloroplatinic acid required to achieve platinum contents of 0.5 and 1 wt% was dissolved in 9ml of ethanol in a round bottomed flask. 3g of the support material (Al_2O_3 or ZrMn50-cp) was added to the Pt solution and stirred for 30 minutes. The solvent was then removed by rotary evaporation at 70°C. The sample was then dried at 45°C overnight and calcined at 630°C for 15 minutes in a static air furnace.

The calcined products from co-precipitation, those purchased from Aldrich and noble metal supported catalysts prepared by impregnation are herein referred to as "fresh samples". Fresh samples were then aged at 800°C for 8 hours in static air in a muffle furnace.

4.2.2 Catalyst Characterisation

The activity of the oxides for the combustion of both methane and propane were determined using the procedures outlined in Chapter 2. The phases present were identified using XRD and the surface areas determined using nitrogen adsorption, the procedures of which are detailed in Chapter 2. Uncalcined samples or dried precipitates were analysed with TG-SDTA and SIP-MS, while the redox properties of fresh and aged samples were investigated with TPR-MS. The experimental procedures for all of the thermal analysis techniques used have been detailed previously in Chapter 2

Sample	Wt (g)		Vol H_2O (ml)	Stirring Time Before add (mins)	Precipitation Conditions					Drying Conditions		SA (m^2g^{-1}) ^
	$ZrOCl_2$. $8H_2O$	$Mn(NO_3)_3$. $4H_2O$			Vol NH_4OH * (ml)	Beaker Size (ml)	Rate of Add (ml/min)	Time for NH_4OH Add (mins)	Final pH	Hours @ 45°C	Hours @ 110°C	
ZrMn50-cp"	7.79	10.03	25	0	10	300	1	10	nd	O/n	O/n	115 ± 11
1	7.79	10.03	25	0	10	nd		< 5 sec	nd	O/n	O/n	130 ± 6
2	7.79	10.03	25	0	10	100	0.50	20	9.15	O/n	O/n	138 ± 5
3	7.79	10.03	25	0	10	100	0.16	60	9.01	O/n	O/n	124 ± 4
4	7.79	10.03	25	0	5	300	0.33	15	2.54	O/n	O/n	11
5	7.79	10.03	25	0	20	300	0.33	60	9.43	O/n	O/n	112 ± 6
6	3.22	5.00	12	0	5	100	0.08	60	9.05	1	O/n	122.5 ± 5
7	3.22	5.00	12	0	5	100	0.33	15	nd	1	O/n	119.5 ± 3
8	3.22	5.00	12	0	5	300	0.33	15	nd	1	O/n	111.5 ± 2
9	3.22	5.00	12	0	5	300	0.08	60	nd	1	O/n	111.5 ± 8
10	3.22	5.00	100	0	5	100	0.08	60	nd	1	O/n	156.5 ± 0.7
11	3.22	5.00	100	0	5	100	0.08	60	nd	1	O/n	152 ± 4
12	3.22	5.00	100	0	10	100	0.16	60	nd	1	O/n	163 ± 0.0
13	3.22	5.00	12	20	5	100	0.08	60	nd	1	O/n	128.5 ± 9
14	3.22	5.00	12	60	5	100	0.08	60	nd	1	O/n	153 ± 4
15	7.79	10.03	25	60	10	100	0.16	60	nd	1	O/n	152 ± 4

Table 4.2: Effect of preparation conditions on a 50 mol % Mn sample (ZrMn50-cp), O/n represents overnight and * Ammonium Hydroxide. ^ For surface areas determined by the BET method (SA), the values shown are the mean of two measurements of the same sample and the error between those two separate measurements. For example for sample 1, two BET values of values of 126 and 134 m^2g^{-1} were obtained, resulting in a mean value of 130 m^2g^{-1} and a error between them of 6 m^2g^{-1}. " unoptimised sample.

4.3 Results and Discussion

4.3.1 Effect of preparation conditions on surface areas of fresh samples

From Table 4.2, it was observed that the rate of addition of ammonium hydroxide had no significant effect on the surface area of the final oxides, all other variables remaining equal. Results from samples 1, 2 and 3 show that immediate addition and addition over 20 minutes result in the same surface area values with a slight reduction in surface area with addition over 60 minutes. The quantities used in the preparation of sample 3 were scaled down by a half in the preparation of sample 6 with ammonium hydroxide added at half the rate compared to sample 3. A very similar surface area was obtained confirming that the rate of ammonium hydroxide addition is not significant factor in affecting surface areas of final products. Also confirmed with samples 6 and 7, showing no significant difference in surface area. This is in agreement with studies by Srinivasan et al (17), where it was found that slowly and rapidly precipitated zirconia at pH10.4 had similar surface areas of approx $35m^2g^{-1}$, where precipitation times were 0, 1, 2, 4 and 8 hours.

Okada et al (18) examined the effect of the rate of precipitation in the preparation of 9.4 mol % Al_2O_3–SiO_2 from aluminium nitrate and tetraethylorthosilicate. When ammonia addition to the precursor solution was fast (rapid addition) and slow rate (4 ml/min), surface areas after calcinations at 300°C were 564 and 402 m^2g^{-1} respectively. It is important to note that the rates used by Okado et al (18) were significantly faster than those reported in this thesis but Okado et al (18) concluded that the rate of addition had little effect on the porous properties of gels. Oh et al (19) prepared hydrotalcites (Mg-Al) oxides by the addition of two different precipitating agents, NaOH and urea. Urea and NaOH were chosen since slow and fast precipitation reactions are associated with each respectively and hence the effect of the rate of precipitation on the particle size of the oxides could be determined. The urea method increased particle sizes compared to the NaOH method but in the case of the former, precipitation times of at least 6 hours were employed, far longer than those used in this thesis.

The effect on surface areas of the volume of ammonia added was compared for samples 3, 4 and 5 and the pH curves of pH of the solution against volume of ammonium hydroxide added are shown in Fig 4.1.

In the current study, it was found that a minimum amount of ammonia was required to yield a high surface area product. After 5 ml of ammonium hydroxide addition, a final pH of 2.5 was observed and a very low surface area sample was obtained (see sample 4 in Table 4.2). Increasing ammonium hydroxide addition to 10 ml resulted in a dramatic increase in pH to approx 9 and a large increase in surface area. In comparison, further addition of ammonium hydroxide increased the pH slightly and the curve (trace 3 in Fig 4.1) levelled off to a final pH of 9.43 but this did not result in any increase in surface area. This is in slight contrast to literature results: for the preparation of Mn_2O_3 (20) via the addition of manganese nitrate to 5M sodium hydroxide, it was observed that the larger amount of base used, the higher the specific surface area. Tichit et al (21) also found that on increasing the final pH from 4 to 6, 8 and 10, the surface area of corresponding uncalcined zirconia increased from 19 to 58,150 and 191 m^2g^{-1} respectively. From Table 4.2, an increase in surface area from 11 to 138 m^2g^{-1} was observed on increasing pH from 2.5 to 9 but not with greater additions as the pH did not increase significantly. All traces in Fig 4.1 follow the standard acid/base titration curves of sigmoidal shape.

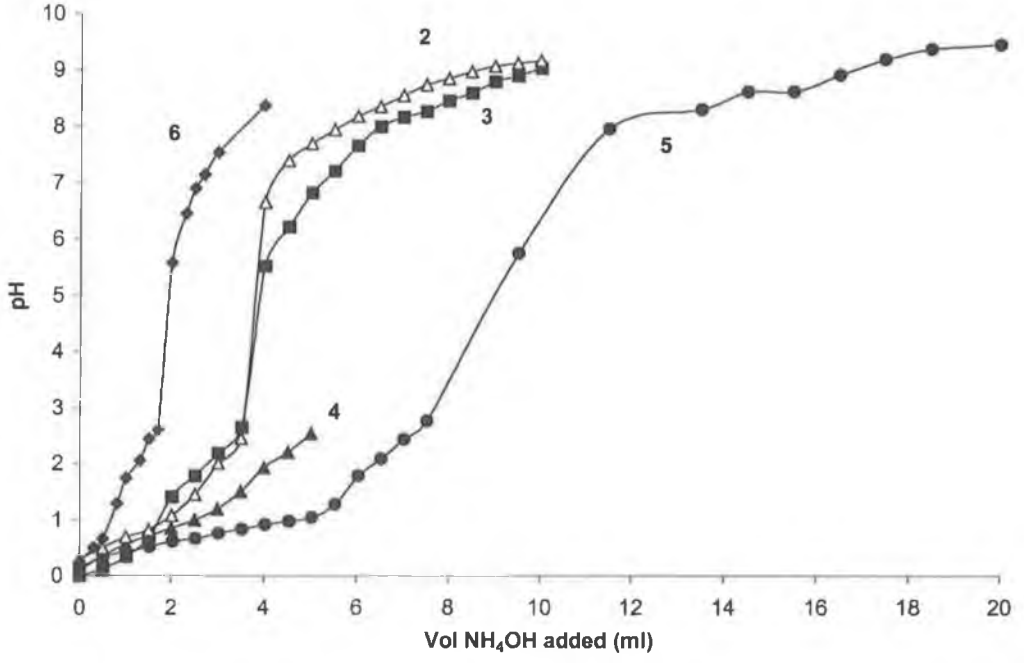

Fig 4.1:pH titration curves of selected samples detailed in Table 4.2, where the number beside each trace refers to the corresponding sample number.

In sample 10, the concentration of the precursor solution was decreased by approx 8 fold by increasing the initial volume of water from 12 to 100 ml. This resulted in a significant increase in surface area from 123 m^2g^{-1} to 156 m^2g^{-1}. (Comparing samples 6 and 10 in Table 4.2). A similar result was observed for Mn_2O_3 prepared from manganese nitrate solutions of different concentrations (20). After calcination at 500°C, surface area increased on decreasing concentration for 0.5M to 0.025M from 27 to 42 m^2g^{-1}. Stichert and Schüth (22) also found that the concentration of a zirconyl chloride octahydrate solution had a significant effect on the crystallite size and hence the specific surface area of zirconia. The authors observed that the more dilute the solution, the smaller the crystallites of one particular phase were. After calcination at 550°C, a decrease in concentration from 0.1M to 0.01M decreased the particle size from 21 nm to 9 nm, with simultaneous increase in surface area from 50 m^2g^{-1} to 110 m^2g^{-1}. However other studies (18) have reported the opposite where surface area of aluminosilicate gels increased and crystallite size decreased on increasing concentration. On increasing the concentration of the precursor solution of aluminium nitrate and tetraethylorothosilicate from 0.2M to 2M, an increase in surface area of the oxides from 468 to 576m^2g^{-1} was observed (18). Another study (23) observed that for the preparation of $ZnGa_2O_4$ from a precursor solution of zinc sulfate and gallium sulfate, an increase in the metal salt concentration from 0.01 M to 1.0 M decreased crystallite size from 28 to 5nm. According to Skoog and West (24), addition of the precipitating agent causes a solution to be momentarily supersaturated. This condition can then be relieved by formation of a precipitate. For freshly precipitated precipitates, the particle size has been reported to be governed by the extent to which nucleation or particle growth predominates over the other. Both mechanisms have previously been described in section 2.2.1. Nucleation increases exponentially with relative supersaturation while particle growth has a linear relationship with this parameter. Hence at high supersaturations the former is the predominant mechanism and a precipitate with a number of small particles are formed, while at low supersaturations, rate of particle growth may be greater and a small number of larger particles are produced. Sample 11 was prepared in exactly the same way as sample 10 and surface areas agreed within experimental errors, showing the preparation method was reproducible. The results of sample 10 and 11 indicate that in a more dilute solution, precipitation of smaller precursor primary particles occurred. This was unexpected in light of the relationship between supersaturation and growth mechanisms put forward by Skoog and West. However, the solution chemistry of zirconium is quite complicated on addition of a base, with the formation of polymer networks via olation

and oxolation mechanisms. It is possible that the precursor concentrations have an effect on the nature of the solution species, which could also have an influence on particle size. A similar effect was also observed for zirconia (22) and manganese oxide (20) and hence a similar phenomenon for manganese-zirconia mixed oxides is possible. Stichert and Schüth (22) also observed that crystallites of zirconia samples prepared at higher concentrations seemed to agglomerate more readily than crystallites prepared at lower concentrations. Agglomerates consist of primary particles joined with aggregates (i.e. collections of primary particles attached to each other). The use of a more diluted solution may have helped to prepare a low-agglomerated high-dispersed precipitate.

In sample 12, addition of 10 ml of ammonium hydroxide instead of 5 ml slightly increased the surface area beyond experimental error. This result is different than that obtained for the samples 3 and 5 prepared in 25 ml of water where addition of the extra ammonium hydroxide slightly decreased the surface area. This could be attributed to the presence of the excess water, which may have affected the pH. In batches 6,13 &14, 15, the effect of stirring time of the mixed precursor solution prior to the addition of the base was observed. Increasing the stirring time to 20 minutes had no effect on surface area (within experimental error) but a significant increase was observed when it was increased to one hour. The scale of preparation did not affect the surface area (see samples 15 and 16). A study by Okado et al (18) also reported that the mixing time of aluminium nitrate (ANN) and tetraethylorthosilicate (TOES) solution prior to the addition of ammonia had an affect on porosity. Mixing times of 1,15, 60, 180, 360 and 1440 minutes increased surface area from 123 to 297, 350, 390 and 390 m^2g^{-1} respectively. No specific reason was suggested by the authors except that mixing state of Si and Al components varied with mixing time. TEM photographs of the Si-Al precipitates formed indicated that while the size of the primary particles were independent of mixing time, the agglomerated structure became more dense with increasing stirring time. In Chapter 3 of this work, it was reported that the homogeneity of the sol-gel techniques resulted in higher surface areas. It is possible that the mixing of the precursor solution for an hour resulted in the formation of a more homogeneous solution where the cationic and anionic species of the two different precursors were distributed evenly within the solution.

Table 4.1 summarises preparation conditions and the surface areas obtained for various mol % of manganese-zirconia oxides prepared by co-precipitation. From Table 4.1, the

mixed oxides have significantly greater surface areas than the pure zirconium or manganese oxide. Using the same preparation conditions, the surface area increased with manganese content up to a maximum of $115 m^2 g^{-1}$ for ZrMn50-cp and then decreased for the higher manganese concentrations. Lopez et al (25) reported maximum specific surface areas for manganese-zirconia systems with manganese contents between 50 and 80 atom %.

The effect of stirring times (20 and 60 mins) was investigated for ZrMn10-cp, ZrMn30-cp and ZrMn50-cp. Samples with codes a and b were stirred for 20 and 60 minutes respectively. Increasing the stirring time before the addition of base increased surface area at each manganese level, the largest increase being observed for ZrMn10-cp. For mixed oxides with mol % >50, some interesting results were observed. For ZrMn70-cp, the surface area of the oxide was increased by (i) either increasing the volume of ammonium hydroxide from 10 to 40 ml or (ii) decreasing the initial amounts of precursor by half while keeping the amount of ammonia added constant at 10 ml. The latter (see sample ZrMn70-cp-1 in Table 4.1) had a much greater affect on surface area with an increase in the surface area of 91%. In comparison, an increase in surface area of 45% was observed with an increase in the volume of ammonium hydroxide (see sample ZrMn70-cp-2 in Table 4.1). For ZrMn85-cp, decreasing the initial precursor amount by approx a quarter didn't have an effect on the surface area. The pH and/or volume of ammonium hydroxide added can significantly alter the surface area obtained, which has been seen previously, but conflicting results were obtained for ZrMn70-cp versus ZrMn85-cp.

4.3.2 XRD Characterisation of fresh samples.

The XRD data for selected samples in Table 4.1 are shown in Fig 4.2 - 4.6 and summarised in Table 4.3. The main XRD peaks and the corresponding interplanar spacings (d_{hkl}) of selected samples are reported in Table 4.3. The XRD of pure zirconia has been already been discussed in Chapter 3 and consists of metastable tetragonal or cubic structure and small amount of monoclinic zirconia. For samples up to 50 mol % of manganese, the XRDs are similar to those reported by Lopez (25,26), with metastable tetragonal zirconia observed for $Mn_{0.5} Zr_{0.5}$, $Mn_{0.2} Zr_{0.8}$, $Mn_{0.1} Zr_{0.9}$ and $Mn_0 Zr_1$ after calcination at 600°C.

Sample	Main Peaks-2θ (°)	Main Peaks-d_{hkl} (Å)	Relative Intensity (%)	Phase
ZrMn0-cp	30.2, 50.3, 28.2, 31.35, 60.15, 35.2	2.96, 3.16, 2.85, 1.81, 1.54, 2.55	100, 43, 32, 50, 28, 25	m and t - ZrO_2
ZrMn10-cp	30.60, 50.90, 60.55, 35.45	2.93, 1.79, 1.53 2.53	100, 39, 28, 25	t and/or c ZrO_2
ZrMn10-cp-a	30.51, 50.93, 50.68, 35.39, 29.65,	2.93, 1.79, 1.80, 2.53, 1.53, 3.01	100, 38, 35, 30, 29,17	t and/or c ZrO_2
ZrMn10-cp-b	30.43, 30.05, 50.87, 35.37, 63.02	2.93, 2.97, 1.79, 2.54, 1.47	100, 76, 54, 38, 21	t and/or c ZrO_2
ZrMn30-cp	30.75, 51.15, 60.9, 35.50	2.91, 1.79, 1.52, 2.53	100, 43, 33, 28	t and/or c ZrO_2
ZrMn30-cp-a	30.68, 30.35,60.74, 33.79, 28.25, 64.67	2.91, 2.94,1.52, 2.65, 3.16,1.43	100, 71, 47, 40, 31, 30	t and/or c ZrO_2
ZrMn30-cp-b	30.34, 31.58, 28.87, 50.25, 48.34, 44.75	2.94, 2.83, 3.09, 1.81,1.88, 2.02	100,83, 74, 67, 58, 56	t and/or c ZrO_2
ZrMn50-cp				Amorphous
ZrMn50-cp-a				Amorphous
ZrMn50-cp-b				Amorphous
ZrMn70-cp	33.00, 30.85, 55.15, 51.4, 38.2, 49.35	2.71, 2.90, 1.66, 1.77, 2.36, 1.85	100, 60, 39, 28, 27, 26	t –ZrO_2 and Mn_2O_3
ZrMn85-cp	33.00, 30.9, 55.15, 29.8, 29.15, 28	2.71, 2.89,1.66, 3.00, 3.07, 3.19	100, 69, 40, 36, 35, 30	t –ZrO_2 and Mn_2O_3
ZrMn100-cp	32.97, 55.22, 23.13, 38.24.	2.71,1.66, 3.84, 2.35	100, 24, 20, 18	Mn_2O_3
Mn_2O_3-Aldrich	33.00, 55.25, 23.2, 38.3	2.71,1.66, 3.83, 2.35	100, 29, 21, 18	Mn_2O_3
Mn_3O_4-Aldrich	36.15, 32.4, 59.9, 28.95	2.49, 2.76, 1.55, 3.08	100, 69, 44, 38	Mn_3O_4

Table 4.3: XRD data for selected mixed oxides and pure oxides where m, t and c represents monoclinic, tetragonal and cubic respectively. The main diffraction peaks are represented in 2θ and d_{hkl} , the interplanar spacing corresponding to each peak. Relative Intensity is the intensity of that peak compared to the most intense peak in diffraction pattern.

In agreement with Lopez et al (25) and Zhao and Shih (20), the pure manganese oxide sample prepared by precipitation consisted of tetragonal α-Mn_2O_3 (bixbyite ICDD file no: 24-508), with the most intense peak observed at $2\theta = 33°$. This phase was also observed for the Mn_2O_3 purchased from Aldrich as expected. This peak was clearly observed in samples, ZrMn70-cp and ZrMn85-cp. For ZrMn50-cp, the broadness of the peak made it difficult to establish clearly the presence of any peaks. ZrMn10-cp and ZrMn30-cp presented as single phase cubic or tetragonal zirconia, although in the latter a very small shoulder at approx 33° could indicate the presence of Mn_2O_3. Table 4.3 shows that addition of Mn to zirconia decreased the lattice parameter slightly, thus indicating some substitution of Zr cations by manganese, taking into account the ionic radii of Zr^{4+}, Mn^{4+} and Mn^{3+}, as 86pm, 67pm and 72 pm respectively (27). A decrease in the d_{hkl} of the most intense [1,1,1] peak of ceria due to the smaller ionic radius of zirconia compared to ceria has also been reported by Vlaic et al (28). The possibility of the formation of cubic zirconia cannot be ruled out since the interplanar spacings observed of 2.93Å and 2.91Å for the most intense peaks are also close to that reported for cubic zirconia of 2.93Å (29). The stabilisation of the tetragonal or cubic phase of zirconia at the expense of the thermodynamically stable monoclinic phase by the addition of transition metal dopants such as Mn has been reported in previous studies (11,25). In contrast, no change in the interplanar spacing of the main peak (d_{hkl} = 2.71Å) corresponding to bixbyite Mn_2O_3 was observed in any of the mixed oxide samples, indicating zirconium doesn't substitute for manganese atoms in the Mn_2O_3 structure. For Mn_3O_4 purchased from Aldrich, two possible forms α-Mn_3O_4 (80-0382) and γ-Mn_3O_4 (18-0803) have been reported ([30]). By comparison with the data reported by Stobbe et al (7), the XRD is that of the former α-Mn_3O_4. While Lopez (25) concluded that the metastable tetragonal polymorph was observed at low manganese contents, other studies (10-15) have reported the presence of cubic zirconia instead. Mercera et al (31) concluded that the XRD patterns of cubic and tetragonal phases are nearly identical, the only difference being the presence of extra peaks of higher order and lower intensity. If the peaks are quite broad, it was nearly impossible to establish if it is metastable cubic or tetragonal phases that are present using XRD alone. Another study also noted that both cubic and tetragonal phase have diffraction patterns at nearly overlapping angles and hence a large peak could be attributed to either (32). Small angular difference between [1,1,1]c and [1,1,1]t diffraction peaks leads to overlap, so analysis must be performed at higher angles, which are usually weak and broad (33). A

peak at 35° was attributed to tetragonal rather than to cubic zirconia in alumina zirconia powders (34).

Ali and Zaki (29) also pointed out the lack of XRD resolution to deal with largely isomorphs (short range structures), makes it difficult to distinguish between t and c zirconia. The strongest peak of t-zirconia and c-zirconia occurs at $2\theta = 30.17°$ (JCPDS # 17-923) and 30.48° (JCPDS # 27-997). The d_{hkl} spacings based on the peak with the strongest diffraction peak are 2.96Å and 2.93Å for cubic and tetragonal respectively. At 600°C, a peak with a d_{hkl} of 2.931Å was observed, indicating t-rich ZrO_2. At 400°C, the interplanar spacing observed of 2.946Å was intermediate between t and c, indicating the formation of t- and /or c-ZrO_2.

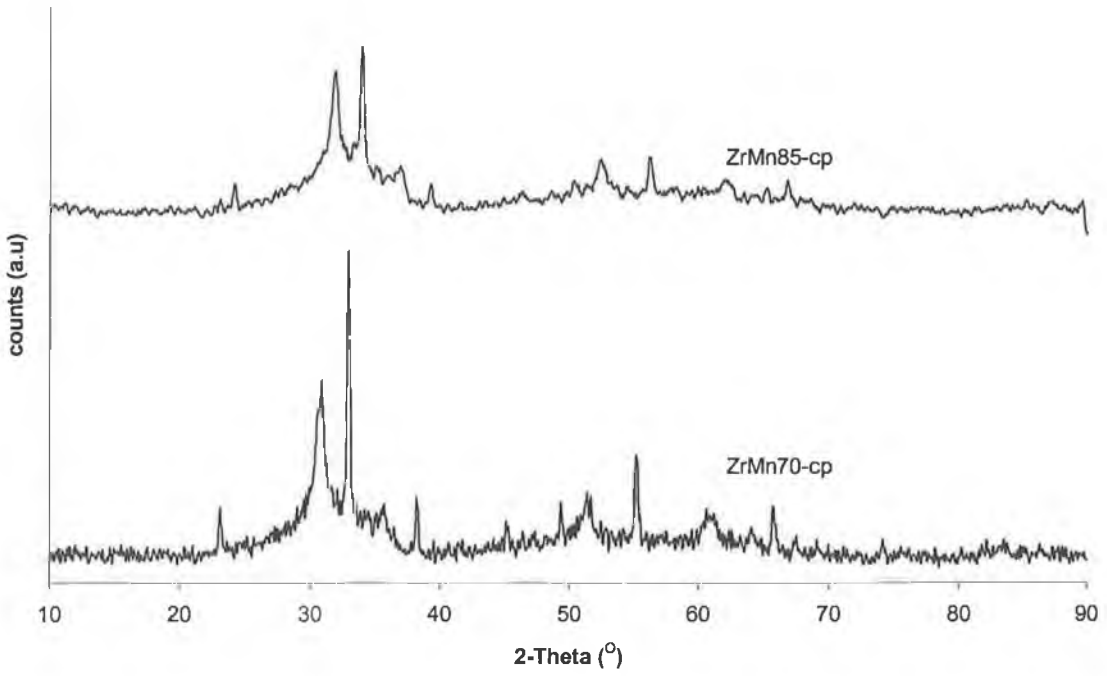

Fig 4.2: XRD data for ZrMn85-cp and ZrMn70-cp.

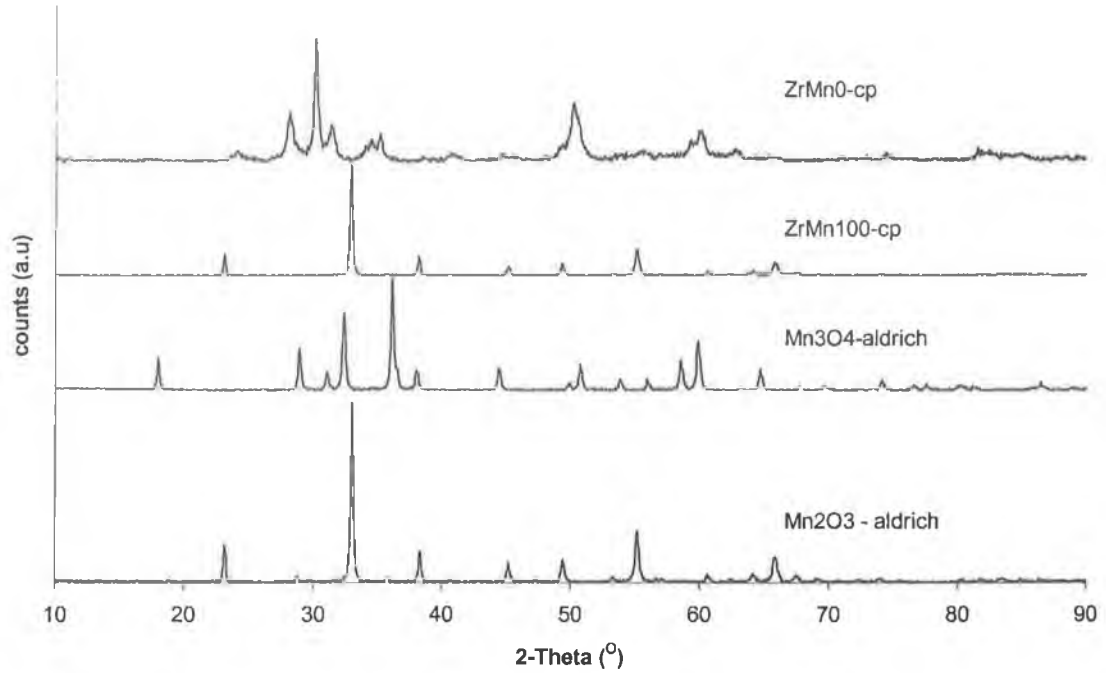

Fig 4.3: XRD data for pure manganese oxides and zirconium oxide.

XRDs were also performed on the samples where the stirring time was varied. As observed from Fig 4.4 – 4.6, the width of the peaks increased as the stirring time increased. This is attributed to the line broadening effect caused by the presence of smaller crystalline particles as indicated by the increasing surface area as described by the following equation proposed by Scherrer

$$L = \frac{K\lambda}{\beta \cos\theta'}$$

where L is the mean dimension of the crystallites comprising the powder, β is the breadth of the diffraction peak on the 2θ scale in radians, and K is a constant (35).

However the peaks appear to be structurally similar with identical interplanar spacings calculated except for MnZr30-cp-b, where multiple peaks were found. This was most likely due to more severe broadening of the peak and not a structural change in the sample.

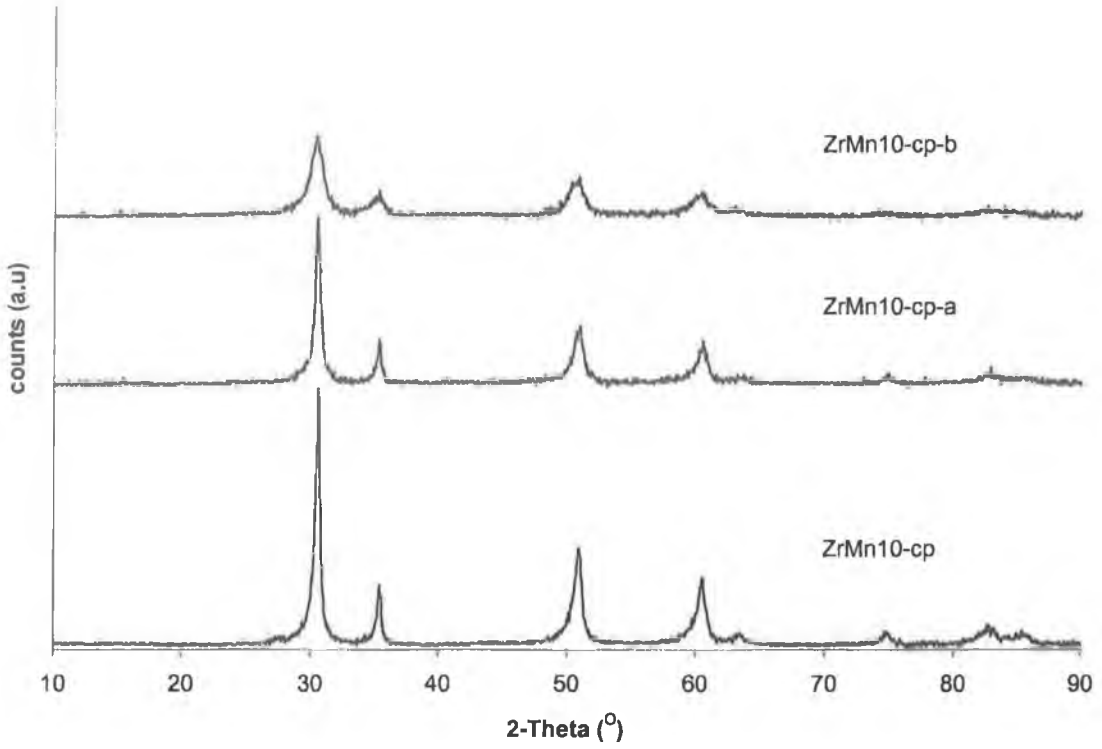

Fig 4.4: XRD data for ZrMn10-cp, ZrMn10-cp-a and ZrMn10-cp-b.

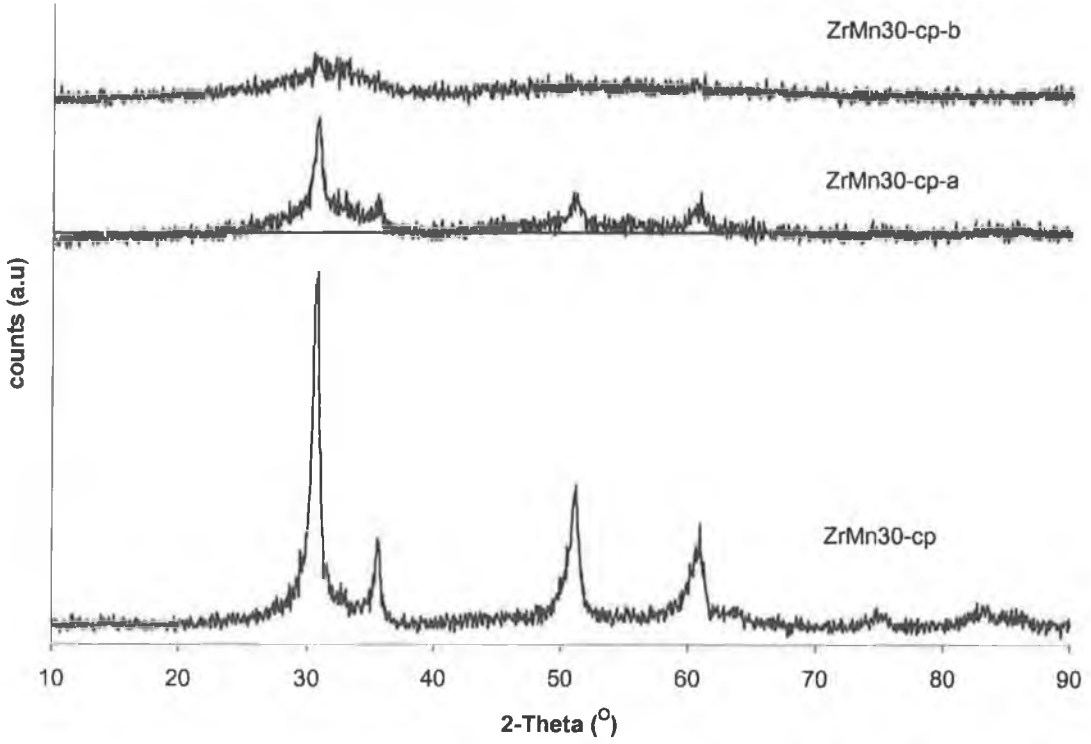

Fig 4.5: XRD data for ZrMn30-cp, ZrMn30-cp-a and ZrMn30-cp-b.

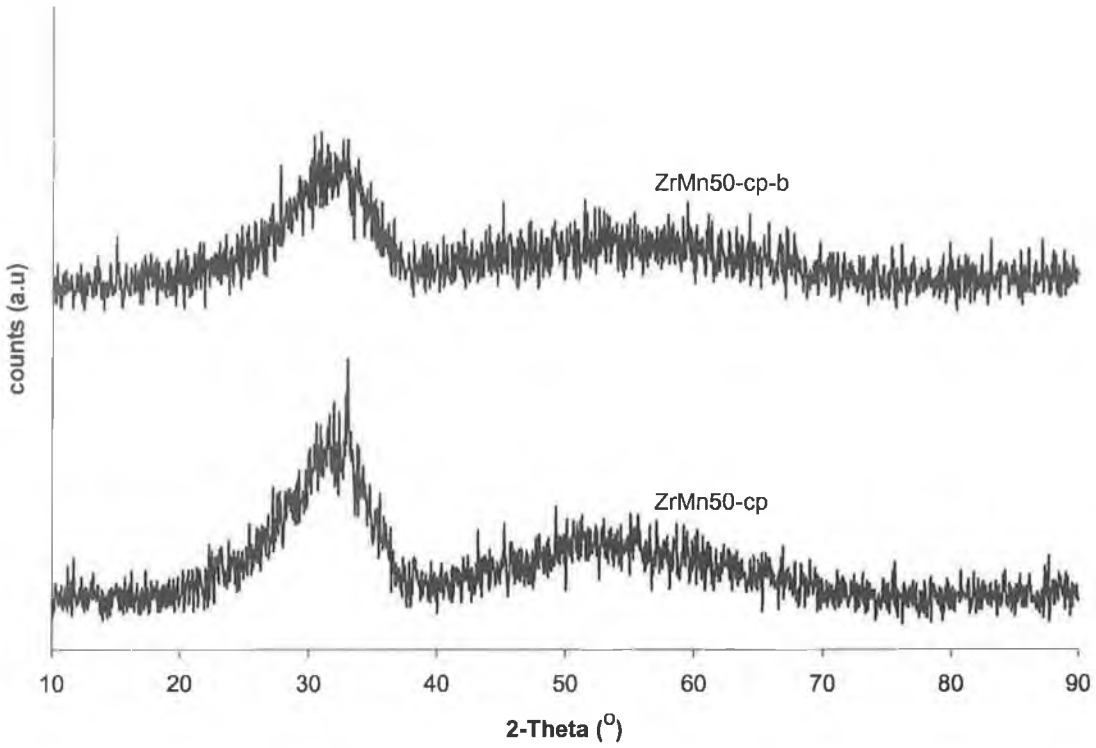

Fig 4.6: XRD data for ZrMn50-cp and ZrMn50-cp-b.

4.3.3 TG-SDTA and SIP-MS on Dried Precipitates.

The thermal analysis data of the uncalcined ZrMn50-cp and ZrMn100-cp is detailed in Fig 4.7-4.9. Fig 4.7 shows the simultaneous TG-SDTA of uncalcined ZrMn50-cp where both the weight of the sample (TG) and difference between the sample temperature and a reference (SDTA) are plotted as a function of sample temperature.

The weight loss from 60°C to 600°C is 17% as determined by TG. In Chapter 3, it was proposed to take the weight loss above 60°C for pure zirconia in order to eliminate the influence of adsorbed water since at 80°C, it has been reported earlier that decomposition of zirconium oxide hydroxide begins. This weight loss is significantly higher than that observed for pure zirconia, most likely due to the higher surface area of ZrMn50-cp which means that water is more easily adsorbed on the surface and/or the presence of manganese. Keshavaraja et al (10) observed for Zr0.7Mn0.3, a large endothermic peak on the DTA at 143°C with a total mass loss of 13.80% in the TG. The endothermic peak was attributed to dehydration of the oxide hydrate of initial composition $Zr_{0.7}Mn_{0.3}O(OH)_2$. They also observed an exothermic peak at 687°C,

which was attributed to the transition from the amorphous to the crystalline phase. In Fig 4.7, the maximum temperature of heating was 600°C and no such exothermic peak was observed. The transition from the amorphous to crystalline state of ZrMn50-cp could have occurred at a higher temperature than 600°C since the peak maxima of the exothermic peaks was reported to increase with manganese content (10). The final temperature used in the SDTA may have been too low to see the exothermic peak. Hence the SDTA could suggest that at 600°C, the sample is amorphous since the transition from the amorphous to the crystalline state has not occurred before that temperature. A very broad and low intensity peak indicative of an amorphous structure was observed in the XRD of ZrMn50-cp after calcination at 600°C for 6 hours. Another possibility for the absence of the exothermic peak observed in the SDTA of pure zirconia is that the initial manganese-zirconium oxide was crystalline after drying but given the high surface area of the final oxide this is unlikely. It is important to note that the SDTA measurements were performed at a heating rate of 10°C/min, consequently the absolute temperatures can not be compared directly with the XRD results which were obtained after calcination for 6 hours.

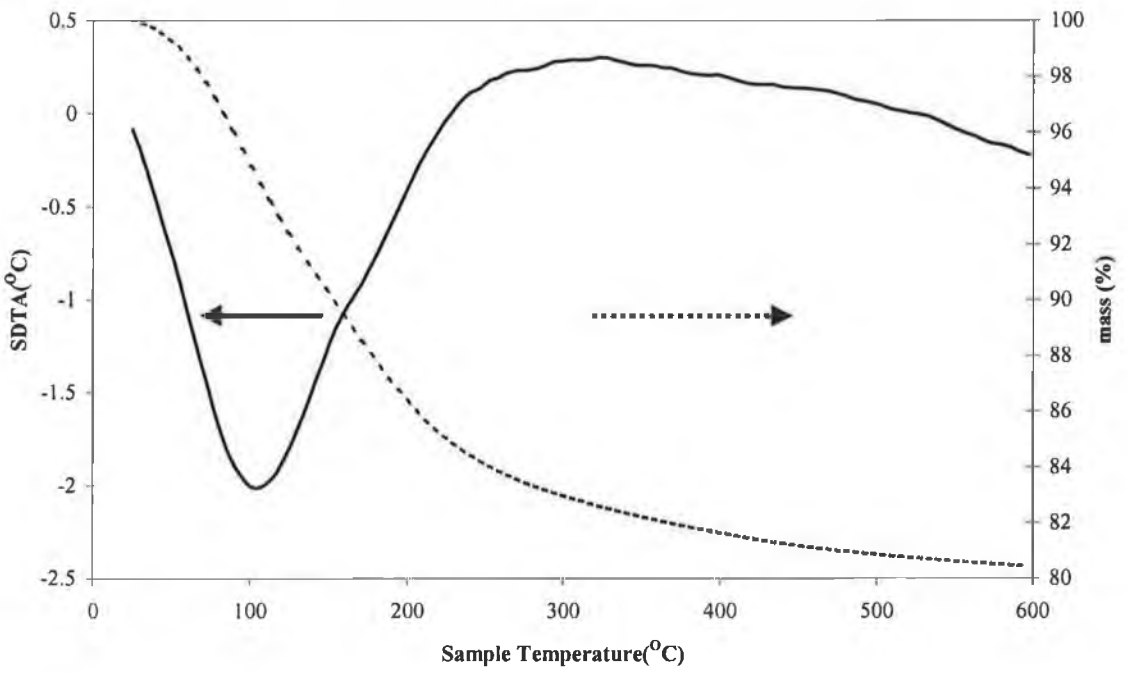

Fig 4.7: Simultaneous TG-SDTA of uncalcined ZrMn50-cp.

The SIP-MS of uncalcined ZrMn50-cp performed in vacuum is shown in Fig 4.8. The MS peaks of 17 and 18 have peak maxima at ca. 86°C and 145°C. The first peak can be attributed primarily to the evolution of physically adsorbed water but it may also indicate the start of dehydration of crystalline water from the zirconium precursor. The latter has been reported to occur between 80 and 161°C and represents dehydration of the oxy hydroxide precursor. Decomposition of a small amount of unreacted nitrates is also indicated between 340 and 400°C.

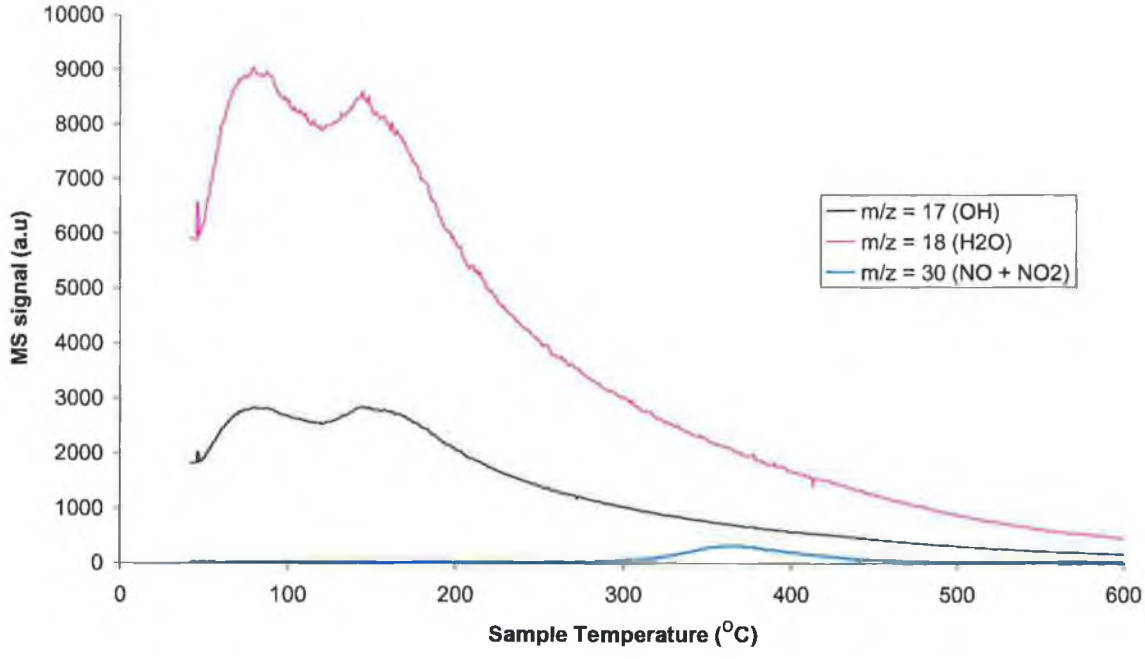

Fig 4.8: SIP-MS of uncalcined ZrMn50-cp at a linear heating rate of 10°C/min.

Fig 4.9 shows the evolution of water and hydroxyl species as a function of temperature for uncalcined ZrMn100-cp. The SIP-MS (Fig 4.9) shows two peak maxima at 233 and 425°C for the evolution of water, with a low intensity signal for unreacted nitrates between 300 and 400°C. The intensity of the water signal is low compared to that of ZrMn50-cp and may have been too small to be observed clearly in the SIP-MS of ZrMn50-cp. The water loss observed could be attributed to the dehydration of $MnO(OH)_2$ to MnO_2, which is reported to be stable up to 500°C (7).

The formation of $MnO(OH)_2$ has been reported on addition of ammonia to Mn^{2+} cations via the following reactions (36):

$$Mn^{2+} + 2NH_3 + 2H_2O \Leftrightarrow Mn(OH)_2\downarrow + 2NH_4^+$$

$$2Mn(OH)_2\downarrow + O_2 \rightarrow 2MnO(OH)_2\downarrow$$

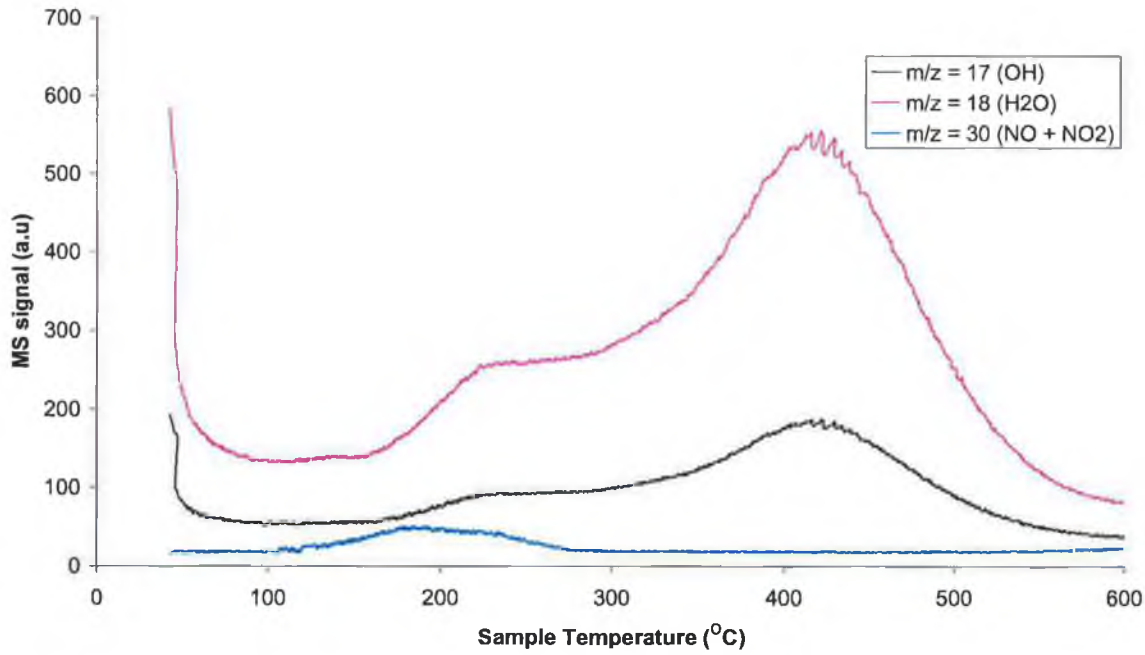

Fig 4.9: SIP-MS of uncalcined ZrMn100-cp at a linear heating rate of 10°C/min.

4.3.4 Reduction characteristics of fresh samples

The reduction profiles (TPR-MS) of fresh mixed oxides are shown in Fig 4.10-15, with pure manganese oxides Fig 4.16-18. Each figure shows the water evolution as a function of sample temperature at different heating rates. In agreement with other studies (37,38,39,40,41) the temperature of maximum reduction (T_{max}) increases as the heating rate increases. This has also been observed in general for other temperature programmed methods such as TG and DTA, whereby for a given temperature interval, the extent of decomposition is greater at a low heating rate than for the same sample heated at higher heating rate (42). The heating rate affects the balance between reaction

time and temperature i.e. at slower heating rates the oxide has more time to react with the hydrogen and an increase in the heating rate decreases the degree of reduction at a certain temperature. Lemaitre (43) proposed the following equation to relate hydrogen consumption in the reactor to experimental conditions such as flow rate and heating rate:

$$\Delta G = \frac{m\beta}{F} * \frac{d\alpha}{dt}$$

where m is the specific molar consumption, F is the specific flow rate of reacting mixture, α is the fraction of solid sample converted, β is the linear heating rate and ΔG is the difference in the concentration of hydrogen between the inlet and outlet of the reactor. It was proposed that since ΔG is proportional to the heating rate, decreasing the latter shifted the peaks towards lower temperatures and decreased the intensity of the peaks. The heating rate used has also been reported to affect the shape and peak areas of V_2O_5 (44) and Fe_2O_3 (45). This was especially apparent for vanadium pentoxide where the resolution, and in turn the number of peaks observed in the TPR profile, varied with the heating rate. In the current study, the shapes and number of peak (s) of the fresh oxides remained constant at all heating rates used, with the exception of MnO_2-Aldrich.

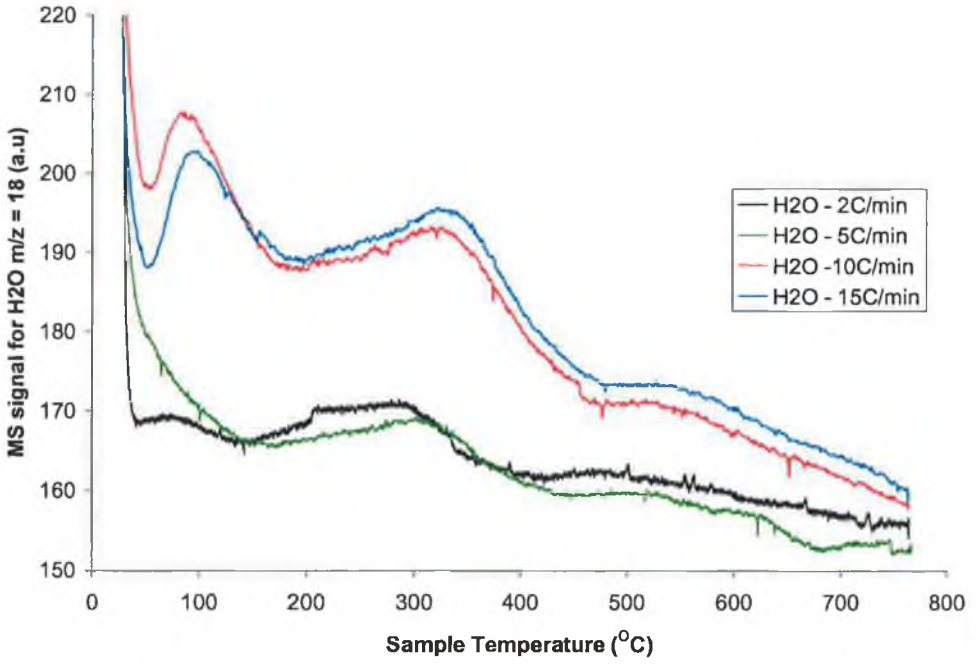

Fig 4.10: TPR-MS at different heating rates of ZrMn10-cp.

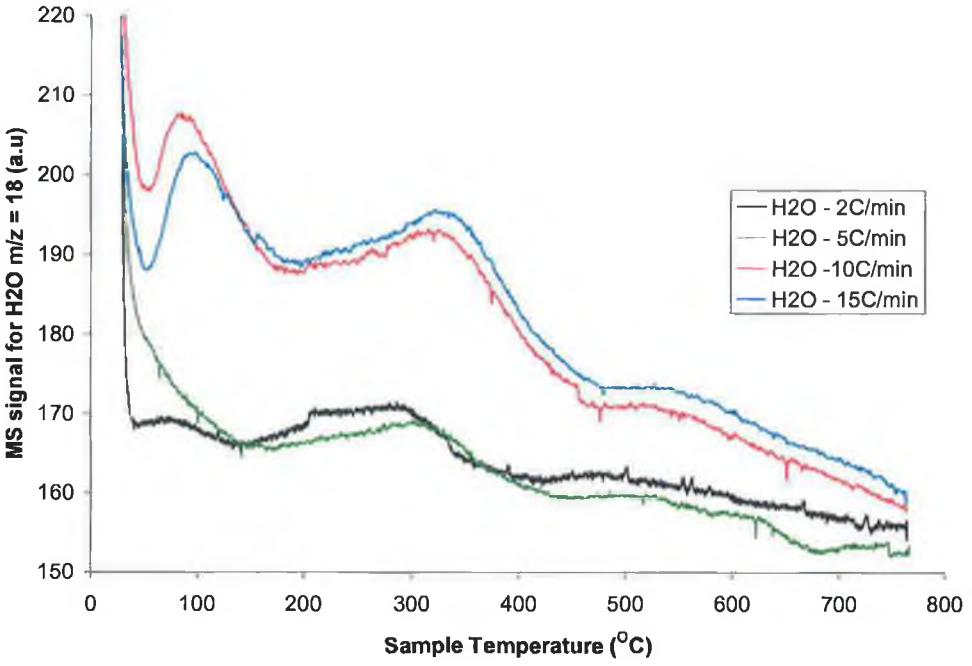

Fig 4.11: TPR-MS at different heating rates of ZrMn30-cp.

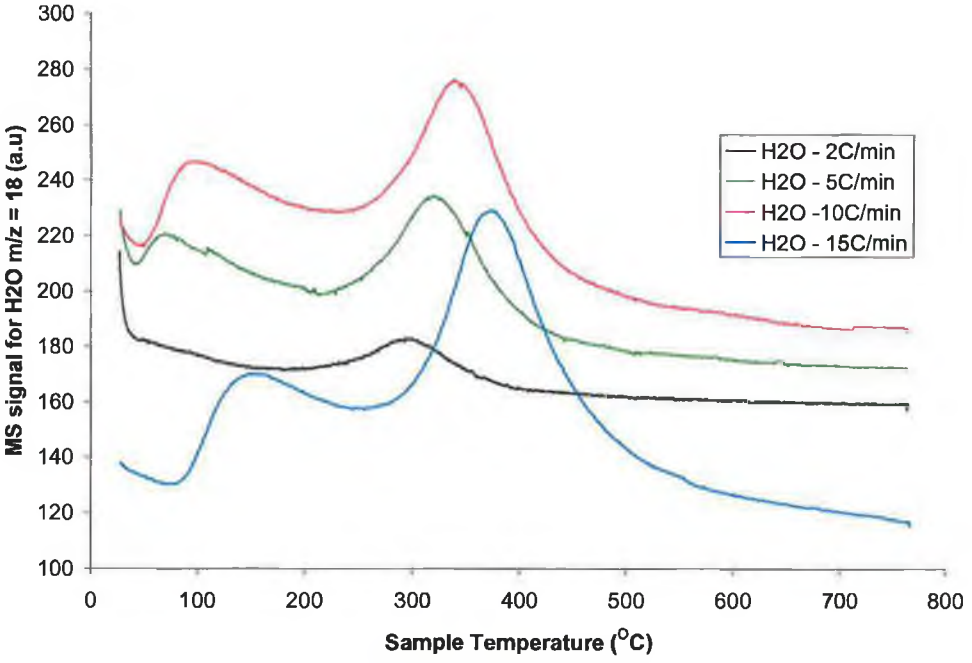

Fig 4.12:TPR-MS at various heating rates of ZrMn50-cp

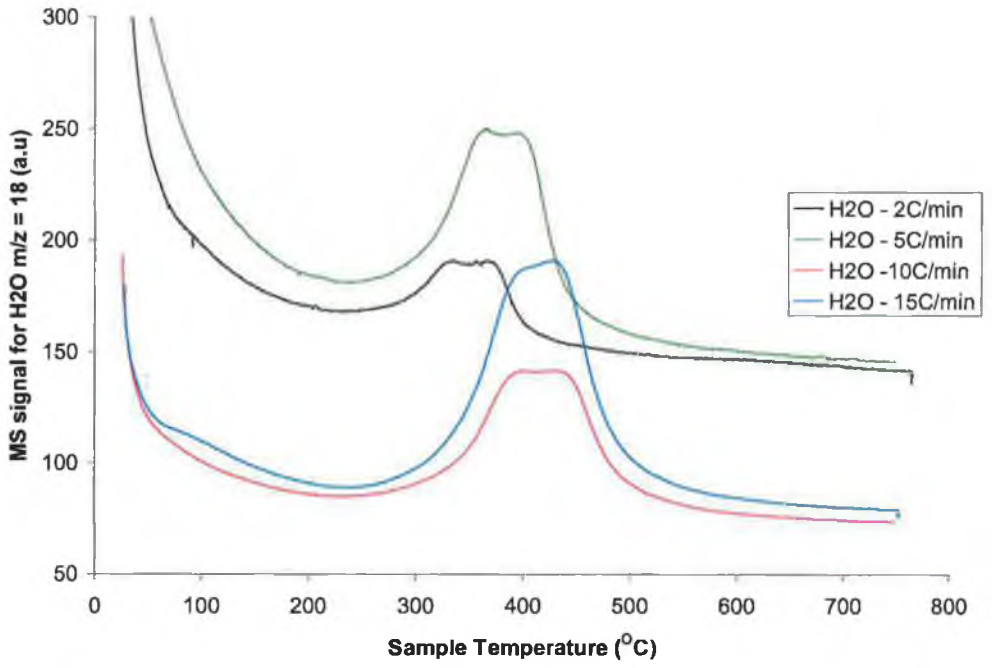

Fig 4.13: TPR-MS at various heating rates of ZrMn70-cp.

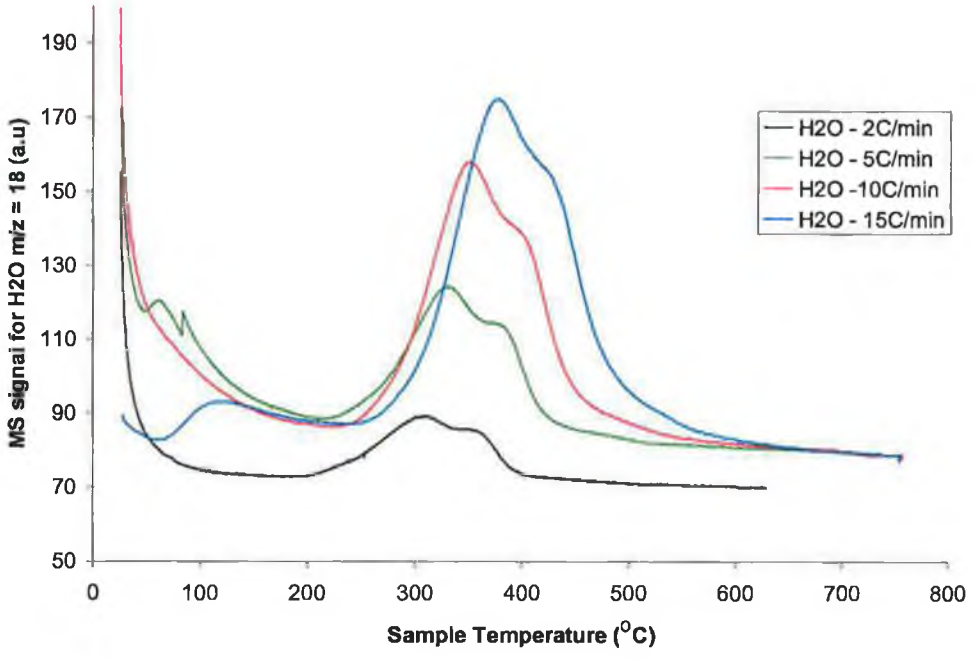

Fig 4.14: TPR-MS at various heating rates of ZrMn85-cp.

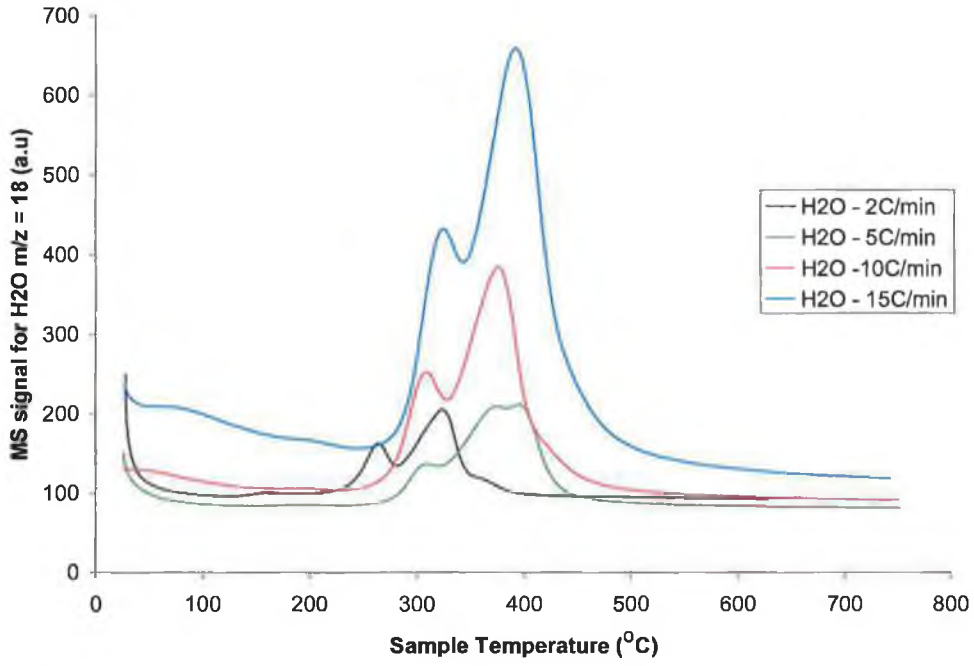

Fig 4.15: TPR-MS at various heating rates of ZrMn100-cp.

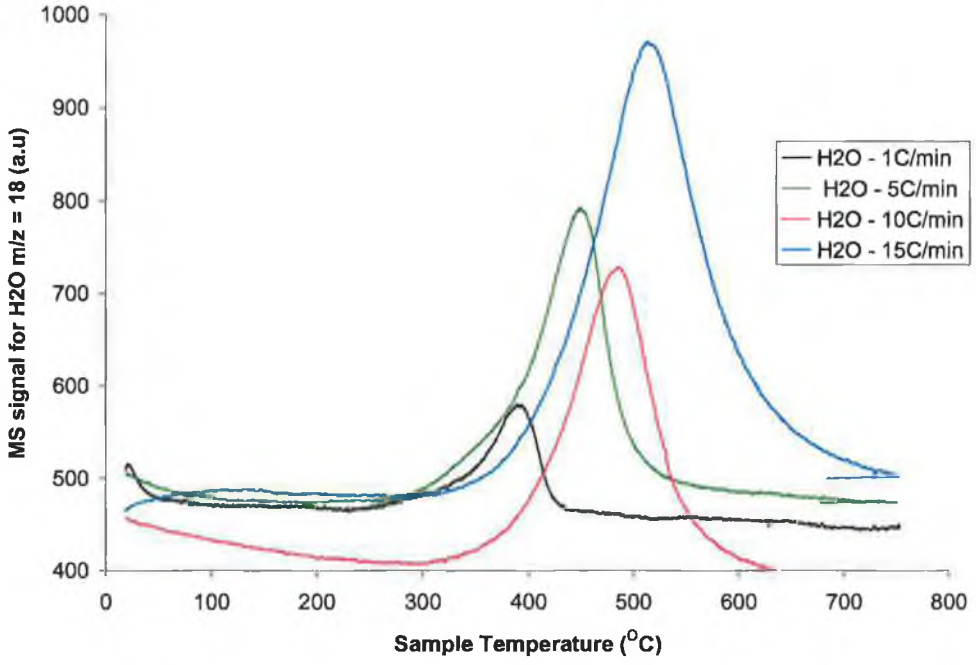

Fig 4.16: TPR-MS at various heating rates of Mn_2O_3-Aldrich.

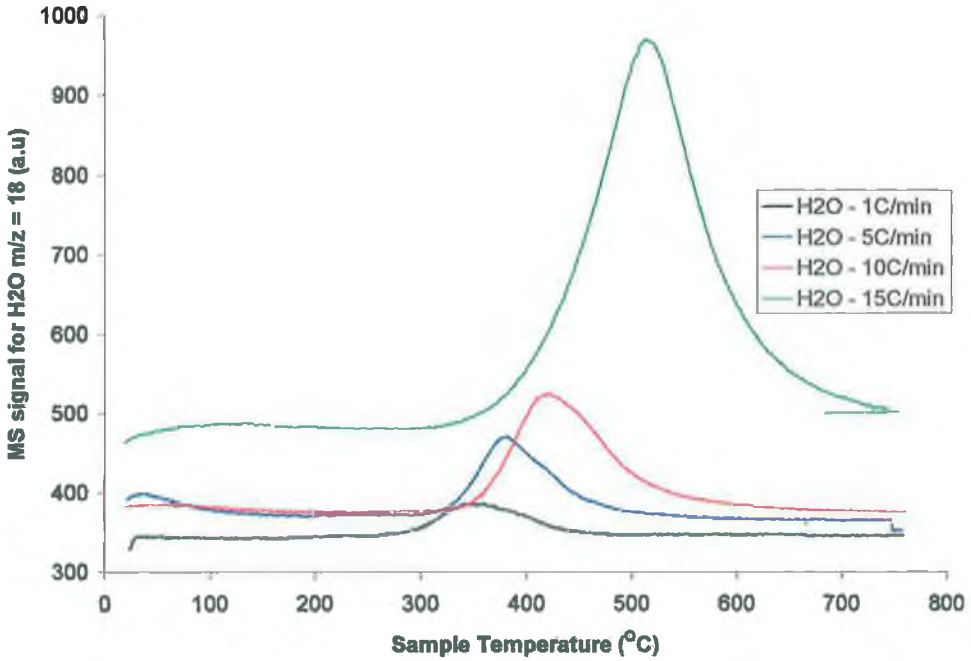

Fig 4.17: TPR-MS at various heating rates of Mn_3O_4-Aldrich.

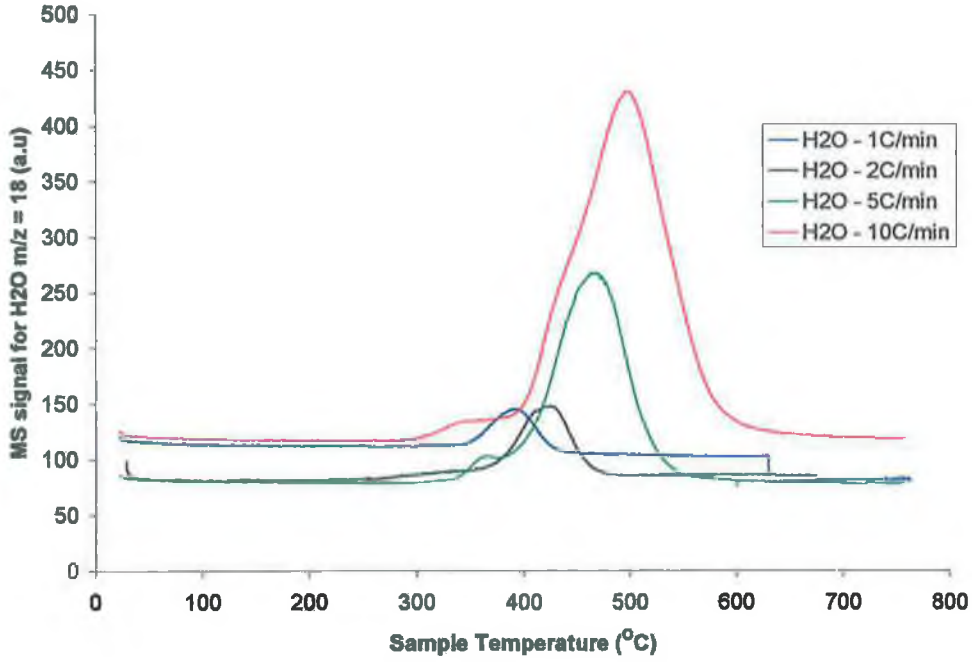

Fig 4.18: TPR-MS at various heating rates of MnO_2-Aldrich.

As well as heating rate other factors, such as hydrogen concentration, amount of sample and the flow rate of the reducing mixture, can affect the temperature programmed reduction profiles. Monti and Baiker (39) proposed the following parameter K to facilitate the selection of suitable operating variables:

$$K = S_0/V*c_0.$$

where S_0 is the initial amount of reducible species (μmol), c_0 is the hydrogen concentration at the reactor inlet (μmolcm^{-3}) and V is the total flow rate of the reducing gas (cm^3/s).

For heating rates between 6°C/min and 18°C, K values between 55 and 140s means that the following two requirements are met: (i) that the amount of hydrogen consumed at the peak maximum doesn't exceed the 2/3 of the hydrogen feed in the reactor and (ii) the minimum conversion at the peak maximum is 10%. When K is lower than 55, the sensitivity is too low and above 140, the quantity of hydrogen consumed is too high.

Malet and Caballero (46) also derived a parameter P to select appropriate experimental conditions for any reduction process that is first order in hydrogen; defined as :

$$P=\beta S_0/VC_0$$

This is very similar to that of Monti and Baiker (39) but also includes the heating rate (β) and the remaining terms are the same as for parameter K.

For a one step stimulated reduction process, increasing β/C_0 increased maximum temperature values but didn't affect peak shape. At different values of P above P=60, the reduction peaks became very flat at their maxima, which was attributed to hydrogen consumptions which were greater than 66% of the hydrogen content of the carrier. For stimulated reduction processes with two steps, an increase in the β/C_0 ratio led to less resolved curves. At low P values (P=6), two well resolved peaks were observed but as P was increased to values greater than 20, a single peak was observed. The TPR profiles of CuO also showed a decrease in resolution with increasing amounts of reducible species e.g. for 63 micromoles of CuO, 3 peaks were observed while for 378 micromoles, one peak was observed. Hence it was confirmed that the TPR profile depended on the mass of sample through the parameter P.

The P and K values were calculated for the TPR system used in the study for pure manganese oxides, Mn_2O_3 and Mn_3O_4 and are shown in Table 4.4. K values of 69s and 47s were calculated respectively. The latter is slightly lower than that recommended by Monti and Baiker for optimal selection of operating conditions. The P values obtained for both oxides were low and didn't exceed 20K at any heating rate as recommended by Malet and Caballero.

Sample	c(μmol H_2/cm^3)*	S_0 (μmol) ^	F (cm^3s^{-1}) "	β (K/s^{-1}) ~	K (s)	P (K)
Mn_2O_3-Aldrich	2.23	128	0.83	0.017	69	1
	2.23	128	0.83	0.083	69	6
	2.23	128	0.83	0.167	69	11
	2.23	128	0.83	0.250	69	17
Mn_3O_4-Aldrich	2.23	87	0.83	0.017	47	1
	2.23	87	0.83	0.083	47	4
	2.23	87	0.83	0.167	47	8
	2.23	87	0.83	0.250	47	12

Table 4.4: Calculated K and P values for Mn_2O_3-Aldrich and Mn_3O_4-Aldrich where * based on 5% H_2/Ar ^amount of reducible species of Mn_2O_3 and Mn_3O_4 based on 20 mg samples " Flow rate of 50 ml/min ~ heating rates of 1, 5, 10 and 15°C/min used which were then converted into K/sec of 0.017,0.083, 0.167 and 0.250 respectively.

In order to compare samples to each other, the data obtained using the same heating rate must be used. TPR curves for the TPR (from 25 to 750°C at a linear heating rate of 10°C/min) of the various oxides are compared in Fig 4.19. The TPR curves reflects the reactivity of lattice oxygen with the higher the TPR peak temperature, the lower the reactivity of the lattice oxygen. The shape, peak maximum temperatures and peak intensities were seen to vary depending on the manganese content. For ZrMn10-cp, a weak signal was observed, which could be attributed to the small amount of manganese present. The temperature of the main peak between 300°C and 350°C for ZrMn10-cp is significantly lower than that expected for zirconia, which has been reported to show no reduction up to 1000°C (47). A smaller shoulder is also observed at between 500 and 600°C (see Fig 4.10). Keshavaraja and Ramaswamy (11) have reported the presence of two peaks for 10 mol % manganese at approx 300C and 610°C, corresponding to the

For both ZrMn30-cp and ZrMn50-cp, single peaks are observed, the former being broader in width than the latter, in the temperature range of 300-400°C at a heating rate of 10°C/min. Choudhary et al (15) reported that the Mn-doped mixed oxides with a Mn/Zr ratio of 0.25 and 1 showed two peaks at 362°C and 549°C and three peaks at 355, 457 and 554°C respectively. TPR conditions involved a heating rate of 10°C/min in a H_2-Ar flow consisting of 37 mol % H_2. Choudhary et al (15) concluded that the reactivity of the lattice oxygen as indicated by the temperature of the TPR peak was greater when Mn doped zirconia was in a cubic form. For ZrMn70-cp and ZrMn85-cp, two poorly resolved peaks are observed, suggesting the presence of an additional Mn_2O_3 phase since Mn_2O_3 prepared by co-precipitation showed two reduction peaks. Temperature of reduction for ZrMn70-cp is slightly shifted up to 350-500°C compared with lower content samples and ZrMn85-cp is shifted back to between 300° and 450° compared to ZrMn70-cp (see Fig 4.19). Pure manganese oxide prepared by precipitation shows two well resolved peaks at 313 and 329°C corresponding to the reported reduction of Mn_2O_3 to Mn_3O_4 and Mn_3O_4 to MnO respectively (see Fig 4.15 and 4.19). Mn_2O_3-Aldrich and Mn_3O_4-Aldrich both showed one step reduction profiles. Temperatures of maximum reduction at 487 and 422°C were recorded respectively (see Fig 4.19). MnO_2 also purchased from Aldrich showed a main peak at 500°C, with a shoulder at 435°C and a small peak at 346°C (see Fig 4.17). In general, the intensities of all the mixed oxides were considerably smaller than all pure manganese oxides, most likely due to the reduction in quantity of bulk manganese oxide species.

Christel et al (41) found that low surface area Mn_3O_4 (0.2 m^2g^{-1}) reduced in a single step at 420°C while higher surface area Mn_2O_3 (22 m^2g^{-1}) reduced in two steps at 277 and 347°C at a heating rate of 0.03°Cs^{-1}. Furthermore a decrease in the surface area of Mn_2O_3 to 6m^2g^{-1} shifted the reduction profile about 20°C towards higher temperatures. The reduction of Mn_3O_4 has also been reported to be influenced by the preparation procedure and surface area (7). The study (7) found that lower surface area Mn_3O_4 (1m^2g^{-1}) reduced at higher temperatures (between 450 and 500°C) than Mn_3O_4 with a higher surface area (8 m^2g^{-1}). In addition, the peak of the higher surface area Mn_3O_4 at between c.a 350 and 450°C appeared wider, with the development of a low temperature shoulder. A similar effect was noticed for Mn_2O_3 purchased from Aldrich and that

prepared by co-precipitation in this thesis (see Fig 4.14 and 4.16). As shown in Fig 4.16, a single peak was observed for the very low surface area Mn_2O_3-Aldrich sample although depending on the heating rate used widening of the peak was observed shown. In contrast, the sample prepared by precipitation showed two well resolved peaks at all heating rates. Since the presence of Mn_2O_3 in both samples was confirmed by XRD, the only difference between the samples is the significantly lower surface area of that supplied by Aldrich. The higher surface area sample also reduced at significantly lower temperatures at the same heating rate e.g. at 10°C/min the higher surface area sample reduced at 313°C with a second peak at 383°C compared with 487°C for the lower surface sample.

Christel et al (41) attributed the difference in the number of reduction peaks in the TPR of MnO_2 supplied by different companies to the particle size of the oxide. MnO_2 (0.2 m^2g^{-1}) from Ventron showed only one reduction peak while a sample from Merck showed the expected three reduction peaks (61m^2 g^{-1}). Stobbeset al (7) observed that MnO_2 with a very low surface area (9.3 m^2g^{-1}) also showed one step reduction at 500°C, while Mn_2O_3 with a surface area of 26 m^2g^{-1} showed two reduction peaks at ca 300 and 400°C. Tonge (48) observed that the temperature of maximum reduction increased as particle size increased for NiO powders, while Stobbe et al (7) concluded that it is the surface area and not the oxidation state of manganese oxides, namely MnO_2, Mn_2O_3 and Mn_3O_4, that determines reducibility by hydrogen. Hence it is also likely that the peak positions of the mixed oxides are also affected by surface area.

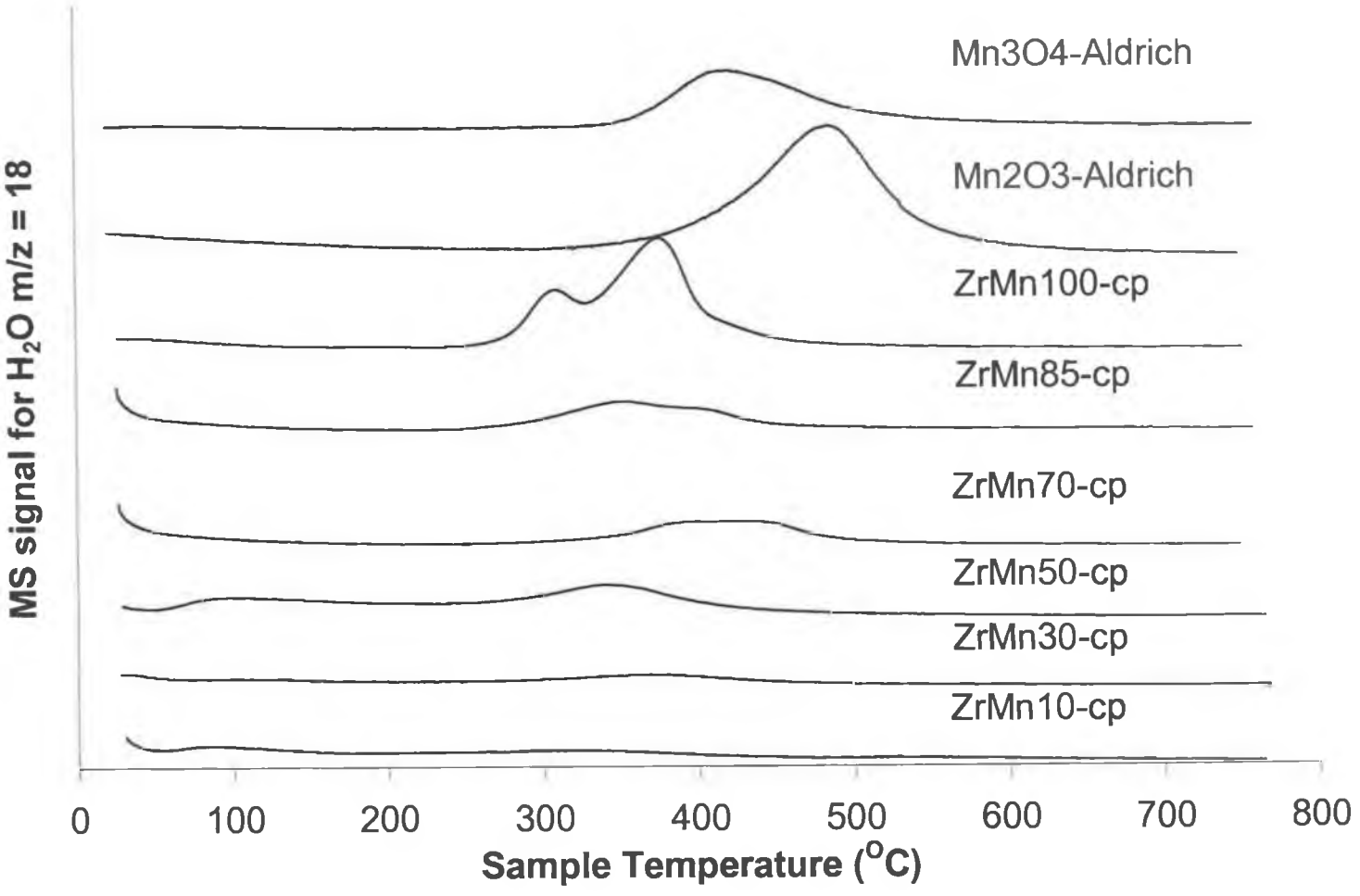

Fig 4.19: Comparison of TPR profiles of selected mixed oxides at a linear heating rate of 10°C/min. For each trace water evolution as a function of sample temperature is plotted and each curve is displaced for ease of comparison. Intensity data should be obtained from corresponding Fig 4.10-4.18.

Kissinger (49) first proposed a method by which to calculate activation energies from DTA plots by measuring the displacement of the DTA peak maximum as a function of the heating rate. He stated that the solid → solid + gas reaction could be described using nth order kinetics whereby

$$\frac{dx}{dt} = A(1-x)^n e^{\frac{-E}{RT}} \quad (4.3)$$

where dx/dt was the rate, x was the fraction reacted, n was the order of the reaction and T was the temperature in Kelvin.

Using the assumptions that the maximum rate of the reaction occurred when d/dt(dx/dt)was zero, that T_m was the temperature at which the maximum rate occurred and at constant heating rate (ϕ), the following equation was derived:

$$\frac{d(\ln \phi / T_m^2)}{d(1/T)} = \frac{-E}{R} \quad (4.4)$$

Wimmers et al (45) then proposed that the nth order kinetics were not suitable due to their simplicity for gas-solid reactions such as temperature programmed reduction and hence proposed the following general equation:

$$r = \frac{d\alpha}{dt} \; d\alpha/dt = k_1 (T)\, f(\alpha)\, f'(p_{H2}, p_{H2O}) \quad (4.5)$$

where α is the degree of conversion of the solid reactant, k_1 is the reduction rate constant, f (α) is the mechanism dependent term of the reduction rate equation and f'(p_{H2}, p_{H2O}) is the gas phase dependent term and p_{H2} and p_{H2O} are the partial pressures of hydrogen and water in the reactor.

By assuming differential conditions whereby the partial pressure of hydrogen remained constant throughout the reaction and any water formed was assumed to have a negligible effect on the observed rate of reaction due its effective removal, the gas dependent term can be taken as constant. Applying other assumptions, including

constant heating rate (ϕ) to relate temperature to time, and expression of the new rate constant using the Arrhenius equation, yielded the following equation (45):

$$\frac{d\alpha}{dT} = \frac{A}{\phi}\exp\left(\frac{-E}{RT}\right) f(\alpha) \qquad (4.6)$$

where A is the pre-exponential factor, E is the activation energy and R is the gas constant.

By assuming, similar to Kissinger, that at the maximum of the TPR peak, that the following equation held (45):

$$\left[\frac{d}{dT}\left(\frac{d\alpha}{dT}\right)\right]_{T=T\,max} = 0 \qquad (4.7)$$

and assuming that the reduction model f (α) and the extent of reduction at T_{max} ($\alpha_{T=Tmax}$) were independent of the heating rate (ϕ) used, equation 4.8 was derived (45):

$$\ln\left(\frac{\phi}{T_{max}^2}\right) = \frac{-E}{RT} + \ln\left(\frac{AR}{E}\right) + C \qquad (4.8)$$

Equation 4.8 was found to hold for various reduction models and hence could be generally applied to determine the activation energy from TPR measurements at various heating rates.

Hence a plot of $\ln\left(\frac{\phi}{T_{max}^2}\right)$ vs $\frac{1}{T_{max}}$ gave straight lines with a slope of –E/R.

The Ozawa method (50) has also been proposed for determination of activation energy E from linear heating experiments using equation 4.9

$$\log\phi = -0.4567\left(\frac{E}{RT}\right) + C \qquad (4.9)$$

where E is calculated from the slope of a plot of log ϕ vs 1/T.

The values of the activation energies calculated by both above equations has been reported to be meaningful if equations 4.8 and 4.9 are linear in a broad range of heating rates. Wimmers et al (51) also concluded that the generalised Kissinger equation (eq. 4.8) can lead to an error of 5% in the activation energy for some kinetic models and that this error has the same order of magnitude as the error caused by the measuring method.

Apparant activation energies of reduction (E_a) were determined for all Mn-Zr mixed oxides and pure manganese oxides by measuring the displacement of the temperature at which maximum reduction takes place (T_{max}) as a function of heating rates. The peak positions (T_{max}) were determined by measuring the temperatures corresponding to a maximum value of water evolution at each heating rate and are shown in Table 4.5. The accuracy of T_m was ± 5°C. The apparent activation energies of reduction (E_a) were obtained using both equation 4.8 and 4.9, the results of which and their respective linear regression coefficients are also shown in Table 4.5.

The errors for each activation energy value were calculated using the LINEST function in excel, which allows the calculation of the error in the slope of a line based on the linear regression coefficient R^2. Once the error in the slope was known, a maximum and minimum Ea value could be calculated for each sample and the difference between the two indicated the error in the measurement. For example ZrMn30-cp, using the Kiss equation, a straight line with a slope of –10875.2 was obtained and an E_a of 90 $kJmol^{-1}$ was calculated using that value. Using the LINEST function, an error in the slope of 1175.2 was calculated based on a R^2 value of 0.977. Addition and substraction of the error in the slope to and from the actual slope obtained allowed the calculation of a maximum and minimum slope value. Each of these values was then divided by the universal gas constant and multiplied by 1000 to yield the maximum and minimum activation energy possible, (in the case of ZrMn30-cp, 100 and 81 $kJmol^{-1}$). Subtraction of these two values and division by two gave the error in the activation energy of $10kJmol^{-1}$. Hence the value quoted for ZrMn30-cp is 90 ± 10 $kJmol^{-1}$. The same procedure was repeated for values obtained using the Oz method.

Table 4.5 shows that the Oz method gave higher E_a values than the Kiss method for all samples (% higher) and for both methods, the E_a value decreased with Mn is addition up to 50 mol%. Low E_a values were obtained for pure manganese oxides in the range 79-88 $kJmol^{-1}$, which compare well with those reported by Christel et al (41). The authors

(41) calculated the activation energies for the reduction of Mn_2O_3 with two different surface areas of 22 and 6 m^2g^{-1} from the slope of the line $\ln\beta/T_m^2$ vs $1/T_m$. For step 1 and 2, values of 85 ± 5 and 98 ± 5 kJmol $^{-1}$ for the low surface area sample and 92 ± 5 and 104 ± 5 $kJmol^{-1}$ for the high surface sample were determined. For one step reduction of Mn_3O_4, a activation energy of 97 kJmol $^{-1}$ was observed. It was concluded that the activation energies didn't depend on particle size and that the activation energy of the two steps differed by approx 10-15 $kJmol^{-1}$.

Sample	T_{max} (°C) @					E_a ($kJmol^{-1}$)		R^2	
	1°C/ min	2°C/ min	5°C/ min	10°C/ min	15°C/ min	Kiss	Oz	Kiss	Oz
ZrMn10-cp		291	307	324	334	121 ± 6	124 ± 5	0.996	0.997
ZrMn30-cp		322	343	374	384	90 ± 10	96 ± 9	0.977	0.982
ZrMn50-cp		303	323	342	377	74 ± 17	80 ± 16	0.907	0.928
ZrMn70-cp									
Peak 1		337	367	403	407	82 ± 10	88 ± 9	0.972	0.978
Peak 2		371	400	431	434	100 ± 12	106 ±11	0.972	0.977
ZrMn85-cp									
Peak 1		312	332	356	380	84 ± 12	89 ± 11	0.960	0.974
Peak 2		360	385	402	428	100 ± 13	105± 12	0.967	0.974
ZrMn100-cp									
Peak 1									
Peak 2		266	314	313	328	79 * ± 2	84 ±0.9	0.999	0.999
		326	378 (393)	379	394	88* ±0.2	93 ±0.1	1.000	1.000
Mn_2O_3-Aldrich	389		450	487	514	87 ± 7	94 ± 6	0.989	0.992
Mn_3O_4-Aldrich	351		383	422	456	83 ± 20	90 ± 19	0.897	0.919
MnO_2-Aldrich	395	427	470	500.8 (sh 435, 346)		81 ± 3	88 ± 3	0.997	0.998

Table 4.5: Apparent activation energies for the reduction of various metal oxides by hydrogen calculated by equation 4.8 (Kiss) and equation 4.9 (Oz) where R^2 is the linear regression coefficient and T_{max} is the temperature of maximum water evolution at each heating rate. * only 2, 10 and 15°C/min profiles were used for this sample see text.

The linear regression coefficients (R^2) of the Kiss and Oz plots for the majority of the data are above 0.95, indicating reasonable linearity and errors of typically 5-10% were observed with good linearity. However poor linearity was observed for ZrMn50-cp and Mn_3O_4, with corresponding larger error associated with the activation energy. It has been reported in the literature (41) that even for R^2 value of 0.999, errors of approx 5% have been observed e.g. 92 ± 5 $kJmol^{-1}$. For ZrMn70-cp, the shape of the peak made it difficult to determine if one or two step reduction processes were occurring. Since at 15°C/min a second peak was more clearly observed and to ensure the most accurate determination of temperatures of maximum reduction, a two-step reduction process was assumed and two activation energies for peak 1 and 2 were calculated. For ZrMn85-cp and ZrMn100-cp, two peaks were observed and the activation energy was determined for each peak separately. For the latter, only three (2,5 and 15°C/min) instead of four points were used in the determination of the activation energy since the peaks at 5 and 10°C/min were very similar to each other and had identical T_{max} values. The profile obtained at 5°C/min was not used in the calculation of the activation energies since the main peak was split into two peaks. For all other samples, 4 heating rates or points were used in the determination of Ea. Various authors have used a different number of linear heating rates to calculate Ea. Tiernan et al (38) also used 4 heating rates to calculate the activation for CuO and found the value agreed well with previous studies. Christel et al (41) used five linear heating rates at 2, 5, 8, 10 and 12°C/min for pure manganese oxides and since the values reported by Christel et al are in general agreement with the values of E_a reported in Table 4.5, 4 points are sufficient to obtain reasonable values of E_a. Wimmers et al (45) have reported the use of 6 linear heating rates, although 4 of those were below 2K/min. Several heating rates at low values would not have been possible in the current study due to the limited time available on the TPR-MS equipment.

4.3.5 Oxidation activities of fresh samples

The catalytic activity of the fresh oxides was determined by measuring their activity for the combustion of propane and methane, using the procedure described in chapter 2. As described previously in section 4.2.1, "fresh" refers to oxide samples calcined at 600°C for 6 hours and pure manganese oxides supplied by Aldrich and used without further treatment. Tables 4.6 and 4.7 summarises the oxidation activities for both propane and methane combustion of selected samples respectively. The T_{10}, T_{50} and T_{90} values correspond to temperatures where 10, 50 and 90 % conversion were recorded and activity will be discussed in these terms unless otherwise stated.

Sample	T_{10} (°C)		T_{50} (°C)		T_{90} (°C)	
	Run 1	Run 2	Run 1	Run 2	Run 1	Run 2
ZrMn0-cp	432	356	>>475	>>475		
ZrMn10-cp	267	258	309	311	320	323
ZrMn30-cp	251	251	262	261	274	275
ZrMn50-cp	206	224	236	237	267	248
ZrMn70-cp	253	132	273	260	294	272
ZrMn85-cp	240	203	262	225	273	246
ZrMn100-cp	201	135	212	211	224	223
Mn_2O_3-Aldrich	226	211	284	333	299	350
Mn_3O_4-Aldrich	153	201	211	211	222	223

Table 4.6: Activity of selected oxides for the combustion of propane where T_{10}, T_{50} and T_{90} refer to temperatures of 10, 50 and 90% of propane conversion. Samples were initially tested (run 1) and then cooled to room temperature and retested in the same sample tube (run 2).

Sample	T_{10} (°C)		T_{50} (°C)		T_{90} (°C)	
	Run 1	Run 2	Run 1	Run 2	Run 1	Run 2
ZrMn0-cp	546	539	>600	>600	>>600	>>600
ZrMn10-cp	434	402	479	466	558	547
ZrMn10-cp-a	413	414	463	469	550	576
ZrMn10-cp-b	378	388	416	419	525	525
ZrMn30-cp	393	285	415	412	514	487
ZrMn30-cp-a	382	374	418	421	501	525
ZrMn30-cp-b	379	nd	418	nd	497	nd
ZrMn50-cp	370	362	410	406	480	494
ZrMn50-cp-b (*)	333	341	366	389	443	477
ZrMn50-cp-b (^)	347	357	368	390	461	477
ZrMn70-cp	410	350	436	424	492	484
ZrMn70-cp-1	371	385	388	389	444	479
ZrMn70-cp-2	376	365	412	392	473	468
ZrMn85-cp	375	365	431	424	480	478
ZrMn85-cp-1	352	363	371	389	509	485
ZrMn100-cp	370	391	416	420	559	555
Mn_2O_3-Aldrich	451	441	541	554	>600	>600
Mn_3O_4-Aldrich	354	408	386	448	517	510

Table 4.7: Activity of selected oxides for the combustion of methane where T_{10}, T_{50} and T_{90} refer to temperatures of 10, 50 and 90% of methane conversion. Samples were initially tested (run 1) and then cooled to room temperature and retested in the same sample tube (run 2). For sample ZrMn50-cp-b, two samples were tested -* and ^ refers to sample 14 and 15 respectively from Table 4.2, the difference between being that sample 14 was prepared using a two fold reduction in all reagents compared to sample 15.

The reproducibility in the procedures for determining methane and propane have been determined in Chapter 2. For methane combustion, reasonably small errors were observed in T_{10} and T_{50} values of 4 and 1°C respectively, with a larger error in T_{90} of 8°C. For propane, a very large error was observed in the T_{10} value for ZrMn100-cp. This would indicate that the variations observed in T_{10} values in Table 4.5 between run 1 and run 2 are an artifact from the experimental technique. The T_{10}'s are recorded at

the start of the experiment and equilibrium may not have been reached or the gases may not have mixed properly at this stage. The flow rate of propane (2ml/min) is quite slow compared to that of the air (50 ml/min) and a longer mixing time may be required. For both reactant gases, no significant error was observed in the T_{50} value and therefore the activity of the samples will be discussed herein in terms of the temperatures at which 50% conversion of propane or methane occurs (T_{50}), known as "light-off temperatures", only, unless stated otherwise.

Tables 4.6 and 4.7 show clearly that the addition of a small amount of manganese to zirconia dramatically improves propane and methane combustion activity. On addition of 10 mol% of manganese to zirconia, light-off temperatures for both hydrocarbons decrease dramatically despite only a moderate increase in surface area of 6 m^2g^{-1}. T_{50} values of 309 and 479°C for propane and methane respectively were observed for ZrMn10-cp while pure zirconia (ZrMn0-cp) doesn't reach 50% conversion within the temperature ranges tested. For propane, the T_{50} values decreased up to 50 mol% manganese and then increased from 50 mol% to 85% manganese. For methane combustion, T_{50} values decreased up to 30 and 50 mol% manganese and then increased up to 85 mol% Mn. Choudhary et al (14) investigated a number of transition metals (viz. Mn, Co, Cr, Fe and Ni) doped zirconia with transition metal/Zr molar ratio of 0.25 for the combustion of methane and propane. The Mn-doped catalyst was the most active for methane but was less active than the Co-doped catalyst for propane. In our study, a minimum T_{50} was observed for ZrMn50-cp, while for methane combustion, minima were observed for both ZrMn50-cp and ZrMn30-cp.

All the pure manganese oxides, namely ZrMn100-cp, Mn_2O_3-Aldrich and Mn_3O_4-Aldrich were significantly more active than zirconia (see Table 4.6 and 4.7). Temperatures in excess of 400°C are required to achieve at least 50% conversion of propane for ZrMn0-cp (pure ZrO_2) while over 90% conversion is achieved for all pure manganese oxides by 300°C. Mn_2O_3-Aldrich and Mn_3O_4-Aldrich were both tested since they have been reported to be stable above 600 and 800°C respectively (7), which are the temperature ranges used in the preparation, aging and catalytic testing of the samples in this work. Of the two samples, Mn_3O_4-Aldrich is significantly more active than Mn_2O_3-Aldrich for both methane and propane combustion. T_{50} values of 211 and 386°C for propane and methane combustion respectively were recorded for the former,

while higher T_{50} values of 284°C and 541°C for propane and methane combustion respectively were observed for the latter.

The increased reactivity of Mn_3O_4-Aldrich compared to Mn_2O_3-Aldrich is most likely due to the increased reducibility and higher surface area of the former. A greater difference in T_{50} values between Mn_2O_3-Aldrich and Mn_3O_4-Aldrich was observed for methane than propane (155°C versus 70°C respectively). This effect could be due to the low surface area of Mn_2O_3-Aldrich, which may have a greater detrimental effect on methane which is more difficult to combust. Baldi et al (4) also investigated Mn_2O_3 and Mn_3O_4 for the oxidation of propane and found that Mn_2O_3 was slightly more active than Mn_3O_4. However it is important to note that our samples are characterized by different surface areas and synthesis conditions. Baldi et al (4) reported that Mn_2O_3 and Mn_3O_4 studied had surface areas of 9 and 24 m^2g^{-1} respectively. As Table 4.1 shows, the surface areas of Mn_2O_3-Aldrich and Mn_3O_4-Aldrich used in our study are 2 and 12 m^2g^{-1} respectively. The significantly lower activity of Mn_2O_3-Aldrich versus ZrMn100-cp is also attributed to a surface area effect, since both samples have the same structure as confirmed by XRD. ZrMn100-cp is also very active despite its relatively low surface area. The activity is comparable to that of the manganese-zirconia mixed oxides due to the relatively higher manganese content.

The activity of pure manganese oxides was expressed in terms of surface area using the following equation, similar to that proposed by Milt et al (52):

$$r = X_{CH4} * F_{CH4}/mS \ (\mu mols^{-1}min^{-1}m^{-2}) \qquad (4.10)$$

Where X_{CH4} = conversion of methane (%)

F_{CH4} = flow rate of methane (μmol CH_4 min^{-1})

m = mass of catalyst sample used (g)

S = specific BET area (m^2g^{-1})

When the activity for methane combustion is expressed in terms of surface area in Table 4.8, it was observed that the reaction rates of manganese oxides are in general one order of magnitude higher than the mixed oxides at all selected temperatures. This is to be expected considering that both ZrMn100-cp and Mn_3O_4-Aldrich showed good activity despite significantly lower surface areas. Surprisingly Mn_2O_3-Aldrich shows very high

activity rates when expressed in terms of surface area, indicating that the high light-off temperature observed is due to the extremely low surface area primarily.

Sample	r (μmol $min^{-1}m^{-2}$) * at						
	350°C	375°C	400°C	425°C	475°C	500°C	550°C
ZrMn10-cp	0.011 (1)	0.011 (1)	0.032 (3)	0.064 (6)	0.520 (49)	0.765 (72)	0.935 (88)
ZrMn30-cp	0 (0)	0.012 (2)	0.070 (12)	0.435 (75)	0.498 (86)	0.510 (88)	0.539 (93)
ZrMn50-cp	0.023 (6)	0.043 (11)	0.105 (27)	0.303 (78)	0.349 (90)	0.357 (92)	0.372 (96)
ZrMn70-cp	0	0.005(1)	0.016 (2)	0.159 (20)	0.701 (88)	0.725 (91)	0.773 (97)
ZrMn85-cp	0.022 (3)	0.074 (10)	0.119 (16)	0.335 (45)	0.662 (89)	0.677 (91)	0.714 (96)
ZrMn100-cp	0.178 (4)	0.535 (12)	1.026 (23)	2.855 (64)	3.435 (77)	3.703 (83)	3.926 (88)
Mn_2O_3-Aldrich	0.446 (2)	0.669 (3)	0.892 (4)	1.338 (6)	3.890 (17)	5.799 (26)	12.26 (55)
Mn_3O_4-Aldrich	0.112 (3)	1.301 (35)	2.639 (71)	2.788 (75)	3.123 (84)	3.271 (88)	3.457 (93)

Table 4.8: Intrinsic reaction rates (r) calculated for selected mixed samples using equation 4.10 where the numbers in parenthesis represent the percentage conversions of methane at that temperature.

The T_{50} values of the oxides tested for both propane and methane combustion for run 1 and 2 are compared in Fig 4.20. In general the same trend in activities were observed for both methane and propane combustion on initial testing, with higher temperatures for 50% conversion required for methane. The lower reactivity of methane is attributed to the fact that the C-H bond energy in a hydrocarbon decreases with increasing of carbon atoms and consequently the oxidation reaction rate of propane is increased (1). Hence, the strongest C-H bond is found in methane and higher temperatures are required to activate the bond. The trend in methane combustion from run 1 to run 2 in terms of T_{50} values is similar to that of propane with the exception of pure manganese oxides. For propane combustion, the T_{50} values of ZrMn10-cp, ZrMn30-cp and ZrMn50-cp from run 1 to run 2 were within experimental error, while for ZrMn70-cp and ZrMn85-cp, an increase in activity was observed from run 1 to run 2. For methane combustion, the mixed oxides had very similar T_{50} values for run 1 and 2. For the pure manganese oxides, for propane oxidation, no change in T_{50} values were observed between run 1 and 2 for the more active manganese oxides, namely MnZr100-cp and

Mn_3O_4 –Aldrich. In contrast, Mn_2O_3–Aldrich showed an increase in the T_{50} from 284 to 333°C on run 2. This could be attributed to the fact that the more active catalysts were only heated up to approx 225-250°C due to their high activity compared to Mn_2O_3 – Aldrich that had to be heated up to a higher temperature (325-350°C) to achieve complete combustion. In the case of methane combustion, the T_{10} and T_{50} of Mn_3O_4– Aldrich increased by 54 and 62°C respectively on going from run 1 to run 2. This deactivation may be due to the transformation of Mn_3O_4-Aldrich to Mn_2O_3 during run 1, as a result of heating to 600°C. According to Arnone et al (53), this transformation occurs at 400°C. For methane, both ZrMn100-cp and Mn_2O_3 showed higher stability than Mn_3O_4 with only small increases on the light-off temperatures on run 2.

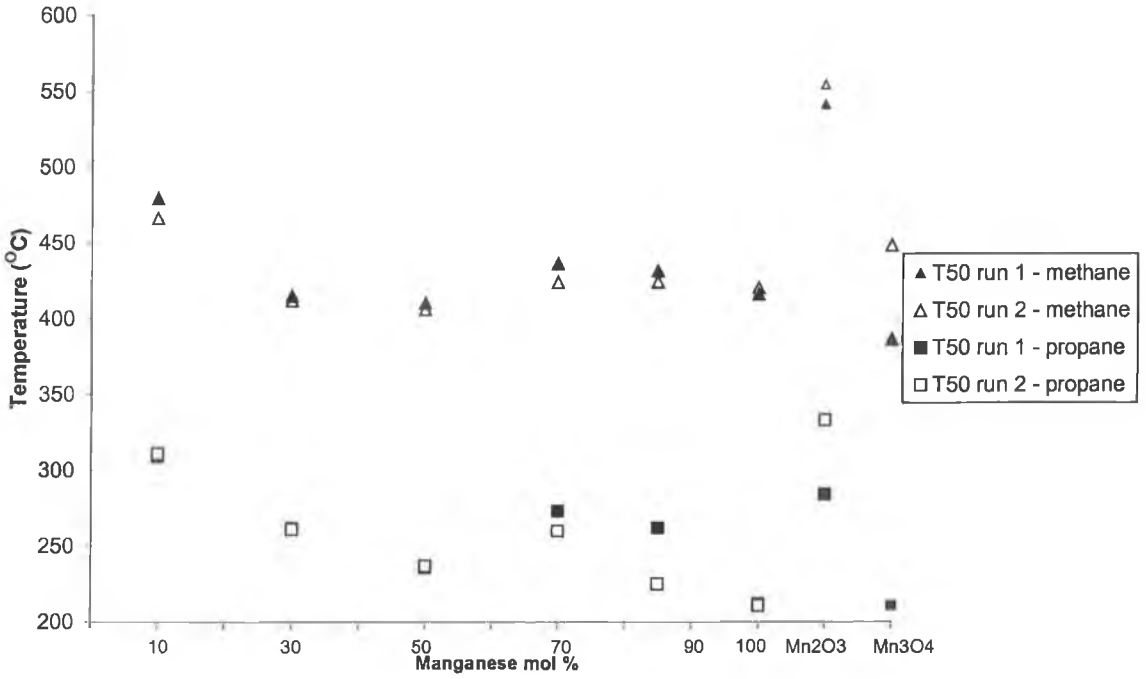

Fig 4.20: Temperature (°C) of 50% conversion of methane and propane (T_{50}) for both run 1 and 2 of Mn-Zr mixed oxides of the form ZrMnX-cp, where X is the mol % of manganese and of Mn_2O_3-Aldrich and Mn_3O_4-Aldrich.

In general, apart from ZrMn10-cp, similar T_{50} values were found for the mixed oxides despite significantly different surface areas. Fig 4.21 plots the surface area of each catalyst sample versus light-off temperatures for propane and methane on initial testing.

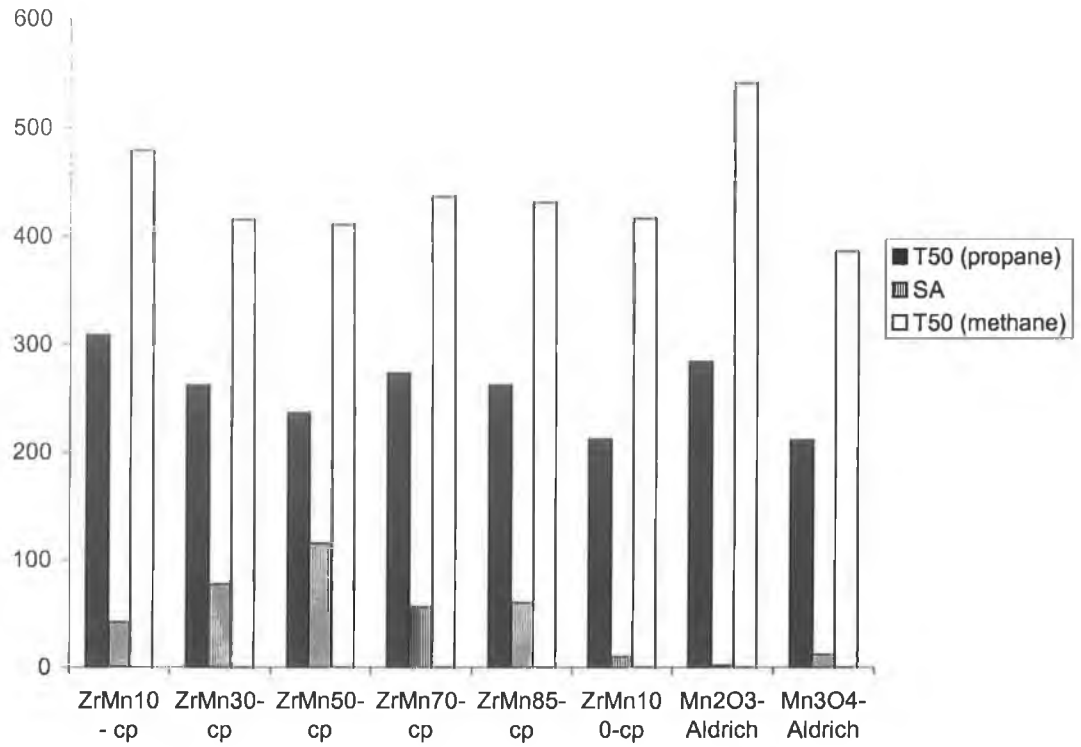

Fig 4.21: BET surface areas (SA) and temperatures (°C) of 50% conversion of methane and propane (T_{50}) for run 1 for selected samples as identified on the horizontal axis.

In general, more data points were collected for methane combustion due to its lower reactivity and the methane oxidation rate was calculated per unit surface area to ascertain more clearly the effect of surface area. These have been calculated at selected temperature using an equation proposed by Milt et al (52), which has been used in chapter 3 and has been already been detailed in Table 4.8. As mentioned previously, the reaction rates per surface area of the pure manganese oxides were an order of magnitude higher than that of the mixed oxides. Choudhary et al (15) observed that pure manganese oxide prepared by the precipitation method had a structure corresponding to MnO_2 and that all the mixed oxides were more active than pure manganese oxide when the activity was expressed per unit surface area at 450°C. In contrast, Lopez et al (25) found that with co-precipitated samples for the oxidation of isopropanol, activity increased with an increase in manganese content up to $Mn_{0.8}Zr_{0.2}$ and approached the activity of pure manganese oxides. Here the pure phase was Mn_2O_3. Both studies by Choudhary et al (15) and Ramasawamy and Keshavaraja (12) used the same preparation method and only reported activity for samples up to a maximum of 50 mol % of Mn. Ramasawamy and Keshavaraja reported a maximum

activity for butane oxidation for a manganese-zirconia mixed oxide sample with 20 mol % of Mn. The sample also had the highest surface area of the mixed oxides tested of $105m^2g^{-1}$. Choudhary et al also found that a mixed oxide sample with a similar Mn content (Mn/Zr transition metal ratio of 0.25) was the most active for methane combustion and the oxide also exhibited the highest surface area (90 m^2g^{-1}) of the manganese-zirconia mixed oxide samples (15). However a maximum surface area of $115m^2g^{-1}$ was found for 50 mol% of manganese in our work. Taking into account the surface area, the activities of ZrMn30-cp become comparable to that of ZrMn50-cp, especially 400 and 425°C (see Table 4.8). The lower manganese samples (ZrMn10-cp and ZrMn30-cp) also show a tetragonal/cubic structure that was identified by Choudhary et al (15) as being the main contributor to good activity of the mixed oxide with Mn/Zr ratio of 0.25. For manganese-zirconia mixed oxides prepared by the sol-gel method (26), the activity of the pure manganese material (Mn_2O_3) was less than the manganese-rich mixed oxides for the combustion of heavy hydrocarbons e.g. phenantrene. This was attributed to the synergistic effect of zirconia, although pure manganese oxide had a lower surface area than the mixed oxides.

As mentioned in the section 4.2.1, all of the above mixed oxides (ZrMnX-cp) were prepared using a precipitation procedure based on approx 10 g of Zr precursor and the addition of 10 ml of concentrated ammonium hydroxide. Variation in the above procedure included a decrease in the concentration of the precursor concentration while keeping the volume of ammonium hydroxide added at 10ml (ZrMnX-cp-1) or no change in the concentration of the precursor concentration while increasing the volume of ammonium hydroxide to 40ml. These variations were investigated for ZrMn70-cp and ZrMn85-cp and an effect on surface area was observed, as shown in Table 4.1. Hence the methane activity of these samples, namely ZrMn70-cp-1, ZrMn70-cp-2 and ZrMn85-cp-1 was determined and compared to the activities determined for ZrMn70-cp and ZrMn85-cp in Fig 4.22. For ZrMn70-cp, ZrMn70-cp-1 and ZrMn70-cp-2 a correlation between surface area and T_{50} values was observed, whereby the lowest T_{50} was observed for the sample with the highest surface area namely ZrMn70-cp-1. In contrast for ZrMn85-cp and ZrMn85-cp-1, despite identical surface areas, the activity of ZrMn85-cp-1 was significantly greater than ZrMn85-cp. The T_{50} value was lower than that of pure manganese oxide (see Table 4.7). Using the same preparation method, ZrMn70-cp-1 and ZrMn85-cp-1, the latter had a lower T_{50} (371 vs 388°C) despite a twofold decrease in surface area. This could be attributed to the higher manganese

content. In general, ZrMn70-cp and ZrMn85-cp prepared by the various methods showed good thermal stability with similar T_{50} values (± 10°C) from run 1 to run 2.

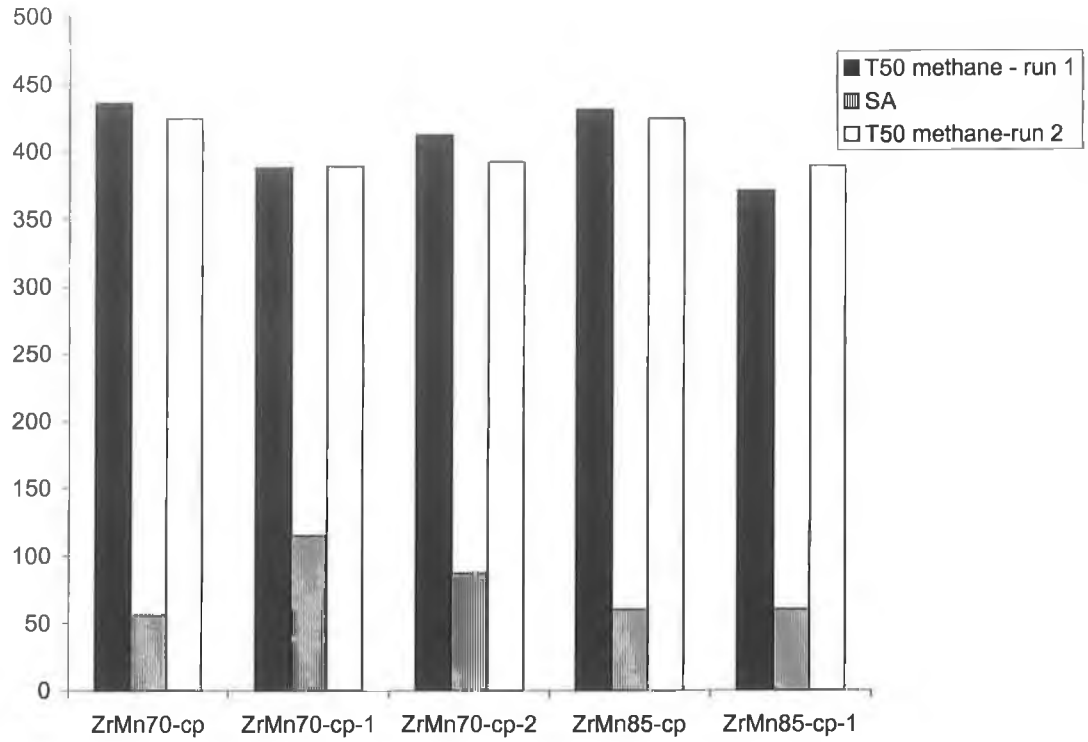

Fig 4.22: BET surface areas (SA) and temperatures (°C) of 50% conversion of methane for both run 1 and run 2 for selected samples as identified on the horizontal axis. For the difference in preparation methods used, see text and Table 4.1.

When the activity is expressed in terms of surface area (see Table 4.9), larger values are observed for ZrMn85-cp-1 compared to ZrMn70-cp-1 and ZrMn70-cp-2, although all of the same order of magnitude (with the exception of 375°C). On comparing the reaction rates per unit surface area of ZrMn70-cp-1, ZrMn85-cp-1 and ZrMn85-2 to ZrMn70-cp and ZrMn85-cp in Table 4.9, they are significantly higher at 375, 400 and 425°C.

Sample	r (μmol $min^{-1}m^{-2}$) at						
	350°C	375°C	400°C	425°C	475°C	500°C	550°C
ZrMn85-cp-1	0.037 (5)	0.461 (62)	0.513 (69)	0.543 (73)	0.632 (85)	0.669 (90)	0.710 (95)
ZrMn70-cp-1	0.012 (3)	0.052 (13)	0.334 (83)	0.350 (87)	0.378 (94)	0.390 (97)	0.394 (98)
ZrMn70-cp-2	0.010 (2)	0.046 (9)	0.167 (33)	0.395 (78)	0.461 (91)	0.482 (95)	0.492 (97)
ZrMn70 -cp	0	0.005 (1)	0.016 (2)	0.159 (20)	0.701 (88)	0.725 (91)	0.773 (97)
ZrMn85 -cp	0.022 (3)	0.074 (10)	0.119 (16)	0.335 (45)	0.662 (89)	0.677 (91)	0.714 (96)

Table 4.9: Intrinsic reaction rates (r) observed for selected mixed samples using equation 4.10 where the numbers in parenthesis represent the percentage conversions of methane at that temperature.

Finally the activities of samples prepared using various stirring rates were tested (see Tables 4.1 and 4.7) and their relationships with surface area are shown in Fig 4.23. For 10 and 50 mol% Mn, as the surface area was increased on increasing stirring time prior to addition of base, the activity also increased as indicated by lower light-off temperatures. For ZrMn50, a large increase in surface area ($38m^2g^{-1}$) was accompanied by a decrease in T_{50} from 411 to 363°C. ZrMn50-cp-b was prepared on a full scale and also by a two-fold decrease in all preparation conditions (see Table 4.2). As can be observed from Table 4.7 (samples ZrMn50-cp-b * and ZrMn50-cp-b ^ respectively), the light-off temperatures were very similar and within experimental error on run 1, demonstrating that the optimised method was reproducible and that scaling down all reagents and concentrations in proportion to each other had no effect on the surface area or catalytic activity of the sample. For ZrMn10-cp and ZrMn30-cp, the effect of both stirring times of 20 and 60 minutes on the methane activity were determined. In the case of ZrMn10-cp increasing the stirring time to 20 minutes increased the surface area and decreased the T_{50} value by $35m^2g^{-1}$ and 16°C (compare ZrMn10-cp and zrMn10-cp-a). A further increase in the stirring time from 20 to 60 minutes resulted in a further comparable increase in surface area of $36m^2g^{-1}$ but a relatively larger decrease in T_{50} of 44°C (compare ZrMn10-cp-a and ZrMn10-cp-b). Hence no linear correlation between activity and surface area was observed. In contrast, the activity of ZrMn30-cp remained

at the same value of ca. 416°C for samples prepared with all stirring times. Increasing the stirring time from 0 to 20 minutes and 20 to 60 minutes increased surfaces areas significantly from 77 m^2g^{-1} to 109 m^2g^{-1} and from 109 m^2g^{-1} to 121 m^2g^{-1} respectively, but these changes had no effect on the T_{50} values obtained.

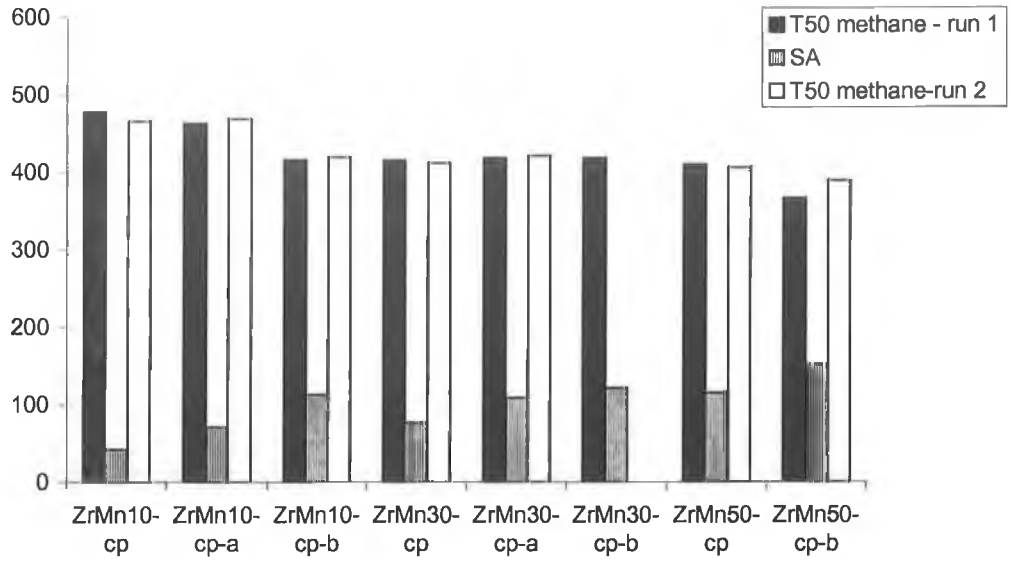

Fig 4.23: BET surface areas (SA) and temperatures (°C) of 50% conversion of methane for both run 1 and run 2 for selected samples as identified on the horizontal axis.

For fresh mixed oxide, a steep rise in activity over a narrow temperature range (typically 25°C) was observed. In general catalytic combustion, as the temperature is increased, oxidation begins at a temperature dependent, which is dependent on both the hydrocarbon and the catalyst (54). Further increase in temperature then leads to an exponential increase in the rate of reaction. The reaction then becomes mass transfer controlled until all the reactants are depleted. Mass transfer limitations occur when the reaction rate is faster than the rate of reactant and/or product transport to and from the surface and the catalytic surface temperature is higher than in the bulk gas stream. Light-off refers to the temperature at which mass transfer becomes rate controlling or when conversion rises from low values to almost completion for a small temperature increase.

As mentioned in the literature survey, noble metal catalysts are commonly used as oxidation catalysis and, while the focus of this thesis is combustion using non-noble

metal catalysts, platinum supported on alumina was also tested for comparison. A prepared sample ZrMn50-cp was also impregnated with a 0.5 wt% platinum loading to investigate its suitability as a support. The activity data for the fresh supported catalysts are reported in Table 4.10.

Sample	SA	CH_4			C_3H_8		
	(m^2g^{-1})	T_{10}	T_{50}	T_{90}	T_{10}	T_{50}	T_{90}
ZrMn50-cp	115	370	410	480			
0.5 wt % Pt/Al_2O_3	184	445	484	499			
0.5 wt % Pt/MnZr50-cp	54	339	412	476			
1 wt % Pt/Al_2O_3	nd				201	212	224

Table 4.10: Activity of fresh supported oxides for the combustion of methane and propane. T_{10}, T_{50} and T_{90} refer to temperatures of 10, 50 and 90% of conversion in °C and SA represents the surface area determined by the BET method

The activity for methane combustion of all fresh mixed oxides and pure manganese oxide ZrMn100-cp was higher that observed for 0.5 wt% Pt/Al_2O_3 sample in terms of T_{50} values. Indeed impregnation with 0.5 wt% platinum had no effect on the light-off temperature (T_{50}) of ZrMn50, although a significant decrease in surface area (115 versus 54 m^2g^{-1}) was observed on impregnation. This decrease could be attributed to blocking or filling of the pores of the original high surface area support (ZrMn50-cp) by platinum particles. Another reason for the decrease in surface area on impregnation could be due to the acidity of the preparation method used rather than the platinum particles. A blank impregnation with an acid e.g. HCl would help confirm the reason for the decrease in surface area. However, the important point to note is that for methane combustion, 0.5 wt% Pt/ZrMn50 was more active than 0.5 wt% Pt/Al_2O_3 and that the support was just as active in terms of T_{50} values without the addition of the noble metal. Similar to that observed for the mixed oxide samples on aging no significant decrease in the T_{50} value was observed. For propane, 1% Pt/Al_2O_3 was more active than all of the manganese-zirconia mixed oxides prepared with different compositions (compare Table 4.7 and 4.10). However a major difference noted between the noble metal catalysts and the mixed oxides especially for methane combustion was the difference between T_{50} and T_{90} values. In the case of the fresh mixed oxides, differences in the range of approx 56-100°C was observed between T_{50} and T_{90}, while

larger differences were observed for pure manganese oxides. In comparison (see Table 4.10), for fresh Pt/Al_2O_3, a difference of 15°C was observed between T_{50} and T_{90}. Addition of platinum to ZrMn50-cp had no significant effect on this property either. This indicates that at higher conversions, above 80%, the oxides were less active than the noble metal supported catalysts. This could be interpreted as different oxidation mechanisms operating between the noble metal and oxide catalysts. The results on comparing mixed oxides prepared in this study compared to that of noble metals could also suggest that at high conversion, the reaction over metal oxides comes under mass transfer control where the rate of reaction at the surface is higher than the transport of the products from the surface. Similar results have also been reported by Arai et al (55) on comparing the activity of perovskites to Pt/Al_2O_3 for methane combustion. It was found that the rate of activity increase at high conversion levels was more gradual for the perovskites than for the noble metal catalyst. For noble metal catalysts, adsorbed oxygen reacted with adsorbed methane following Langmuir-Hinshelwood type kinetics at all temperatures. For perovskites at elevated temperatures lattice oxygen dominated combustion and rapid incorporation of gaseous oxygen into the lattice occurred (55).

The TPR-MS data of the oxides (ZrMnX-cp where X is the mol % of Mn) has been discussed previously in section 4.3.2 and the activity results obtained will now be discussed in terms of redox properties. Choudhary (15) concluded that for various transition metal oxides with a metal/Zr ratio of 0.25, the temperature of the first TPR peak provides information on the relative reactivity of their lattice oxygen. Hence the temperature of maximum reduction of the first or only TPR peak observed (T_{max}) was plotted against the light-off temperature (T_{50}) of both propane and methane in Fig 4.24. The TPR peak positions used were the values recorded in Table 4.5 at a linear heating rate of 10°C/min. A similar relationship was observed between the T_{50} values for both methane and propane and temperature of maximum reduction except for ZrMn10-cp and Mn_3O_4-Aldrich. For the former, the temperature of maximum reduction was considerably lower than the other mixed oxides, but the sample was the least active of the mixed oxides for both methane and propane combustion. A rather wide and misshapen peak in comparison to the more gaussian shape of peaks of ZrMn30-cp and ZrMn50-cp was observed (see Fig 4.10), hence possibly leading to an error in determination of temperature of maximum reduction. Mn_3O_4-Aldrich had a comparable activity to ZrMn100-cp, reduced at a higher temperature. However since both samples

have a different manganese phase present and hence a different number of peaks present, a comparison of the two samples may be difficult.

Choudhary et al (14,15) showed the involvement of lattice oxygen in both propane and methane combustion by pulsing pure propane and methane in the absence of oxygen over the samples. The authors observed the conversion of propane under those conditions at 500°C, while pulsing methane accompanied by increasing temperature resulted in the appearance of CO_2, indicating oxidation was occurring in the absence of oxygen. Reducibility is of crucial importance for catalysts operating via the Mars- Van Krevelen mechanism and hence for catalysts working via this mechanism, TPR characterises one aspect of catalytic activity. As discussed in chapter 1, lattice oxygen has been proposed to be involved in the total oxidation of paraffins in other studies (1,56,57). Choudhary et al (15) observed a link between TPR and activity in that Mn doped Zr with a metal/Zr ratio of 0.25 was more active and more reducible than MnO_2. A temperature of maximum reduction of 362°C were observed for the former sample compared to temperatures of maximum reduction of 355, 457 and 554°C for the latter. Arnone et al (53) also observed a correlation between the ease of reducibility of transition metal oxides and activity in the combustion of methane.

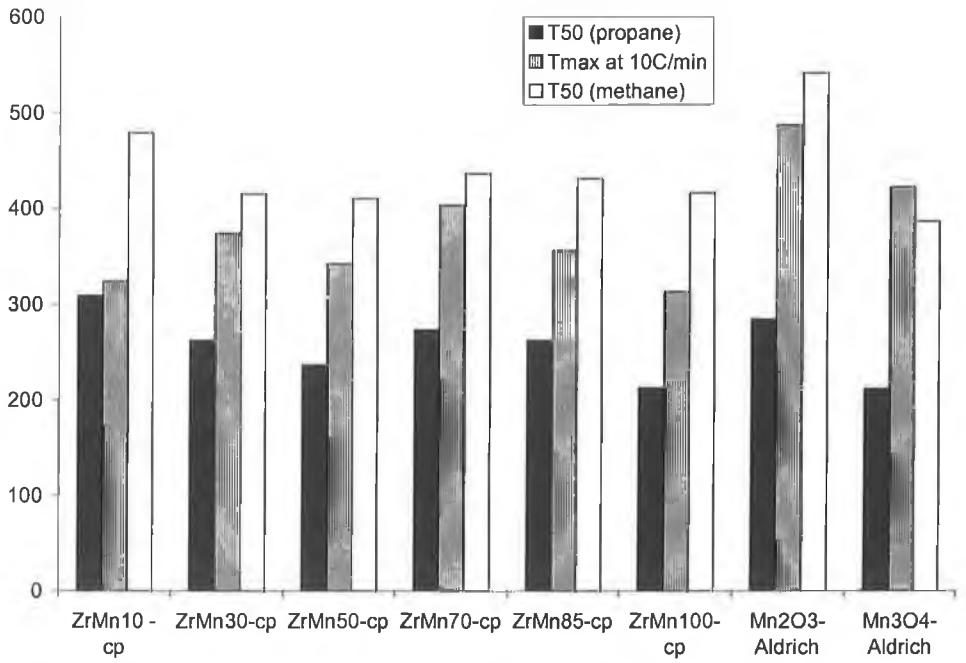

Fig 4.24: Plot of temperature of maximum reduction for first TPR peak (T_{max}) at heating rate of 10°C/min from Table 4.4 and temperature of 50 % conversion (T_{50}) for propane and methane for various oxides.

For the mixed oxides, both activation energies and T_{50} values for propane and methane combustion follow a similar trend (see Fig 4.25). All the pure manganese oxides showed similar activation energies and the difference between the values of ZrMn100-cp, Mn_2O_3 -Aldrich and Mn_3O_4-Aldrich were much smaller than the differences in light-off temperatures. To date in the literature, no reduction kinetics have been investigated for pure or mixed manganese oxides, with the exception of Christel et al (41). Christel et al (41) concluded that the activation energy values for pure manganese oxides are independent of particle size, while temperature-programmed reduction peaks and catalytic activity are dependent on particle size and surface area respectively. The activation energies of each oxide are quite hard to compare with each other due to the relatively large error associated with some of the activation energies (e.g. see ZrMn50-cp in Table 4.4). In general activation energies are determined by the reduction mechanism and once calculated, are generally used to determine the underlying reduction mechanism [f(α) in equation 4.1].

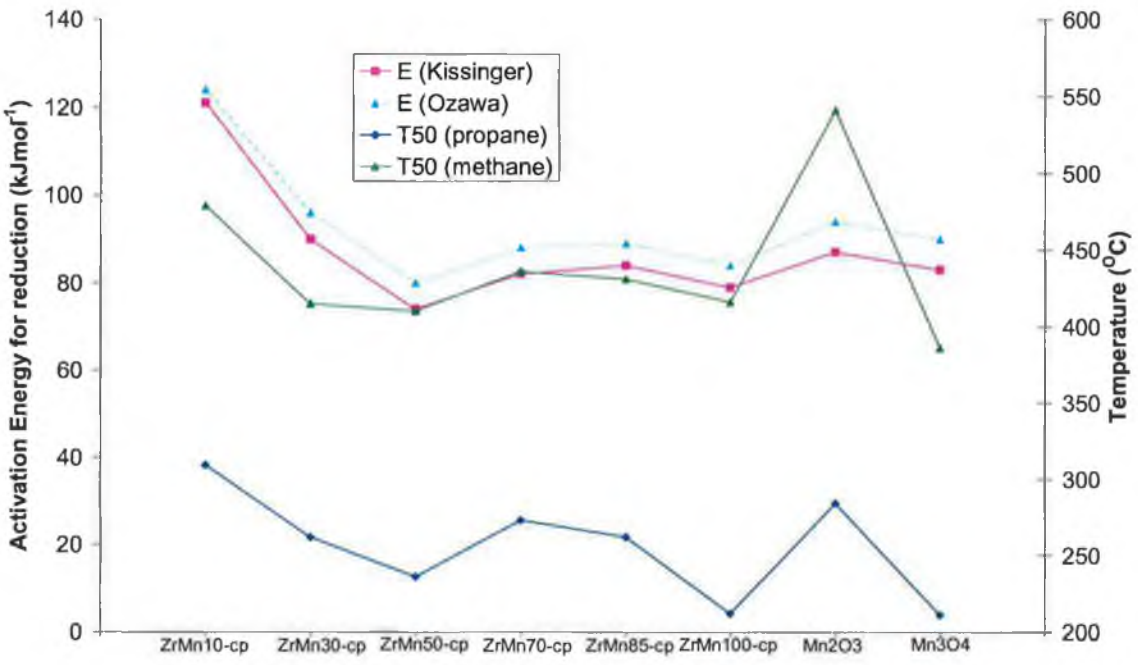

Fig 4.25: Plot of activation energies of reduction calculated via the Kissinger and Ozawa equations for the first reduction peaks in the TPR from Table 4.5. Temperatures of 50% conversion of both propane and methane are shown.

4.3.6 Effect of aging on surface areas and structural characteristics of selected oxides.

Selected mixed oxides and pure oxides were aged at 800°C for 8 hours in a static air furnace. The aged samples were analysed for surface area and phase changes using the BET method and X-Ray diffraction respectively using the experimental procedures outlined in Chapter 2 and the results are reported in Table 4.11.

A comparison of the surface areas before (fresh) and after aging (aged) is represented in Fig 4.26. Of the two single oxides prepared by co-precipitation, manganese oxide shows the better stability compared to zirconia with losses in surface area after aging of 40% and 85% respectively. ZrMn10-cp, ZrMn30-cp and ZrMn50-cp show very similar losses in surface area of 77%, 77% and 73% respectively. Hence it suggests that incorporation of manganese reduces the surface area loss on aging compared to pure zirconia. ZrMn70-cp and ZrMn85-cp show similar smaller losses in surface area of 54% as that of pure manganese oxide (ZrMn100-cp). This can be attributed to the presence of a separate phase of Mn_2O_3 that was observed in the XRD pattern of ZrMn70-cp and ZrMn85-cp. Mn_2O_3 was also observed in the XRD of aged ZrMn100-cp and Mn_2O_3-Aldrich, indicating that no phase transformation of Mn_2O_3 was observed in the temperature range 600-800°C. This is in agreement with Stobbe et al (7) who proposed that Mn_2O_3 was stable in air up till 900°C. Of the pure manganese oxides, Mn_3O_4-Aldrich showed the largest decrease in surface area of 79%.

The transformation from Mn_3O_4 to Mn_2O_3 has been proposed to occur at 400°C (53). In agreement with this, the presence of Mn_2O_3 only was observed in the XRD pattern of Mn_3O_4-Aldrich after heating to 800°C (see Table 4.11). The surface area of Mn_2O_3-Aldrich-ag could not be determined using the Gemini Micrometrics equipment available, suggesting a surface area below $1 m^2 g^{-1}$. For the mixed oxides on aging at 800°C, similar structural features were observed compared to those after calcinations at 600°C (see Chapter 4, Table 4.3). The bixbyite phase (Mn_2O_3) was observed for aged ZrMn70-cp-ag, ZrMn85-cp-ag and ZrMn100-cp-ag.

Sample	Main Peaks-2θ (°)	Main Peaks-d_{hkl} (Å)	Relative Intensity (%)	Phase	SA (m^2g^{-1})
ZrMn0-cp-ag	27.60, 30.85, 49.50 33.65, 34.70, 29.45	3.23, 2.89,1.84, 2.66, 2.58, 3.03	100, 75, 47, 33, 28, 19	m-ZrO_2, minor t-ZrO_2	5 ± 0.7
ZrMn10-cp-ag	30.25, 50.60, 60.20, 35.2	2.96, 1.80, 1.54, 2.55,	100, 53, 37, 23	t-ZrO_2	10 ± 2
ZrMn30-cp-ag	30.65, 49.95, 73.50, 60.35	2.92, 1.83, 1.29, 1.53	100, 95, 43, 33	t-ZrO_2	18 ± 1
ZrMn50-cp-ag	30.30, 30.50, 32.90, 50.20, 35.7, 60.50,	2.95, 2.93,2.72, 1.82, 2.52, 1.53	100,98, 52, 56, 51,37	t-ZrO_2 + Mn_2O_3	35 ± 1
ZrMn70-cp-ag	32.90, 30.30, 30.85, 50.20, 55.10, 60.15	2.72, 2.95, 2.90, 1.82, 1.67, 1.54	100, 97, 87, 45, 42, 34	t-ZrO_2, * Mn_2O_3	26 ± 1
ZrMn85-cp-ag	31.20, 31.60, 33.20, 36.20, 34.60, 52.05, 60.80	2.87, 2.83, 2.70, 2.48,2.59, 1.76, 1.52	100, 85, 65, 38, 28, 32, 45	t-ZrO_2, * m-zrO_2 Mn_2O_3	28 ± 2
ZrMn100-cp-ag	32.98, 55.16, 23.13, 38.23	2.71, 1.66, 3.84, 2.35	100, 26, 18, 18	Mn_2O_3	6 ± 1
Mn_2O_3-Aldrich-ag	33.10, 55.30, 23.30, 38.40	2.71, 1.66, 3.81, 2.34	100, 29, 19, 17	Mn_2O_3	< 2
Mn_3O_4-Aldrich-ag	33.00, 55.20, 23.20, 38.20	2.71,1.66, 3.83, 2.35	100, 30, 18, 16	Mn_2O_3	2.5 ± 1

Table 4.11: XRD data for selected aged mixed oxides and pure oxides where - ag represents aged samples and m, t and c represents monoclinic, tetragonal and cubic respectively. The main diffraction peaks are represented in 2θ and d_{hkl}, the interplanar spacing corresponding to each peak. Relative Intensity is the intensity of that peak compared to the most intense peak in diffraction pattern. The surface area values shown are the mean of two measurements of the same sample and the error of measurement for each sample. *For ZrMn70-cp –ag and ZrMn85-cp-ag, the phases present are only tentatively suggested due to the broadness and noisiness of the corresponding diffraction peaks – see previous text.

For ZrMn10-cp-ag, the single phase structure of tetragonal or cubic zirconia observed in the fresh sample is maintained after aging. A small increase in the interplanar spacing of ZrMn10-cp from 2.93 to 2.96Å was observed on aging, indicating possible transformation from cubic to tetragonal phase, although this is tentatively suggested due to the absence of raman spectra. For ZrMn30-cp, only one peak with a similar

interplanar spacing of 2.92Å was identified. For ZrMn70-cp-ag and ZrMn85-cp-ag, some shoulders and splitting appeared on the main broad peak between 2θ = 30° and 32°, which could indicate the presence of traces of monoclinic zirconia. As the peak was quite noisy, several small peaks were detected and quantative identification of the zirconia phases present was difficult. In contrast, pure zirconia underwent a severe structural transformation to monoclinic form on aging as identified by the main peaks at 2θ values of 30.85°and 27.6° and the tetragonal phase virtually disappeared. Hence the incorporation of manganese did hinder the transformation of zirconia to the monoclinic phase and resulted in higher surface areas for the mixed oxides after aging compared to zirconia.

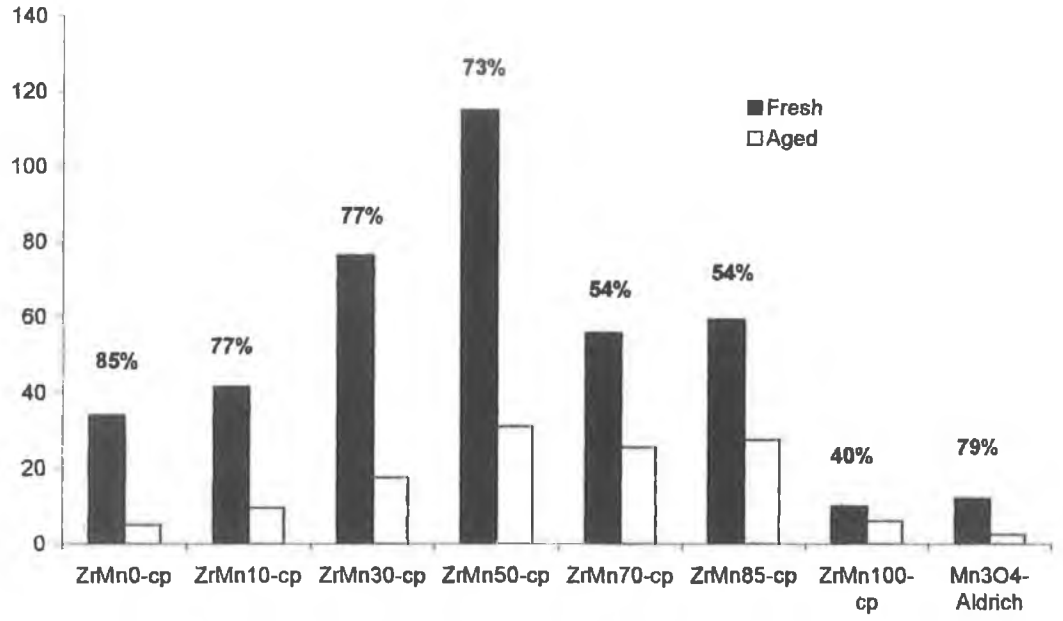

Fig 4.26: Comparison of the surface areas determined by the BET method (m^2g^{-1}) of selected oxides before and after aging. The % loss in surface area on aging for each sample is given in bold above each individual bar chart.

The XRD findings are similar to that reported by Lopez et al (25), who observed that for co-precipitated manganese-zirconia mixed oxides calcined at 800°C, the phases present were the same as those observed in the same samples calcined at 600°C, except for $Mn_{0.9}Zr_{0.1}$. On increasing the calcination temperature from 600 to 800°C, tetragonal ZrO_2 was observed as an extra phase for $Mn_{0.9}Zr_{0.1}$. The same study also found that on increasing the calcination temperature, Mn_0Zr_1 (pure zirconia) showed a significant amount of monoclinic zirconia as well as tetragonal zirconia and all oxides showed a

decrease in surface areas on increasing calcinations temperature. Another study (26) using samples prepared by the sol-gel method found that after calcination at 800°C, a minor phase of Mn_3O_4 was observed in samples $Mn_{0.5}$ $Zr_{0.5}$, $Mn_{0.8}$ $Zr_{0.2}$, $Mn_{0.9}$ $Zr_{0.1}$ and Mn_1 Zr_0. This was the first time that this phase had been reported at that temperature and was attributed to the preparation method used. Another reason could have been the surface area. Choudhary et al (15) observed for that increasing calcination temperature from 500 to 800°C, manganese doped zirconia with a Mn/Zr ratio of 0.25 calcined at 800°C showed the presence of mixed cubic and monoclinic crystalline forms. The monoclinic form was clearly observed as two separate peaks at 28° and 32° with a small tetragonal peak in between. In contrast to the samples used in the current study, while the monoclinic phase was indicated in some samples namely ZrMn70-cp-ag and ZrMn85-cp-ag, it couldn't be identified as single peaks and the tetragonal phase was also still present in relatively large quantities.

4.3.7 Effect on aging on Reduction Characteristics of fresh samples

The temperature programmed reduction profiles of the aged samples are shown in Fig 4.27-4.33. The positions of the main peaks are shown in tabulated in Table 4.13. For ZrMn10-cp-ag, a shoulder at the lower temperature side of the main peak was observed at heating rates of 5 and 20°C/min. For ZrMn30-cp-ag, at 1°C/min, a shoulder developed at the high temperature side of the main peak at approx 328°C. In contrast at higher heating rates, a shoulder developed at the low temperature side of the main peak, especially for profiles taken at 10°C/min and 15°C/min. For ZrMn50-cp-ag, the same peak shape was observed at all heating rates with small shoulders developing at both the high and low temperature side of the main peak. Similarly for ZrMn70-cp-ag, the same peak shape was observed at all heating rates, with two peaks observed. The second peak located at a higher temperature was more defined than the first peak observed at the lower temperature. Furthermore, the peak shape was significantly different than that of the fresh sample where a flat maximum was observed for the second peak.

In contrast for MnZr85-cp-ag, multiple peaks were observed at all heating rates. Two main peaks were observed at all heating rates but the number of shoulders observed on both the high and low temperature side of the main peaks depended on the heating rate used. At 1 and 5°C/min, a small shoulder on the low temperature side of the first peak at 272 and 311°C is suggested, which becomes more evident at higher heating rates. In addition, at the highest heating rate, a shoulder (approx 450°C) at the high temperature side of the second peak is observed. For Mn_2O_3–Aldrich-ag, a slight shoulder was observed at the lowest heating rate, but in general only one peak was observed at all other heating rates, with the peak appearing wider at 10 and 15°C/min than the one observed at 5°C/min. For Mn_3O_4-Aldrich-ag, a distinct shoulder was observed at approx 305°C at the lowest heating rate. The shoulder was less distinct with the other heating rates but still present, with the same basic peak shape at all heating rates.

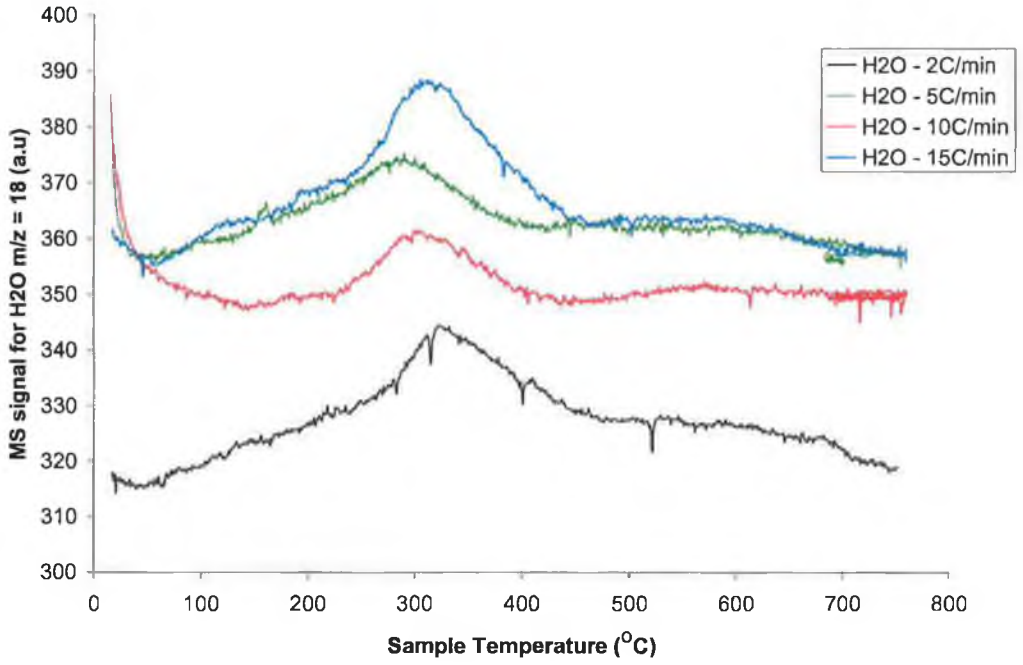

Fig 4.27: TPR-MS at various heating rates of ZrMn10-cp-ag

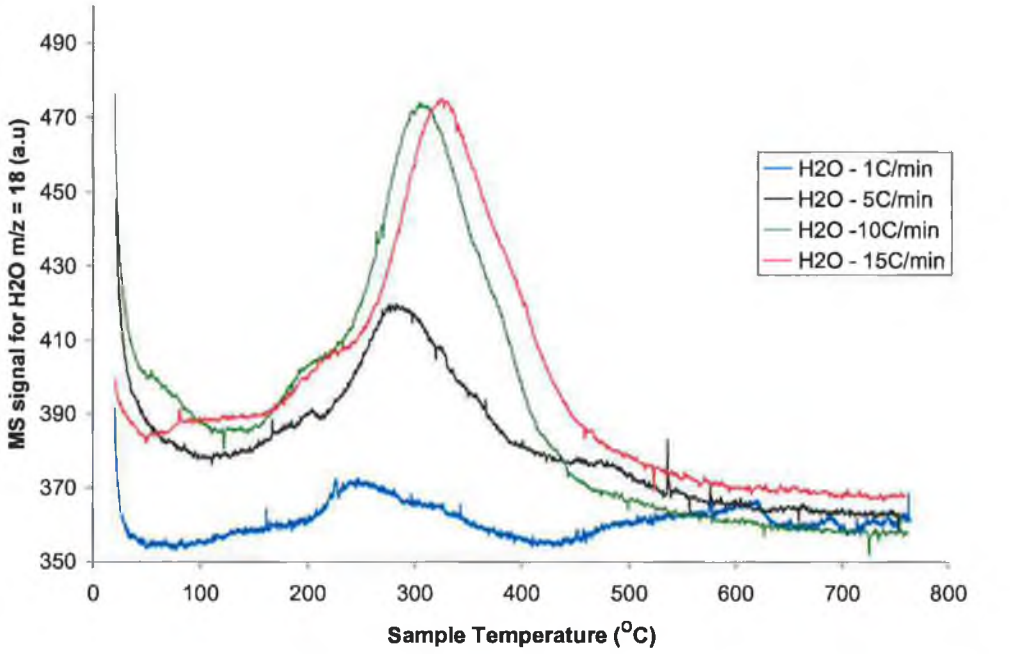

Fig 4.28: TPR-MS at various heating rates of ZrMn30-cp-ag

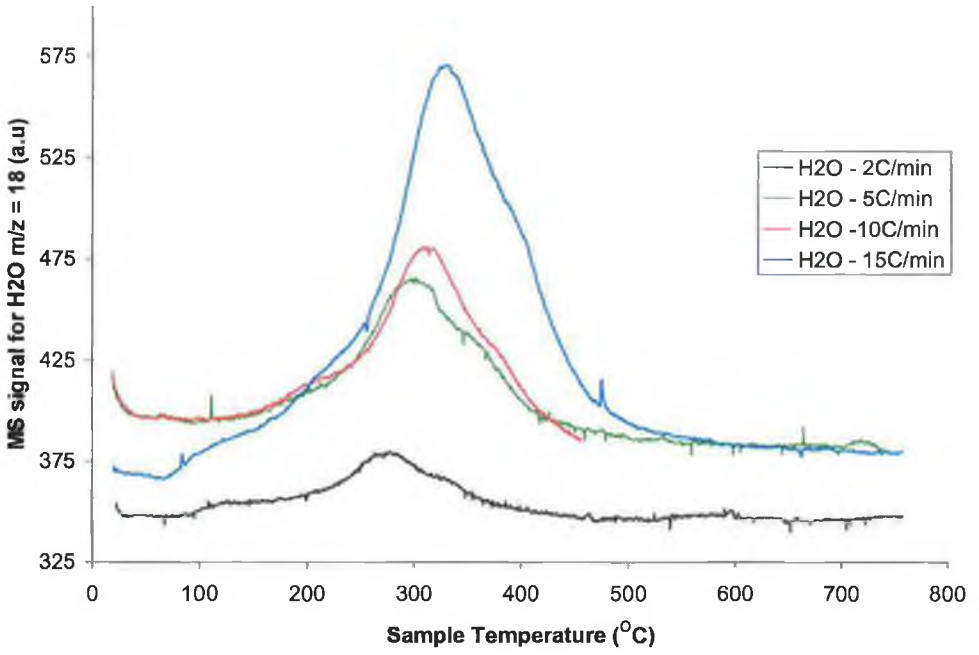

Fig 4.29:TPR-MS at various heating rates of ZrMn50-cp-ag.

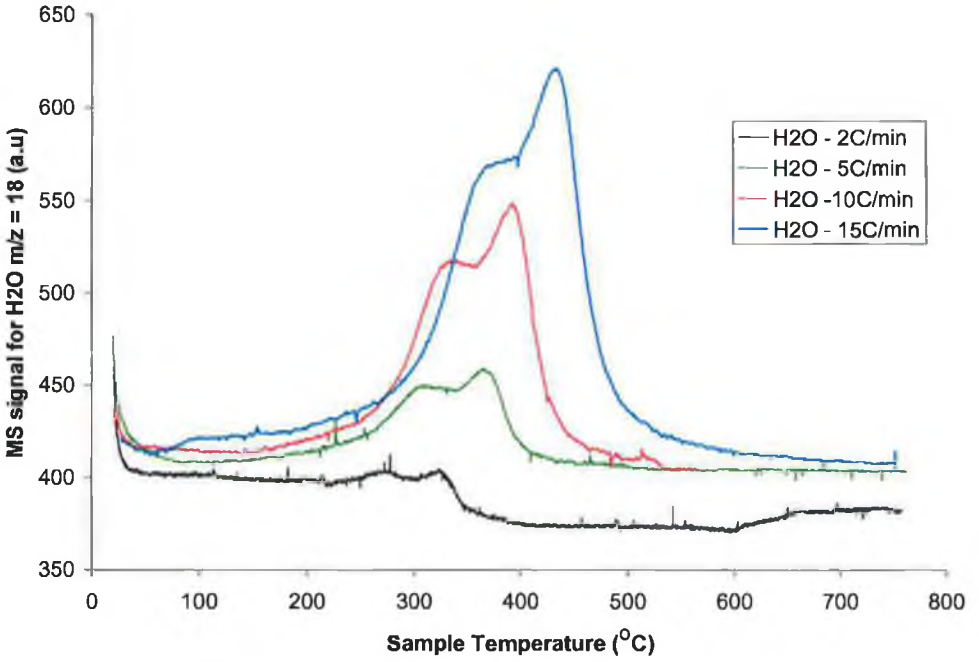

Fig 4.30: TPR-MS at various heating rates of ZrMn70-cp-ag

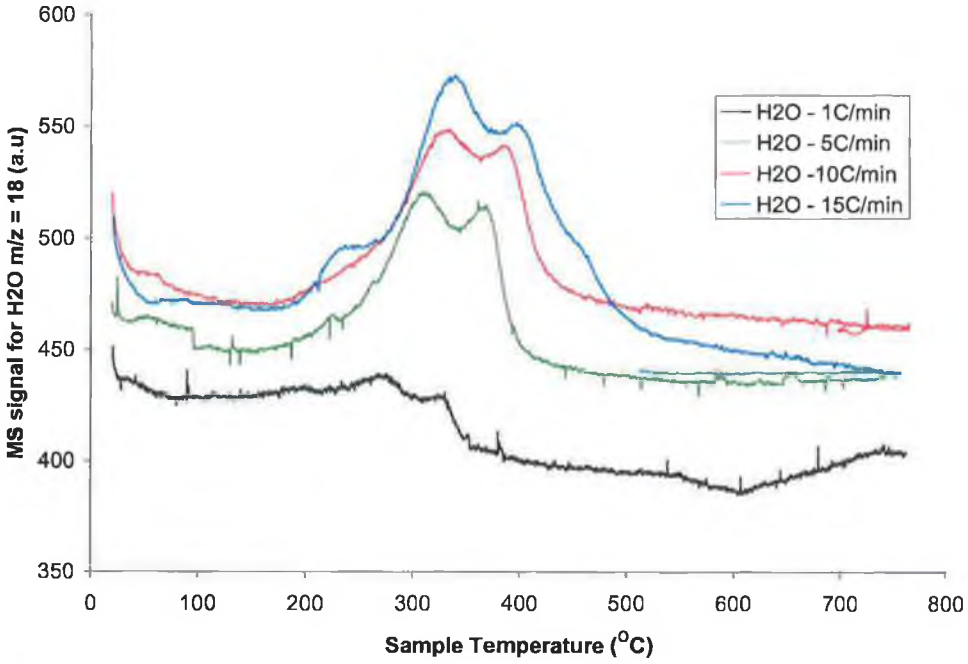

Fig 4.31: TPR-MS at various heating rates of ZrMn85-cp-ag

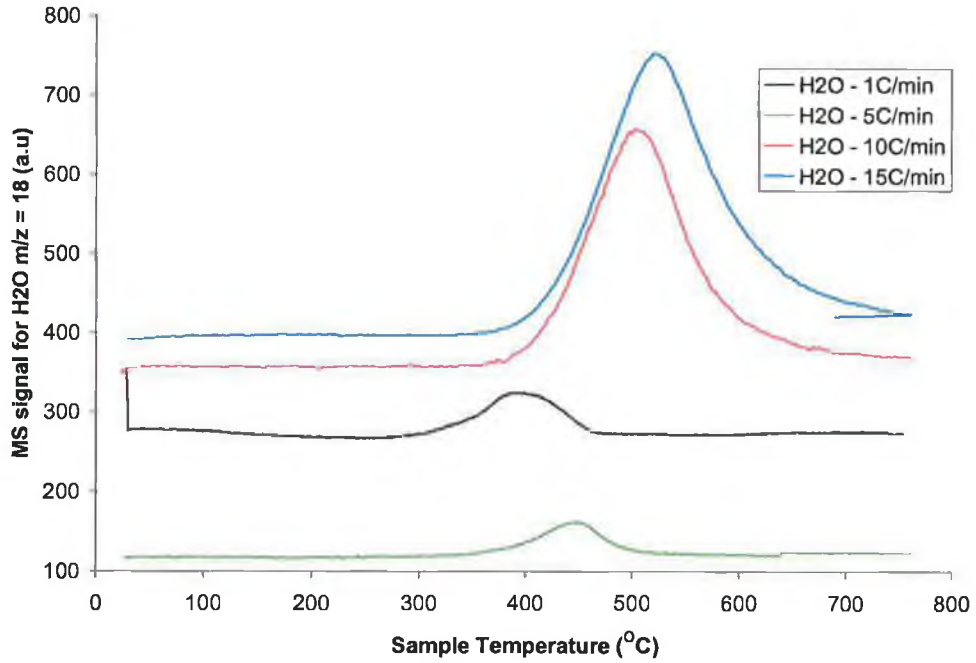

Fig 4.32: TPR-MS at various heating rates of Mn_2O_3-Aldrich-ag

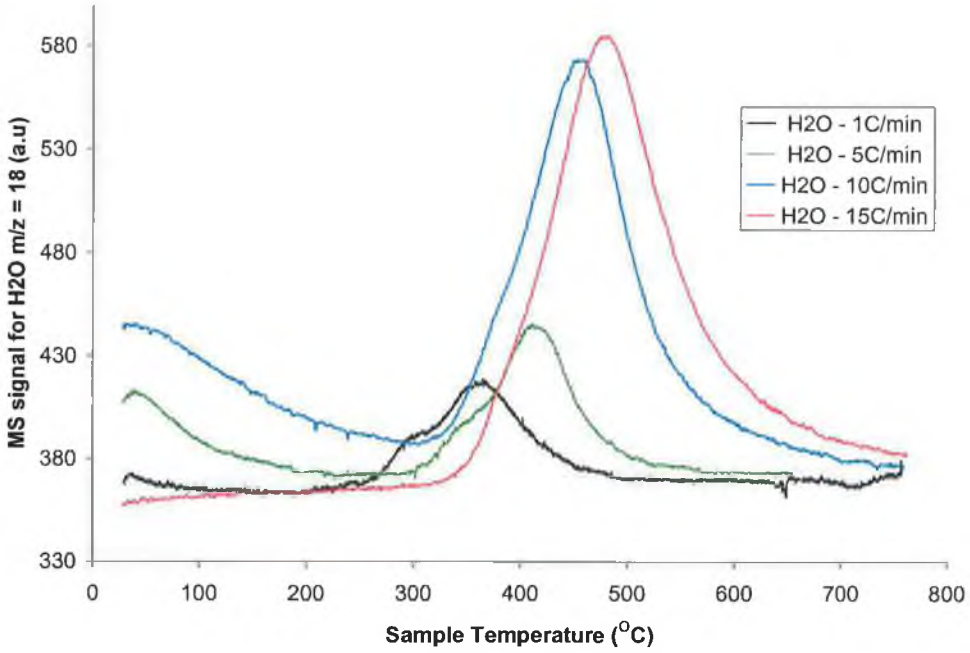

Fig 4.33: TPR-MS at various heating rates of Mn_3O_4-Aldrich-ag

In order to compare the temperature programmed reduction profiles of each catalyst properly to each other, the profiles at 10°C/min are shown in Fig 4.34. ZrMn10-cp-ag, ZrMn30-cp-ag and ZrMn50-cp-ag, show very similar peak shapes in similar temperature ranges, with the intensity of ZrMn10-cp-ag considerably less than that of the other two catalysts. Only very small differences in the T_{max} were observed for the aforementioned catalysts. For ZrMn70-cp-ag and ZrMn85-cp-ag, similar peak shapes were observed, except that for ZrMn70-cp-ag, the second peak appeared more pronounced. The first reduction peak of both samples occurred at slightly higher temperatures than reduction peaks observed for the lower manganese content samples. The second peak occurred at significantly higher temperatures. Mn_2O_3-Aldrich-ag and Mn_3O_4-Aldrich-ag showed higher temperatures of reduction than the mixed oxides. The intensities of the reduction peaks of the mixed oxide were increased on aging, with the exception of ZrMn10-cp-ag, while no change was observed for Mn_2O_3-Aldrich and Mn_3O_4-Aldrich. The increase in peak intensities cannot be due to use of a larger sample size during analysis since if this were the case, an increase in the temperatures of maximum reduction would be expected. Instead as discussed later, a decrease in temperatures of maximum reduction was observed.

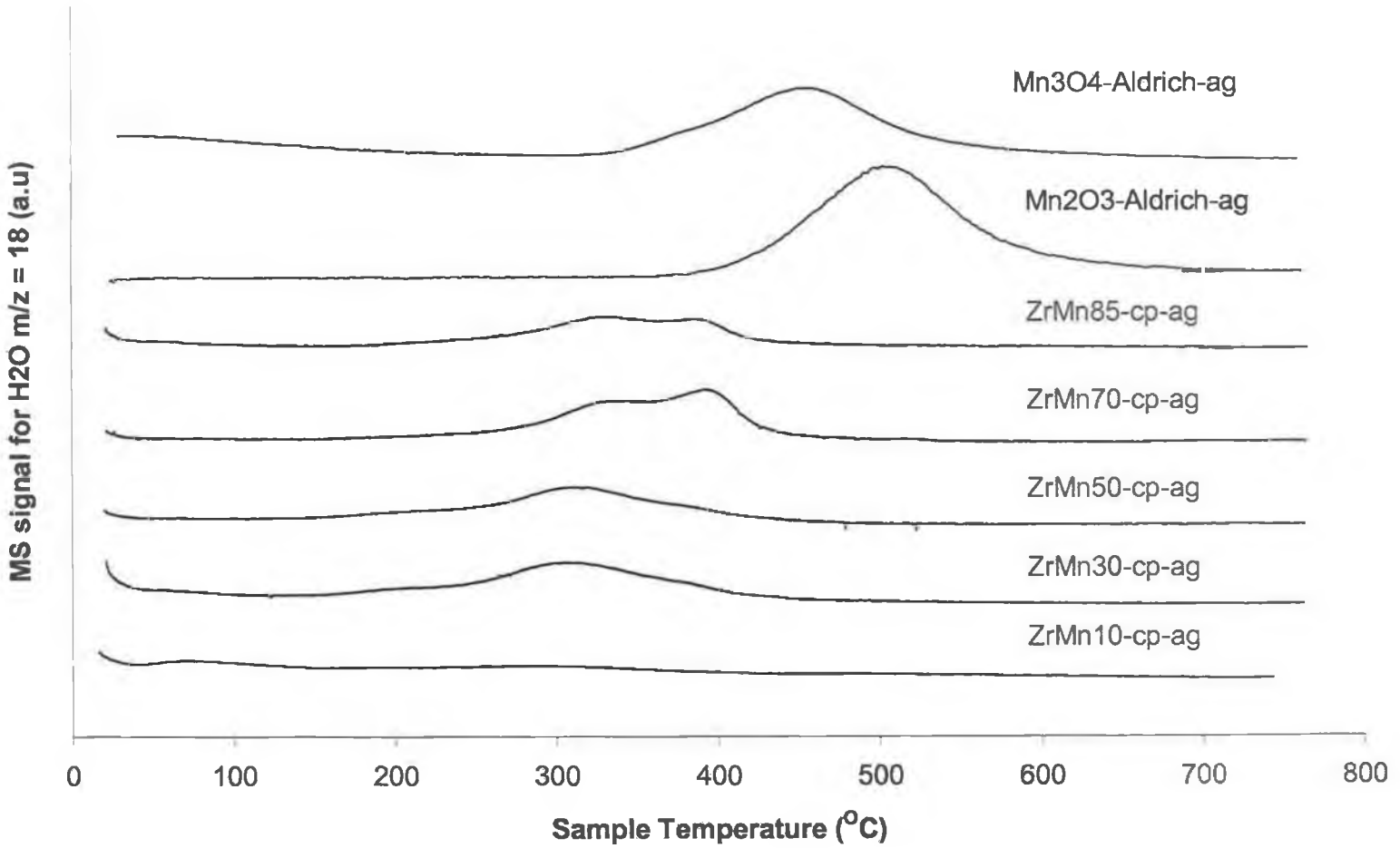

Fig 4.34: Comparison of TPR profiles of selected aged oxides at a linear heating rate of 10°C/min.

XRD was performed on aged Mn_2O_3 and Mn_3O_4 after temperature programmed reduction experiments at a linear heating rate of 1°C/min. Since only small amounts of sample (approx 20mg) were actually used during the TPR run, peaks attributed to the copper sample holder were observed in the XRD patterns, which masked the presence of other peaks. Hence neglecting those peaks due to the sample holder (at 2θ values of 43, 49.95 and 73.45°), the remaining peaks are reported in Table 4.12. In the case of Mn_2O_3-Aldrich-ag, all characteristic peaks of MnO are observed, indicating that the final reduction product is MnO, in agreement with Stobbe et al (7). For Mn_3O_4-Aldrich-ag, the absence of one characteristic peak means that the presence of MnO can only be tentatively suggested.

Sample	**Main Peaks-2θ**	**Main Peaks-d_{hkl} (Å)**	**Relative Intensity (%)**
Mn_2O_3 aged after TPR at 1°C/min	34.9,40.5, 58.65, 70.1	2.57, 2.23, 1.57, 1.34	67, 100, 63 27
Mn_3O_4 aged after TPR at 1°C/min	40.55, 58.75 70.05	2.23, 1.57 1.34	100, 70 62
MnO JCPDS : 7-230		2.22, 2.57 1.57, 1.34	100, 60, 60 20

Table 4.12: Comparison of XRD data of aged Mn_2O_3 and Mn_3O_4 after TPR runs under hydrogen with that of MnO.

The temperatures of maximum reduction at 10°C/min for the first main peak of both fresh and aged samples are shown in Fig 4.35. On aging, the temperatures of maximum reduction decreased compared to the fresh samples, the magnitude of which depended on the composition of the sample All mixed oxides showed a decrease in temperature of maximum reduction of the main peak in the case of ZrMn10-cp, ZrMn30-cp and ZrMn50-cp and the first peak in the case of ZrMn70-cp and ZrMn85-cp.. The largest decreases were observed for ZrMn30-cp and ZrMn70-cp, with very similar smaller decreases observed for the remaining mixed oxides. In contrast, commercial Mn_2O_3 and Mn_3O_4 showed increases in T_{max}, with a larger increase being observed for the latter. For ZrMn70-cp and ZrMn85-cp with two peaks, the second peak position also decreased by 37 and 16°C respectively. The trend in reduction temperatures also changed on aging for the mixed oxides. Previous authors have reported a relationship between the temperatures of reduction and the particle size surface area and crystallinity of manganese oxides (7,13). Hence it may be expected that the decrease in surface area

would cause an increase in the reduction temperatures of the aged samples. Hence while some of the decreases in T_{max} are not very large, it is proposed that there was a marked increase in the reducibility to counteract the effects of surface area on the reduction profiles of the mixed oxides.

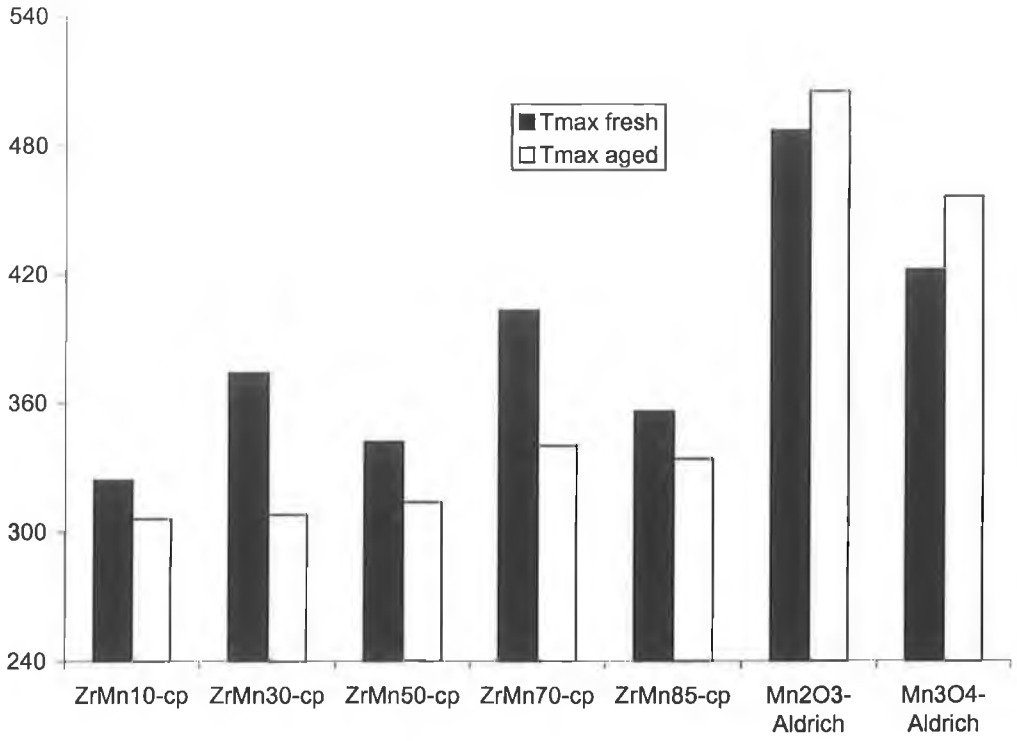

Fig 4.35:Comparison of temperatures of maximum reduction (T_{max}) of first peak of fresh and aged oxides at a linear heating rate of 10°C/min. T_{max} values used were taken from Table 4.4 and 4.13 respectively.

The T_{max} values determined at each heating rate were used to calculate the activation energies of reduction by both Kiss and Oz methods (see Table 4.13) and a comparison of E_a values determined for the first reduction peak between equivalent fresh and aged samples is represented in Fig 4.36. As observed for the fresh samples, apparent activation energies calculated by the Ozawa method are higher than those observed for the Kissinger method, but the same trend for both methods are observed. For ZrMn10-cp and ZrMn30-cp, the apparent activation energies of reduction are lower for the aged samples, while the reverse is observed for ZrMn50-cp, ZrMn70-cp and ZrMn85-cp. As observed for the fresh samples, apparent activation energies calculated by the Ozawa method are higher than those observed for the Kissinger method, but the same trend for both methods are observed. For ZrMn10-cp and ZrMn30-cp, the apparent activation

energies of reduction are lower for the aged samples, while the reverse is observed for ZrMn50-cp, ZrMn70-cp and ZrMn85-cp, even though T_{max} for all aged mixed oxides are lower than fresh samples. However when errors are taken into account as shown in Fig 4.40, no change observed in the activation energies on aging except for ZrMn10-cp.

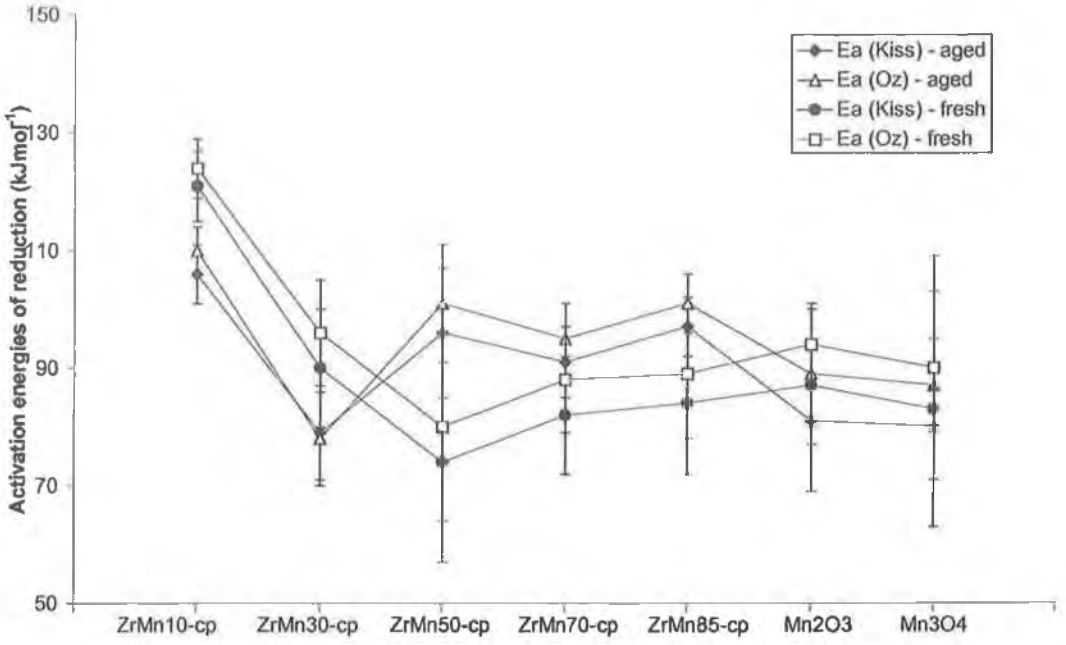

Fig 4.36 :Comparison of activatation energies of reduction calculated via the Kissinger (Kiss) and Ozawa (Oz) equations for the first reduction peaks in the TPR from Table 4.4 and 4.13 respectively.

Sample	T_{max} (°C) @						E_a (kJmol^{-1})		R^2	
	1°C /min	2°C /min	5°C/ min	10°C/ min	15°C /min	20°C /min	Kiss	Oz	Kiss	Oz
ZrMn10-cp-ag			s 291	306	316	s 325	106 ± 5	110 ± 4	0.996	0.997
ZrMn30-cp-ag	248 s		285	s 308 s	329 s		79 ± 8	78 ± 8	0.978	0.983
ZrMn50-cp-ag		s278s	s 303 s	s 314 s	s 333 s		96 ± 11	101 ± 10	0.975	0.979
ZrMn70-cp-ag										
Peak 1	274		313	340	349		91± 6	95 ± 6	0.991	0.993
Peak 2	324		366	394	405		101± 5	106 ± 5	0.994	0.995
ZrMn85-cp-ag										
Peak1	s 272		s 311	s 334	s 341		97 ± 5	101 ± 5	0.995	0.996
Peak 2	327		366	386	399 s		117 ± 2	122± 2	0.999	0.999
Mn_2O_3-Aldrich-ag	399		448	505	522		81 ± 12	89 ± 12	0.955	0.967
Mn_3O_4-Aldrich-ag	s 364		s 414	s 456	s 481		80 ± 9	87 ± 8	0.975	0.981

Table 4.13:Activation energies for the reduction (E_a) of various aged metal oxides by hydrogen calculated by equation 4.8 (Kiss) and equation 4.9 (Oz) equations where R^2 is the linear regression coefficient and T_{max} is the temperature of maximum water evolution at each heating rate. s to the right and/or left of the peaks indicate low temperature or high temperature shoulders respectively.

4.3.8 Effect of aging on the oxidation activities of fresh samples

The catalytic activity of the oxides after aging at 800°C for 8 hours was determined by measuring their activity for the combustion of propane and methane, using the procedure described in Chapter 2. Tables 4.14 and 4.15 summarises the oxidation activities for both propane and methane oxidation of selected aged samples respectively. Errors in the experimental determination of T_{10}, T_{50} and T_{90} values for both methane and propane combustion have been estimated and discussed in section 4.3.4 for fresh samples and the same values will be used in this section. Herein, the activity will be discussed primarily in terms of T_{50} values for the reasons outlined in section 4.3.4.

Sample	T_{10}(°C)		T_{50}(°C)		T_{90}(°C)	
	Run 1	**Run 2**	**Run 1**	**Run 2**	**Run 1**	**Run 2**
ZrMn0-cp-ag						
ZrMn10-cp-ag	206	226	261	235	271	246
ZrMn30-cp-ag	200	150	212	210	224	223
ZrMn50-cp-ag	155	179	209	211	223	222
ZrMn70-cp-ag	215	197	235	210	247	222
ZrMn85-cp-ag	161	226	234	236	247	247
Mn_2O_3-Aldrich-ag	297	315	369	395	501	>500
Mn_3O_4-Aldrich-ag	256	233	292	293	374	381

Table 4.14: Propane combustion activity of selected oxides after aging at 800°C for 8 hours where T_{10}, T_{50} and T_{90} refer to temperatures at which 10, 50 and 90% conversion of propane occurred. Samples were initially tested (run 1) and then cooled to room temperature and retested in the same sample tube (run 2).

Sample	T_{10}(°C)		T_{50}(°C)		T_{90}(°C)	
	Run 1	**Run 2**	**Run 1**	**Run 2**	**Run 1**	**Run 2**
ZrMn30-cp-ag	358	364	420	420	490	498
ZrMn50-cp-ag	372	360	417	417	489	496
ZrMn70-cp-ag	354	312	380	367	>575	>575
ZrMn85-cp-ag	366	367	432	430	516	521
ZrMn100-cp-ag	414	nd	444	nd	562	nd
Mn_2O_3-Aldrich-ag	484	486	587	586	>>600	>>600
Mn_3O_4-Aldrich-ag	416	478	457	458	563	568

Table 4.15: Methane combustion activity of selected oxides after aging at 800°C for 8 hours where T_{10}, T_{50} and T_{90} refer to temperatures at which 10, 50 and 90% conversion of methane occurred. Samples were initially tested (run 1) and then cooled to room temperature and retested in the same sample tube (run 2).

The plot of T_{50} values for runs 1 and 2 for both propane and methane for each aged sample are shown in Fig 4.37. A similar trend was observed for the activity of the mixed oxides after aging for both methane and propane oxidation on run 1 with the exception of ZrMn70-cp-ag. A large increase in the activity, as indicated by the significant decrease in light-off temperature, compared to the other mixed oxides was observed for methane oxidation, while a smaller decrease in the T_{50} value was observed for propane. Higher activity is observed for Mn_3O_4-Aldrich-ag compared to Mn_2O_3-Aldrich-ag for both gases. On run 2, nearly identical values were recorded for methane combustion for all oxides, with the exception of ZrMn70-cp-ag where a decrease in T_{50} of 13°C was observed. A similar decrease in T_{50} was also observed for the same sample for propane oxidation on run 2. ZrMn10-cp-ag also showed a significant increase in T_{50} values from run 1 to run 2.

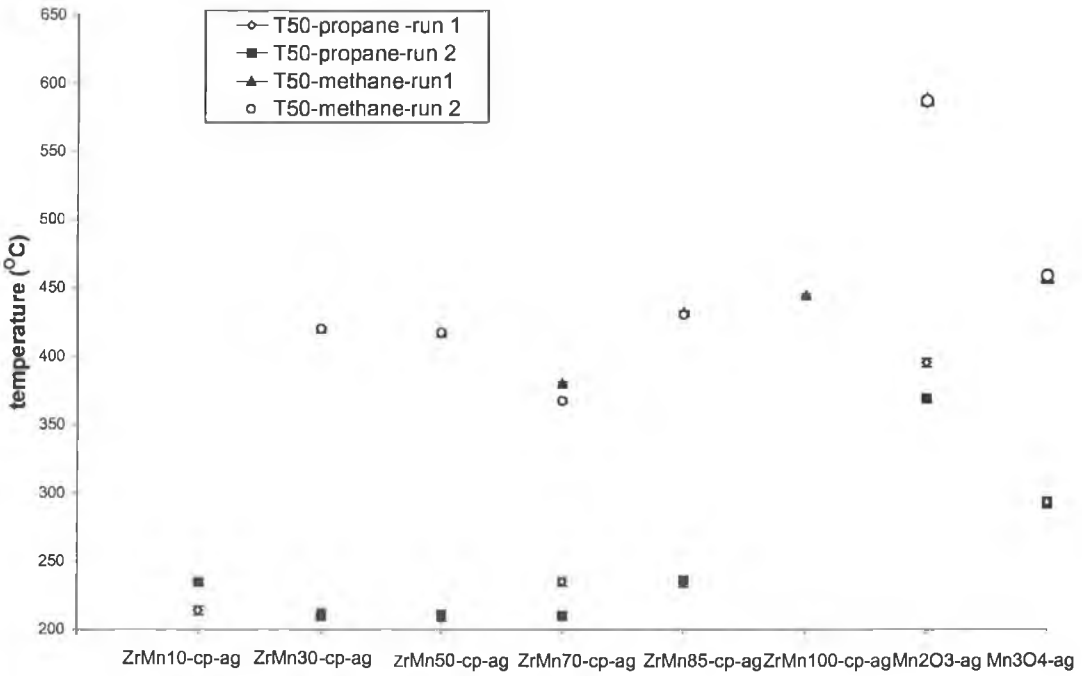

Fig 4.37: Temperature (°C) of 50% conversion of methane and propane (T_{50}) for both run 1 and 2 of samples prepared by method 1 after aging treatment. ZrMn10-cp-ag and ZrMn100-cp-ag were not tested for methane and propane oxidation respectively and hence are not included in Fig 4.37.

Similarly to that observed for fresh Mn_2O_3-Aldrich, an increase in T_{50} on run 1 to run 2 was observed for propane oxidation, but not for methane oxidation. In the case of ZrMn100-cp, a moderate decrease in activity by approx 28°C for methane combustion was observed. This was in the range of the decrease observed for Mn_2O_3-Aldrich for methane, with an increase in light-off temperature of 56°C. Mn_3O_4-Aldrich was the least thermally stable, with its light-off temperature increasing by 71°C to 457°C for methane. This decrease in activity can be attributed to the formation of the less active Mn_20_3, which occurred at 400°C (53). This transformation was confirmed experimentally by XRD on the Mn_3O_4-Aldrich-ag (see Table 4.11). In contrast, both Mn_2O_3-Aldrich and ZrMn100-cp retained the bixbyite structure on aging as indicated by the XRD data in Table 4.11.

The relationship between oxidation activity of the aged samples and their surface areas are shown in Fig 4.38. As observed for the fresh samples, there is no obvious relationship between surface area and activity of the aged mixed oxides. Despite almost double its surface area, ZrMn50-cp-ag has a similar to ZrMn30-cp-ag. ZrMn10-cp-ag has the lowest surface area and also shows the highest light-off temperature of the mixed oxides for propane. The activity of ZrMn70-cp-ag shows two different trends between surface area and light-off temperature depending on whether propane or methane gas was used. For propane oxidation, a decrease in surface area compared to ZrMn50-cp-ag results in an increase in the light-off temperature (T_{50}), while for methane oxidation, a decrease in the light-off temperature was observed. Similarly to the fresh samples, the pure manganese oxides have lower surface area than the mixed oxides. The least active sample for both methane and propane oxidation is Mn_2O_3 with the highest light-off temperature and lowest surface area. Despite a difference in surface area, ZrMn100-cp-ag and Mn_3O_4-Aldrich-ag have similar activities for methane combustion, with the latter being slightly less active. The activity of aged Mn_3O_4 is similar to ZrMn100-cp-ag for methane oxidation but is less active than the mixed oxides for propane oxidation. For propane, any decrease in surface area resulted in a small but non linear increase in T_{50}. For methane, general agreement was observed where an increase in surface area resulted in an increase in T_{50} from ZrMn50-cp-ag to ZrMn85-cp-ag.

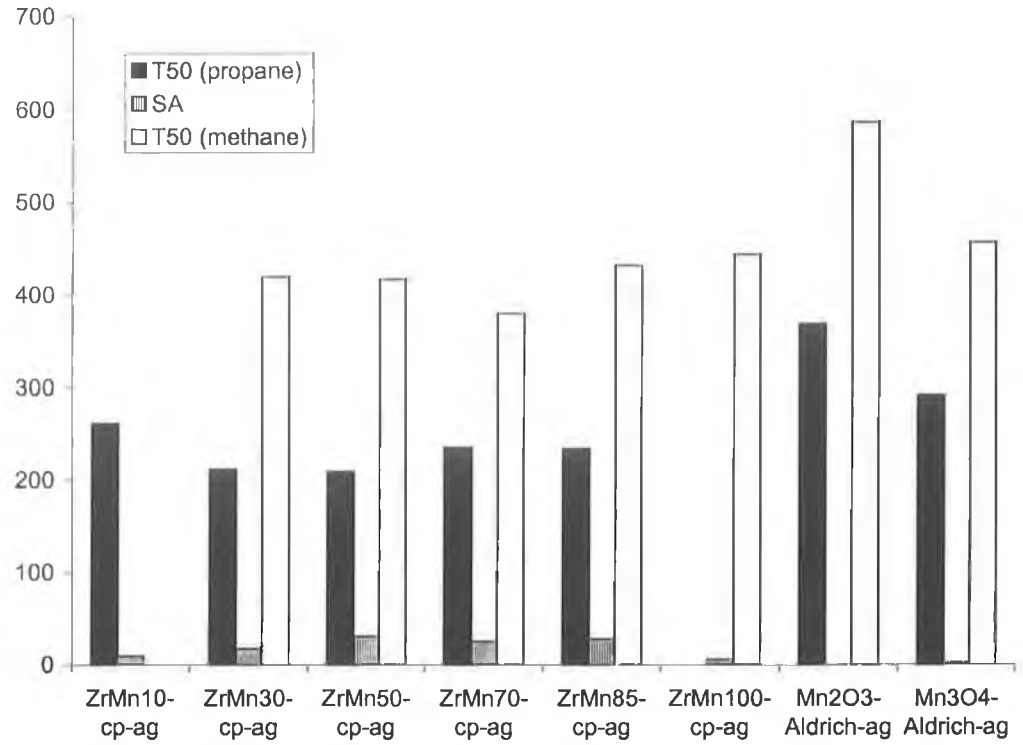

Fig 4.38: BET surface areas (SA) and temperatures (°C) of 50% conversion of propane and methane for run 1 of selected samples as identified on the horizontal axis. No experimental value for oxidation of propane and methane were obtained at the time for ZrMn100-cp-ag and ZrMn10-cp-ag respectively.

The reaction rates per surface area for the aged oxides for methane combustion were calculated using equation 4.10 and are shown in Table 4.16. On comparison to the fresh samples (see Table 4.8), an increase in r of at least one order of magnitude was observed for the samples. This is to be expected since for the mixed oxides, the surface areas decreased while the percentage conversions remained constant. Of the aged mixed oxides, ZrMn30-cp-ag exhibits a higher intrinsic reaction rate (per m^2) than ZrMn50-cp-ag and ZrMn85-cp-ag at the majority of the temperatures selected. Of ZrMn100-cp-ag and Mn_3O_4-Aldrich-ag, the latter is more intrinsically active at temperatures greater than 400°C due to its lower surface area.

Sample	r (μmol $min^{-1}m^{-2}$) at						
	350°C	375°C	400°C	425°C	475°C	500°C	550°C
ZrMn30 -cp-ag	0.198 (8)	0.372 (15)	0.694 (28)	1.512 (61)	2.082 (84)	2.305 (93)	2.330 (94)
ZrMn50 -cp-ag	0.076 (6)	0.153 (12)	0.357 (28)	0.803 (63)	1.058 (83)	1.173 (92)	1.211 (95)
ZrMn70 -cp-ag	0.103 (6)	0.738 (43)	1.338 (78)	1.424 (83)	1.493 (85)	1.510 (88)	1.150 (88)
ZrMn85 -cp-ag	0.112 (7)	0.207 (13)	0.287 (18)	0.653 (41)	1.275 (80)	1.370 (86)	1.514 (95)
ZrMn100 -cp-ag	0.149(2)	0.297 (4)	0.446 (6)	1.041 (14)	5.279 (71)	5.725 (77)	6.989 (94)
Mn_3O_4-Aldrich-ag	0.114 (1)	0.595 (4)	1.041 (7)	1.933 (13)	10.85 (73)	11.59 (78)	13.08 (88)

Table 4.16 :Intrinsic reaction rates of selected aged oxides samples for methane combustion at various temperatures using equation 4.10.

The reduction profiles of the aged samples were determined from TPR-MS as for the fresh samples and have been discussed in section 4.3.5. Single peaks were observed for ZrMn10-cp-ag, ZrMn30-cp-ag and ZrMn50-cp-ag, while two main peaks were observed for ZrMn70-cp-ag and ZrMn85-cp-ag. In a similar fashion to the fresh oxides, the temperature of maximum reduction (first peak or in the case of some oxides the only peak observed) of the aged samples was plotted against the light-off temperature (T_{50}) of both propane and methane in Fig 4.39. The maximum reduction temperatures are recorded in Table 4.13 at a linear heating rate of 10°C/min. ZrMn30-cp-ag and ZrMn50-cp-ag have similar T_{50} values for both methane and propane oxidation and also temperatures of maximum reduction. The temperature of maximum reduction of ZrMn10-cp-ag is also the same as that observed for ZrMn30-cp-ag and ZrMn50-cp-ag but the activity for propane oxidation was lower than the other two samples. It is important to note that on run 2 for ZrMn10-cp-ag, a lower T_{50} value of 235°C was observed. For ZrMn70-cp-ag, a correlation between temperature of maximum reduction and T_{50} was observed for propane but not for methane. An increase in T_{max} compared to the lower manganese content samples resulted in an increase in T_{50} of propane but a decrease in T_{50} for methane combustion. For ZrMn85-cp-ag, a slight increase in T_{max}

compared to ZrMn30-cp-ag and ZrMn50-cp-ag resulted in a similar increase in T_{50} values for both propane and methane combustion compared to those samples. The highest T_{50} values for both propane and methane combustion and highest reduction temperature were associated with Mn_2O_3-Aldrich-ag. A decrease in T_{max} of Mn_3O_4-Aldrich-ag compared to Mn_2O_3-Aldrich-ag resulted in a lower T_{50} values for both propane and methane, but the magnitude of difference between the activity results of Mn_3O_4-Aldrich-ag when compared to the other mixed oxide samples varied depending on the reactant gas used. In the case of propane, the T_{50} value was much higher than the mixed oxides.

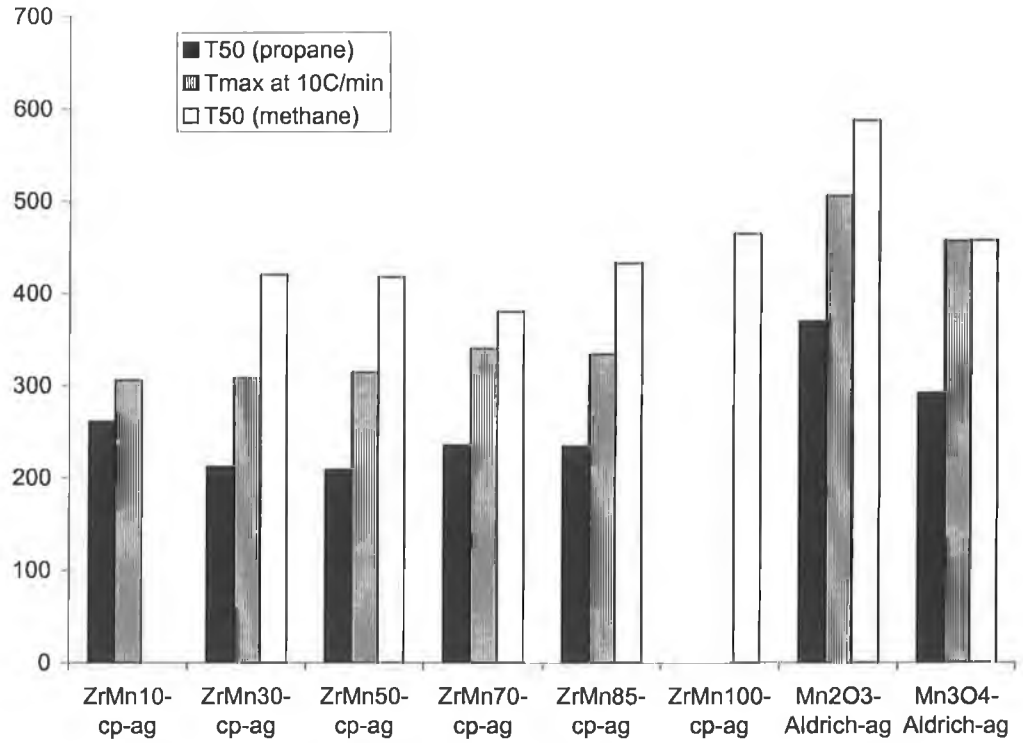

Fig 4.39: Plot of temperature of maximum reduction for first TPR peak (T_{max}) at heating rate of 10°C/min from Table 4.13 versus temperature of 50 % conversion (T_{50}) for propane and methane for various aged oxides.

The activities of the fresh and aged samples for both propane and methane oxidation are compared in Fig 4.40. In general, the aged mixed oxides show similar or reduced T_{50} on aging in comparison to the pure manganese oxides which all show an increase in T_{50} on aging. The effect of aging is greater for propane than for methane. The same trend between activity and Manganese content is the same on fresh and aged samples for propane oxidation.

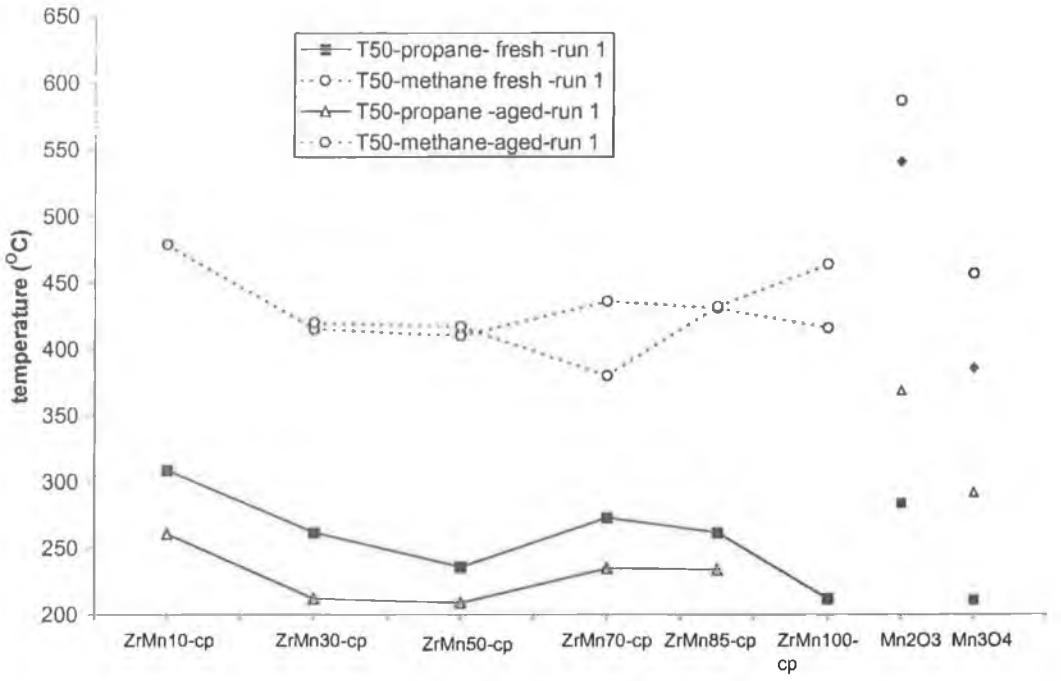

Fig 4.40: Plot of temperatures of 50% conversion for methane and propane on initial testing for fresh and aged samples as indicated on the horizonal axis.

Alifanti et al (58) have proposed that methane combustion over perovoskites corresponded to a simple first order rate model, while propane oxidation was consistent with the Mars-Van-Krevelen type mechanism (58,59). For methane combustion, the initial C-H bond was broken homolytically to form a methyl radical and hydroxyl component (58). The second step was reported to involve movement of the methyl radical and reaction with the oxygen species coordinated around the positively charged metal. Surface bound carbon dioxide and water then resulted which were desorbed at a comparatively slow rate. The final step involves reoxidation of the reduced metal cations via dissociation of dioxygen. Overall reaction kinetics depended on the availability of the oxygen species and coordination of the oxygen species to the surface.

The overall reaction rate has been reported to be controlled by the activation of the C-H bond or by the final reoxidation step, depending on the initial strength of the C-H bond and consequently the temperature controlling the rates of the individual steps (58). The activation temperature for methane reaction is high and at the temperatures required to activate it, oxygen mobility becomes sufficiently fast and the rate of catalytic combustion is nearly oxygen independent (58). In contrast the more facile oxidation of

lighter hydrocarbons such as propane means that oxidation takes place at lower temperatures and that the reoxidation rate is quite slow, which in turn influences the combustion rate. The study (58) proposed that the variation in activity with composition of the perovskite catalysts was more noticeable in the low temperature activity region of propane compared to the higher temperature region associated with methane. Hence the increased reactivity of propane in comparison to that of methane could be the reason for larger changes in light-off temperatures of the former.

The fresh and aged activities show the reverse trend to surface area results where lower surface areas due to sintering are observed for all oxides on aging. In the case of Mn_3O_4, a complete structural transformation to Mn_2O_3 was also observed. Choudhary et al (15) investigated the effect of increasing calcination temperatures from 500 to 800C on the activity of manganese-doped zirconia (Me/Zr ratio of 0.25). The methane combustion activity of the sample calcined at 500 and 700°C were nearly the same despite surface areas of $105m^2g^{-1}$ compared to $107m^2g^{-1}$. The same sample calcined at 600°C had a much lower T_{50} and hence higher activity than samples calcined at 500 and 700°C with an intermediate surface area of 90 m^2g^{-1}. The maximum activity of the sample calcined at 600°C was attributed to the presence of the cubic phase. After calcination at 800°C, the activity decreased due to the presence of the mixed monoclinic and cubic phases.

Alifanti et al (58) found that for selected perovskite samples, specific surface area had little or only a minor effect on the total amount of evolved oxygen as detected by O_2-TPD and that samples with the lowest surface areas after extensive aging at 923K, 1135 and 1223K evolved more oxygen than from the samples having surface areas three times higher. In general activity has been perceived to be due to two main factors: an intrinsic factor relating to composition and crystalline structure and an extrinsic factor, which was related to texture and surface morphology. As discussed in Section 1.4.3 of Chapter 1, studies on ceria-zirconia have also reported no direct relationship between OSC and surface area. Alifanti et al (58) proposed that in aged samples, a high oxygen mobility can compensate for the negative effect of lower surface area and the low number of active sites. On decreasing surface area, the bulk properties of perovskites become more important for catalytic activity.

Hence, in the current study, the reduction properties of the mixed oxides improved on aging, which compensated for the lower surface area and, in the case of propane,

improved the oxidation activity. For methane the initial activity of the mixed oxides was maintained. Another important point is that pure manganese oxide prepared by precipitation with ammonia only showed a moderate decrease in activity on aging for methane combustion. At the time of testing of the mixed oxides for propane oxidation, the activity of aged ZrMn100-cp was not determined. To check that the moderate increase in activity observed in methane was reproducible, the ZrMn100-ag sample was also tested for propane. On retesting, a large increase in the peak areas corresponding to unreacted propane at the start of the experiment was observed, despite use of the same flow rates. Hence, the fresh sample of ZrMn100-cp was retested as well as fresh and aged ZrMn70-cp. Only a slight increase in T_{50} value of 12°C was observed on aging of ZrMn100-cp. For ZrMn70-cp, a decrease in T_{50} of 77°C was observed on aging when the activity of both fresh and aged sample was retested under the same conditions as ZrMn100-cp. This indicates that while the preparation method is very important to maintaining the activity of the samples on aging, the increase in activity for propane is only observed when zirconium is present in the mixed oxides.

The activity of the supported oxides after aging were determined, the results of which are reported in Table 4.17.

Sample	**SA**	**CH_4**			**C_3H_8**		
	(m^2g^{-1})	**T_{10}**	**T_{50}**	**T_{90}**	**T_{10}**	**T_{50}**	**T_{90}**
ZrMn50-cp-ag	35	372	417	489			
0.5 wt % Pt/Al_2O_3-ag	148	448	486	508			
1 wt % Pt/Al_2O_3-ag	nd				99	182	196

Table 4.17: Activity of aged supported oxides after aging at 800°C for 8 hours for the combustion of methane and propane. T_{10}, T_{50} and T_{90} refer to temperatures of 10, 50 and 90% of conversion in °C and SA represents the surface area determined by the BET method.

For methane combustion, aged mixed oxides and pure manganese oxide prepared by co-precipitation showed T_{50} that were lower than that observed for 0.5 wt% Pt/Al_2O_3 . For propane oxidation, as observed for the mixed oxides, the activity of the platinum catalyst increased on aging but aged 1 wt%/Pt/ Al_2O_3 was more active than aged manganese-zirconia mixed oxides.

4.4 Conclusions

The co-precipitation method using ammonia as the precipitating agent was used to prepare high surface area mixed manganese-zirconium oxides, ZrMnX-cp with X values of 0, 10, 30, 50, 70, 85 and 100, which denoted the calculated mol% of manganese. The surface areas of the mixed oxides were in the range 41-115m^2g^{-1} and were significantly higher than those observed for pure zirconia and pure manganese oxide. The preparation parameters namely, rate of ammonia addition, amount of ammonia added, stirring time of precursor solution prior to addition of ammonia and volume of water, were varied for one sample in order to ascertain the effect of preparation conditions on surface area. Of these preparation parameters, stirring time of the solution prior to addition of the base and volume of water used had the most significant effect on the surface area. Varying both of these parameters could significantly improve the surface areas of ZrMn50-cp. An optimised preparation procedure including 1 hour stirring time and addition of base over 1 hour increased the surface area from approx 115m^2g^{-1} to 152 m^2g^{-1}. Large increases in surface area were also observed for samples with lower manganese contents when the same optimised procedure was applied to them. SIP-MS of the selected oxides prepared by precipitation indicated the presence of hydroxide species in the precipitated samples, which were evolved as water on heating to 600°C.

XRD analysis showed that the presence of manganese stabilises the tetragonal and/or cubic phase of zirconia in all the mixed oxides. In the case of the low manganese content samples, ZrMn10-cp and ZrMn30-cp, the presence of the cubic phase couldn't be identified conclusively with the use of XRD alone. This was in contrast to that observed for pure zirconia where a mixture of monoclinic and tetragonal zirconia was observed after calcination at 600°C. The effect of manganese on crystal structure was even more evident following aging at 800°C for 8 hours in air, where pure zirconia transformed completely into the monoclinic phase with a concurrent loss of surface area. In contrast, ZrMn10-cp maintained the tetragonal structure. A decrease in the interplanar spacing of zirconia was also observed on incorporation of zirconia, proving solid solution formation.

The oxides prepared by co-precipitation showed good activity for propane and methane combustion. The manganese-zirconia mixed oxides were more active for methane

combustion compared to a 0.5 wt% Pt/Al_2O_3 in terms of temperatures of 50% conversions (T_{50}). This is a significant result indicating that manganese containing catalysts have the ability to act as cheaper but just as efficient combustion catalysts. Manganese oxide was significantly more active than zirconia for both propane and methane oxidation. For propane oxidation over mixed oxides a minimum T_{50} was observed for ZrMn50-cp, while for methane, minima were observed for both ZrMn30-cp and ZrMn50-cp. Of the pure oxides, ZrMn100-cp and Mn_3O_4-Aldrich showed similar activities, both of which were greater than the mixed oxides while the least active manganese oxide was Mn_2O_3-Aldrich. This was attributed to the extremely low surface area of $2m^2g^{-1}$ recorded for the sample. On aging at 800°C at 8 hours in air, the activities of the mixed oxides remained constant for methane and increased for propane combustion respectively, despite a decrease in surface area. Maximum activities were observed for ZrMn30-cp-ag and ZrMn50-cp-ag for both propane and methane. In contrast, a decrease in activity was observed for the manganese oxides, although in the case of the sample prepared by co-precipitation the decrease was quite moderate. Mn_3O_4 was the least thermally stable.

A similar trend between fresh and aged samples was observed for the reduction profiles of the mixed oxides based on manganese content, where the temperatures of maximum reduction decreased on aging. Fresh and aged samples also showed similar trends when activity in terms of T_{50} was plotted against temperatures of maximum reduction of the first peak observed. Hence it was proposed that activity behaviour on aging was due to increased reducibility and more reactive lattice oxygen, which compensated for the negative effect of the loss of surface area. No significant decrease in activity was observed for ZrMn100-cp, which was prepared by the same method as the mixed oxides. This indicates that the preparation of high surface area Mn_2O_3 could be an important factor in the aging behaviour of the mixed oxides. Repeat activity tests for propane oxidation confirmed that the increase in activity on aging for propane is a reproducible property of the mixed oxides. Without the presence of Zr, no significant increase in activity was observed; instead a very small decrease was observed. No TPR-MS was performed on aged ZrMn100-cp at the same time as the mixed oxides and without that data it cannot definitely concluded whether the increase in reducibility on aging is due to the preparation method or the presence of zirconia. The different activity results for fresh and aged samples between propane and methane was discussed in terms of differing reactivity and activation temperatures of the two gases. While high

surface area plays an important role in the initial activity of the mixed oxides compared to pure manganese oxide, bulk properties such as oxygen mobility also have a role in activity and this becomes more important when the surface area was decreased.

References

(1) Boreskov. G. K., "*Catalytic Oxidation Of Dioxygen*", (Anderson, J. R, Boudart. M.,eds.), Catalysis, Science and Technology, Vol.3, pages 40-137 , Springer-Verlag, NY, 1982.

(2) Golodets, G. I., "*Heterogeneous Catalytic Reactions Involving Molecular Oxygen*", Elsevier, Amsterdam, 1983.

(3) Moro-oka,Y., Morikawa,Y., Ozak, A., *J. Catal.*, 7, 23 (1967).

(4) Baldi, M., Sanchez Escribano, V., Gallardo Amores. J. M., Milella, F., Busca, G., *Appl. Catal., B.* **17** L175 (1998).

(5) Finocchio, E., Busca, B., *Catal. Today* **70,** 213 (2001)

(6) Baldi, M., Finocchio, E., Milellab, F., Busca, G., *Appl. Catal., B* **16,** 43 (1998)

(7) Stobbe, E. R., De Boer, B. A., Gues, J. W., *Catal. Today* **47**, 161 (1999).

(8) Chang, Y., McCarty, J.C., *Catal. Today* **30,** 163 (1996).

(9) Zwinkels, M. F.M., Järås, S., Menon, P.G., *Catal. Rev. Sci. Eng.* **35,** 319 (1993).

(10) Keshavaraja, A., Jacob, N. E., Ramaswamy, A. V., *Thermochim. Acta* **254,** 267 (1995).

(11) Keshavaraja, A., Ramaswamy, A. V., *J. Mater. Res.* **9**, 837 (1994)

(12) Keshavaraja, A., Ramaswamy, A. V., *Appl. Catal., B* **8,** L1 (1996).

(13) Choudhary, V. R., Uphade, B. S., Pataskar, S. G., Keshavaraja, A., *Angew. Chem. Int. Ed. Engl.* **3,** 2393 (1996).

(14) Choudhary, V. R., Banerjee, S., Pataskar, S. G.,. *Appl. Catal., A* **253**, 65 (2003).

(15) Choudhary, V. R., Uphade, B. S., Pataskar, S. G., *Appl. Catal., A* **227**, 29 (2002)

(16) Unpublished work in catalysis group, DCU.

(17) Srinivasan, R., Harris, M. B., Simpson, S. F., De Angleis, R., Davis, B. H., *J. Mater. Res.* 3, 787 (1988).

([18]) Okado, K., Tomita, T., Kameshima, Y., Yasumori, A., Yano. T., Mackenzie, K. J. D., *Microporous and Mesoporous Materials* **37**, 355 (2000).

(19) Oh, J- M., Hwang, S- H., Choy, J- H., *Solid State Ionics* **151,** 285 (2002).

(20) Zhao, Q., Shih, W- H., *Microporous and Mesoporous Materials,* **53,** 81 (2002).

(21) Tichit, D., El Alami, D., Figueras. F., *Appl. Catal., A* **145,** 195 (1996).

(22) Stichert, W., Schüth, F., *Chem. Mater.* **10,** 2020 (1998).

(23) Hirano, M., Okumura, S., Hasegawa, Y., Inagaki, M., *International Journal of Inorganic Materials* **3,** 797 (2001).

(24) Skoog, D. A., Donald M. W., *"Fundamentals Of Analytical Chemistry"*. Fort Worth, Saunders College Pub, 1996.

(25) Fernández-López, E., Escribano, V. S., Resini, C., Gallardo-Amores, J. M., Busca, G., *Appl. Catal., B* **29,** 251 (2001).

(26) Fernández-López, E., Escribano, V. S., Resini, C., Gallardo-Amores, J. M., Busca, G., *Solid State Sciences* **4,** 951 (2002).

(27) Huheey, J. E., "*Inorganic Chemistry: Principles of Structure and Reactivity*"- 4th ed. - New York, Harper Collins College Publishers, 1993.

(28) Vlaic, G., Di Monte, R., Fornasiero, P., Fonda, E., Kaspar, J., Graziani, M., *J. Catal.* **182,** 378 (1999).

(29) Ali, A. A. M., Zaki, M. I., *Thermochim. Acta* **387**. 29 (2002).

(30) Boyero Macstre, J., Fernandez-Lopez, E., Gallardo-Amores, J. M., Ruano Casero, R., Sanchez Escribano, V., Perez Bernal, E., *International Journal of Inorganic Materials*, **3,** 889 (2001).

(31) Mercera, P.D.L., Van Ommen, J.G., Doesburg, E. B. M., Burggraaf, A. J., Ross, J. R. H., *Appl. Catal.* **57,** 127 (1990).

(32) T. Nguyen, T., Djurado, E., *Solid State Ionics* **138,** 191 (2001).

(33) Lee, W. E., Rainforth, W. R., "*Ceramic Microstructures*" London, Chapman and Hall, 1994.

(34) Sallé, C., Grosseau, P., Guilhot, B., Iacconi, P., Benabdesselam, M., Fantozzi, G., *J. Eur. Ceram. Soc.* **23,** 667 (2003).

(35) Klug, H. P., Alexander, L.E., *"X-Ray diffraction procedures for polycrystalline and Amorphous materials"*, Wiley-Interscience, Toronto, 1973.

(36) Vogel, A. R., "*Qualitative Inorganic Analysis*", London, Longman, 1996.

(37) Lin, H-Y., Chen, Y-W., Li, C., *Thermochim. Acta* **400**, 61 (2003).

(38) Tiernan, M. J., Barnes, P. A., Parkes, G. M. B., *J. Phys. Chem., B* **103,** 338 (1999).

(39) Monti, D. A. M., Baiker. A., *J. Catal.* **83,** 323 (1983).

(40) Bosch, H., Kip. B. J., Van Ommen, J. G., Gellings, P. J., *J. Chem. Soc., Faraday Trans. 1*, **80,** 2479 (1984)

(41) Christel, L., Pierre, A., Duprat, A., Rousset, A., *Thermochim. Acta* **306**, 51 (1997).

(42) Wendlandt, W. M., "*Thermal Analysis*", New York, John Wiley and son, 1985.

(43) Lemaitre, J. L., "*Characterisation of Hetereogeneous Catalysis*", Marcel Dekker Inc, New York, 1984.

(44) Barnes, P.A., Parkes, G. M. B., Brown, D. R., Charsley, E. L., *Thermochim. Acta* **269/270**, 665 (1995).

(45) Wimmers, O. J., Arnoldy, P., Moulijn, J. A., *J. Phys. Chem.* **90,** 1331 (1986).

(46) Malet, P., Caballero, A., *J. Chem. Soc., Faraday Trans. 1*, **84,** 2369 (1988).

(47) Bhaskar, T., Reddy, K. R., Kumar, C. P., Murthy, M. R. V. S., Chary, K. V. R., *Appl. Catal., A* **211,** 189 (2001).

(48) Tonge, K. H., *Thermochim. Acta* **74,** 151 (1984).

(49) Kissinger, H. E., *Anal. Chem* **29,** 1702 (1957).

(50) Málek, J., Šesták, J., Rouquerol, J., Criado, J. M., Ortega. A., *J. Therm. Anal* **38,** 71 (1992).

(51) Wimmers, O. J., *Thermochim. Acta* **95**, 67 (1985).

(52) Milt, V. G., Lombardo, E. A., Ulla, M. A., *App. Catal., B* **37**, 63 (2002).

(53) Arnone. S., Bagnasco. G., Busca. G., Lisi. L., Russo. G., Turco. M., in "Natural Gas Conversions V" (Parmaliana, A., Sanfilippo, D., Frusteri, F., Vaccari,A., Arena, F., eds.), Studies in Surface Science and Catalysis, Vol.119, 65-70, Elsevier, Amsterdam, 1998.

(54) Lee, J. H., Trimm, D. L., *Fuel Processing Technology* **42,** 339 (1995).

(55) Arai, H., Yamada,T., Eguchi, K., Seiyama, T., *Appl. Catal.* 265 (1986).

(56) Doornkamp, C., Clement. C., Ponec.V., *Appl. Catal., A* **188,** 325 (1999).

(57) Finocchio, E., Busca,G., Lorenzelli, V., Willey, R. J., *J. Catal.* **151**, 204 (1995).

(58) Alifanti, M., Kirchnerova, J., Delmon, B., Klvana, D., *Appl. Catal., A* 2004 in press.

(59) Song, K. S., Klvana, D., Kirchnerova, J., *Appl. Catal., A* **213,** 113 (2001).

Chapter 5:

Preparation and Investigation of Cobalt-Zirconia And Copper-Zirconia Mixed Oxide Combustion Catalysts.

5.1 Introduction

As discussed in Chapter 4, pure and mixed manganese oxides prepared by co-precipitation with ammonium hydroxide were very active in the combustion of methane. Studies on the oxidation of methane in excess air over various metal oxides by Boreskov (1) indicated that maximum specific activities were observed for Co_3O_4 and CuO compared to MnO_2 and NiO. Golodets (2) also observed very high activity for general oxidation of paraffins on Co_3O_4, while moderate activities were observed for CuO. Moro-oka et al (3) found that of a series of oxides namely, ThO_2, CeO_2, Fe_2O_3, NiO, MnO_2, CuO, Cr_2O_3 and Co_3O_4, that Co_3O_4 had the highest activity for the oxidation of propane. Sokolovskii (4) also noted that Co_3O_4 was one of the most active metal oxide combustion catalysts due to its ability to bind oxygen at a fast rate, resulting in a large concentration of highly reactive surface oxygen species. In general, noble oxide catalysts commonly supported on alumina are expensive compared to metal oxide catalysts and hence active transition metal oxides such as Co_3O_4 and CuO supported on alumina have been investigated (5,6, 7, 8, 9, 10,11). However, despite the high activity of unsupported Co_3O_4 for the oxidation of hydrocarbons, impregnation on alumina significantly decreased its activity (12). The formation of copper and cobalt aluminates has also been observed (8,9,12,13). Hence zirconia has been investigated in the literature as a support for both cobalt (9,14,15) for the combustion of methane and copper (10,11) for the oxidation of carbon monoxide. The preparation technique used in these studies was impregnation of the metal precursor solution on the support to form supported oxides. However relatively few publications have been observed for the preparation of cobalt-zirconium mixed oxides and copper-zirconium mixed oxides using bulk preparation techniques such as co-precipitation and the sol-gel technique.

Choudhary (16,17) has investigated a cobalt-zirconium mixed oxide prepared by co-precipitation for both propane and methane combustion. For copper-zirconium mixed oxides, co-precipitated mixed oxides have been investigated for the oxidation of propene (18) and reduction of methane (19), while structural (20) and TPR (19) data for the mixed oxides have also been reported. Dongare et al (21) investigated the oxidation of methane on samples prepared by a sol-gel technique, along with the structural properties of samples (22).

In the literature reported to date, low copper and cobalt contents were investigated, up to 33 mol % for the latter. Hence in this chapter, a higher loading of 50 mol% of both copper and cobalt with zirconia were prepared using a co-precipitation technique and their activity as methane combustion catalysts was investigated before and after aging. The effects of preparation conditions on the activity of the catalysts were also examined and SIP-MS was used to investigate the decomposition of the precursor precipitates.

5.2 Experimental

5.2.1 Preparation

Mixed oxides with a transition metal content of 0, 50 and 100 mol% (noted as ZrT_m0, ZrT_m50 and ZrT_m100 where T_m = Co or Cu respectively), were prepared following the two different methods outlined below (A and B). Sodium hydroxide was used as the precipitating agent instead of ammonium hydroxide in order to prevent the formation of cobalt and copper (II) ammonia compounds as reported in the following reactions (23):

$$Co^{2+} + NH_3 + H_2O + NO_3^- \rightarrow Co(OH)NO_3 \downarrow + NH_4^+$$

$$Co(OH)NO_3 \downarrow + 6NH_3 \rightarrow [Co(NH_3)_6]^{2+} + NO_3^- + OH^-$$

and

$$Cu^{2+} + SO_4^{2-} + 2H_2O + 2NH_3 \rightarrow Cu(OH)_2.CuSO_4 \downarrow + 2NH_4^+$$

$$Cu(OH)_2.CuSO_4 \downarrow + 8NH_3 \rightarrow 2[Cu(NH_3)_4]^{2+} + SO_4^{2-} + 2OH^-$$

Preparation Method A: An appropriate amount of zirconyl chloride octahydrate was dissolved in 25ml of distilled water and an appropriate amount of cobalt or copper nitrate was subsequently dissolved in the same solution. The resulting mixed oxide solution was then added dropwise over approx 20 mins to a certain amount of 4M NaOH , either at room temperature or heated at 70°C. (see Table 5.1). The precipitate formed was left in the mother solution overnight and then filtered and washed with approx 5L of distilled water. The filtrate was then dried overnight at 45°C followed by another overnight at 110°C. The oxide was formed by calcination of the dried filtrate in a static air furnace at 600°C for 6 hours.

Preparation Method B: As for method A except that a certain amount of 4M NaOH was added dropwise to a 25 ml solution containing appropriate amounts of dissolved copper nitrate or copper nitrate and zirconyl chloride octahydrate, either at room temperature or heated at 70°C. The preparation parameters of the calcined oxides are reported in Table 5.1

For pure cobalt oxide, it was observed that increasing the temperature of precipitation from 25 to 70°C while keeping the volume of 4M sodium hydroxide constant at 20 ml resulted in an increase in surface area from 12 to $18m^2g^{-1}$. In accordance with this result and literature data (24) that suggested that precipitation of cobalt hydroxide should be performed at temperatures higher than room temperature, the latter temperature was used to prepare all pure cobalt oxides and zirconia and mixed cobalt-zirconium mixed oxides. No mention in the literature was made of the need to use high temperatures to prepare copper-zirconium mixed oxides and hence pure copper oxide and copper-zirconia mixed oxides were prepared at 25°C.

Sample	Wt (g)		Temp (°C)	4M NaOH (ml)
	$ZrOCl_2.8H_2O$	$T_m(NO_3)_3.H_2O$*		
ZrCo0-40A	10.05		70	40
ZrCo50-20A	9.03	10.00	70	20
ZrCo50-20B	9.03	10.00	70	20
ZrCo50-40A	9.03	10.00	70	40
ZrCo50-40B	9.03	10.00	70	40
ZrCo100-20A		10.00	70	20
ZrCo100-40A		10.00	70	40
ZrCu100-40B		10.00	25	40
ZrCu50-40B	10.00	7.42	25	40
ZrCu50-40A	10.00	7.15	25	40

Table 5.1:Preparation conditions for samples prepared by co-precipitation of the formula ZrTmX-yA or ZrTmX-yB, where X represents mol % of Tm(Co or Cu), y is the volume of sodium hydroxide used and A or B indicates whether the metal precursor solution is added to the sodium hydroxide (A) or the reverse procedure (B). * $Co(NO_3)_3.H_2O$ and $Cu(NO_3)_3.H_2O$ were used for the preparation of ZrCoX and ZrCuX samples respectively.

5.2.2 Characterisation

Uncalcined oxides were characterised using simultaneous SDTA-TG and SIP-MS. Powders calcined at 600°C were characterised using XRD, TPR-MS and BET and tested

for methane oxidation activity. The experimental details of these techniques have already been detailed in Chapter 2.

5.3 Results and discussion

5.3.1 Nature of dried co-precipitates

Selected uncalcined precipitates after drying were analysed using SIP-MS and simultaneous TG- SDTA using the procedures outlined in Chapter 2. The SIP-MS data represents plots of different gaseous ions evolved under a constant linear heating rate up to 600°C under vacuum and the simultaneous TG-SDTA data shows the weight and energy changes of the sample on heating under air. The above thermal analysis techniques were used to investigate the effect of (i) the amount of sodium hydroxide added on the species evolved during heating up to 600°C for pure cobalt oxide and cobalt-zirconium mixed oxides and (ii) the effect of precipitation temperature on the thermal behaviour of the dried precipitates. The SIP-MS data for ZrCo50-20B and ZrCo50-40A are shown in Fig 5.1 and 5.2 respectively showing the effect of amount of sodium hydroxide used on gaseous species evolved while keeping the temperature of precipitation constant at 70°C. One difference between the SIP-MS data for these two samples is that the level of nitrate evolution is significantly higher for the sample prepared with 20ml of 4M NaOH, indicating not enough sodium hydroxide was added for all the cobalt nitrate ions to react during the precipitation procedure.

Peaks in the m/z 17 and 18 traces were observed for both samples, indicating the presence of a mixture of hydroxide species. For ZrCo50-40A, the hydroxide peak evolved at 300°C can be attributed to the decomposition of a cobalt hydroxide species since the same peak is observed for ZrCo100-40A i.e. pure cobalt oxide prepared by method A (see Fig 5.3). The smaller peak in the range 120-200°C can be attributed to decomposition of zirconium oxyhydroxide. In Chapter 3, zirconium oxyhydroxide prepared using ammonium hydroxide showed a peak in the same temperature range with a maximum at approx 159°C (see Fig 3.4, p 133). A smaller peak due to evolved H_2O and OH was also observed at 478°C (see Fig 5.2). This peak was not observed for pure cobalt oxide (see Fig 5.3) but is not as clear in the SIP-MS of ZrCo50-20B (see Fig

5.1). For the latter, a smaller peak is observed just below 300°C. A rise in H_2O and OH evolution is observed between 350 and 400°C and a similar rise in nitrate evolution is also observed. This could indicate that this is related to decomposition of the unreacted nitrate ions, since it was not observed for ZrCo50-40A. Cseri et al (25) observed that for pure cobalt (III) nitrate, loss of water occurred initially in the range 175 to 235°C and decomposition at a higher temperature of 255°C yielding NO_2 as a second step. Tiernan et al (14) also found that water evolution occurred before nitrate decomposition using SIP-MS for pure cobalt nitrate. The same study (14) also found that for zirconia impregnated with 5wt% cobalt, nitrate decomposition was observed over a much wider range 150-400°C compared to pure cobalt nitrate. Decomposition of ZrCo50-20B occurred in a similar temperature range, although a difference in peak shape was observed. The evolution of water on the supported catalysts along with nitrate evolution was not recorded in the study (14) to investigate if water evolution still occurred before nitrate decomposition on the supported catalysts compared to pure cobalt nitrate.

In Summary, the SIP-MS of cobalt-zirconium mixed oxides show that on addition of 20 ml of sodium hydroxide there is only a small amount of cobalt hydroxide formed indicated by the relatively low intensity of the peak at approx 300°C attributed to that compound. In comparison, a significant amount of nitrate species is evolved during heating. However the XRD of the precipitate calcined at 600°C for 6 hours showed the presence of Co_3O_4 (see later in section 5.3.2). For all samples prepared with 40ml of sodium hydroxide, no nitrate species were evolved and a water peak corresponding to dehydration of cobalt hydroxide was observed, proving that 40 ml of sodium hydroxide was sufficient to react with all the cobalt precursor species.

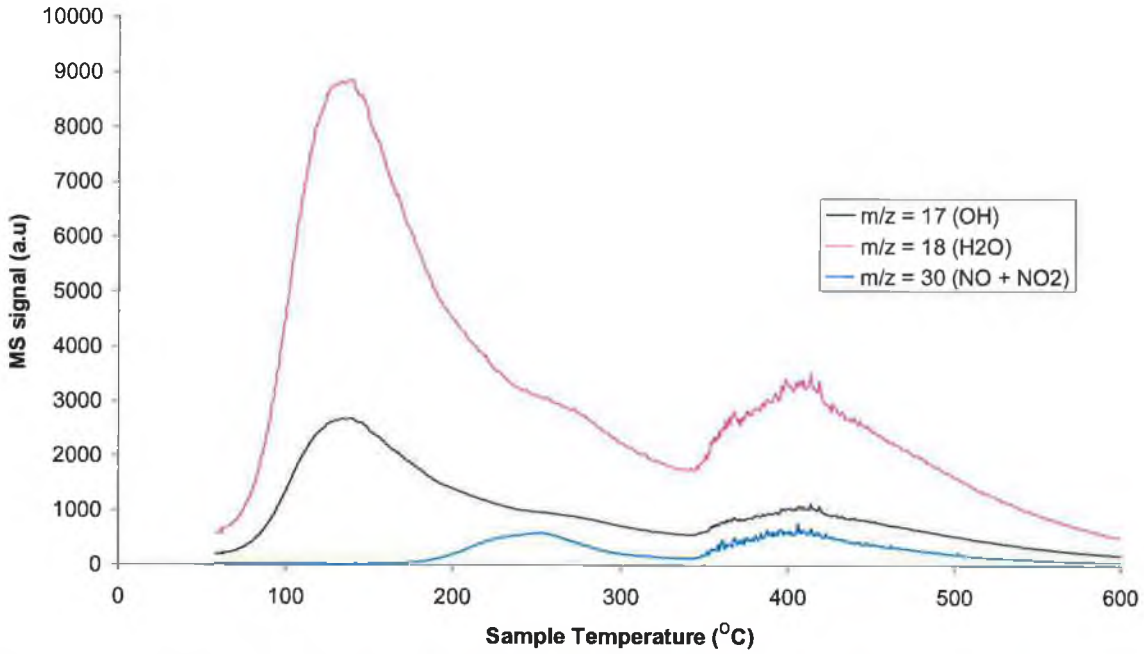

Fig 5.1: SIP-MS of uncalcined ZrCo50-20B at a linear heating rate of 10°C/min under vacuum.

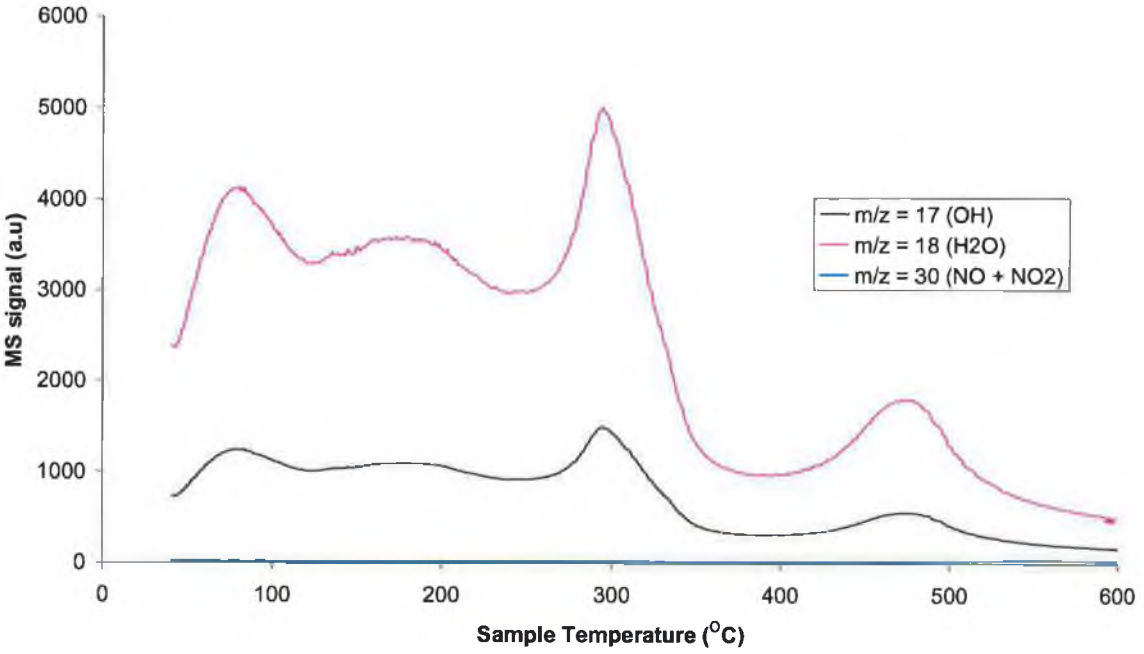

Fig 5.2: SIP-MS of uncalcined ZrCo50-40A at a linear heating rate of 10°C/min under vacuum.

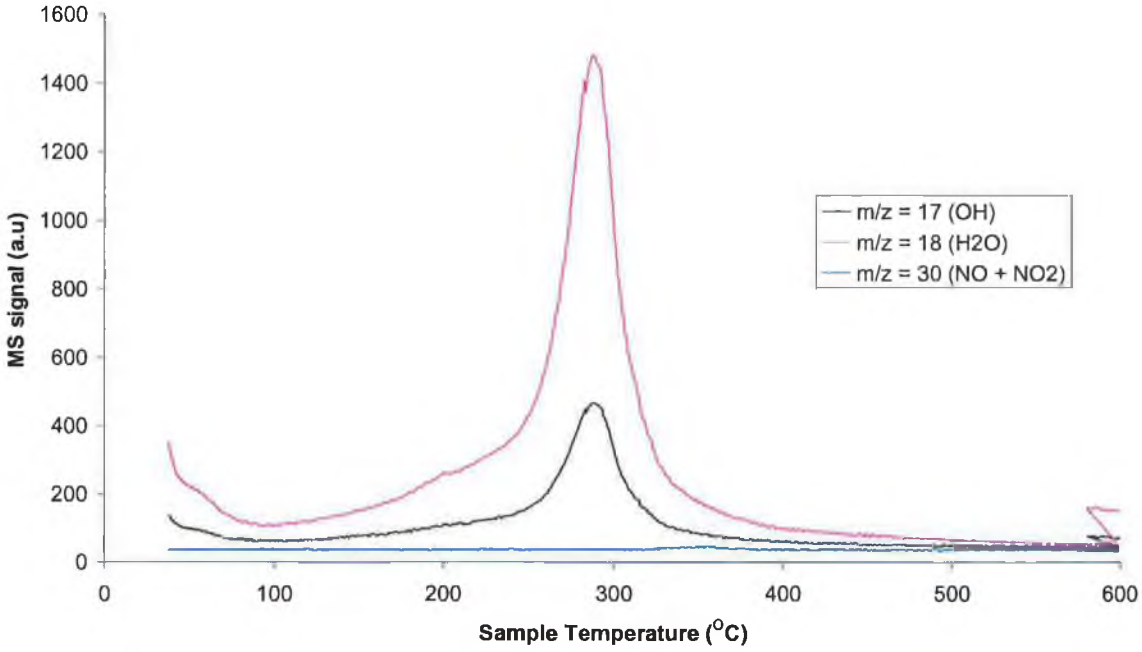

Fig 5.3:SIP-MS of uncalcined ZrCo100-40A at a linear heating rate of 10°C/min under vacuum.

Simultaneous SDTA-TG was also performed on ZrCo100-40A, ZrCo50-40A, and ZrCo0-40A, the results of which are shown in Fig 5.4, 5.5 and 5.6 respectively. Differential analysis (DTG) was also applied to the TG curves, which involved taking the first derivative of the mass of the sample as a function of temperature. This data is not shown but is useful in that it indicates the rate of weight change as a function of sample temperature. For pure cobalt oxide (see Fig 5.4), DTG indicated that the greatest weight loss (8.92%) occurred between approx 229 and 328°C, with a maximum at approx 305°C. A large sharp endothermic peak was also observed in the same temperature range in the SDTA curve, indicating a decomposition rather than crystalline transition or melting. Since the SIP-MS indicated the evolution of hydroxide species in the same temperature range, the dehydration of a cobalt hydroxide intermediate is inferred. The total mass loss of the sample from 100-600°C is 12.74% - only a very small weight loss of 0.9% was observed below this due to loss of adsorbed water. This weight loss is very similar to that calculated (12.69%) for the following reaction (26):

$$12HCoO_2 \Leftrightarrow 4\ Co_3O_4 + 6H_2O + O_2.$$

Hence, the peak in both the SIP-MS and TG-SDTA can be attributed to the decomposition of cobalt oxide hydroxide ($HCo(III)O_2$ or $Co(III)O.(OH)$). Vogel (23) reported that when cobalt ions in the form of cobalt (II) nitrate reacted with sodium hydroxide in cold, a blue salt precipitated according to the following reaction:

$$Co^{2+} + OH^- + NO_3^- \rightarrow Co(OH)NO_3 \downarrow$$

Upon warming with excess alkali, above salt was converted to pink cobalt (II) hydroxide as follows:

$$Co(OH)NO_3 \downarrow + OH^- \rightarrow Co(OH)_2 \downarrow + NO_3^-$$

This was then transformed on exposure to air to brownish black cobalt (III) hydroxide as follows:

$$4Co(OH)_2 \downarrow + O_2 + 2H_2O \rightarrow 4Co(OH)_3 \downarrow$$

It has been reported (26) that cobalt oxide hydroxide ($HCo(III)O_2$) was formed from trivalent cobalt hydroxide in the temperature range 120-190°C before being subsequently converted to Co_3O_4 in the temperature range between 240-300°C.

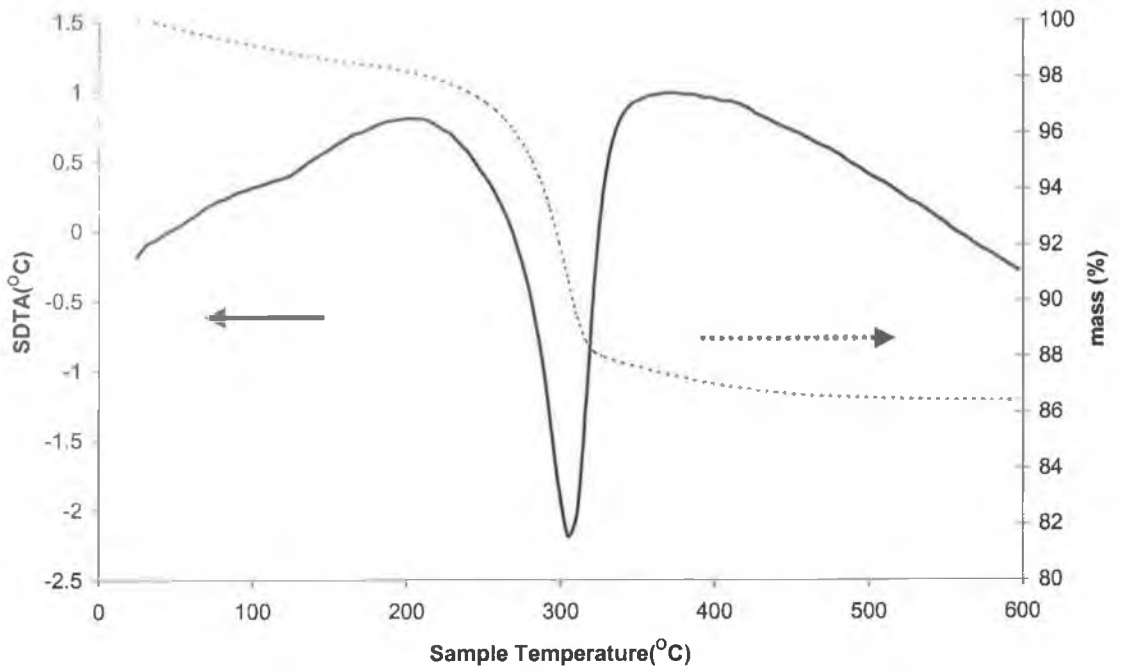

Fig 5.4:Simultaneous TG-SDTA of uncalcined ZrCo100-40A at 10°C/min under air (sample weight (40.44mg)

For ZrCo50-40A, the same peak at a slightly higher value of 315°C is observed in the SDTA, accompanied with a sharp weight loss of approx 3-4% (see Fig 5.5). This can be attributed to the decomposition of cobalt oxide hydroxide, since both samples were prepared in a similar manner. A more gradual weight loss up to approx 300°C is observed and DTG indicates a maximum rate loss at 100°C. This can be attributed to dehydration of zirconium oxide hydroxide, the formation of which has proposed by Vogel on reaction of a hot solution of zirconyl oxychloride with sodium hydroxide (23). A total weight loss between 60 and 600°C was 17.12 % was observed. In the SIP-MS of the same sample, a peak was observed at approx 480°C (see Fig 5.2). Since that peak indicated evolution of hydroxide species, an endothermic peak in the SDTA might also be expected. However the unsteady baseline from 350-600°C onwards makes it difficult to ascertain the absence or presence of a peak in this region.

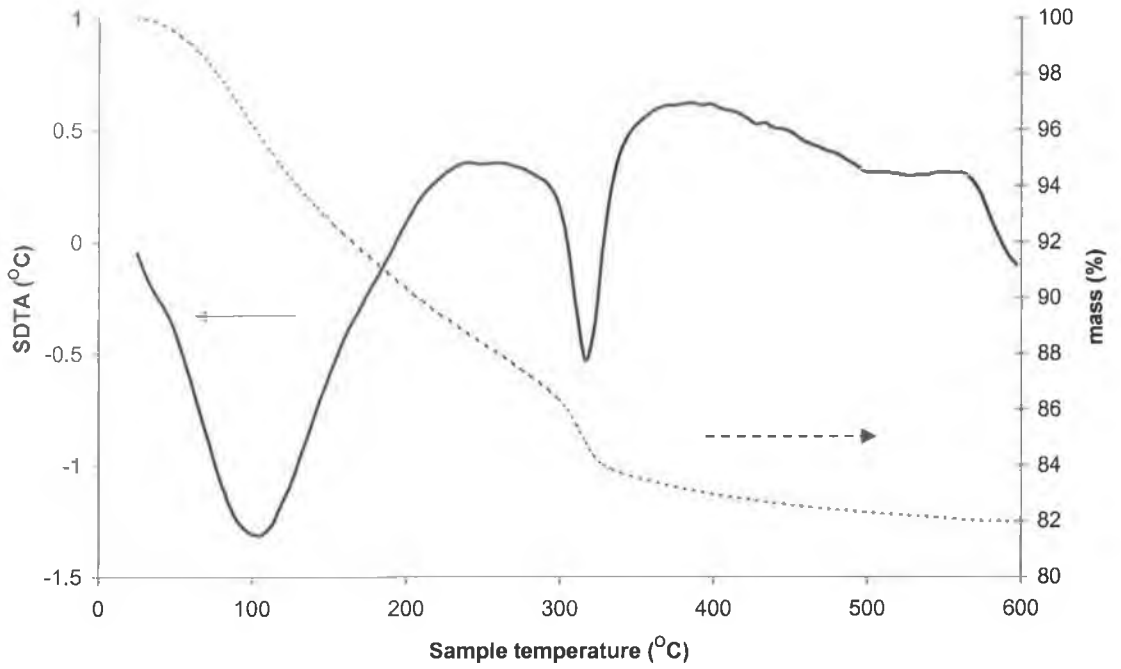

Fig 5.5:Simultaneous SDTA-TG of uncalcined ZrCo50-40A at 10°C/min under air.

Simultaneous SDTA-TG was also performed on ZrCo0-40A, the results of which are shown in Fig 5.6. In contrast to the afore mentioned samples, uncalcined ZrCo0-40A was dried up to 150°C, where it was held for 10 minutes, then cooled to ambient temperature. The sample was then heated up again to 150°C and held for 10 minutes in the same manner, cooled to room temperature and then the TG-SDTA was performed up to 900°C in flowing air. This was performed to see how much physically adsorbed water was on the sample and to see how easily the sample took up moisture from the atmosphere. DTG of the sample (not shown) indicates the two biggest area of mass loss are before 300°C at 100 and 200°C, with weight losses of 2.7 and 9.2 % respectively, with total weight loss of approx 11.9%. The SDTA of the sample is strikingly different to that observed for zirconia prepared with co-precipitation with ammonium hydroxide in chapter 3 (see Fig 3.4 p133). Very large values were observed for the SDTA in comparison to other cobalt-zirconium mixed oxides and other pure zirconia samples prepared in the previous chapters. The instrument had been calibrated prior to running the sample and hence these larger than expected values are not an instrument error. Very broad endothermic drifts were observed, which are associated with slow decomposition or possibly dehydration of the sample. These are caused when heat is

removed from the sample by the gaseous products during decomposition. Since a concurrent, though gradual mass loss, was also observed in the TG on increasing temperature, a decomposition or dehydration, rather than crystalline transitions or melting, are indicated. No exothermic peaks were observed between 400 and 500°C in the SDTA of ZrCo0-40A as observed for zirconia prepared using ammonium hydroxide. This could be attributed to either the preparation method used or it could due to the lengthy drying time that was performed on the sample. The drying up to 150°C before the SDTA-TG could have resulted in partial decomposition of the sample, since decomposition of zirconium oxide hydroxide has been reported to occur at 80°C. Partial decomposition of the oxyhydroxide precursor prior to the SDTA run then caused the very slow decomposition curve observed in the SDTA of the sample after drying. As reported by Sato et al, the exotherm is proposed to be due to crystallization of the amorphous zirconium oxide into the tetragonal or monoclinic phase, depending on the preparation conditions used (27). The pretreatment of this sample makes it difficult to compare quantitatively its TG-SDTA result to that of zirconia prepared in Chapter 3 at a lower temperature and pH.

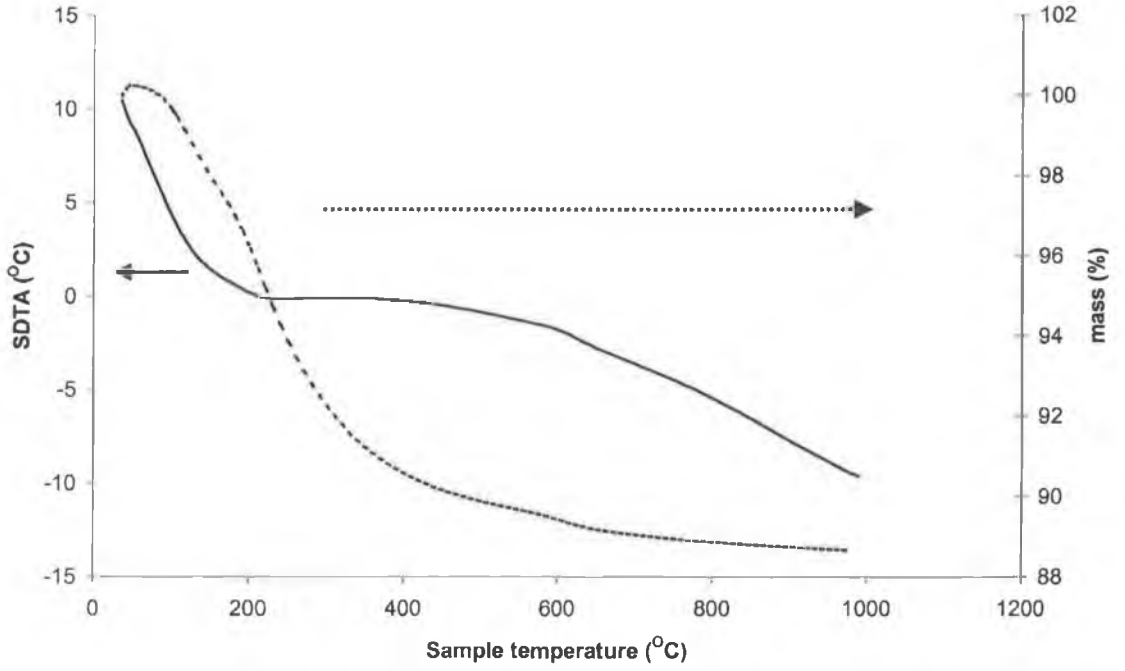

Fig 5.6: Simultaneous SDTA-TG of ZrCo0-40A at 10°C/min under air after two drying runs up to 150°C in air.

The copper-zirconium mixed oxides were prepared in an identical fashion to cobalt-zirconium mixed oxides except that the precipitation procedure was performed at room temperature. The SIP-MS and SDTA-TG data of ZrCu50-40A are reported in Fig 5.7 and 5.10 respectively. In the SIP-MS a large peak due to evolved water is observed at approx 153°C, with a small shoulder at 130°C. This peak is in the same region as that reported in Chapter 3 for the SIP-MS of zirconia prepared by ammonium hydroxide precipitation, as well as for pure copper hydroxide prepared, namely ZrCu100-40B (see Fig 5.8). Note that for ZrCu100-40B, the base was added to the precursor salt solution, while for ZrCu50-40A, the precursor solution was added to base. This difference in order of addition would not be expected to affect the chemical identity of the copper hydroxide species formed. The SIP-MS data for the mixed copper-zirconium oxide is quite difficult to compare directly with the cobalt-zirconium mixed oxide prepared by the same method except at room temperature since both copper oxide and zirconium oxide precursor materials decompose in the same temperature range.

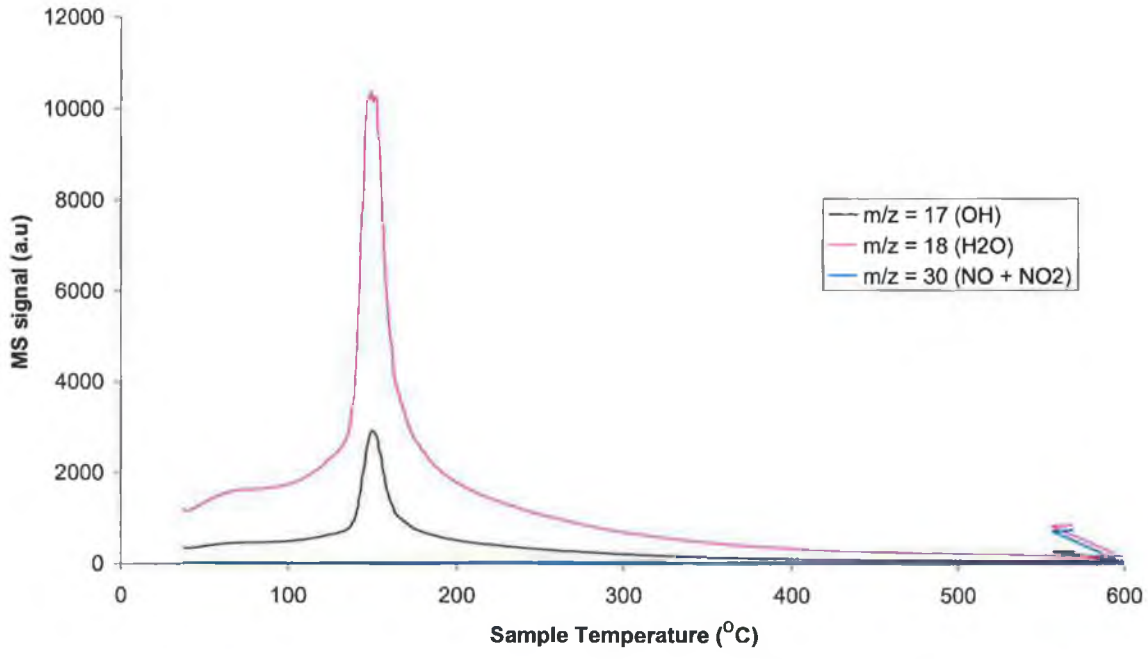

Fig 5.7:SIP-MS of ZrCu50-40A at a linear heating rate of 10°C/min in vacuum.

However, the dehydration peak observed at 480°C in the SIP-MS of ZrCo50-40A was not observed in this sample indicating that the peak is related to the precipitation of

zirconium hydroxide at elevated temperatures. According to Vogel (23) reaction of copper ions with sodium hydroxide produces $Cu(OH)_2$, the decomposition of which has been reported (28) to occur between 137 and 164°C in TG –DSC at linear heating rates between 0.50 and 4.5 °Cmin^{-1}. The reaction involved is as follows:

$$Cu(OH)_2 \rightarrow CuO + H_2O$$

However when the SDTA-TG was performed on the ZrCu100-40B, the only peak observed was a sharp endothermic one at a significantly lower temperature of 60°C accompanied by a sharp weight loss of approx 5% up to 75°C (see Fig 5.9). More gradual and smaller weight-losses were detected in the DTG between approx 170°C and 235°C, while very small peaks were also observed in the SDTA in the same range. The total mass loss for the sample was small at 7.76%, which is significantly lower than the theoretical weight-loss expected for decomposition of the hydroxide of 18.47%.

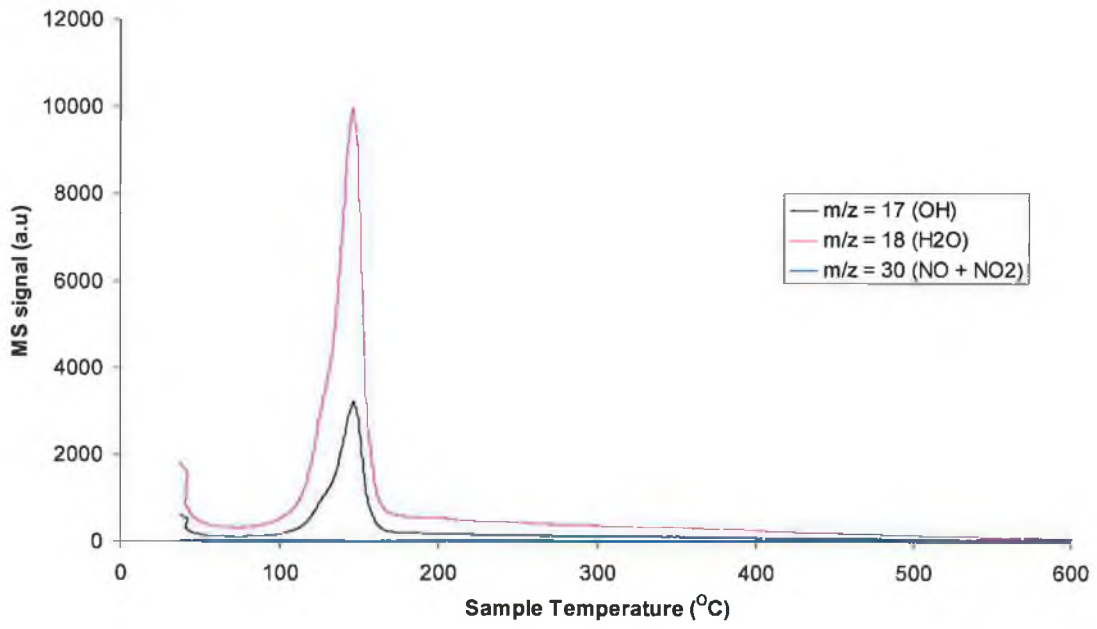

Fig 5.8:SIP-MS of ZrCu100-40B at a linear heating rate of 10°C/min under vacuum.

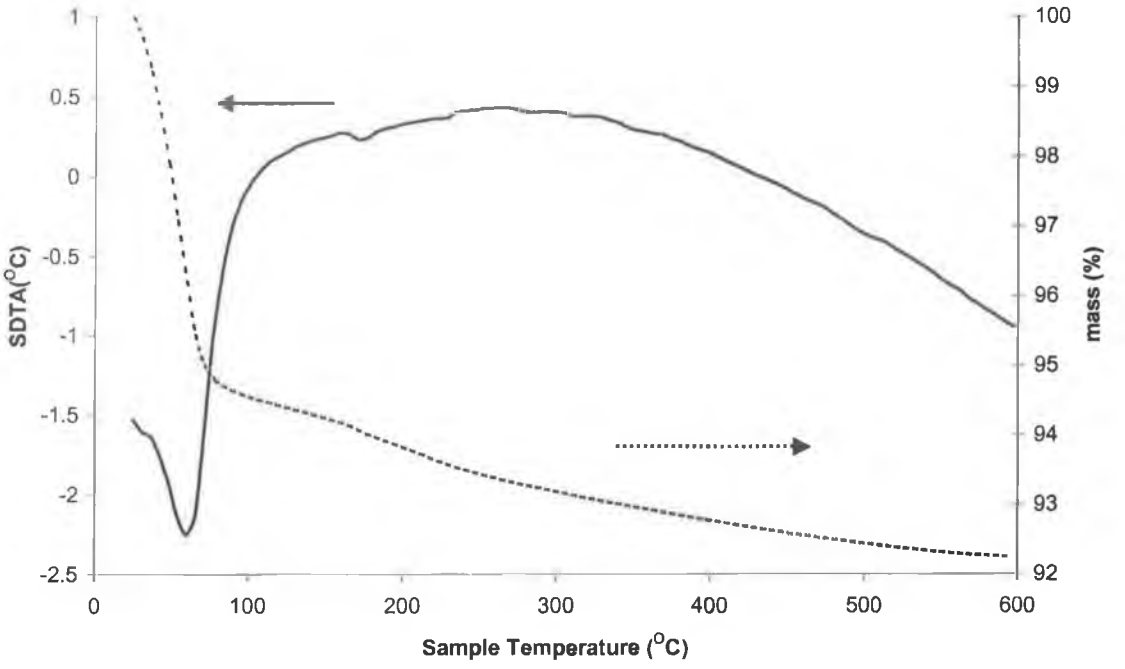

Fig 5.9:Simultaneous SDTA-TG of ZrCu100-40B under air at 10°C/min.

For ZrCu50-40A (see Fig 5.10), the STDA showed an endothermic feature at approx 90°C as well as a sharp endotherm at 195°C. Previous SIP-MS data of the same sample and of pure copper oxide indicated the evolution of water only, indicating that all precipitates were in the form of hydroxides. A narrower endothermic peak at 60°C was observed in the SDTA of pure copper oxide. The low temperature endothermic feature in the copper-zirconium mixed oxides could be attributed to decomposition of both copper oxide and zirconium hydroxide. The second peak at 195°C can be attributed to dehydration of zirconium oxyhydroxide. Peaks in this temperature range have previously been observed for pure zirconia samples, namely ZrCe0-cp (see Fig 3.4 p 133).

Hence in conclusion, the thermal analysis data on the uncalcined samples indicates for all samples prepared with 40 ml of 4M NaOH, no nitrate species were evolved and hydroxide species, namely cobalt oxide hydroxide, zirconium oxy hydroxide and copper hydroxide, are decomposed during heating. The effect of an increase in precipitation temperature is more difficult to ascertain. An increase in digestion temperature has been reported to lead to a more dehydrated oxy-hydroxide and calcination of it gives the

tetragonal phase (29). It has been reported that increasing the pH decreases the water content of the dried gels and using the same pH of 10, the gel formed from addition of precursor to base shows greater weight loss than the gel formed from the reverse procedure (30). ForZrCu50-40A and ZrCu50-40A, the endothermic peaks in the SDTA attributed to zirconium oxyhdroxide precursor are similar to those reported for zirconium oxide prepared by addition of ammonium hydroxide at room temperature in Chapter 3. The peak at 200°C for ZrCu50-40A is much sharper than the cobalt-zirconium mixed oxide sample. In contrast while the TG for ZrCo0-40A shows lower mass losses but similar peak positions to zirconia prepared in Chapter 3, the SDTA of ZrCo0-40A is very different to all other samples and can be attributed to the pretreatment of the sample.

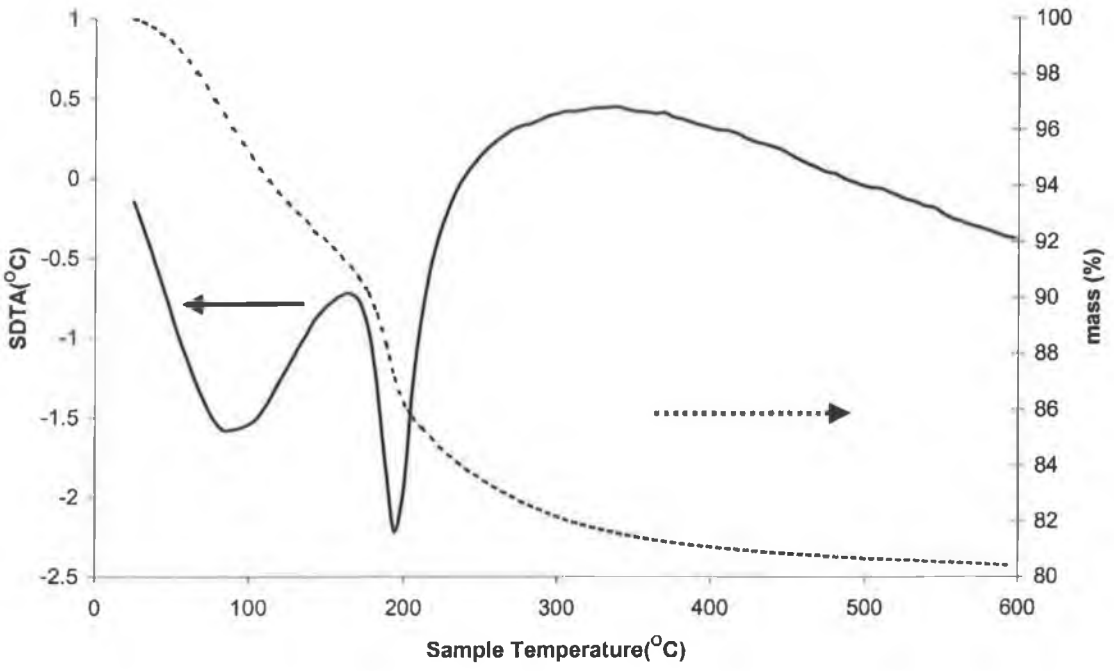

Fig 5.10:Simultaneous SDTA-TG of ZrCu50-40A under air at 10°C/min.

5.3.2 XRD and Specific surface areas of calcined samples

XRD and surface area analysis was performed on pure copper oxide, copper-zirconium mixed oxides, pure cobalt oxide and cobalt-zirconium mixed oxides after calcination

using the experimental procedures outlined in Chapter 2. The main peaks in terms of 2θ values, along with the corresponding interplanar spacings (d_{hkl}) and relative intensities, are given in Table 5.2. In this chapter, the samples marked with * were run on a different diffractometer than the rest of the samples due to installation of a new diffractometer in the Centre of Applied Catalysis in Huddersfield where the all the XRD experiments had to be performed. While the phases present were not affected by the change of equipment, the intensities of all peaks run in the new instrument were lower than those run in the old instrument.

Pure cobalt oxide prepared by precipitation with sodium hydroxide exhibited diffraction features similar to those associated with Co_3O_4 (see Table 5.2 and Fig 5.11), except with different relative intensities. On comparing CoZr sample prepared with either 20 ml or 40 ml of sodium hydroxide, the main difference observed was in the intensity of the peaks at 36.55° and 36.45° respectively. In the former sample, the relative intensity of the peak at 36.55° was half that of the peak observed in the latter sample at 36.45°. Both peaks have the identical d_{hkl} of 2.46Å, which is the same interplanar spacing as that of the main diffraction peak in pure cobalt oxide (ZrCo100-40B). The difference in peak intensities is in agreement with the SIP-MS result which indicated the presence of a greater quantity of unreacted nitrate ions in the CoZr sample prepared with a smaller quantity of base. On comparing ZrCo50-40A and ZrCo50-40B, the only difference in the preparation of the compounds was whether the non-steady pH (method B) or constant pH (method A) was used. Similar diffraction peaks were observed corresponding to both pure cobalt oxide and tetragonal zirconia, although they did differ slightly in the interplanar spacing values and relative intensities. Both ZrCo50-40A and ZrCo50-40B contained a large peak at 2θ values of 30.1° and 30.4° respectively associated with tetragonal zirconia. Zirconia prepared by the constant pH (ZrCo0-40A) method contained a main diffraction peak at 30.35°, corresponding to tetragonal zirconia.

Sample I.D	Peaks -2θ (°)	Peaks -d_{hkl} (Å)	I/I_o	SA (m^2g^{-1})
ZrCo100-40A	36.75, 65.15,59.30, 31.20,	2.45, 1.43, 1.56, 2.87	100, 43, 40, 39	16
ZrCo50-20B	30.20, 50.45, 60.05 35.00, 36.55, 59.15	2.96, 1.81, 1.54 2.56, 2.46, 1.56	100, 60, 44, 29, 24, 20	21
ZrCo50-40A	30.10, 36.45, 50.35 59.85, 31.05, 35.10	2.97, 2.46, 1.81 1.54, 2.88, 2.56	100, 51, 50, 37, 32, 29	55 ~
ZrCo50-40B *	30.40, 36.85, 50.75, 59.30, 60.4, 31.3, 35.30	2.94, 2.44,1.80, 1.56, 1.53, 2.86 2.54	100, 67, 50, 39, 37, 36, 27	33
ZrCo0-40A *	30.35, 50.55, 60.25, 35.05	2.94, 1.80, 1.53 2.56	100, 52, 39, 32	80 ~
Co_3O_4 ^	na	2.43, 2.82, 1.42, 1.55, 2.03	100, 54, 50, 39, 32	
ZrCu100-40B	35.45, 38.65, 48.65, 61.45, 68.00	2.53, 2.33,1.87, 1.51, 1.38,	100, 94, 34, 28, 25	6
ZrCu50-40A	30.45, 35.40, 38.65, 50.90, 60.60, 48.65, 32.45	2.94, 2.54,2.33, 1.80, 1.53, 1.87, 2.76	100, 94, 71, 51, 41, 40, 38	40
ZrCu50-40B*	35.53, 30.50, 38.74, 50.94, 48.83, 60.52	2.52, 2.93, 2.32, 1.79, 1.86, 1.53	100, 93, 75, 49, 37, 36	52

Table 5.2: XRD data for fresh ZrCo and ZrCu oxide samples, 2θ corresponds to the main diffraction peaks, with the calculated interplanar spacing (d_{hkl}) and corresponding relative intensity (I/I_o). Io is the intensity (counts) of the peak with the greatest intensity for each catalyst and I is the intensity of the indicated peak relative to that.^ data taken for commerial Co_3O_4 sample from ref (31).For samples marked with ~ the error in BET surface area was ± 2 m^2g^{-1}.

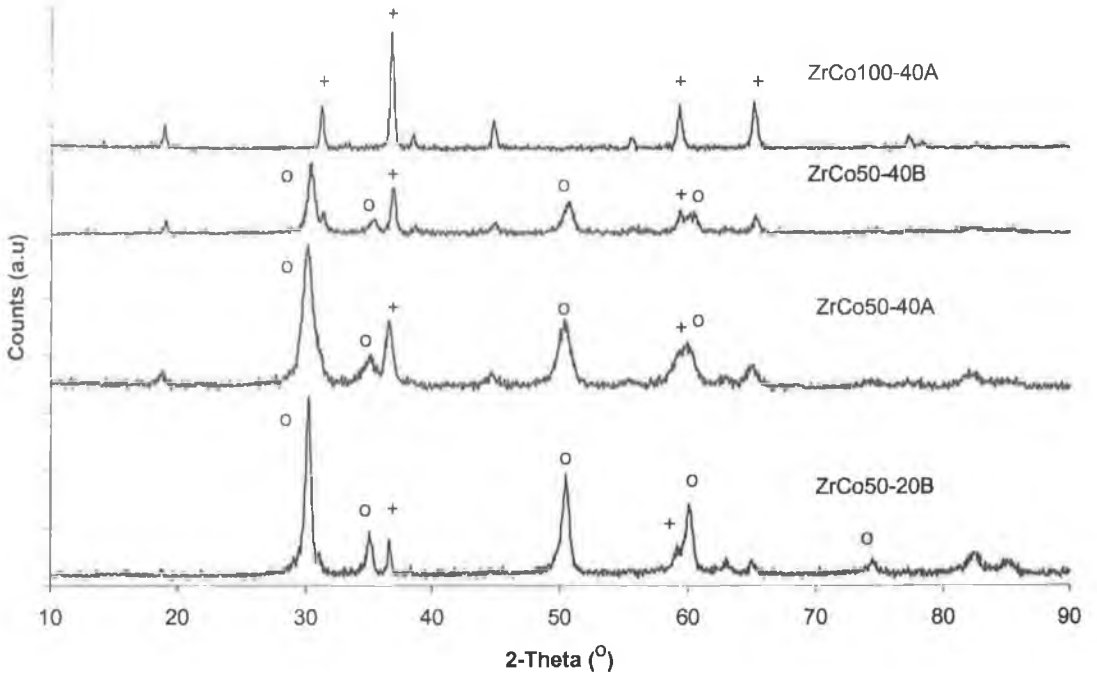

Fig 5.11:XRD patterns of fresh cobalt oxide and cobalt-zirconium mixed oxide, where o and + represent peaks due to tetragonal-ZrO_2 and Co_3O_4 respectively.

Pure copper oxide prepared by precipitation also showed intense peaks at 35.45° and 38.65°, with corresponding interplanar spacings of 2.53Å and 2.33Å, similar to that reported in the literature (32) for CuO of 2.50 and 2.32 Å (see Fig 5.12). Copper–zirconia mixed oxides exhibited features characteristic of both CuO and tetragonal zirconia, but as observed for the cobalt-zirconia mixed oxides, the relative intensities of the peaks varied. For ZrCu50-40B, the peak associated with tetragonal zirconia was slightly smaller than the two main peaks associated with CuO and a small increase in the interplanar spacings was observed compared to ZrCu50-40A. However as observed in Fig 5.12, all the peaks were smaller than those observed for ZrCu50-40A. This could be attributed to either a instrumental effect or a particle size effect which would have been caused by the increased surface area of ZrCu50-40B.

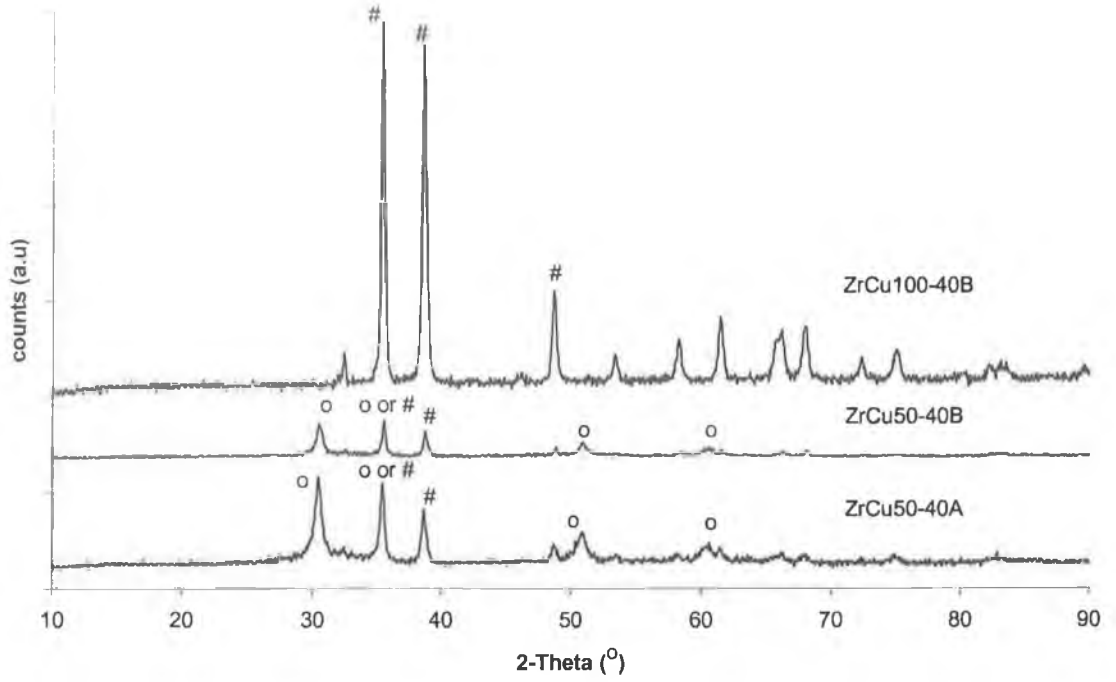

Fig 5.12:XRD patterns of fresh copper oxide and copper-zirconium mixed oxide, where o and # represent peaks of tetragonal –ZrO_2 and CuO respectively.

For comparison sake, the XRD of ZrCo0-40A has been compared to zirconia samples previously investigated in this thesis along with the respective surface areas in Fig 5.13. The zirconia (c in Fig 5.13) prepared by addition of the precursor solution to sodium hydroxide at 70°C had a higher surface area than that prepared by addition of ammonium hydroxide to the same precursor solution at room temperature (b in Fig 5.13). Zirconia with the lowest surface area had the highest percentage of monoclinic phase (a in Fig 5.13). The increase in surface area can be attributed to two factors: the higher and constant pH associated with the former method and the elevated temperature of precipitation. Tichet et al (30) also observed that using the same zirconium salt, the specific surface areas of pure zirconia precipitated via addition of the salt solution to ammonia at pH 10 were 30-60% higher than those precipitated by addition of ammonia to the salt solution up to pH 10. This was attributed to the better equilibrium conditions for the former, where the solution was almost in an equilibrium state. In the latter, it was proposed that equilibrium was never reached during the procedure and hence a mixture of different species were observed in the gel.

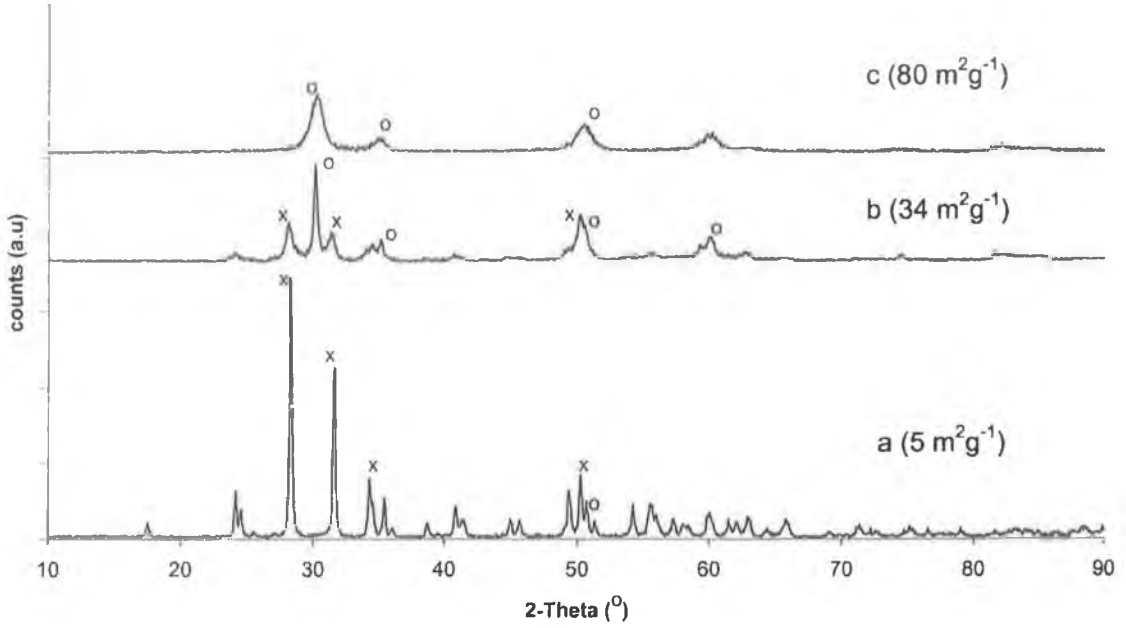

Fig 5.13:XRD patterns for various zirconia (ZrO_2) samples (a) ZrCe0-Aldrich (b) ZrCe0-cp (c) ZrCo0-40B, where the surface areas of each sample is shown in paranthesis. O and X represent peaks attributed to the tetragonal –ZrO2 (JCPDS #17-923) and monoclinic-ZrO_2 (JCPDS # 13-307).

An increase in digestion temperature has also been reported to have a moderate increase in surface area for both ammonia (33,34) and sodium hydroxide addition to the precursor solution. For addition of ammonium hydroxide to zirconium nitrate, an increase in the precipitation and digestion temperatures from 20 to 80°C resulted in an increase in surface areas from 164 to 190m^2g^{-1} respectively (33). Chuah et al (34) also looked at both the order of precipitation and the effect of digestion temperature. Using ammonium hydroxide as precipitating agent, zirconyl chloride was added to aqueous ammonia in the so-called basic method, which reduced the pH from 11.8 to 9.4. In the acidic method, the aqueous ammonia was added to zirconyl chloride up to pH of 9.4. For the basic method temperature of digestion was also investigated from 30-80°C. For digestion temperatures between 30 and 70°C for the basic method, a modest increase in surface area from 54 to 70 m^2g^{-1} was observed. Also the order of addition of reagents during precipitation affected surface area, with higher surface areas observed for the basic procedure. In the former case, the pH stays in the basic region during all of the

precipitation while for the acidic method, a pH change from 1 to 9 is required. In the current study, the use of elevated temperatures meant that the pH of the zirconia sample prepared could not be monitored accurately because the type of pH probe available was not suitable for high temperatures. However, pH results for the addition of cobalt nitrate to 20 ml of 4M NaOH indicated an initial pH of basic solution before addition of precursor to be approx 13.6. After addition of the cobalt precursor, the pH of the resulting solution containing the precipitate was 12.93.

Along with the increase in surface area, an increase in the percentage of the tetragonal phase present also was observed (see Fig 5.13). This was observed by the decreasing intensity of the peaks at approx 28 and 31 ° which are associated with the monoclinic phase on moving from a to c in Fig 5.13. As the surface area is increased, the intensity of the diffraction peak at 30° increases. The sample with the highest surface area also showed line broadening compared to the other samples, indicating the presence of smaller particles and no significant peaks corresponding the monoclinic phase are identified. Garvie (35) has previously proposed that small crystallites stabilize the tetragonal phase.

However for both copper-zirconia and cobalt-zirconia mixed oxides, order of addition of precipitating agents had a different effect on surface area. For cobalt-zirconium mixed oxide, the addition of sodium hydroxide to the precursor solution resulted in a surface area of 33 m^2g^{-1}, lower than that observed for the reverse procedure that gave surface area of 55 m^2g^{-1}. For copper-zirconium mixed oxides, where the same procedures was performed at room temperature instead, a higher surface area of 52 m^2g^{-1} compared to 40 m^2g^{-1} was observed for the addition of sodium hydroxide to the precursor solution. For pure cobalt oxide increasing the temperature of precipitation on the addition of 20ml of sodium hydroxide increased the surface area slightly from 12 to 18 m^2g^{-1}. The temperature used has been reported to have an effect on the formation of cobalt hydroxide instead of cobalt nitrate salt (23). 70°C was chosen as the temperature of precipitation following the method described by Christoskova et al (24) for the preparation of cobalt oxide. Doubling the amount of sodium hydroxide added at the same temperature for method A for pure cobalt oxide resulted in only a negligible decrease of 2 m^2g^{-1}. The lowest surface are of 6m^2g^{-1} was observed for pure copper oxide prepared by method A. In terms of surface area trends, all the cobalt-zirconium

mixed oxides had lower surface areas than pure zirconia prepared by method A at 70°C, but higher than that observed for pure cobalt oxide. Copper zirconium mixed oxides also exhibited lower surface area than pure zirconia, although it is worth noting that this is not directly comparable since zirconia was prepared at 70°C.

5.3.3 Reduction Characteristics of fresh samples

TPR-MS profiles of bulk oxides (ZrCo100-40A, Zr50-40B, ZrCu100-40B and ZrCu50-40A) are shown in Figs 5.14-5.17, illustrating H_2 uptake (m/z = 2) and H_2O and OH evolution (m/z = 18 and 17 respectively) as a function of sample temperature. H_2 and H_2O evolution occurs simultaneously for all the samples, although in some cases the uptake of H_2 occurs at slightly lower temperatures. For ZrCo100-40A (Fig 5.14) the main reduction step occurred at approx 464 and 500°C for hydrogen uptake and water release respectively. A smaller shoulder was noted at the low temperature side at approx 370°C for both traces, although it is more difficult to measure accurately for water evolution due to the asymmetry of the associated peak. Arnone et al (36) observed a TPR profile for bulk Co_3O_4 consisting of two overlapping peaks with maxima at 382 and 470°C respectively. This was attributed to reduction of Co_3O_4 (Co^{3+}) to CoO (Co^{2+}) followed by subsequent reduction of the divalent ions to metallic product. The reduction conditions employed were a 2% H_2/Ar mixture flowing at 25 cm^3 min^{-1} with a linear heating rate of 10°C/min. The TPR of the mixed oxide ZrCo50-40A (Fig 5.15) also shows two overlapping peaks at temperatures of approx 384 and 484°C for water evolution and 373 and 460°C for hydrogen uptake. Considering the considerably higher activity of the pure cobalt oxide, a larger difference in the temperatures of reduction could be expected. Choudhary et al (16) observed for cobalt-doped zirconia prepared by co-precipitation with a Co/Zr ratio of 0.25, the TPR profile consisted of a small hydrogen consumption peak or hump at 410°C followed by a large peak at 545°C.

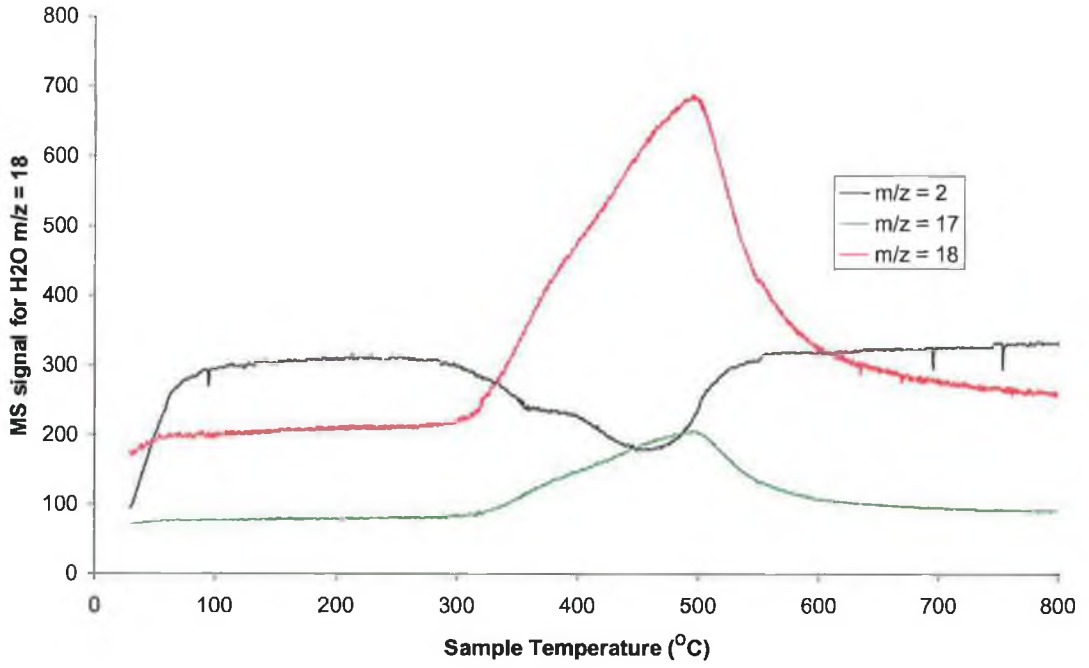

Fig 5.14:TPR-MS of ZrCo100-40A at a linear heating rate of 10°C/min, where the m/z =2, 17 and 18 refer to the MS signal for H_2, OH and H_2O respectively

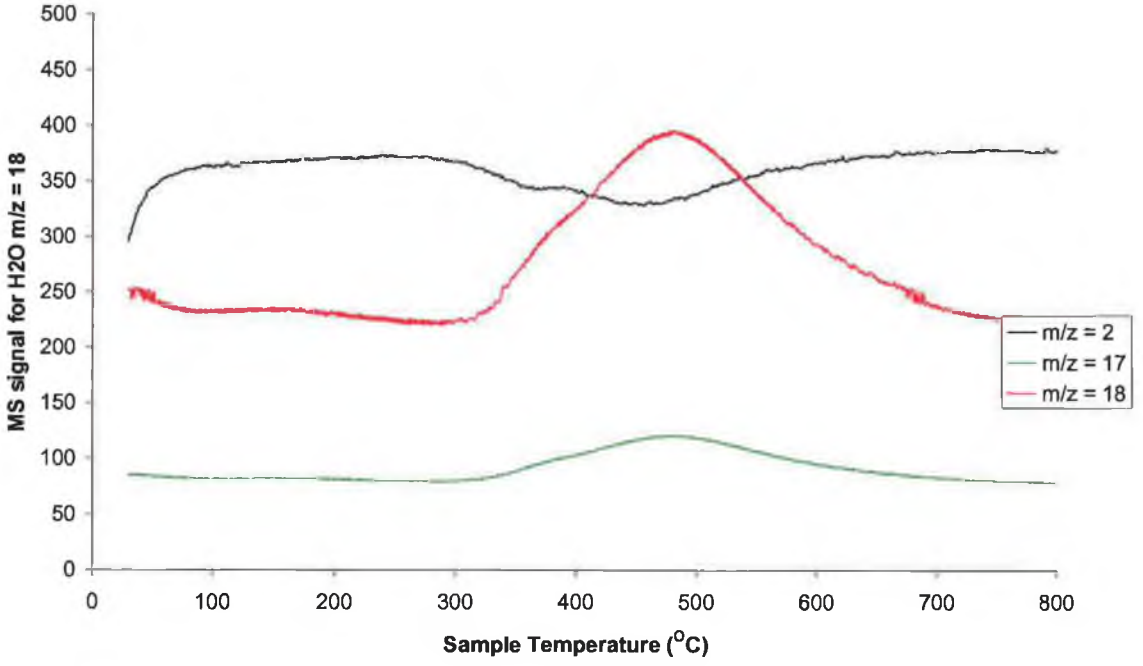

Fig 5.15: TPR-MS of ZrCo50-40A at a linear heating rate of 10°C/min, where the m/z =2, 17 and 18 refer to the MS signal for H_2, OH and H_2O respectively

For pure copper oxide, a single reduction peak with maximum temperatures of reduction at 322 and 303°C for water evolution and hydrogen uptake was observed in the TPR profile (see Fig 5.16). The reduction of bulk copper oxide has been reported more widely in the literature, but the temperatures of reduction vary from study to study. Lin et al reported that CuO is characterised by single peak at 375°C (37), while in another report (38), under TPR conditions of 30 mL/min gas flow of 10 % H_2 in N_2 passed over 50 mg samples and a linear heating rate of 10°C/min, copper oxide was reduced in a single step to metallic copper at 330°C. Kundakovic and Flytzani-Stephanopoulos (19) observed a peak for bulk copper oxide at 230°C under the following TPR conditions: 5% H_2 at a flow rate 500 cm^3min^{-1} and at a linear heating rate of 5°C/min.

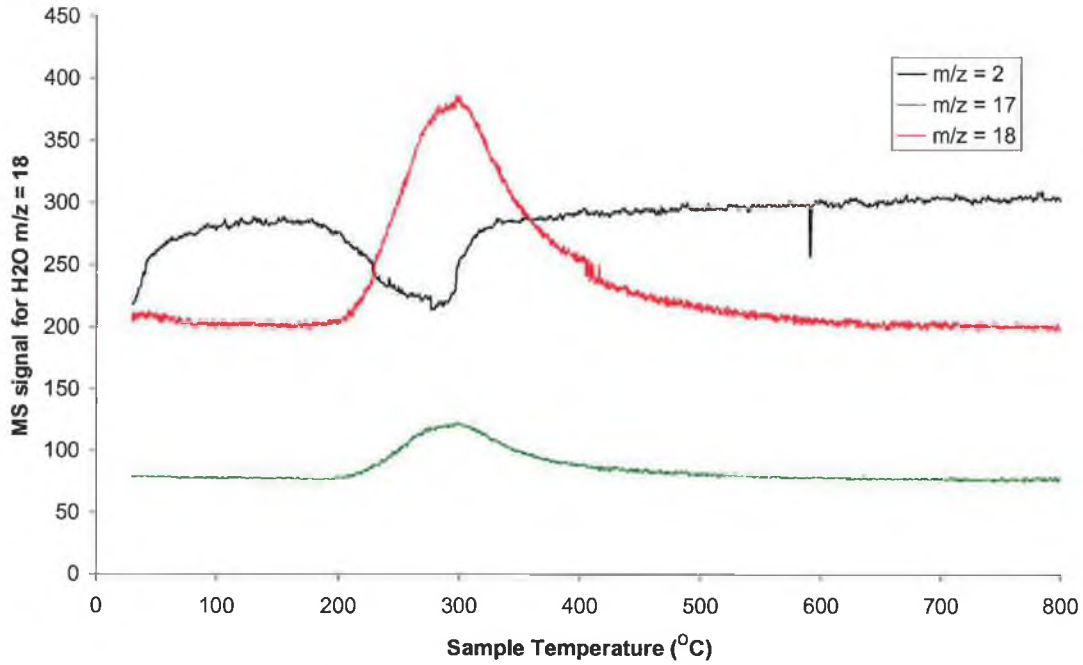

Fig 5.16: TPR-MS of ZrCu100-40B at a linear heating rate of 10°C/min, where the m/z =2, 17 and 18 refer to the MS signal for H_2, OH and H_2O respectively

For the mixed oxide ZrCu50-40A, a single reduction peak was also observed at a slightly lower temperature of maximum reduction of 302°C for water evolution (see Fig 5.17). In the literature (19), the Cu- modified oxides were prepared by urea co-precipitation of nitrate salts with copper loadings of 5, 25 and 40%. For 40 at % Cu, large reduction peak at 175 and small reduction peak at 140°C was observed which

approached that of bulk CuO. At low loadings, highly dispersed copper clusters were present at the surface which were more reducible than bulk CuO. For 10% Cu/ZrO_2, only one reduction peak at 140°C observed. For 15 wt%, a second reduction peak with maximum at 165°C was observed while for 40 at %, large reduction peak at 175°C and small reduction peak at 140°C. The difference in TPR characteristics was attributed to difference in structure with the various copper loadings. At copper loadings greater between 5-20 atom %, copper is present as highly dispersed clusters within the support while at 40 atom %, copper was present mainly as large CuO particles. In another study on the TPR profiles of supported copper on zirconia (39), 5 peaks were observed, namely at ; 185°C (referred to as peak α_1), 220°C (peak α_2, a shoulder of α_1), 278°C (peak β), 360°C (peak γ_1) and 395°C (peak γ_2). The α peaks increased with copper loading and reached a maximum value at 10 wt% copper. The gamma peaks were observed after 5 wt% loading and increased with increase in copper loading leading the authors to conclude that they are related to the reduction of bulk CuO which have no induction factor with the support. An induction factor refers to a synergistic interaction between zirconia and the dispersed copper species, which increases the reducibility of the copper species. In contrast the lower temperature peaks were due to highly dispersed copper species, which were created by an induction effect from the support and were more reducible than bulk CuO. In the current work, no low temperature peaks reported at 174 and 192°C due to an induction factor from the support were observed. This could be related to the high copper content of 50mol% of copper, which is comparative to 50 wt% and 50 atom % and the presence of a large reduction peak due to CuO. The presence of bulk CuO in the mixed oxide was detected in XRD analysis.

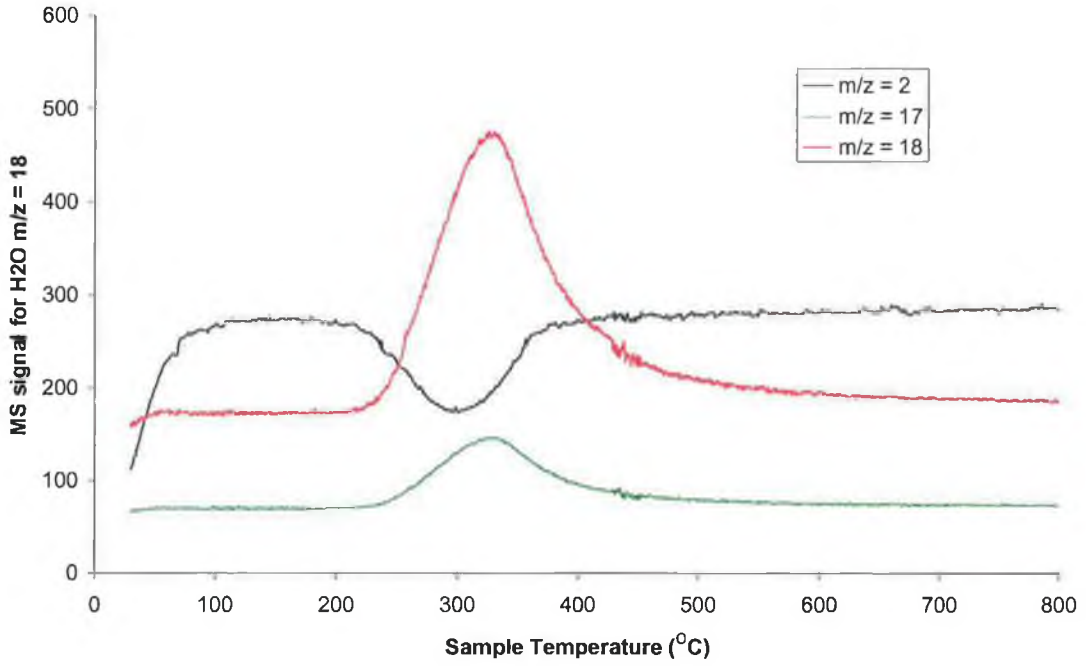

Fig 5.17: TPR-MS of ZrCu50-40A at a linear heating rate of 10°C/min, where the m/z =2, 17 and 18 refer to the MS signal for H_2, OH and H_2O respectively

5.3.4 Oxidation activities of fresh samples

The catalytic activity of the fresh oxides prepared was determined by measuring their activity for the combustion of methane, using the procedure described in chapter 2, the results of which are reported in Table 5.3. Firstly it was observed that the highest activity was observed for all of the pure cobalt oxides irrespective of preparation conditions. The activity is also significantly higher than that observed for pure CuO, although it is worth noting that the latter has a surface area approx 3 times lower than ZrCo100-40A. The T_{50} values for the various cobalt oxides are comparable to those observed by Tiernan et al (14) under the same conditions for cobalt trioxide (Co_3O_4) purchased from Sigma-Aldrich, with a surface area of 23 m^2g^{-1}. In that study (12), T_{50}s of 270 and 330°C were reported for run 1 and 2 for the above sample. Interestingly, for samples ZrCo100-20A and ZrCo100-40B in this current work, no significant decrease in light-off temperature was observed for run 2, as previously observed for Co_3O_4 (12).

Sample	SA (m^2g^{-1})	T_{10} (°C)		T_{50} (°C)		T_{90} (°C)	
		Run 1	Run 2	Run 1	Run 2	Run 1	Run 2
ZrCo100-20A	18	274	275	288	290	365	394
ZrCo50-20A	27	412	410	465	483	552	576
ZrCo50-20B	21	367		454		554	
ZrCo50-40A	55	349	339	408	425	488	550
ZrCo100-40A	16	274	277	288	291	346	350
ZrCo50-40B	33	310	360	412	443	556	581
ZrCu100-40B	6	333	390	390	464	478	533
ZrCu50-40A	40	357	396	408	449	493	556
ZrCo0-40A	52	510	541	Appr 600	>600	>600	>600

Table 5.3: Activity of selected oxides for the combustion of methane where T_{10}, T_{50} and T_{90} refer to temperatures of 10, 50 and 90% of methane conversion. Samples were initially tested (run 1) and then cooled to room temperature and retested in the same sample tube (run 2).

All the oxides were heated up to 600°C on run 1, with the exception of ZrCo100-40A, which was heated up to 500°C. The activities of the cobalt-zirconium mixed oxides were considerably lower than pure cobalt oxide despite a higher surface area (see Table 5.3). The magnitude of the decrease in activity depended on the preparation method of the mixed oxide. The lowest activity was observed for the samples prepared with 20 ml of sodium hydroxide with a T_{50} of 454 and 464°C, depending on the order of addition of the reagents. For the samples prepared with 40 ml of ammonia at 70°C, similar T_{50} values of 408 and 412°C were observed. On run 2, both samples suffered further deactivation. In the case of ZrCo50-40A, a lower surface area of 30 m^2g^{-1} was determined for the sample obtained after run 2 in methane. Hence the deactivation can be related to a 45% loss in surface area and sintering. The similar values obtained were surprising considering the lower surface area of the sample prepared by addition of base to the precursor solution, indicating that ZrCo50-40B is intrinsically more active. Similarly, for cobalt-zirconium mixed oxides prepared at 70°C but with 20ml of sodium hydroxide, ZrCo50-200B had a slightly lower surface area than ZrCo50-20A, but a comparable activity as indicated by similar temperature of 50% conversion. The

difference in activities between the samples prepared with 20 ml and 40 ml of sodium hydroxide can be attributed to both the lower surface of the former and/or the presence of more bulk cobalt oxide phase in the latter. A comparison of the activity curves of the different oxides in Table 5.3 are represented graphically in Fig 5.18.

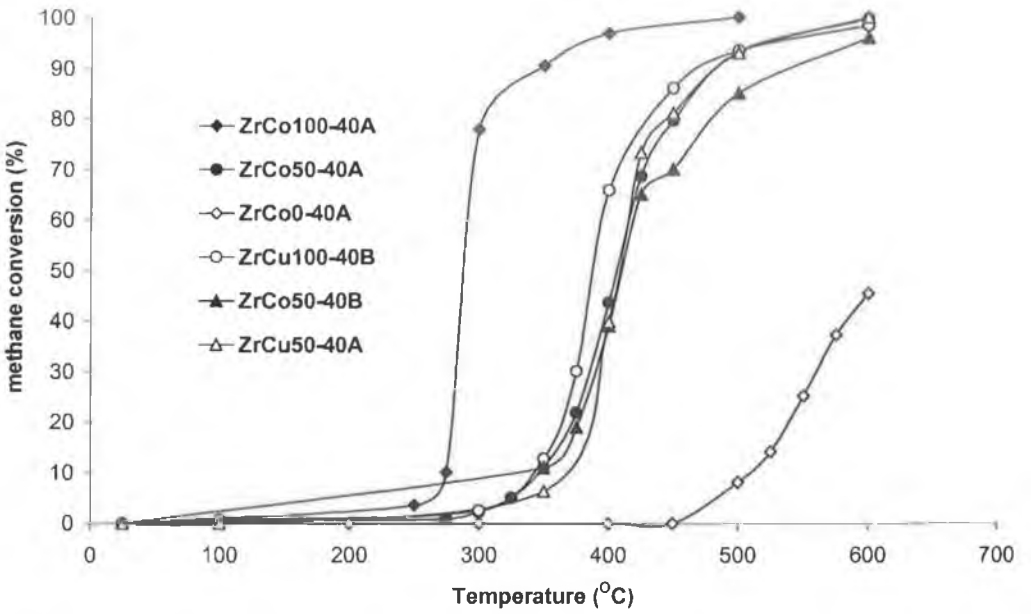

Fig 5.19:Plots of methane conversion (%) as a function of temperature for various fresh samples.

For supported cobalt-zirconia catalysts, Xiao et al (9) observed that the ZrO_2 impregnated with 1, 10 and 15 wt% had reached 50% conversion of methane at 460, 480 and 470°C. Tiernan et al (14) noted that a 15 wt% Co/ZrO_2 calcined at 400 and 600°C had T_{50} values of 395 and 490°C respectively, while 5% wt Co/ZrO_2 had reached 50% conversion at 490°C. Choudhary et al (16) also investigated the activity of cobalt doped zirconia (Co/Zr ratio of 0.25) for propane combustion. Samples were prepared via addition of tetramethyl ammonium hydroxide to a mixture of nitrate salts. On increasing the Co/Zr ratio from 0.11 to 0.43, the activity (in terms of the temperatures required for 50 and 90% conversion) passed through a maximum at a transition metal-zirconia ratio of 0.25. For copper zirconium mixed oxide, ZrCu50-40A, a much smaller increase in the T_{50} value was observed compared to pure CuO (ZrCu100-40B) than for the cobalt-zirconium mixed oxides. For copper oxides supported on zirconia (39), activity for CO oxidation increased greatly up until 10 wt% copper and beyond that

activity decreased mildly as determined by the temperatures at which 98% conversion was reached. Hence it was concluded that the predominant contributors to activity were highly dispersed copper oxide particles while bulk CuO contributed little to the catalytic activity. The conversion of propene by copper-zirconium oxides with Cu/Zr ratios of 0.01 and 0.1 has also been investigated (18). The mixed oxides were prepared the addition of a mixed copper nitrate and zirconium oxychloride solution to an excess of ammonia at pH 10-11 has also been investigated. For propene conversion, the order of catalytic activity for the co-precipitated samples was as follows:

Zr600<Cu 0.01/Zr600<Cu 0.1/Zr600< Cu 0.5 /Zr600.

Where Zr600 refers to zirconia support prepared from calcination of zirconium oxyhydroxide at 600°C, and Cu 0.01/Zr600, Cu 0.1Zr/600 and Cu0.5/Zr600 are co-precipitates prepared by impregnation of Cu/Zr atomic ratios of 0.01, 0.1 and 0.5 respectively calcined at 600°C. The greater content the copper content the more active the catalyst. Addition of copper to zirconia shifted the light-off temperature to lower temperatures. This was greater when copper/zirconium ratio was increased from 0.01 to 0.1, while a small increase in activity was observed on further increase from 0.1 to 0.5. Hence catalyst activity didn't increase proportionally to the copper content, and it was concluded that there was some copper limit above which masking of some active sites occurred. The copper mixed oxide studied in the current work had Cu content of 50 mol% which should compare to the Cu/Zr ratio of 0.5. This was definitely more active than pure zirconia but less active than pure copper oxide by approx 25°C. Dongare et al (21) also found that addition of copper to the zirconia shifted the light-off curve for the combustion of methane to lower temperatures and a maximum activity was observed for the copper loading of 20 mol%. The samples were prepared by a modified sol-gel technique. On increasing the copper content further to 33 mol %, a decrease in activity was observed.

Of all the oxides represented in Table 5.2, zirconia oxide was the least active despite the highest surface area, reinforcing the requirement of a transition metal oxide for good activity. The activity of zirconia with the highest surface area of 80 m^2g^{-1} (ZrCo0-40A) is compared with that of zirconia with a lower surface of 34 m^2g^{-1} (ZrO_2-NH_4OH) in Fig

5.19. As expected the sample with the highest surface area demonstrated the better activity with higher conversions at all temperatures 600°C.

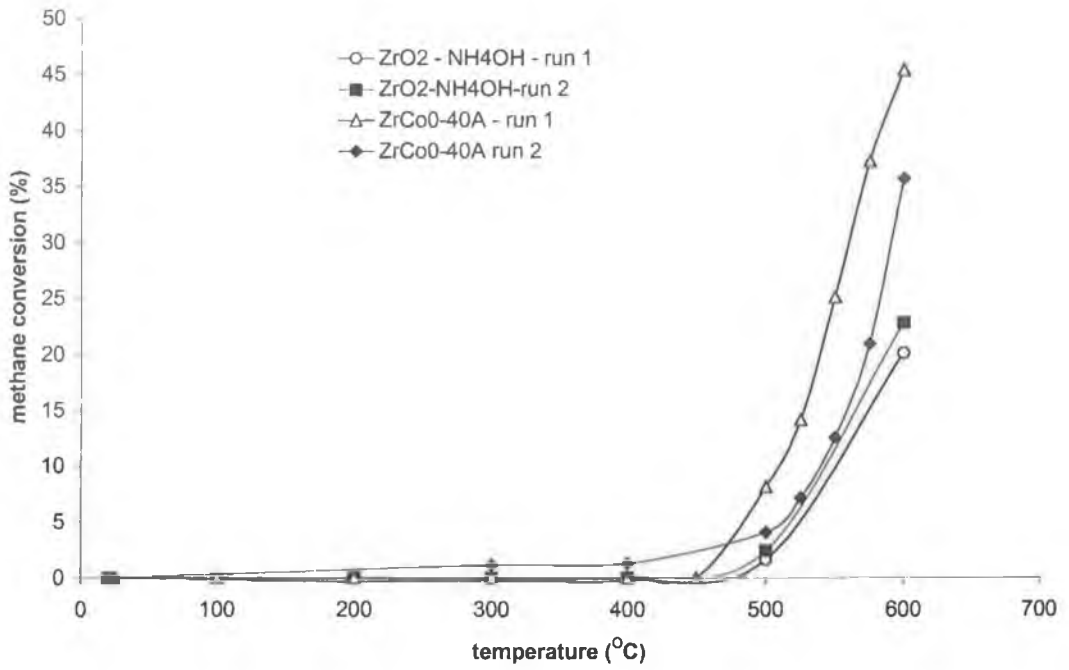

Fig 5.19:Plots of methane conversion (%) as a function of temperature for two zirconia samples with different surface areas.

5.3.5 Effect of aging on the XRD and surface areas on selected oxides

Selected fresh samples were then aged at 800°C for 8 hours in a static air muffle furnace. The XRD data and the surface areas of selected aged samples are reported in Table 5.4.

On aging, a dramatic structural change is noted in all the mixed oxides. For cobalt-zirconium mixed oxides, a significant amount of monoclinic zirconia is observed as evidenced by the two main peaks at approx 28.22° and 31.36°. The second peak at approx 31.36° appears to be split for both the cobalt-zirconium mixed oxides, although only one peak was detected in the peak search tool on analysis. The most likely reason is that that peak represents both a peak due to cobalt oxide and monoclinic zirconia since both occur at the same 2θ angle. The main cobalt oxide peak at approx 36.85°, that was also observed in the fresh sample, is maintained in all three samples (see Fig

5.16). This indicates that the Co_3O_4 phase is retained on aging up to 800°C in air. The peak at approx 30.28°, which represents tetragonal zirconia, is larger for the mixed oxide prepared via addition of the precursor solution to sodium hydroxide (ZrCo50-40A). This could be due to the larger surface area of this sample, whose smaller particle size could stabilise the tetragonal phase in comparison to ZrCo50-40B with the lower surface area.

Sample	**Main Peaks -(2θ)**	**Main Peaks- (d_{hkl})**	**I/I_0**	**SA (m^2g^{-1})**
ZrCu100-40B-ag	35.70, 38.90, 48.90, 61.65, 68.20, 66.35	2.52, 2.32,1.86, 1.50, 1.38, 1.41	100, 99, 33, 29, 24, 24	0.16
ZrCu50-40A - ag	35.50, 38.70, 28.15 31.45, 30.20, 50.15, 48.7, 34.05	2.53, 2.33, 3.17, 2.84, 2.96, 1.82, 1.87, 2.63	100, 97, 97, 72, 65, 48, 39, 35	1.69
ZrCu50-40B-ag*	30.25, 38.75, 35.60 28.25, 31.50, 50.30, 60.20, 48.75	2.95, 2.32,2.52 3.16, 2.84, 1.81 1.54, 1.87	100, 97, 92, 53, 42, 46 , 32, 29.	1.81
ZrCo50-40A-ag *	30.34, 36.93, 28.21, 31.49, 16.06, 50.49, 59.37, 35.36	2.94, 2.43, 3.16, 2.84, 5.51, 1.81, 1.55, 2.53	100, 85, 81, 62, 64, 57, 43, 42	14.5 ^
ZrCo100-40[a]-ag	36.87, 31.30, 65.25, 59.41, 44.84	2.43, 2.85, 1.43 1.55, 2.02	100, 39, 38, 32, 24.	5.00
ZrCo50-40B-ag *	36.85, 28.22, 31.36, 30.28, 50.24, 59.36, 65.30, 44.88	2.44, 3.16, 2.85, 2.95, 1.81, 1.55 1.43, 2.02	100, 72, 58 44, 38, 38, 36 32	6.5 ^

Table 5.4: XRD data and surface areas as determined by the BET method (SA) for aged oxides. For the XRD, the main diffraction peaks are represented in terms of 2θ, with the calculated interplanar spacing (d_{hkl}) and corresponding relative intensity (I/I_o). Io is the intensity (counts) of the peak with the greatest intensity for each catalyst and I is the intensity of the indicated peak relative to that. Error analysis on samples marked with ^ indicated errors of ± 2 m^2g^{-1} for SA (surface area analysis)

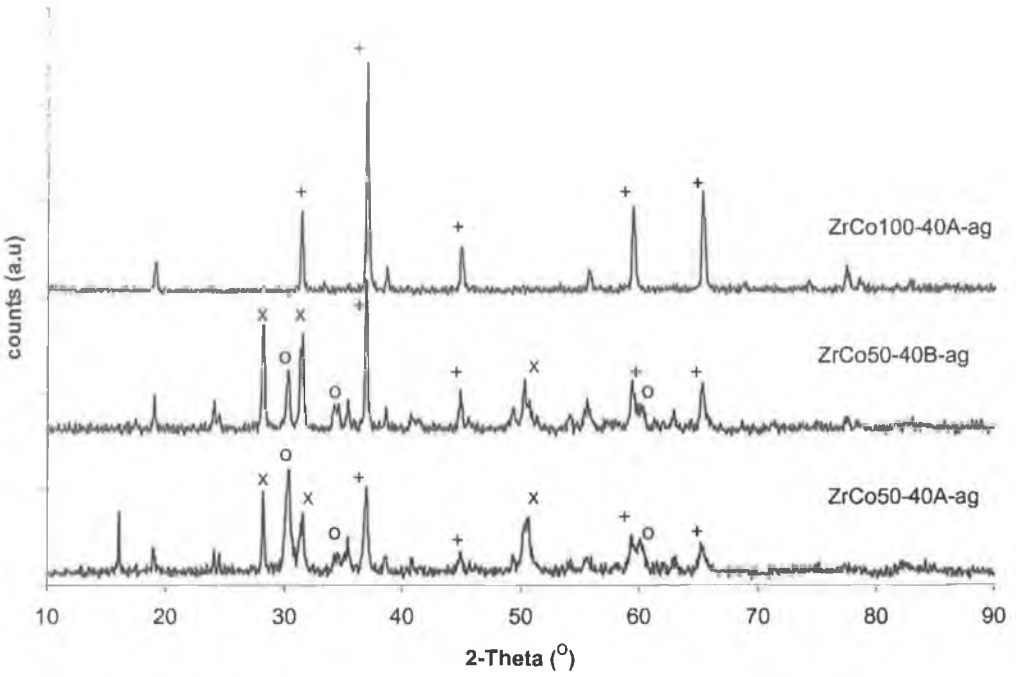

Fig 5.20:XRD data for aged samples where o, x and + represents peaks due to t-ZrO_2, m-ZrO_2 and Co_3O_4 respectively.

For copper-zirconium mixed oxides a similar situation was also observed (see Fig 5.21). Pure CuO retained the same structure on aging and the increased intensity and narrowness of the peaks can be attributed to the very low surface area of the aged sample. Both the monoclinic and tetragonal zirconia are observed in both of the mixed oxides, the quantity of the latter depended on the preparation method used. The monoclinic phase was detected by the peaks at 28.25-28.15° and 31.5°, while the tetragonal was indicated by the presence of a peak at 30.2°. After aging, the sample prepared by method A had a significantly larger amount of monoclinic zirconia present compared to the tetragonal phase. However both oxides had very small surface areas of 1.69 and 1.81 m^2g^{-1} respectively and hence no correlation between phase stabilisation and surface area stabilisation can be observed for these samples.

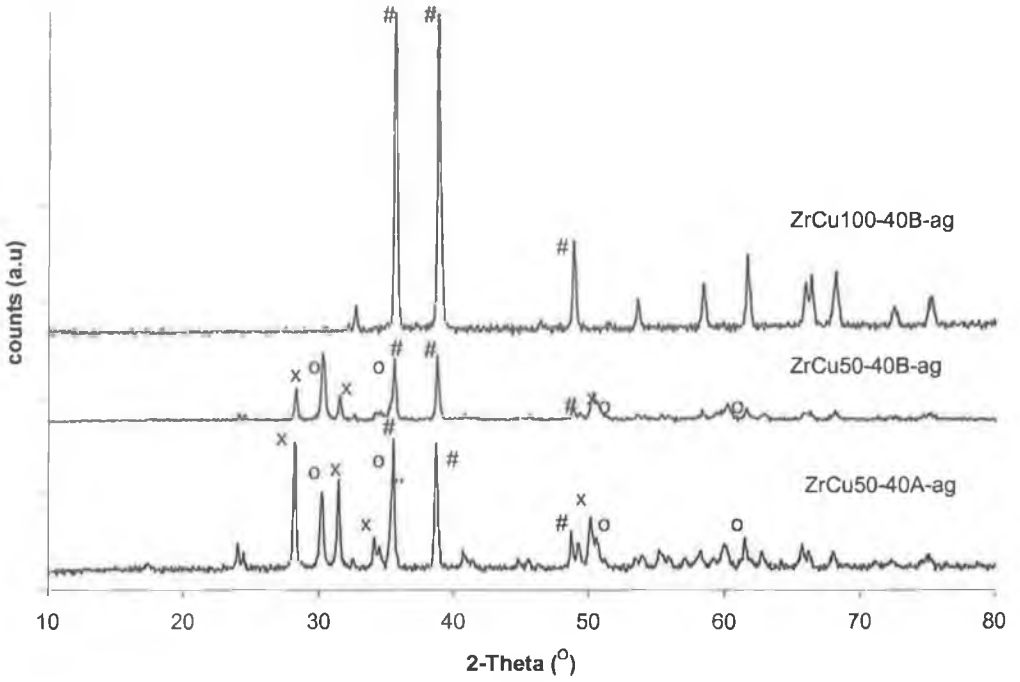

Fig 5.21: XRD data for aged copper and copper zirconium mixed oxides o, x and # represents peaks due to t-ZrO_2, m-ZrO_2 and CuO respectively.

A comparison of the fresh and aged surface areas of selected oxides is shown in Fig 5.22. All oxides showed a significantly lower surface area after aging. Of the pure oxides, ZrCo100-40A and ZrCu100-40B, the latter was the least stable with a loss of 100%. The copper zirconium mixed oxides have similar surface area loss relative to pure CuO, with losses of approx 96%. For the cobalt-zirconium mixed oxides, both ZrCor50-40B and ZrCo50-40B ,show greater losses compared to pure cobalt oxide of 80 and 74% respectively compared to 68% for pure cobalt oxide. Samples of pure CoO and Co_3O_4 (supplied by Sigma-Aldrich) showed decreases in surface area of 75% and 65% respectively.

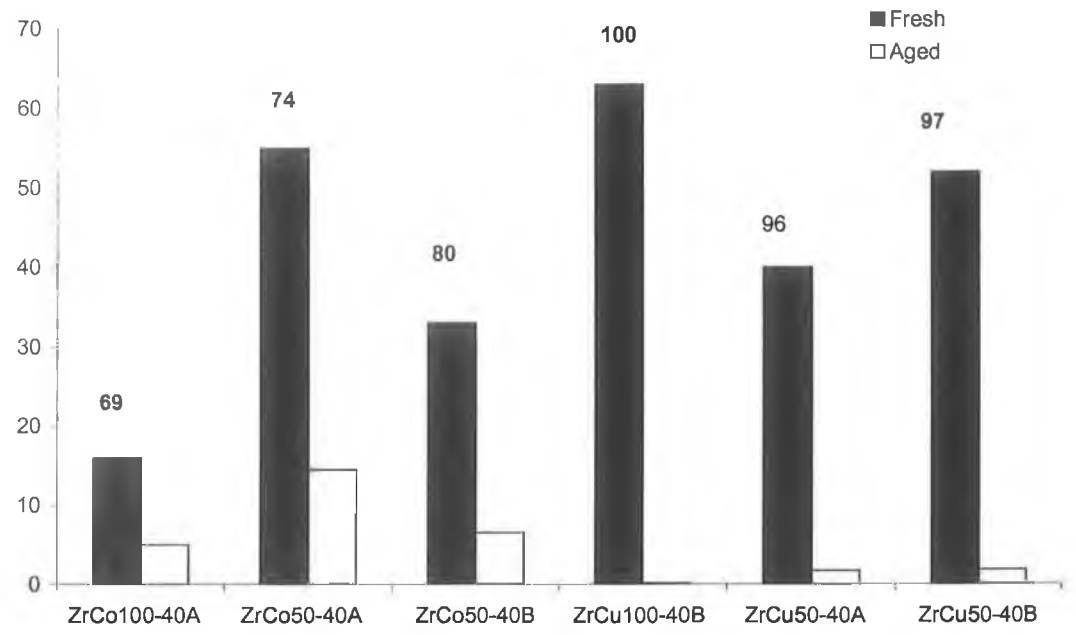

Fig 5.22: Comparison of surface areas before and after aging at 800°C for 8 hours in air for selected mixed oxides.

5.3.6 Oxidation activities of aged samples

The oxidation activities after aging for 800C for 8 hours in air of selected samples were determined using the procedures outlined in Chapter 2 and are given in Table 5.5 in terms of temperatures of 10, 50 and 90% conversion of methane. A significant loss of activity occurred for all the samples relative to fresh samples and some samples didn't even reach 50% conversion within the temperature range tested. The affect of aging on activity is also represented graphically in Fig 5.23 for cobalt oxides and 5.24 for copper oxides. For copper oxide and copper-zirconium mixed oxide, the loss in activity on aging were relatively the same, indicating that the addition of zirconium didn't have a significant effect on influencing the thermal stability (in terms of activity) of CuO.

On the other hand, the results of the cobalt-zirconium mixed oxides were very different. ZrCo100-40A showed a lower loss in activity of approx 130°C in the value of T_{50} than that observed for ZrCo50-40A (approx 189°C). Hence addition of zirconium accelerated the loss of activity compared to pure cobalt oxide. Indeed, the However, the sample

prepared by addition of sodium hydroxide to the mixed cobalt and zirconia precursor (ZrCo50-40B), showed a comparatively smaller loss in T_{50} value of 82°C.

Sample	T_{10} (°C)		T_{50} (°C)		T_{90} (°C)	
	Run 1	**Run 2**	**Run 1**	**Run 2**	**Run 1**	**Run 2**
ZrCo100-40A-ag	320	320	403	394	498	487
ZrCo50-40A-ag	495	507	597	597	>600	>600
ZrCo50-400B-ag	440	388	494	475	600	587
ZrCu100-40B-ag	511	466	>600	>600	>>600	>>600
ZrCu50-40Aa-ag	531	525	>600	>600	>>600	>600
Co_3O_4-Aldrich-ag	352	282	482	472	>600	>600
CoO-Aldrich-ag	387	408	484	489	605	610

Table 5.5 Activity of selected aged oxides for the combustion of methane where T_{10}, T_{50} and T_{90} refer to temperatures of 10, 50 and 90% conversion of methane conversion. Samples were initially tested (run 1) and then cooled to room temperature and retested in the same sample tube (run 2).

Co_3O_4 supplied by Aldrich showed a loss in activity of 200°C in terms of the light-off temperature value on aging. Tiernan et al (14) who had previously studied the activity of the fresh Co_3O_4 proposed that above 450°C, Co_3O_4 was converted to CoO and that this transformation occurred between run 1 and 2, causing an increase in the T_{50} of Co_3O_4 on run 2 of methane. The presence of CoO was indicated in the XRD pattern of the Co_3O_4 sample obtained after run 1 and run 2. In contrast for fresh ZrCo100-40A prepared in the current study, no change in the temperature at which 50% conversion of methane occurred was observed. The XRD of the aged sample was the same as the fresh sample, indicating no phase changes. Simonot et al (40) observed that at 850°C, Co_3O_4 transforms into CoO while Jankowiski et al (41) also noted that Co_3O_4 is transformed to CoO at approx 950°C in air. For the XRD data of Co_3O_4 and CoO the following peaks have been reported using $Cu_{k\alpha}$ radiation (42). For the former, 2θ = 31.2, 36.8, 44.5, 59.3 and 65.1°, while for the latter 36.8, 42.8 and 61.5°. Hence while both forms have a peak at 36.8° that was observed in the aged sample, no major peak was observed at 42.8° for aged ZrCo100-40-70A. Instead peaks at 31.30, 44.84, 59.41 and 65.25 ° were

observed, indicating the absence of any significant amount of CoO. The procedure used to prepare the pure cobalt oxide was similar to that reported by Christoskova (31), with the exception that NaOCl was not used in the current study. The cobalt oxide prepared in that study after calcinations at 300 and 900°C had the same structure, which was similar to that of Co_3O_4 but with different intensities. Transformation to CoO occurred at approx 920°C and was detected in the TG (31). The significant decrease in activity on aging is in contrast to that observed for manganese oxides in chapter 4. Pure manganese oxide prepared by ammonium hydroxide precipitation showed a significantly smaller loss in activity and surface area than both cobalt oxide and copper oxide, indicating that the activity of manganese oxide in itself is more stable on high temperature aging. The XRD of the mixed manganese oxides showed that they didn't undergo as much structural transformation as observed for the mixed copper and cobalt oxides. In the latter the formation of monoclinic zirconia was clearly indicated by the presence of two individual peaks while in the former, splitting but not full deconvolution of the main peak at approx 30° was observed.

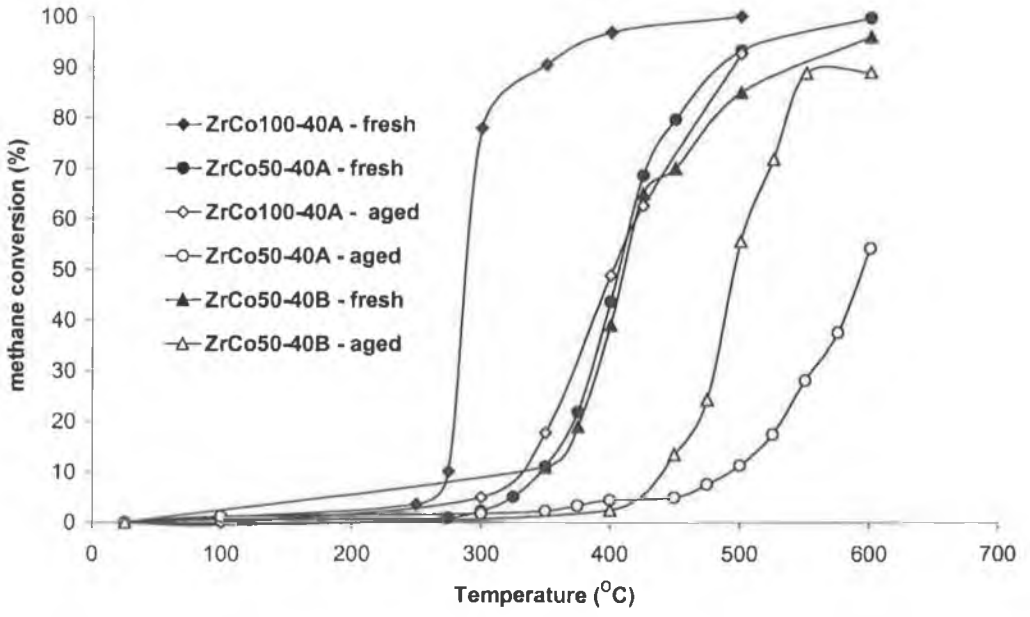

Fig 5.23: Plots of methane conversion (%) as a function for initial testing (run 1) of fresh and aged cobalt and cobalt-zirconium mixed oxides prepared by precipitation.

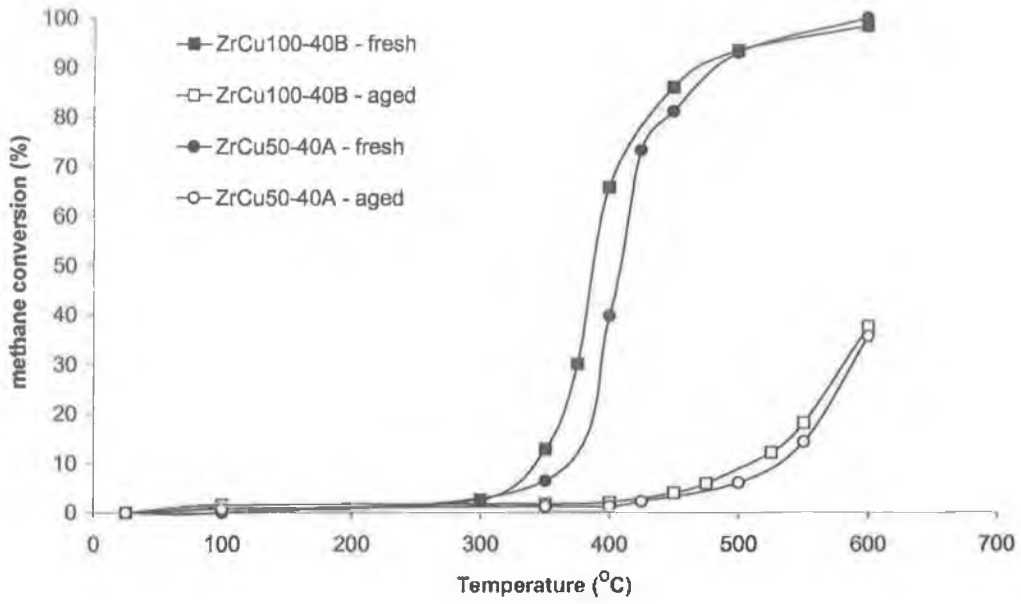

Fig 5.24: Plots of methane conversion (%) as a function of temperature of fresh and aged copper and copper-zirconium mixed oxides prepared by precipitation (Run 1 values used).

5.5 Conclusions

For cobalt-zirconium and copper-zirconium mixed oxides prepared by co-precipitation with sodium hydroxide, incorporation of higher loadings of cobalt and copper oxide (50 mol%) was not beneficial to the activity, surface area and reduction profiles when compared to pure cobalt and copper oxide. The preparation method used had an important effect on the above properties of the mixed oxides in particular. Four methods of preparation were used in general, addition of 4M NaOH to the precursor solution: (Method B) and vice versa (Method A), both at 25 or 70°C. For the mixed oxides, the SIP-MS indicated that 40 mL of base was required to remove all precursor nitrate ions. At 20 mL of base, the evolution of nitrate ions in the SIP-MS was evident. The SIP-MS spectra of the other catalysts tested indicated a mixture of hydroxide species, with the confirmation of the presence of cobalt oxide hydroxide via TG for cobalt containing samples during calcination. For copper and copper zirconium mixed oxides, the presence of $Cu(OH)_2$ is tentatively suggested.

The specific surface areas of the fresh samples were lower than those observed for pure zirconium oxide but higher than that observed for pure cobalt oxide and copper oxide. The higher surface area of zirconium oxide prepared by method A at 70°C compared to that prepared by ammonia addition by method B at room temperature in Chapter 3 is proposed to be due to a higher and more constant pH and/or higher temperature of precipitation. More study is required to elucidate the exact contribution of each. The percentage of tetragonal phase also increased with an increase in the surface area of various zirconia samples. Fresh mixed samples consisted of a mixture of phases of tetragonal zirconia and Co_3O_4 or CuO and the XRD data was affected by the order of addition of the reagents i.e. whether the base was added to the precursor solution or vice versa.

The activities of cobalt-zirconium mixed oxides were significantly lower than pure cobalt oxide. While the surface area was higher, it was still not high enough to compensate for the reduction in active cobalt phase compared to pure cobalt oxide, possibly due to coverage by zirconia particles. Samples prepared by method B were intrinsically more active than corresponding samples prepared by method A. In

comparison, a much smaller decrease in activity for copper-zirconia mixed oxides compared to pure CuO was observed. The activity of the copper-zirconium mixed oxide prepared by method B was not tested but its higher surface area could cause an increase in activity.

On aging at 800°C for 8 hours in air, a severe loss in activity for both pure and mixed oxides was observed. For copper-zirconium mixed oxides, both the pure and mixed oxide lost relatively the same activity. For cobalt-zirconium mixed oxides, the loss in activity depended on the preparation method used, with the sample prepared by method B exhibiting the smallest loss in activity of all the cobalt containing catalysts. The decrease in activity for the mixed oxide sample prepared by method A was larger than pure cobalt oxide prepared by the same method. Aged ZrCo100-40B had a similar T_{50} value to both of the fresh cobalt-zirconium mixed oxides prepared. The severe loss in activity of the mixed oxides is attributed to structural transformation and formation of monoclinic zirconia at the expense of tetragonal zirconia and the intrinsic instability of the pure cobalt and copper oxides.

References

(1) Boreskov, G. K., "*Catalytic Oxidation Of Dioxygen*", (Anderson, J. R., Boudart. M.,eds.), Catalysis, Science, and Technology, Vol.3, pages 40-137, Springer-Verlag, NY, 1982.

(2) Golodets, G. I., "*Heterogeneous Catalytic Reactions Involving Molecular Oxygen*", Elsevier, Amsterdam, 1983.

(3) Moro-oka,Y., Morikawa.Y., Ozak, A., *J. Catal.* **7**, 23 (1967).

(4) Sokolovskii, V. D., *Catal. Rev. Sci. Eng.* **32,** 1 (1990).

(5) Lin, P. Y., Skoglundh, M., Lowendahl, L., Otterstedt, J. E., Jansson, K., Nygren, M., *Appl. Catal., B* **6,** 237 (1995).

(6) Torncrona, A., Skoglundh, M., Thormählen, P., Fridell, E., Jobson, E., *Appl. Catal., B* **14,** 131 (1997).

(7) Skoglundh, M., Torncrana, A., Tormahel, P., Fridell, E., Drewsen, A., Jobson, E., in "*Catalysis and Automotive Control IV*" (Kruse, N., Frennet, A., Bastin, J.-M., eds.), Studies in Surface Science and Catalysis IV, Vol. 116, 113-123, Elsevier, New York, 1998.

(8) Garbowski, E., Guenin, M., Marion, M-C., Primet, M., *Appl. Catal., A.* **64**, 209 (1990).

(9) Xiao, T., Ji, S., Wung, H., Coleman, K. S., Green. M. L. H., *J. Mol. Catal. A: Chem.* **175**, 111 (2001).

(10) Zhou, R., Jiang, X., Mao, J., Zheng, X., *Appl. Catal.* **162,** 213 (1997).

(11) Dow, W-P., Huang, T. J., *J. Catal.* **160**, 171 (1996).

(12) Anderson, R. B., Stein, K. C., Feenan, J. J., Hofer, J. E., *Ind. Eng. Chem.* **53,** 809 (1961).

(13) Marion, M. C., Garbowski, E., Primet, M., *J. Chem. Soc., Faraday Trans.* **86**, 3027 (1990)

(14) Tiernan, M. J., Fesenko, E. A., Barnes, P. A., Parkes, G. M. B., Ronane, M., *Thermochim. Acta* **379,** 163 (2001).

(15) Milt, V., Lombardo, E. A., Ulla, M. A., *Appl. Catal., B* **37,** 63 (2002).

(16) Choudhary, V. R., Banerjee, S., Pataskar, S. G., *Appl. Catal., A* **253,** 65 (2003).

(17) Choudhary, V. R., Uphade, B. S., Pataskar, S. G., Keshavaraja, A., *Agnew. Chem. Int. Ed. Engl.* **35,** 2393 (1996).

(18) Labaki, M., Lamonier, J.-F., Siffert, S., Zhilinskaya, E. A., Aboukaïs, A., *Colloids and Surfaces A; Physicochem. Eng. Aspects* **227,** 63 (2003).

(19) Kundakovic, L. Flytzani-Stephanopoulos, M., *App. Catal., A* **171,** 13 (1998).

(20) Bhagwat, M., Ramaswamy, A. V., Tyagi, A. K., Ramaswamy, V., *Mater. Res. Bull.* **38,** 1713 (2003).

(21) Dongare, M. K., Ramaswamy, V., Gopinath, C. S., Ramaswamy, V., Scheurell, S., Brueckner, M., Kemnitz, E., *J. Catal.* **199,** 209 (2001).

(22) Dongare, M. K., Dongare, A. V., Tare, V. B., Kemnitz, E., *Solid State Ionics* **152,** 455 (2002).

(23) Vogel, A. R., "*Qualitative Inorganic Analysis*", London : Longman, 1996.

(24) Christoskova, St. G., Stojanova, M., Georgieva, M., Mehandzhiev, D., *Mater. Chem. Phys.* **60,** 39 (1999).

(25) Cseri, T., Bekassy, S., Kenessey, G ., Liptay, G., Figueras, F., *Thermochim. Acta* **288,** 137 (1996).

(26) Xu, Z. P., Zeng, H. C., *J. Mater. Chem.* **8,** 2499 (1998).

(27) Sato, T., Ozawa, F., Nakumura, T., Watanabe, H., Ikoma, S., *Thermochim. Acta* **34,** 211 (1979).

(28) Tanaka, H., Sadamoto, T., *Thermochim. Acta* **54,** 273 (1982).

(29) Chuah, G. K., Jaenicke, S. A., Cheong, S. A., Chan, K. S., *Appl. Catal., A* **145,** 267 (1996).

(30) Tichit, D., El Alami, D., Figueras, F., *Appl. Catal., A* **145,** 195 (1996).

(31) Christoskova, St. G., Stojanova, M., Georgieva, M., Mehandzhiev, D., *Thermochim. Acta* **292,** 77 (1997).

(32) Radwan, N. R. E., Mokhtar, M., El-Shobaky, G. A., *Appl. Catal., A* **241,** 77 (2003).

(33) Calafat, A., in "*Preparation of Catalysts VII*", (Delmon, B., Jacobs, P. A., Maggi, R., Martens, J. A., Grange, P., Poncelet, G., eds). Studies in Surface Science and Catalysis, Vol.118 , 837-843, Elsevier, New York, 1998.

(34) Chuah, G. K., Jaenicke, S., Cheong, S. A., Chan, K. S., *Appl. Catal., A* **145,** 267 (1996).

(35) Garvie, R. C., *J. Phys. Chem.* 1238 (1964).

(36) Arnone. S., Bagnasco. G., Busca. G., Lisi. L., Russo. G., Turco. M., in "*Natural Gas Conversions V*" (Parmaliana, A., Sanfilippo, D., Frusteri, F., Vaccari,A., Arena, F., eds.), Studies in Surface Science and Catalysis, Vol.119, 65-70, Elsevier, Amsterdam, 1998.

(37) Rui, L., Luo, M-F., Zhong, Y-J., Yan, Z-L., Liu, G-Y ., Liu, W-P., *Appl. Catal., A* **255,** 331 (2003).

(38) Buciuman. F. C., Patcas, F., Hahn, T., *Chemical Engineering and Processing,* **38,** 563 (1999)

(39) Zhou, R., Yu, T-M ., Jiang, X, Chen, F., Zheng, X., *Appl. Surf. Sci.* **148,** 263 (1999).

(40) Simonot, L., Garin. F., Maire. G., *Appl. Catal., B* **11,** 167 (1997).

(41) Jankowiski, J., Thomas, G., Camby, L. P., *Solid State Ionics*, 1997

(42) Zhang, X., Lee, C.S-M., Mingos, D. M. P., Hayward, D. O., *Appl. Catal., A* **248,** 129 (2003).

6. General Conclusions

In this thesis, transition metal mixed oxides have been prepared and characterised with the aim of evaluating their potential as catalysts for the total oxidation of hydrocarbons such as propane and methane. The transition metal mixed oxides prepared consisted of a metal (manganese, copper, cerium or cobalt) oxides and zirconium dioxide. The mixed oxides have been prepared by two different methods: modified sol-gel technique and co-precipitation. Characterisation techniques used include temperature-programmed reduction, solid insertion probe-mass spectrometry, simultaneous thermogravimetry-differential thermal analysis in air and X-Ray diffraction. Specific surface areas have been evaluated from nitrogen adsorption at 77K and catalytic activity for methane and propane combustion have been performed in continuous flow reactors.

For all the oxides studied, the preparation method used had a significant effect on the structure and surface area, and hence also in general their catalytic activity. Activities were compared by comparison of T_{50} i.e. temperatures required for 50% conversion of methane and propane. The least active oxide for both propane and methane combustion was pure zirconia, despite a relatively high surface area compared to some of the mixed oxides (ceria-zirconia mixed oxides). Of the other pure oxides, namely CeO_2, Mn_2O_3, CuO and Co_3O_4, ceria was the least active for the propane oxidation. In the majority of cases, addition of the active transition metal to zirconia improved the catalytic activity for combustion of both hydrocarbons, with the exception of ZrCe10-sg.

The surface areas of the mixed oxides also depended on the preparation method used and also on the identity of the transition metal oxide. Using the same amount of ammonium hydroxide and precursor concentration in the co-precipitation technique resulted in low surface area ceria-zirconia mixed oxide samples while significantly higher values were observed for manganese-zirconia mixed oxides. This was attributed in part to lower pH values for the former. The sol-gel method proved to be effective for the ceria-zirconia mixed oxides, with higher surface areas and lower light-off temperatures (T_{50}) than the corresponding samples prepared by the co-precipitation method. TPR indicated that the former was also more reducible than the latter.

Higher surface areas were recorded for manganese-zirconium, cobalt-zirconium and copper-zirconium mixed oxides prepared by co-precipitation using ammonium hydroxide or sodium hydroxide. Of these the highest surface area was obtained for a 50 wt% Mn sample after optimisation of the preparation technique. Of the parameters varied, namely amount of ammonium hydroxide added, rate of ammonia addition, stirring time of precursor solution prior to reaction and extent of dilution of precursor solution, the latter two factors had the most significant effect on resultant surface areas. The oxides were more active than 0.5 wt%Pt/Al_2O_3 sample for methane combustion. In the case of the manganese-zirconia and ceria-zirconia mixed oxides, the presence of manganese and cerium stabilised the presence of the metastable tetragonal zirconia. In pure zirconia prepared by both precipitation with ammonium hydroxide and the sol-gel technique, a mixture of monoclinic and tetragonal phases were observed. In the case of manganese-zirconia, formation of a solid solution or single phase was observed up till 30 mol% Mn.

The effect of aging at 800°C for 8 hours on catalytic activity depended on the transition metal oxide system investigated and the preparation method used. Incorporation of zirconia into ceria via the sol-gel method decreased the loss in activity and surface area on aging at 800C for 8 hours. For manganese-zirconia mixed oxides, an increase in the oxidation activity for propane was observed, while for methane the T_{50} values remained within experimental error of the fresh samples with the exception of ZrMn70-cp (70 mol % manganese sample). Pure manganese oxide also prepared by precipitation with ammonium hydroxide showed a small increase in T_{50} values for both propane and methane under the same aging conditions. The reducibility of the manganese-zirconia mixed oxides increased on aging and it was proposed that the more reactive lattice oxygen observed compensated for the negative effect of the loss in surface area. It could not be definitively concluded if the increase in reducibility was due to the preparation method used as well as the presence of zirconium since no TPR-MS was performed on aged manganese oxide. However, other pure manganese oxides purchased from Aldrich showed a decrease in both reducibility and activity on aging.

No significant changes in the XRD patterns of the manganese-zirconia mixed oxides were observed on aging and the tetragonal zirconia phase remained the predominant phase. This was in contrast to pure zirconia, where transformation to the monoclinic phase was observed under the same aging conditions.

The addition of 50 mol% of copper and cobalt oxides to zirconia did not prevent the transformation of the tetragonal phase to the monoclinic phase. Large losses in the oxidation activities of the mixed copper-zirconium, cobalt-zirconium, pure copper and cobalt oxides prepared by precipitation with sodium hydroxide were observed after heating at 800°C for 8 hours. The behaviour of the mixed cobalt-zirconium oxides under aging conditions varied depending on whether the precursor solution was added to the base or if the base was added to the precursor solution. The cobalt-zirconium mixed oxide prepared by the latter method had a lower initial surface area and showed the smallest loss in activity than the same sample prepared by the former method. However, the addition of zirconia to the pure cobalt and copper oxides had no beneficial effect with aged pure cobalt oxide still more active than both fresh cobalt-zirconium mixed oxide samples. The severe loss in activity was attributed to the structural transformation to monoclinic zirconia on aging and the intrinsic instability of the pure cobalt and copper oxides.

Manganese-zirconia mixed oxides prepared by precipitation with ammonium hydroxide show good activity as catalysts in methane and propane combustion and that activity is maintained or improved during aging at 800C for 8 hours. Hence they may be viewed as potential alternatives to platinum supported catalysts for hydrocarbon oxidation.

APPENDIX A:

BET ISOTHERM AND CALCULATION OF SURFACE AREA.

Physisorption of nitrogen can be use to calulate specific surface area. The simplest adsorption isotherm is the Langmuir isotherm, which describes the variation of fractional surface coverage with pressure at a given temperature (1). However one of its main assumptions is that adsorption cannot proceed beyond monolayer coverage. In the case of physical adsorption of nitrogen on a surface, multilayer adsorption can occur above a certain pressure (P_o). Below this pressure, one layer of nitrogen molecules covers the surface. Above this value, nitrogen condenses onto the surface and adsorbs onto the existing monolayer. This causes the volume adsorbed to rise infinitely over a certain pressure. Hence, Brauner, Emmet and Teller derived the BET equation to take into account multi-layer adsorption (2).

$$\frac{p}{V(p_o - p)} = \frac{1}{V_m * c} + \frac{(c-1)}{V_m * c}\frac{p}{p_o} \qquad (1)$$

where p_o is the saturated vapour pressure of nitrogen at adsorption temperature(77K)
V is the volume adsorbed at pressure p
V_m is the volume required to give monolayer coverage
c is a large constant.

A plot of $p/V(p_o-p)$ against P/P_o yields a straight line the slope and intercept of which can be used to calculate V_m. By expressing the specific monolayer volume in m^3/g, the nimber of molecules adsorbed in the monolayer can be calculated with the following equation

$V_m/0.0224 * 6.023 * 10^{23}$

Once the surface area of each nitrogen molecule is known the surface area at 77K can be easily calculated.

References

(1) Atkins, P.W., "*Physical Chemistry*", Oxford Press, Oxford, 1987.

(2) Thomas, J.M., Thomas, W.J., "*Principle and practice of heterogeneous catalysis*" VCH, New York, 1997.